
SURFACE AND INTERFACE PHENOMENA IN ORGANIC THIN FILM TRANSISTORS

SIMON J. NOEVER



München 2016

SURFACE AND INTERFACE PHENOMENA IN ORGANIC THIN FILM TRANSISTORS

SIMON J. NOEVER

Dissertation
durchgeführt an der Fakultät für Physik
der Ludwig–Maximilians–Universität
München

vorgelegt von
Simon J. Noever
aus Starnberg

München, den 10. Mai 2016

Erstgutachter: PD. Dr. Bert Nickel

Zweitgutachter: Prof. Jose A. Garrido

Tag der mündlichen Prüfung: 28. Juli 2016

"[...] I am still confused, but on a higher level."

Enrico Fermi (1901 - 1954)

SUMMARY

The processing of organic electronic devices differs substantially from the smart layout of strongly and weakly doped or oxidized areas within one semiconducting material, as used in conventional inorganic electronics. In contrast, it is mainly realized by successive layering of different materials. This way, the efficiency of organic devices strongly depends on the quality of the inherent interfaces. In systems such as organic thin film transistors for example the semiconducting layer forms interfaces with the electrodes and the dielectric, respectively. Moreover, especially for those devices which show commercial promise, like organic light emitting diodes and photovoltaics, the charge transfer at the interface between two semiconductors plays a significant role.

The cumulative thesis at hand focuses on the investigation of these three important interfaces. For this purpose, three model systems are used to demonstrate the development and optimization of methods to analyze and fabricate semiconductor structures.

First, the evolution of charge transport within an ambipolar pentacene-C₆₀ thin film transistor is investigated *in-situ*, i.e. during semiconductor growth under high vacuum conditions. To this end, a p-conducting pentacene based top-contact transistor with an active layer thickness of 20 nm was contacted inside a high vacuum chamber. Then the characteristic curves were measured while the n-conducting C₆₀ film was deposited at a rate of ca. 0.1 Ås⁻¹. The thickness resolution revealed for the first time, how the threshold voltage of the p-conducting channel quickly shifts towards more positive values when the C₆₀ film starts to percolate. This is explained by the Fermi-level alignment of the two semiconductors, which leads to positive charge transfer from pentacene to C₆₀ and negative charge transfer from C₆₀ to pentacene. In addition, the completed device showed well balanced high charge carrier mobilities of ca. 0.28 cm²V⁻¹s⁻¹ for holes and 0.18 cm²V⁻¹s⁻¹ for electrons, respectively. The deposition setup and the *in-situ* measuring station employed in this experiment were designed and optimized in the course of this thesis. The structure of the pentacene-C₆₀ double layer was investigated at a synchrotron via grazing incidence X-ray diffraction, while its topography was recorded using atomic force microscopy, in order to support the interpretation of the afore mentioned results. The results of the X-ray investigation showed that the typical thin film phase growth of pentacene was not influenced by the subsequent fullerene deposition. The C₆₀ film forms a crystalline FCC structure oriented in [111]-direction. The drop-like topography of C₆₀, which traces the pyramidal surface of pentacene was resolved by atomic force microscopy. Moreover, it could be shown that films below their percolation limit aggregate as disjoint droplets whose spatial distribution depends on the grain size of the pentacene film.

In a second *in-situ* experiment, the growth mode of pentacene on a rough parylene-C dielectric (rms ca. 7 nm) was determined. Although the roughness of the employed dielectric is decidedly larger than the length of a pentacene molecule, the fabrication of efficient thin film transistors is not prohibited. Conventional methods to resolve structure and topography cannot quantify sub-monolayer growth of films that are considerably thinner than the vertical roughness of the substrate surface. Measuring the characteristic curves of a bottom-contact thin film transistor *in-situ* provided evidence that the pentacene film percolated on parylene-C before the first nominal monolayer was completed. This means that during the critical initial stage of film formation, pentacene grows layer-by-layer. Combining these findings with atomic force microscopy micrographs, the film formation could be determined to follow the Stranski-Krastanov growth mode.

In addition to the *in-situ* measuring station, a new method was developed to laminate semiconducting nanosheets of vacuum deposited small aromatic molecules to any kind of water stable technical surfaces or cavities. To this end, we partially crosslinked fragile, van der Waals bound pentacene thin films with a thickness of only 50 nm. Here, only a very thin layer located at the film surface is mechanically stabilized via crosslinking, while the rest of the film stays unchanged, i.e. it keeps its crystalline structure and semiconductor properties. The films were irradiated with low energy electrons, where a charge carrier energy of 500 eV, a duration of 20 minutes and a dose of ca. 3 mCcm⁻² lead to a good compromise between stability and semiconductor quality. Using depth controlled grazing incidence X-ray diffraction it could be verified that the crosslinking starts from the top surface of the film. In addition, UV-VIS and FTIR spectra confirmed the manner in which the films crosslink as well as their thickness. The nanosheets could be transferred under water using tweezers to new substrates, as well as spanned over macroscopic cavities, by employing a sacrificial, water soluble poly-vinyl-alcohol layer. As a first application, pentacene thin films were transferred to gold bottom-contact transistor structures. This way, the contact resistance of the device could be reduced by over two orders of magnitude, from ~ 10⁷ Ω to ~ 10⁵ Ω, with respect to deposited films. This is explained by the fact that sublimated films show significant dewetting close to gold structures and impaired growth on top of polycrystalline gold surfaces. In the case of transferred films on the other hand infrared scanning near field microscopy unveiled that the molecular structure, as well as the topography stay intact. The method could constitute a basis for new kinds of sensors and air- or vacuum-dielectric thin film transistors.

ZUSAMMENFASSUNG

Die Hauptkomponenten organischer Elektronik werden grundlegend anders prozessiert als durch die geschickte geometrische Anordnung von stark und schwach dotierten, beziehungsweise oxidierten Bereichen eines bestimmten Halbleiters, so wie es für klassische, anorganische Bauteile der Fall ist. Sie werden vielmehr durch die Schichtung unterschiedlicher Materialien, die ihren jeweiligen Zweck erfüllen, realisiert. Somit entsteht eine starke Abhängigkeit der Effizienz organischer Bauteile von der Qualität der in ihnen auftretenden Grenzschichten. In Systemen wie organischen Dünnschichttransistoren sind dies im Wesentlichen die Grenzschichten zwischen dem Halbleiter und den Elektroden, beziehungsweise dem Dielektrikum. Doch gerade in denjenigen Komponenten, die heute schon kommerziellen Erfolg genießen, wie organischen Licht emittierenden Dioden und Solarzellen, spielt auch der Ladungstransport an der Grenzschicht zwischen zwei unterschiedlichen Halbleitern eine entscheidende Rolle.

Der Fokus der vorliegenden, kumulativ verfassten Doktorarbeit liegt auf der Untersuchung der drei Hauptgrenzschichten an drei unterschiedlichen Modellsystemen und der Vorstellung der dabei entwickelten und optimierten Methoden zur Analyse und zur Herstellung von organischen Halbleiterstrukturen.

Die erste Arbeit untersucht *in-situ*, das heißt im Hochvakuum während der Sublimation einer Halbleiterschicht, die Entwicklung des Ladungstransportes in einem ambipolaren Pentacen- C_{60} Dünnschichttransistor. Hierzu wurde ein p-leitender Top-Kontakt Transistor auf Pentacen Basis mit einer Halbleiterschichtdicke von 20 nm in einer Hochvakuumkammer kontaktiert. Anschließend wurde der n-leitende C_{60} Film mit einer Geschwindigkeit von ca. 0.1 \AA s^{-1} auf das Bauteil aufgedampft, während stetig die Transistorkennlinien aufgenommen wurden. Durch die Schichtdickenauflösung der charakteristischen Kennlinien konnte zum ersten Mal gezeigt werden, dass die Schwellenspannung des p-leitenden Kanals ab der eintretenden Perkolation des C_{60} Films einen Sprung zu positiveren Gate-Spannungen macht. Dies wurde damit erklärt, dass durch das angleichen der Fermi-Level der beiden Halbleiter Elektronen in den Pentacenefilm, beziehungsweise Löcher in den C_{60} -Film transferieren. Der fertige Transistor zeigte zudem sehr ausgeglichene und hohe Ladungsträgermobilitäten von ca. $0.28 \text{ cm}^2 \text{ V}^{-1} \text{ s}^{-1}$ für Löcher und $0.18 \text{ cm}^2 \text{ V}^{-1} \text{ s}^{-1}$ für Elektronen. Das für diesen Versuch genutzte Sublimationssetup, sowie die *in-situ* Messstation wurden im Rahmen der Doktorarbeit entworfen und optimiert.

Um die Messergebnisse besser interpretieren zu können, wurde das Pentacene- C_{60} Doppelschichtsystem zusätzlich strukturell mittels Röntgenstreuung unter streifendem Einfall am Synchrotron und topografisch mittels Rasterkraftmikroskopie untersucht. Die Röntgenstrukturanalyse ergab, dass das typische Dünnschichtphasenwachstum des Pentacene Films nicht durch das nachträgliche Aufdampfen der

Fullerenschicht beeinträchtigt wurde. Dem C₆₀ Film konnte wiederum eine FCC Struktur in [111]-Richtung nachgewiesen werden. Die Rasterkraftmikroskopie ergab, dass der C₆₀ Film eine tropfenartige Topographie bildet, die der darunterliegenden pyramidalen Oberfläche des Pentacens folgt. Filme unterhalb der Perkolationsschichtdicke aggregieren in disjunkten Tröpfchen, deren räumliche Anordnung wiederum von der Korngröße des Pentacensfilms abhängt.

In einem weiteren *in-situ* Experiment wurde der Wachstumsmodus von Pentacen auf einem rauen Parylene-C Dielektrikum (rms ca. 7 nm) bestimmt. Obwohl die Rauigkeit dieses Dielektrikums deutlich größer ist, als die Moleküllänge des Halbleiters, können auf diesem effiziente Dünnschichttransistoren realisiert werden. Mit herkömmlichen strukturellen und topografischen Methoden ist es nicht möglich das Sub-Monolagenwachstum von Filmen zu quantifizieren, welche deutlich dünner sind, als die vertikale Rauigkeit des Untergrunds. Mittels *in-situ* Charakterisierung der Kennlinien eines Bottom-Kontakt Dünnschichttransistors konnte hier jedoch festgestellt werden, dass der Pentacensfilm unterhalb der nominellen Schichtdicke einer Monolage auf der Parylen-C Oberfläche perkoliert. Dadurch konnte nachgewiesen werden, dass sich der Halbleiter auch auf dem hier verwendeten Dielektrikum, in der entscheidenden Anfangsphase des Wachstums Schicht für Schicht anordnet. Zusammen mit Rasterkraftmikroskopie Messungen wurde als Wachstumsmodus schließlich das Stranski-Krastanov Wachstum identifiziert.

Zusätzlich zu dem *in-situ* Messaufbau wurde eine neue Methode entwickelt, die es erlaubt, Halbleiter-Nanofolien aus Vakuum verdampften kleinen aromatischen Molekülen auf wasserstabile technische Oberflächen oder über Löcher im Substrat zu laminieren. Hierzu werden fragile van-der-Waals gebundene Pentacens Dünnschichten mit einer Dicke von nur 50 nm teilweise quervernetzt. Dabei wird nur eine dünne Schicht an der Filmoberfläche vernetzt und somit mechanisch stabilisiert, während der Rest des Filmes unverändert bleibt, also die kristalline Struktur und seine halbleitenden Eigenschaften beibehält. Die Filme wurden hierfür mit niederenergetischen Elektronen bestrahlt, wobei Ladungsträgerenergien von 500 eV bei einer Bestrahlungsdauer von 20 Minuten und einer Dosis von ca. 3 mCcm⁻² einen guten Kompromiss aus Stabilität und Halbleiterqualität des Films darstellten. Mittels Eindringtiefe kontrollierter Röntgenstreuung unter streifendem Einfall konnte nachgewiesen werden, dass die Vernetzung wie erwartet an der Filmoberfläche stattfindet. Zusätzliche UV-VIS und FTIR Spektren konnten die Art und Weise der Vernetzung, sowie die Dicke der vernetzten Schicht, bestätigen. Durch die Verwendung einer wasserlöslichen Poly-Vinyl-Alkohol Opferschicht als Substrat konnten die Nanofolien unter Wasser mit einer Pinzette sowohl auf unterschiedliche neue Oberflächen transferiert, als auch über makroskopische Abstände gespannt werden. Eine erste Anwendung wurde demonstriert, indem Pentacensfilme auf Bottom-Goldkontakt Transistorstrukturen transferiert wurden. Dadurch wurde der Kontaktwiderstand im Bauteil im Vergleich zu direkt aufgedampften Filmen um mehr als zwei Größenordnungen von ~ 10⁷ Ω auf ~ 10⁵ Ω reduziert. Dies begründet sich darin, dass sublimierte Pentacens Filme nahe Goldkontakten deutliche Entnetzung zeigen und auf polykristallinem Gold sehr ungerichtet wachsen. Für transferierte Filme konnte jedoch mittels infrarot-Rasternahfeldmikroskopie gezeigt werden, dass die molekulare Struktur und die Topographie der transferierten Filme auf Golduntergrund erhalten bleiben.

Die vorgestellte Methode könnte als Ansatz für neue Sensoren oder Dünnschichttransistoren mit Luftbeziehungsweise Vakuum-Dielektrikum dienen.

CONTENTS

SUMMARY	i
ZUSAMMENFASSUNG	iii
1 INTRODUCTION	1
1.1 MOTIVATION	1
1.2 BASIC CONCEPTS OF ORGANIC SEMICONDUCTORS	4
1.3 MATERIALS	6
1.4 GROWTH MECHANISMS	8
1.5 THIN FILM TRANSISTORS	9
2 STRUCTURAL CHARACTERIZATION OF ORGANIC THIN FILMS	11
2.1 MICROSCOPY	11
2.2 X-RAY DIFFRACTION	12
3 ELECTRONIC IN-SITU CHARACTERIZATION OF OFETs	19
3.1 FILM THICKNESS DEPENDENT EVOLUTION OF ELECTRONIC PROPERTIES	19
3.2 DEPOSITION SETUP AND IN-SITU SAMPLE HOLDER	22
3.3 FILM PERCOLATION ON ROUGH TECHNICAL SURFACES	25

3.4	IN-SITU INVESTIGATION OF THE FORMATION OF A PENTACENE - C ₆₀ AMBIPOLAR TFT	26
4	PREPARATION AND TRANSFER OF ORGANIC SEMICONDUCTOR NANOSHEETS	29
4.1	CROSSLINKING OF SEMICONDUCTOR THIN FILMS VIA ELECTRON IRRADIATION	29
4.2	TRANSFER OF ORGANIC THIN FILMS	33
4.3	POTENTIAL FOR FUTURE APPLICATIONS	33
5	FINAL WORDS	37
A	PUBLICATIONS	39
A.1	DUAL CHANNEL OPERATION UPON <i>n</i> -CHANNEL PERCOLATION IN A PENTACENE - C ₆₀ AMBIPOLAR ORGANIC THIN FILM TRANSISTOR	41
A.2	TRANSFERABLE ORGANIC SEMICONDUCTOR NANOSHEETS FOR APPLICATION IN ELECTRONIC DEVICES	47
A.3	SUB-MONOLAYER PERCOLATION OF PENTACENE ON ROUGH PARYLENE-C DIELECTRICS	54
A.4	MICRODIFFRACTION IMAGING - A SUITABLE TOOL TO CHARACTERIZE ORGANIC ELECTRONIC DEVICES	59
A.5	α, ω -DIHEXYL-SEXITHIOPHENE THIN FILMS FOR SOLUTION-GATED ORGANIC FIELD-EFFECT TRANSISTORS	70
A.6	CHROMIUM/SCANDIUM MULTILAYER MIRRORS FOR ISOLATED ATTOSECOND PULSES AT 145eV	76
A.7	SURFACE-DIRECTED MOLECULAR ASSEMBLY OF PENTACENE ON AROMATIC ORGANOPHOSPHONATE SELF - ASSEMBLED MONOLAYERS EXPLORED BY POLARIZED RAMAN SPECTROSCOPY	81
B	SUPPORTING INFORMATION	91
B.1	SUPPORTING INFORMATION FOR "DUAL CHANNEL OPERATION UPON <i>n</i> -CHANNEL PERCOLATION IN A PENTACENE-C60 AMBIPOLAR ORGANIC THIN FILM TRANSISTOR"	91

B.2 SUPPORTING INFORMATION FOR "TRANSFERABLE ORGANIC SEMICONDUCTOR NANOSHEETS FOR APPLICATION IN ELECTRONIC DEVICES" . . .	97
B.3 SUPPORTING INFORMATION FOR "SUB-MONOLAYER PERCOLATION OF PENTACENE ON ROUGH PARYLENE-C DIELECTRICS"	108
B.4 SUPPORTING INFORMATION FOR " α, ω -DIHEXYL-SEXITHIOPHENE THIN FILMS FOR SOLUTION-GATED ORGANIC FIELD-EFFECT TRANSISTORS"	113
B.5 SUPPORTING INFORMATION FOR "SURFACE-DIRECTED MOLECULAR ASSEMBLY OF PENTACENE ON AROMATIC ORGANOPHOSPHONATE SELF - ASSEMBLED MONOLAYERS EXPLORED BY POLARIZED RAMAN SPECTROSCOPY"	118
BIBLIOGRAPHY	125
ACKNOWLEDGEMENTS	132

INTRODUCTION

1.1 MOTIVATION

For many years, organic electronics had to compete with the extremely high efficiency of classic anorganic electronic devices, be it with its high charge carrier mobility or very long life time and stability. Lately, however, the field has found its own identity, evolving to develop a complementary market instead of being mere competition. Besides low cost, low energy material synthesis, the most enticing reasons to invest in organic electronics are its mechanical and structural flexibility. By designing the chemical composition and structure, it is possible to tune electronic and optical properties of the organic semiconductor to meet its specific application. Furthermore, organic semiconductor thin films profit from an intrinsic mechanical flexibility, which is owed to the van der Waals nature of their intermolecular bonds. This flexibility allows organic electronics to be used in highly specialized applications where the active materials are designed to serve a particular purpose [8]. Their softness and often non-toxicity guarantee manifold possibilities for medical applications, like sensing devices [9, 10], artificial skin with pressure and temperature sensitivity [11–14], and employment in implants [15]. Last but not least, a new movement to develop sustainable electronics is emerging. To prevent new waves of electronic waste, biodegradable electronics are developed to be used in disposable applications [16].

When striving for improvement, perhaps every field of applied physics comes down to relying on two aspects. One key objective is, quite obviously, the optimization of the employed materials themselves. Purification, modification or the synthesis of all new materials define and expand the building blocks for any kind of technology. The most crucial aspect however may be, how these materials interact. The quality of interfaces within a system is, in the end, the bottleneck to any functional device; in mechanical systems these are parameters like friction, stress and strain between two materials, whereas in optics the transition between refractive indices is utilized. In electronic devices, interfaces determine charge transport, injection and extraction. While classical semiconductor devices profit from the inherently high

quality interface between differently doped regimes within one material, in organic electronics, especially when using molecular deposited small molecules, interface phenomena become more crucial. Here, the growth modes, which follow the laws of diffusion limited aggregation, and consequently the electronic properties of the semiconductor films, are strongly influenced by the subjacent kind of material, its structure, surface energy, and topography. This work focuses exemplarily on the understanding and improvement of the three essential interfaces in organic field effect transistors (OFETs). These are the electrode-semiconductor interface, the gate dielectric-semiconductor interface, and the interface between two semiconductors itself. Addressing these three types of interfaces covers the fundamental kinds of organic electronic devices, such as organic photovoltaics (OPVs) [17], light emitting diodes (LEDs) [18, 19], and transistors [20]. Of course, there are also various special applications that include additional layers, e.g. for encapsulation purposes, electrolyte gating, or in novel van der Waals LEDs [21, 22].

On the one hand, to obtain better understanding of interface formation, it is necessary to

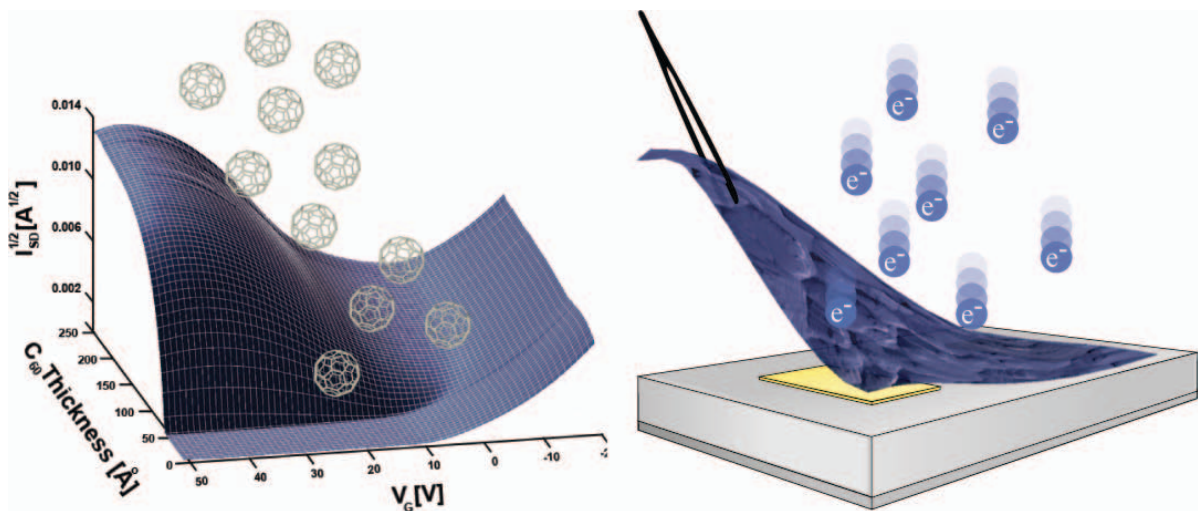


Figure 1.1: Illustrations of *in-situ* characterization of an organic ambipolar thin film transistor during fullerene deposition (left) and transfer of a pentacene nanosheet to a new substrate after being crosslinked via low energy electrons (right). Inspired by [1] and [3].

develop new techniques that unravel electronic phenomena on the nanoscopic scale. On the other hand, to overcome obstacles and limitations of device fabrication, new methods for interface creation are desirable. In the course of this dissertation, both of those needs were met (see Fig. 1.1):

Electronic in-situ characterization:

An *in-situ* setup was optimized to address the organic-organic interface formation in an ambipolar transistor employing the two semiconductors pentacene and fullerene C_{60} as active materials. The research on ambipolar transistors is gaining more and more momentum, as they are showing increasing potential for unique applications. It could be shown, that they can be successfully implemented in logic gate circuits, such as organic inverters [23, 24]. Organic light emitting field effect transistors (OLEFETs), which use the luminescent recombination of

holes and electrons in the ambipolar regime, are raising even more attention [25–30]. Apart from their application as functional devices they also represent a lateral model system for the investigation of the energy alignment of the molecular energy states, which is of crucial interest not only in transistors and diodes but also to understand charge transfer in organic solar cells, especially the role of charge transfer (CT) complexes [31]. The organic heterojunction, especially between fullerenes or their derivatives and p-type aromatic molecules, is subject to intense theoretical and experimental investigation. Linares et al. have modeled the pentacene-C₆₀ heterojunction depending on their respective orientation [32] and many other groups have contributed elaborate studies to complete the picture of heterojunction formation in organic bilayer systems [33–41]. Despite the common picture of localized charge generation from separated excitons at the organic interface, ultra-fast (femtosecond range), i.e. delocalized charge separation could be observed in fullerene derivatives for bilayered systems in the group of Richard H. Friend [42], but also for other blend photovoltaic systems [43, 44]. In this work we recorded characteristic curves of thin film transistors (TFTs) *in-situ*, i.e. during film formation. Thereby, the evolution of the conduction channels within an ambipolar transistor could be followed with sub-monolayer resolution. This technique offers insights into early stage accumulation channel formation and thickness resolved charge transport at the organic-organic interface.

The *in-situ* technique was also applied to unipolar TFTs growing on rough dielectric surfaces, which are present in many potential commercial applications. Here, as roughness manifests on the same length scales as molecular monolayer thickness, common topographic and structural techniques like atomic force microscopy and X-ray analysis reach their limits. Recording the evolution of conduction channel characteristics *in-situ* overcomes these limitations.

Transferable organic nanosheets:

To address the need for new fabrication techniques, we developed a method that allows to transfer large sheets of thin pentacene film without exposure to aggressive chemical treatment. The technique is inspired by the fabrication of crosslinked aromatic self assembled monolayers, which can be used as stable, transferable, and functionalizable nano membranes [45]. Translating this technique to organic semiconductor thin films is desirable, in order to decouple device fabrication from active film formation. This way, a high quality, fully functional thin film can be grown, and then applied, as is, on a variety of surfaces and geometries, e.g. on surfaces that impede well defined film formation, over cavities like grids or pores, or as a further class of materials that can be employed in van der Waals heterostructures [46]. To this end, the films are crosslinked via irradiation with low energy electrons. The work comprises the detailed description of the transfer technique, as well as thorough structural investigation to understand the crosslinking of the film and its impact on functionality.

Part of this work has been published or been prepared for publication [1–7]. Here, [1] focuses on the afore mentioned ambipolar TFTs. The growth behavior of physical vapor deposition grown pentacene on rough parylene-C dielectrics is discussed in [2]. Finally, the described transfer technique is presented in [3]. The remaining articles contain various contributions to successful collaboration work. The full text articles and manuscripts are attached in appendix

A. The respective supporting information is given in appendix B.

In the following, the basic concepts that underlie the outcomes of these publications are presented. For detailed information on experiments and discussions, the reader is kindly referred to the original publications provided in the appendices. Sections 1.2-1.5 include fundamentals on organic semiconductors, growth mechanisms and the concept of thin film transistors. In chapter 2, this thesis covers an excursus on the structural characterization of organic thin films, which explains standard microscopic and X-ray methods and their application in the appended publications. Finally, chapter 3 and chapter 4 discuss the experimental details and considerations beyond the corresponding publications of the *in-situ* technique and the fabrication of organic nanosheets, respectively. Some conclusive remarks are presented in chapter 5.

1.2 BASIC CONCEPTS OF ORGANIC SEMICONDUCTORS

The term "organic" refers to the main elemental composition of the semiconductor materials. They are either polymers or small molecules consisting primarily of hydrocarbons and heterocyclic compounds [47]. Hydrocarbons form structures featuring alternating single and double bonds. Consequently, conjugated polymers and aromatic molecules develop a combination of strong, sp^2 -hybridized σ bonds with localized electrons, and a delocalized π -system consisting of the overlapped p-orbitals (cf. Fig. 1.2 a & b). This work focuses on aromatic molecules, which are based on one or many benzene structures (or arenes). Here, the sp^2 -hybridization leads to planar rings of six hydrocarbons which form angles of 120° , respectively. Hence, one has to distinguish the origins of the semiconducting behavior of organic and inorganic semiconductors like silicon or germanium. In the case of the latter, the crystallization of specific atoms, i.e. the formation of a periodic lattice potential, leads to the formation of a band structure. In organic electronics, the single molecule itself is a semiconductor. The specific structure of bonds within aromatic molecules results in molecular orbitals with discrete energy levels. In the ground state, these energy levels are filled up to the highest occupied molecular orbital, or "HOMO" (Fig. 1.2 c). The lowest unoccupied molecular orbital, or LUMO, is energetically separated by the molecular band gap. The HOMO is the last unexcited, binding state of the π -orbital, while the LUMO represents the first excited, anti-binding energy state. Organic molecules can form large semiconducting van der Waals crystals.

Charge transport in organic semiconductors is part of ongoing research and has to be discussed in a case specific way. It is safe to say that there are two border cases of charge transport mechanisms, namely classical band-like transport in very pure organic single crystals and the so called hopping transport. They can occur very discretely or as intermediate states between each other. The polaron model helps to develop an understanding for the energy situation of a charge carrier passing through an organic semiconductor [48]. In this model, the charges polarize the surrounding lattice as they move through the crystal. The charge carriers together

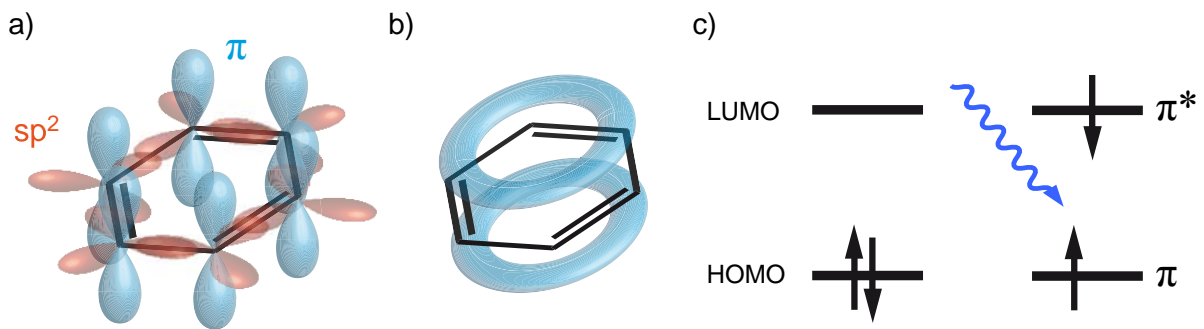


Figure 1.2: Sketch of the formation of energy levels in a benzene molecule. a) Molecular orbitals of carbon atoms with sp^2 hybridization in benzene. b) Delocalization of π -system. c) Energy diagram of HOMO and LUMO in ground state (left) and first excited state (right).

with the polarization they generate are called polarons, whose energy states are dispersed in a Gaussian distribution. In the image of classic band-like transport this translates to smeared out conduction and valence bands. The energy gap of an organic crystal is smaller than that of the single molecule, as the band energy levels are reduced by the respective polarization energies for holes and electrons.

In most cases however, charge transport cannot be explained solely by assuming a band structure. Allen Miller and Elihu Abrahams have developed a model based on the tunneling, or "hopping", of charge carriers from one molecule to another [49]. It predicts a hopping rate ν , which is depending on the wave function overlap of the two neighboring molecules and the energetic difference ΔE between the initial and the final state:

$$\nu = \nu_0 \exp(-2\alpha R) \begin{cases} \exp\left(-\frac{\Delta E}{k_B T}\right), & \Delta E > 0 \\ 1, & \Delta E < 0 \end{cases} \quad (1.1)$$

ν_0 is the phonon frequency of the crystal, R the distance between two neighboring molecules. The constant α includes the exponential decrease of the charge carrier wave function, $k_B T$ is the thermal energy. In addition, the model includes the existence of charge trap states.

The transition between band like and hopping transport can be evaluated by performing temperature dependent charge carrier mobility measurements. An increasing mobility with decreasing temperature is indicative for band like transport, while a decreasing mobility points to thermally activated hopping transport [50]. For a more detailed discussion, I want to refer to the books of Markus Schwörer et al. [47] and Martin Pope et al. [48].

All this leads to a second conceptual difference between organic and inorganic electronics. Whereas in inorganic electronics the selectivity of majority charge carriers is realized by doping with different elements, the selection in organic electronics is more intrinsic. Molecules are mostly either better hole conductors or better electron conductors. Eventually, the decision of whether to use a material as hole or electron conductor is made by choice of the electrode material and dielectric. The electrodes do not consist of a highly doped zone of the prominent semiconductor like for inorganic semiconductors, but consist of a different material, e.g. a

metal or highly conductive polymer. The injection and extraction of charge carriers is limited by the matching of the material work function to either the HOMO or LUMO of the semiconductor, to achieve either hole or electron transport, respectively. Junction devices like diodes, solar cells, or ambipolar transistors are then achieved by subsequent application of two different semiconductors, semiconductor blends, or by employing two different electrode materials.

1.3 MATERIALS

The first authorship publications presented in this thesis highlight the characterization of two prominent aromatic molecules, namely pentacene and fullerene C₆₀. Both molecules show among the best performances as active layers in OFETs and can be prepared as highly crystalline thin films. Their properties and the fact that they are well studied make them suitable candidates for use in model systems.

PENTACENE

Pentacene (C₂₂H₁₄) is a small molecule consisting of five linearly condensed benzene rings. It is established as one of the most prominent organic semiconductors, showing high mobilities of over $\mu = 2 \frac{cm^2}{Vs}$ [51] and forming very well defined and thoroughly studied crystalline thin films, when grown via sublimation under UHV conditions. In very pure single crystals, mobilities can reach significantly higher values [52], which means that transistor engineering parameters, like the choice of dielectric, contacts resistance reduction, etc. still leave room for optimization.

Pentacene appears in four known polymorphs [53]. For TFT applications, two of them are of prior importance. The thin film phase (TFP) is substrate induced and thus only appears in very thin films [54]. It is the prominent form of pentacene examined in this work and the following descriptions refer to it. The more stable bulk phase (BP) can be partially induced at the dielectric surface by increased substrate temperatures during film growth [55] or chemical treatment, as preliminary results indicate, and begins formation on top of TFP surfaces after the film exceeds a certain thickness, i.e. a certain distance from the substrate. When grown via molecular beam deposition, TFP pentacene forms a polycrystalline film with grain sizes between 100 nm and several μm in diameter. It has been shown that the morphology and structure of these grains strongly impact the spatial and energetic distribution of trap states in thin film devices [56, 57]. Its crystal structure has been thoroughly studied by Stefan Schiefer et al. [58], revealing layered growth with a triclinic unit cell, which condenses in a so called herringbone structure and is tilted to the substrate surface plane by 8.75° (Fig. 1.3 a & b). The layers show a spacing of 15.4 Å, which is easily identifiable via X-ray reflectometry, as will be shown in chapter 2.

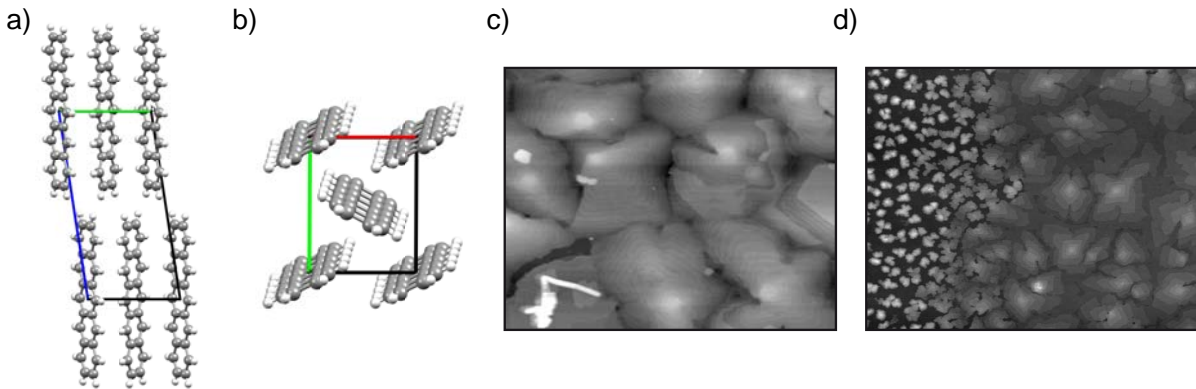


Figure 1.3: Structure of pentacene. a) View along the a-axis of the TFP unit cell. b) View along the c-axis of the TFP unit cell. c) AFM micrograph of pentacene on SiO₂ (4 μm x 5 μm , height scale: 40 nm). d) AFM micrograph of pentacene near a gold electrode (4 μm x 5 μm , height scale: 15 nm).

The topography of TPF pentacene is dominated by fractal or pyramid shaped grains (depending on the growth parameters [59]) stacking up in monolayer terraces (see Fig. 1.3 c), when grown on many smooth dielectric surfaces. On and near metal surfaces, on the other hand, the morphology is less controlled. Directly on top of Au surfaces the pentacene films stack up to pillar and rod like structures [60], while close to Au structures the films show severe dewetting (Fig. 1.3 d) [61, 62].

Its electronic properties originate in its band gap of $E_{bg} = 1.8 \text{ eV}$, with $E_{HOMO} = 5.0 \text{ eV}$ and $E_{LUMO} = 3.2 \text{ eV}$ [63]. As the HOMO energetically lies close to the work function of gold $W = 5.1 \text{ eV}$, gold is often used as electrode material in pentacene based hole conducting TFTs.

FULLERENE C₆₀

Fullerenes are a class of non hydrogen terminated aromatic molecules, that form ball shaped structures. The only spherical fullerene is also the most prominent one, namely the Buckminster fullerene, Buckyball, or simply C₆₀, consisting of 20 carbon hexagons and 12 pentagons [64, 65]. Some of the highest performances of electron conducting, organic TFTs have been realized using C₆₀, topping values of $\mu = 5 \frac{\text{cm}^2}{\text{Vs}}$ [51] and its derivative Phenyl-C₆₁-butyric acid methyl ester (PCBM) is one of the most used in organic photo voltaic devices [66]. Its structure is shown in Fig. 1.4 a. At room temperature, bulk structures of the molecule crystallize in fcc, with a lattice constant of 14.17 Å [67], while the rotational degrees of freedom of each molecule stay free [68]. In thin films it has not been clarified whether body centered cubic (bcc) or fcc was the predominant crystal structure for a long time. We could show that thin films at room temperature crystallize in fact fcc in [111] direction with respect to the substrate surface (Fig. 1.4 b, cf. chapter 2). They develop a bulgy topography with grain sizes that depend on film thickness and growth temperature. The topography stays unchanged, whether it is grown on smooth SiO₂ or gold surfaces (see Fig. 1.4 c).

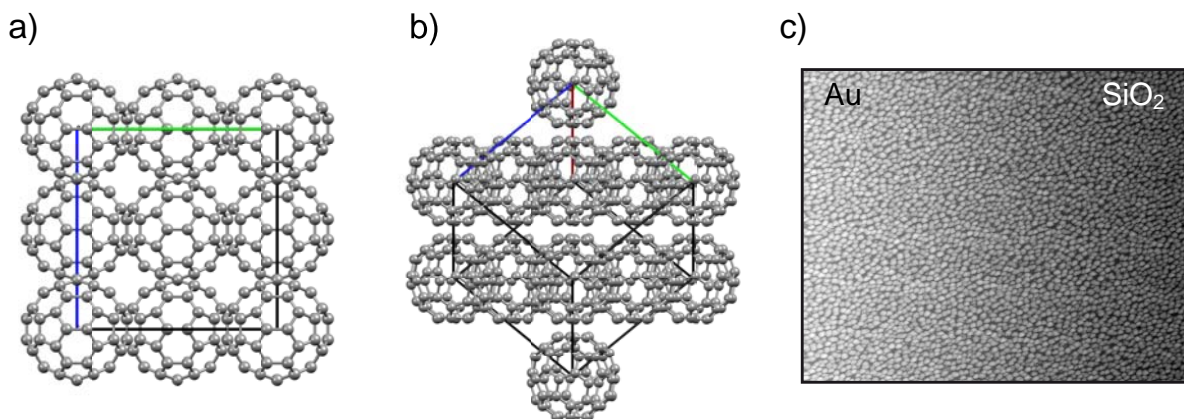


Figure 1.4: Structure of C₆₀. a) Side view of the fcc unit cell (the first two layers are depicted). b) Side view of the fcc unit cell in [111] direction. c) AFM micrograph of 10 monolayers of C₆₀ on the edge between Au and cyclic-olefin-copolymer (COC) coated SiO₂ (4 μm x 5 μm , height scale: 50 nm).

Its band gap is $E_{bg} = 1.7 \text{ eV}$, where $E_{HOMO} = 6.2 \text{ eV}$ and $E_{LUMO} = 4.5 \text{ eV}$ [69]. It is almost exclusively used as electron conducting material, because its intrinsic electron conductivity surpasses the hole conductivity by approximately four orders of magnitude [70]. The major challenge of employing C₆₀ in commercial devices is its instability under ambient conditions [71]. Oxygen intercalates quickly into the tetraeder gaps of the unit cells, trapping electrons, and thus, quenching charge transport. Thus, encapsulation of fullerene thin films is a heavily studied subject.

1.4 GROWTH MECHANISMS

There are several ways to coat a substrate with organic semiconductor films, for example by spin coating, drop casting, doctor blading or printing. All these rely on solution processing, and hence, on soluble materials. Within the scope of this work, we focus on well ordered films made from pristine materials, i.e. materials containing no additional chemical modification to guarantee solubility. Thus, only molecular beam deposition (MBD) is used. During MBD, the semiconductor is heated to its sublimation temperature under high vacuum (HV) to ultra high vacuum (UHV) conditions. This can either be done in an open crucible to evaporate the material homogeneously into all directions, or by using a so called Knudsen cell, which offers a certain degree of collimation (cf. chapter 3). The molecular beam is directed onto a substrate of choice, where the molecules condensate and form thin films of different morphology.

For most molecules growth on insulating surfaces can be described by the theory of diffusion limited aggregation [72]. During its diffusion on the surface, the interplay of several processes determines the final film morphology (see Fig. 1.5 a) [73, 74]. Depending on the growth parameters, i.e. sample temperature and deposition rate, as well as surface roughness and surface energy of the substrate, three predominant growth modes arise (Fig. 1.5 b). In the

case of the Frank - van der Merwe growth, the binding strength between the substrate and the molecules is stronger than the intermolecular bonding. This leads to layer-by-layer growth, where a new molecular layer is formed only after the previous layer is complete. The opposite case, in which the molecules are bound more strongly to each other, than to the substrate, is called Vollmer-Weber, or island growth. For instance, fullerene C_{60} is known to form disjoint island on SiO_2 , before forming a closed thin film. In this work we will show that the same holds for growth on pentacene surfaces and how that effects its electronic properties in thin film transistors. The Stranski-Krastanov, or layer-plus-island growth mode is the intermediate case, where islands are formed after the completion of a few molecular layers. Pentacene on SiO_2 usually aggregates in this growth mode.

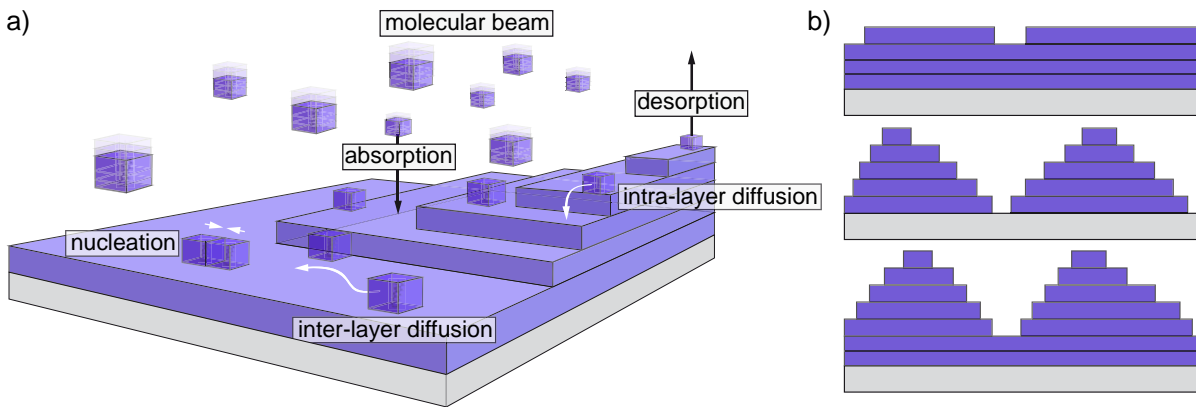


Figure 1.5: Sketch of the different growth mechanisms and modes. a) Molecular diffusion mechanisms of MBD grown organic semiconductor. b) Growth modes (top to bottom): Frank - van der Merwe, Vollmer-Weber, Stranski-Krastanov.

1.5 THIN FILM TRANSISTORS

The field effect transistor (FET) is an electronic device which uses an electric field, applied by a gate electrode, to modulate the current between a second and a third electrode, namely source and drain. FETs can be realized in a vast variety of geometries. As most organic electronic devices are fabricated layer by layer and feature thin films of active material on an insulating dielectric, the thin film transistor (TFT) geometry will be discussed here.

The semiconductor is separated by the gate electrode by a thin dielectric layer. The energetic situation is therefore comparable to that of a classic metal-insulator-semiconductor (MIS) junction. Following the deduction from Simon M. Sze [75] for unipolar transistors, the surface charge Q_s can be written in terms of the surface potential Ψ_s , the Debye length λ_D , and the ratio of the equilibrium electron and hole densities $\frac{n_0}{p_0}$:

$$Q_s = \epsilon_S E_s = \pm \epsilon_S \frac{\sqrt{2} k_B T}{e \lambda_D} \left[\left(e^{\left(\frac{e \Psi_s}{k_B T} \right)} + \frac{e \Psi_s}{k_B T} \right) 1 + \frac{n_0}{p_0} \left(e^{\left(\frac{e \Psi_s}{k_B T} \right)} - \frac{e \Psi_s}{k_B T} \right) 1 \right]^{\frac{1}{2}} \quad (1.2)$$

E_s is the electric field at the dielectric surface and ϵ_s is the permittivity of the semiconductor. The dependency of Q_s to the surface potential is depicted in Fig. 1.6, where Ψ_B is a measure for doping, as it is proportional to the difference between the intrinsic and the actual Fermi level of the semiconductor. In contrast to most inorganic applications, organic TFTs are mostly operated in accumulation. To illustrate the relevant interfaces in TFTs, Fig. 1.7 sketches the layouts of a unipolar bottom contact TFT and an ambipolar TFT with top contact hole conducting layer and bottom contact electron conducting layer. The extraction of transistor parameters like charge carrier mobility, threshold voltage and hysteresis will be discussed in chapter 3, together with the *in-situ* characterization setup.

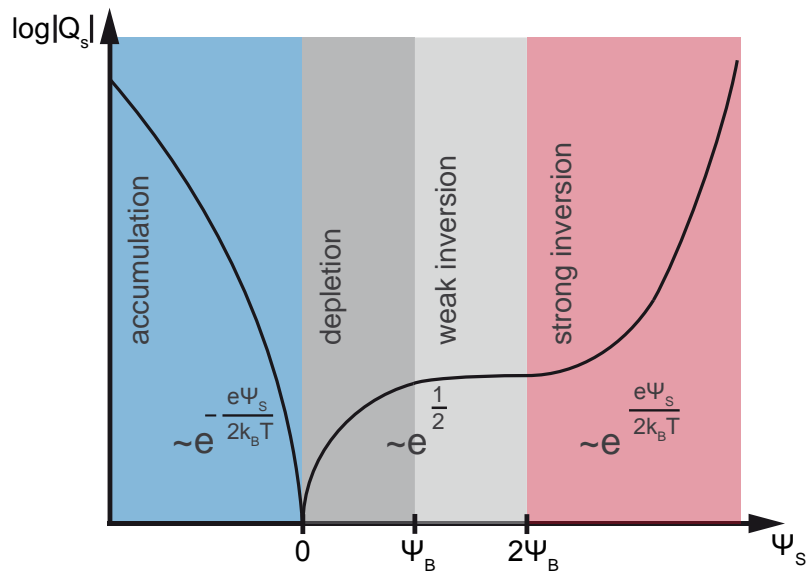


Figure 1.6: Schematic plot of the logarithmic surface charge dependence on surface potential.

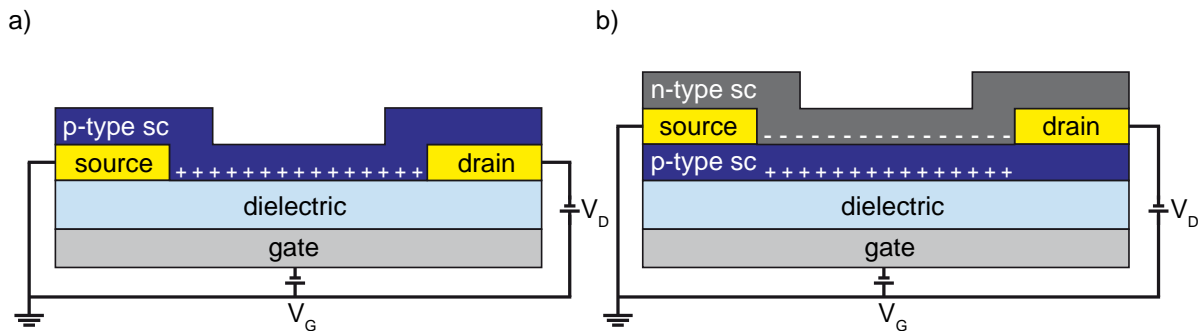


Figure 1.7: Transistor geometries. a) Unipolar bottom contact p-type TFT. b) Ambipolar bilayer TFT.

For a detailed introduction to junction theory, I would like to refer to the book of K. Brennan [76].

STRUCTURAL CHARACTERIZATION OF ORGANIC THIN FILMS

Part of the findings presented in this chapter have been published [1, 3]. The full articles are attached in appendix A.

All systems, i.e. the pentacene-C₆₀ double layer, partially crosslinked pentacene, and pentacene grown on rough parylene-C, have been thoroughly studied via microscopy and X-ray diffraction techniques to gain insight into topography and structure of the organic thin films. Here, the principals of these methods are shortly introduced and the most relevant results gained for the articles [1] and [3] are presented.

2.1 MICROSCOPY

Some topographical and morphological aspects can be determined using standard microscopic techniques, such as atomic force microscopy (AFM) and scanning electron microscopy (SEM). Throughout the studies in [1–3] all AFM measurements were performed using a Veeco Dimension 3100 AFM in the clean room of the former chair of Prof. Jörg Kotthaus. The measurements were carried out in tapping mode, setting the Si tip to an oscillation frequency near its resonance, and measuring the topography induced amplitude changes via a laser, which is focused on the cantilever tip. The reflected beam is read out by a four field diode. The height of the cantilever is constantly readjusted accordingly via a feedback loop, which controls a piezo stage, resulting in a high resolution topography map. This way, height differences as small as a few Ångströms can be detected, while the lateral resolution is limited mainly by the tip shape (usually around 20 nm).

Besides quality and roughness control of dielectric surfaces for electronic devices, AFM contributed substantially to the understanding of fullerene C₆₀ growth on crystalline pentacene

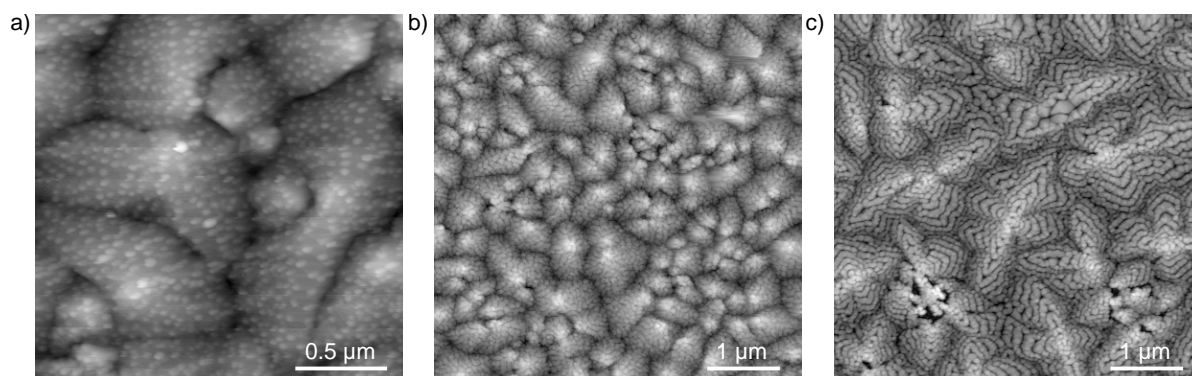


Figure 2.1: AFM micrographs of C_{60} growth on pentacene (height scale: 40 nm). a) Sub monolayer C_{60} . The fullerene forms small disjoint islands. b) 25 nm C_{60} grown on small pentacene grains. The C_{60} retraces the subjacent pentacene with a random distribution of grains. c) 25 nm C_{60} grown on large pentacene grains. The fullerene grains follow the subjacent pentacene monolayer terraces.

surfaces (see Fig. 2.1). Early stage thin films form disjoint islands, which stack up to several monolayers before film percolation (Fig. 2.1 a). This leads to delayed on-set of electron conductivity in ambipolar transistors (cf. chapter 3). At higher film thicknesses these islands grow together and form a bulged surface which retraces the subjacent pentacene topography. Here, the spatial distribution of fullerene grains strongly depends on the lateral dimensions of the pentacene monolayer terraces (Fig. 2.1 b and c). When pentacene is grown on Si_3N_4 at a rate of around 0.1 \AA s^{-1} at room temperature, pentacene forms relatively small grains with tightly packed terrace structures. This leads to coverage by randomly distributed C_{60} grains. Growing pentacene similarly on SiO_2 surfaces generally results in larger structures with strongly protruding terraces. In this case, the C_{60} droplets adapt to the pentacene terrace landscape, using it as a template to form contour lines. The formation of these fullerene structures has been studied in more detail before [77].

SEM can be used to obtain qualitative (and to some extent quantitative) insights into the out of plane geometry of layered systems such as organic electronic thin film devices. In [1] the pentacene/ C_{60} layer system was used to build ambipolar organic FETs, based on an $Si/Si_3N_4/SiO_2$ substrate. An SEM image of the cross-section of such a device is depicted in Fig. 2.2. The image from the channel region (left) reveals how well defined the layer system is. The semiconductor film on the gold electrode surface on the other hand shows strong dewetting with almost column like morphology (cf Fig. 1.3).

2.2 X-RAY DIFFRACTION

Some aspects of the electronic behavior of organic semiconductors are essentially determined by their crystal structures (cf. chapter 1). Therefore, it is important to introduce the basic principles of X-ray diffraction used for structure analysis. A distinction is drawn between two

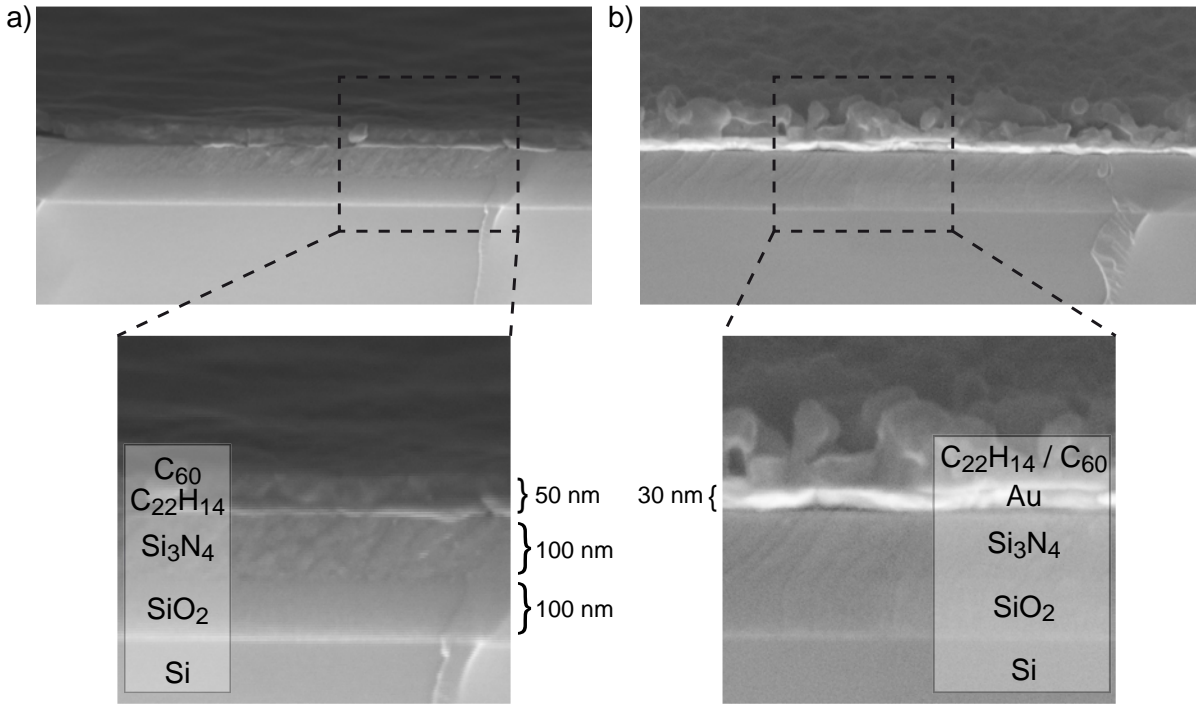


Figure 2.2: SEM cross-section image of an ambipolar pentacene-C₆₀ TFT. a) Channel region. The semiconductor film forms a well defined bilayer. b) Au contact region. The bilayer shows pillar like morphology, induced by the disturbed growth of pentacene on Au surfaces.

X-ray scattering regimes. Small angle X-ray scattering (SAXS) probes for large structures up to several hundred nanometers, while wide angle X-ray scattering (WAXS) solves the crystal structure of matter from several nanometers down to the Ångström regime. The scope of this work focuses mainly on the crystal structure of organic semiconductors, while the investigation of larger morphological structures like the mixing of semiconductor blends is left to other studies. Hence, only WAXS techniques shall be discussed here. For further detail, the reading of Als Nielsen "Elements of Modern X-ray Physics" [78] is highly recommended.

When interacting with ordered matter, X-rays of wavelength λ will interfere constructively with the lattice if the momentum transfer \vec{q} matches a reciprocal lattice vector \vec{G} , i.e.:

$$\vec{q} = \vec{k}_i - \vec{k}_f = \vec{G} \quad (2.1)$$

\vec{k}_i and \vec{k}_f are the incident and final wave vectors, respectively. This Laue equation can be transformed into the famous Bragg equation:

$$n\lambda = 2d \sin \theta \quad (2.2)$$

with $n \in \mathbb{N}$ using $q = \frac{4\pi}{\lambda} \sin \theta$ and $d = \frac{2\pi}{|\vec{G}|}$. Here, θ is the angle between the incoming beam and the lattice plane. The most general expression for \vec{q} , covering the whole two dimensional diffraction pattern, is given in terms of the angle of incidence α_i , the in-plane angle φ , and the

angle between the direct beam and the detector position $2\theta = \alpha_i + \alpha_f$ as follows (cf. Fig. 2.3):

$$\vec{q} = \frac{2\pi}{\lambda} \begin{pmatrix} \frac{1}{2}[\cos(\varphi - \alpha_i + 2\theta) + \cos(\varphi + \alpha_i + 2\theta)] \cos \alpha_i \\ \sin \varphi \\ \frac{1}{2}[\sin(\varphi - \alpha_i + 2\theta) + \sin(\varphi + \alpha_i + 2\theta)] + \sin \alpha_i \end{pmatrix} \quad (2.3)$$

From equation 2.3 all measured angular data can be transformed into wave length independent momentum space.

THETA/2THETA X-RAY DIFFRACTION

The coplanar $\Theta/2\Theta$ scan, also known as reflectometry, is predominantly used to solve scattering length density (SLD) profiles along the sample surface normal and to analyze surface roughness. It is however a very suitable tool to resolve the spacing of crystal structures parallel to the substrate surface plane. In this geometry the reflected, or specular beam is detected with a point detector by scanning the angle between surface and beam Θ , while setting the detector position to match the reflection condition $\alpha_i = \alpha_f$ (see Fig. 2.3 a). The perpendicular momentum transfer then calculates to $q_z = \frac{4\pi}{\lambda} \sin\Theta$, and the respective spacing can be evaluated using $d_z = \frac{2\pi}{q_z}$.

Using a one dimensional line detector instead of a point detector, i.e. including small parts of q_{xy} in the measurement, (Fig. 2.3 b) yields two advantages. First, any possible misalignment of the X-ray setup, which can become very sensitive for highly crystalline samples at high angles, can be immediately compensated from the gained data. Second, rocking and offset scans are included in the recorded data (cf. Fig. 2.5 b). The downside of a one dimensional silicon detector to a point scintillation detector is its lower quantum efficiency for thin chips and high photon energies. Thicker chips on the other hand lower the spatial resolution.

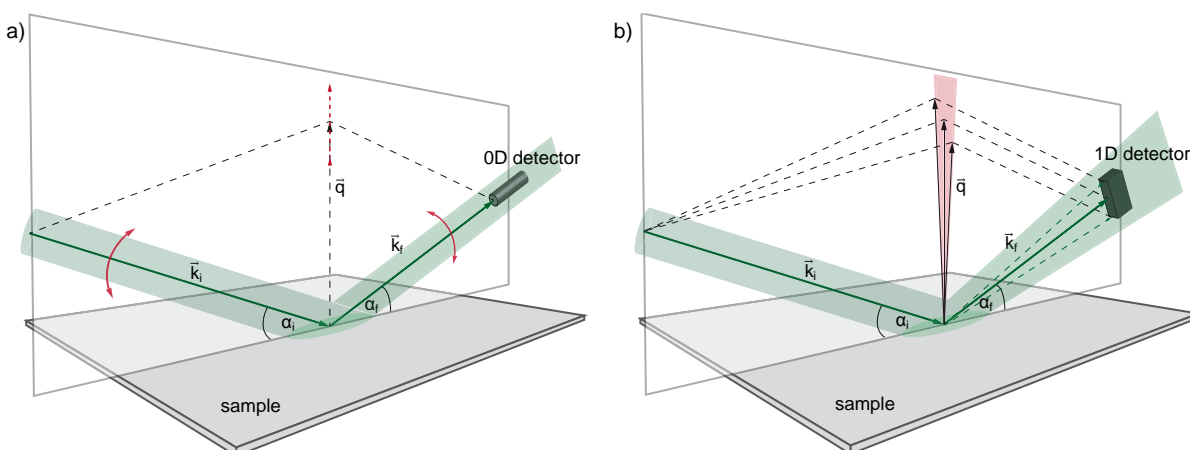


Figure 2.3: Schematic of coplanar X-ray techniques. a) $\Theta/2\Theta$ scans using a point detector. b) $\Theta/2\Theta$ scans using a 1D line detector.

Using X-ray reflectometry we analyzed the crystallinity of pentacene- C_{60} double layers (Fig.

2.4), and optimized the fullerene growth parameters accordingly to gain highest quality films.

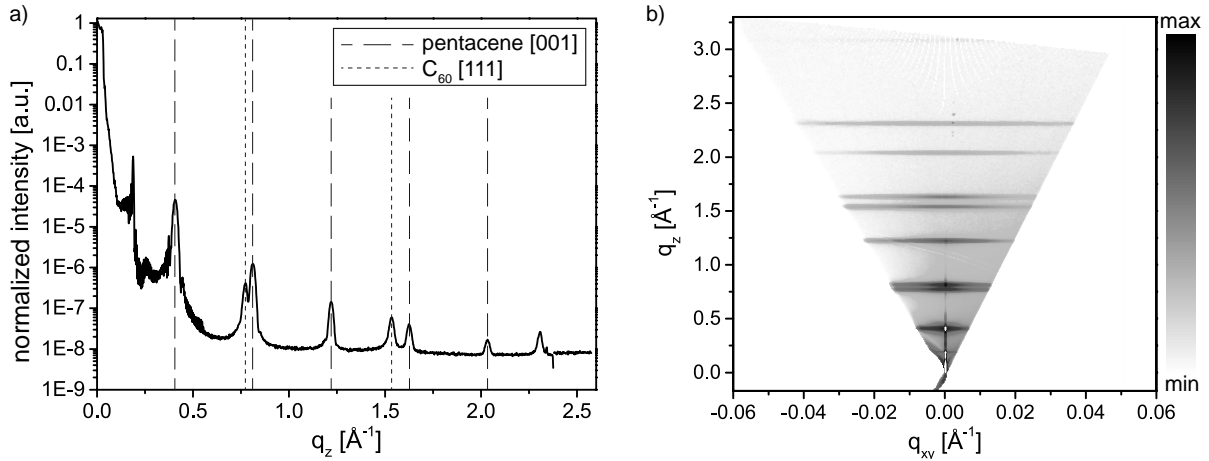


Figure 2.4: $\Theta/2\Theta$ measurements of 25 nm C_{60} grown on 20 nm pentacene. a) Reflectometry measurement. The vertical lines indicate the respective Bragg series signals. b) Line detector scan of the same sample.

Furthermore, X-ray reflectometry was used to evaluate film quality and thin film spacing in the course of several fruitful collaborations (cf. [5–7]).

In [4] we successfully tested microdiffraction imaging in reflection geometry to investigate buried layers and polymorphism in organic electronic devices.

GRAZING INCIDENCE X-RAY DIFFRACTION

Grazing incidence X-ray diffraction (GIXD) is used to obtain very surface sensitive, lateral information about crystal structure. In GIXD, the angle of incidence α_i is kept very small, typically below the critical angle for total reflection α_c . This way, only the evanescent wave of the X-ray beam penetrates the surface. Thus, a high surface sensitivity is achieved, which is desirable when studying thin films. The scan geometry is depicted in Fig. 2.5 a.

Together with according one dimensional scans, the projection of the whole diffraction space can be recorded (see Fig. 2.5 b).

STRUCTURE OF PENTACENE- C_{60} DOUBLE LAYERS

To fully understand the structural nature of pentacene- C_{60} double layers [1], especially for application in electronic devices (cf. chapter 3), it is not enough to be restricted to information perpendicular to the surface. To this end, we used GIXD.

The two dimensional diffraction pattern from the pentacene- C_{60} double layers is given in Fig.

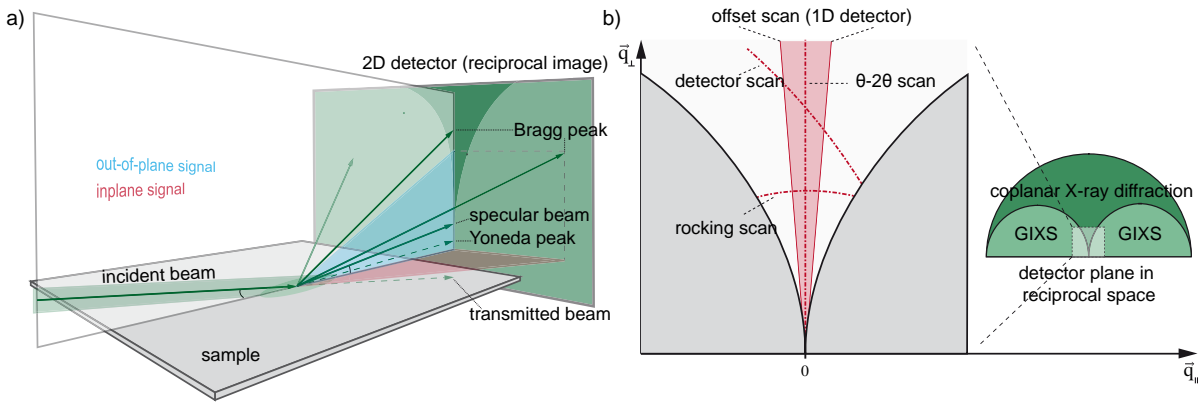


Figure 2.5: Schematic of in-plane X-ray techniques. a) GIXD geometry with all its characteristic signals. b) Scan coverage in reciprocal space.

2.6 a. The pattern shows the previously studied [58] pentacene structure with its characteristic truncation rods. In addition, the fullerene C_{60} pattern superimposes the data. From reflectometry measurements it was not clear if C_{60} condensates to an fcc lattice in [111] direction or to a bcc lattice in [100] direction, since the spacing results in a similar Bragg series. Using GIXD, we could verify the C_{60} fcc structure and, more over, dismiss any extra phases. The fullerene spots could be completely indexed, by solving the momentum transfer equation for a cubic lattice with the normal vector in [111] direction and by considering the fcc specific selection rules for Bragg reflection (Fig. 2.6 b):

$$\vec{q} = \frac{2\pi}{\lambda} \begin{pmatrix} h \\ k \\ l \end{pmatrix} \quad \text{and} \quad \vec{n} = \frac{1}{\sqrt{3}} \begin{pmatrix} 1 \\ 1 \\ 1 \end{pmatrix} \quad (2.4)$$

The Miller indices $h, k,$ and l are used to identify the family of planes. The components then calculate to to:

$$q_z = \vec{q} \cdot \vec{n} = \frac{2\pi}{a\sqrt{3}}(h + k + l) \quad (2.5)$$

$$q_{xy} = |\vec{q} - \vec{q}_z| = \frac{2\pi\sqrt{2}}{a\sqrt{3}} \sqrt{h^2 + k^2 + l^2 - hk - hl - kl} \quad (2.6)$$

DEPTH CONTROLLED GIXD ON PARTIALLY CROSSLINKED PENTACENE FILMS

In [3] thin pentacene films are irradiated by a low energy electron beam in order to crosslink the topmost layers (cf. chapter 4). We used depth controlled grazing incidence diffraction to verify that the crosslinking is restricted to the top surface and to measure the penetration depth of said non crystalline crosslinked layers (Fig. 2.7).

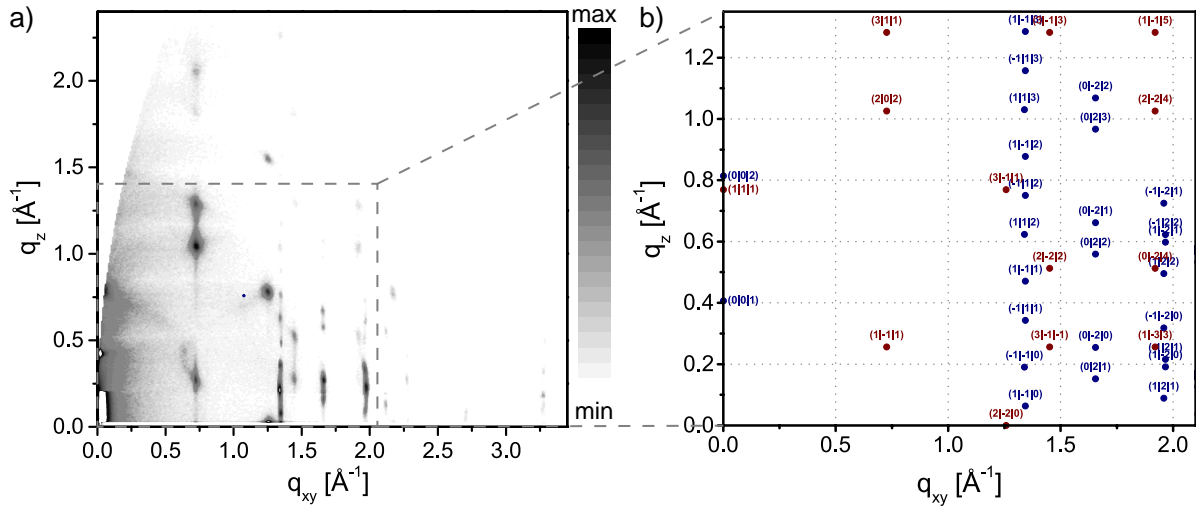


Figure 2.6: Resolving the pentacene- C_{60} bilayer crystal structure. a) GIXD measurement of 25 nm C_{60} grown on 20 nm pentacene. b) Indexing of the measured Bragg peaks (red spots indicate signal stemming from C_{60} , blue spots indicate pentacene).

To quantitatively evaluate the penetration depth, we employed a model by Helmut Dosch et al. [79, 80], which introduces a number of disordered layers on top of the crystal, which do not contribute to the diffraction signal. The total intensity of the scattered beam calculates to the product of transmission functions and the structure factor [81, 82]:

$$I = |T_i^2| S_{-p} |T_f^2| \quad (2.7)$$

The transmission functions calculate to:

$$T_{i,f} = \frac{2 \sin \alpha_{i,f}}{\sin \alpha_{i,f} + \sqrt{\sin^2 \alpha_{i,f} - \sin^2 \alpha_c}} \quad (2.8)$$

while the structure factor is given by the following term:

$$S_{-p} = \frac{|e^{-\frac{pa}{\Delta}} - e^{-iNQ_z a}|^2}{|1 - e^{-iQ_z a}|^2} \quad (2.9)$$

with p dead layers on top of the sample surface, which are non crystalline and thereby do not contribute to the signal. N is the number of molecular layers within the film thickness, Δ is the scattering depth of the evanescent wave, and a is the lattice spacing in z -direction. Q_z is the momentum transfer parallel to the sample surface normal of the examined peak:

$$Q_z = k_i^z - k_f^z = \frac{2\pi}{\lambda} \left[\sqrt{\sin^2 \alpha_i - 2\delta - 2i\beta} + \sqrt{\sin^2 \alpha_f - 2\delta - 2i\beta} \right] \quad (2.10)$$

with $2\delta = \sin^2 \alpha_c$, and $2i\beta = i\frac{\mu\lambda}{2\pi}$, where μ is the absorption factor. The scattering depth of the

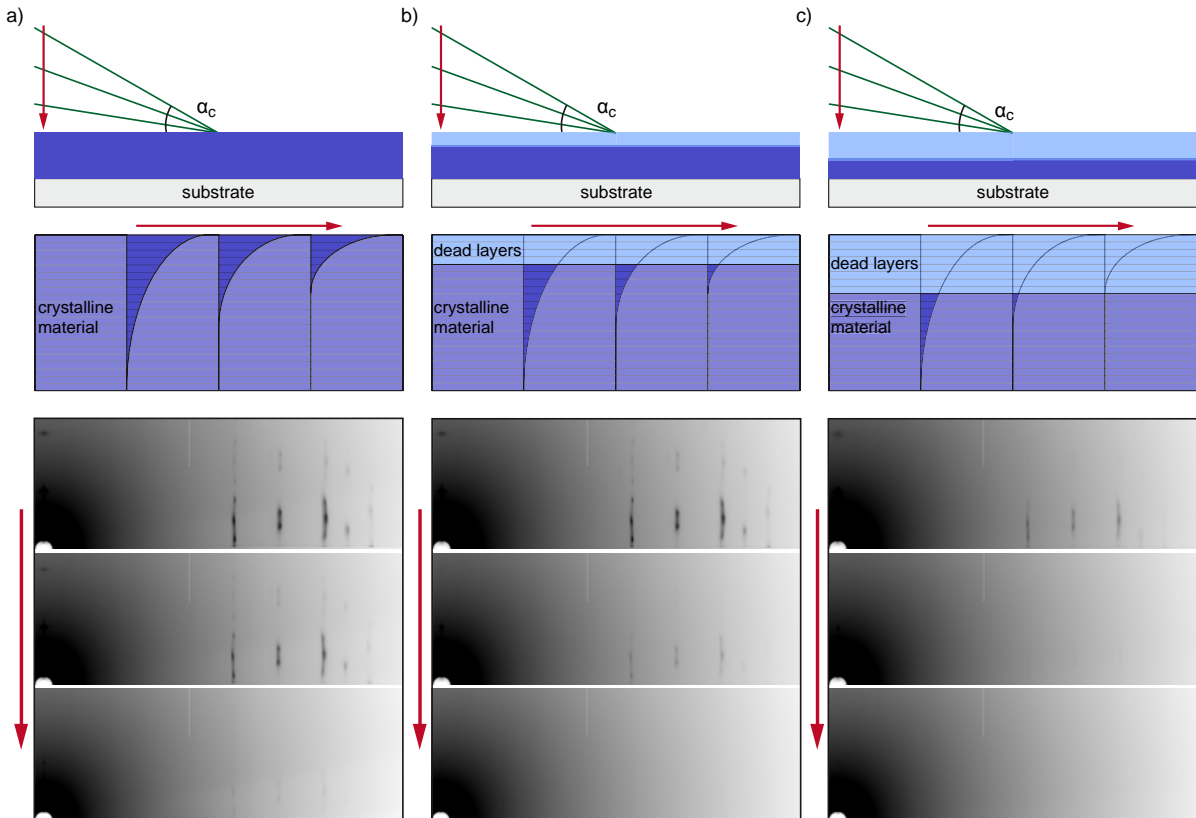


Figure 2.7: Schematic and GIXD measurements to illustrate the connection between number of *dead* layers and Bragg signal loss ($\lambda = 0.6888\text{\AA}$, i.e. a photon energy $E_{ph} = 18\text{keV}$). a) Crystalline pentacene. b) Weakly crosslinked pentacene. c) Strongly crosslinked pentacene.

evanescent wave calculates to:

$$\Delta = \frac{\lambda}{2\pi(l_i + l_f)}$$

$$l_{i,f} = \frac{\sqrt{2}}{2} \sqrt{(2\delta \sin^2 \alpha_{i,f}) + \sqrt{(\sin^2 \alpha_f - 2\delta)^2 + (2\beta)^2}}$$

$\alpha_c = \lambda \sqrt{\frac{\rho}{\pi}}$ is the critical angle with the scattering length density ρ .

This modeling of the depth controlled GIXD measurements shows that the pentacene film is crosslinked from the top, and that the penetration depth of the electrons is of the order of a few monolayers, i.e. several *nm*, depending on the irradiation time and electron energy.

ELECTRONIC IN-SITU CHARACTERIZATION OF OFETs

As motivated in the introduction, a method to electronically characterize organic TFTs under UHV conditions during growth has been optimized. To this end, an *in-situ* measurement station, as well as a deposition setup for organic molecules has been designed and realized during the course of this work.

First, the concept of *in-situ* device characterization is introduced, followed by a detailed description of the respective setups. Then, the main scientific outcome related to publications [2] and [1] is presented and complemented by additional considerations of interest.

3.1 FILM THICKNESS DEPENDENT EVOLUTION OF ELECTRONIC PROPERTIES

Topographical and structural analysis of early stage thin film growth gives valuable information on growth modes and crystallinity. However, they rely on layer formation on sufficiently smooth substrates, especially for the study of sub-monolayer films [83–85]. In addition, the electronic behavior of such films can only be anticipated. Therefore, it is advantageous to directly measure electronic properties during film formation. Due to their lateral geometry, bottom contact TFTs can be prepared in such a way that only the active layer, i.e. the semiconductor film, is missing to form a complete device. Hence it is possible to measure the characteristic curves of the transistor *in-situ*, i.e. while depositing the organic semiconductor [86–88].

To illustrate this principle, the correlation between film topography and electronic characteristics of a thin film transistor is illustrated in Fig. 3.1 for the case of pentacene grown on cyclophosphazene-copolymer (COC) coated Si_3N_4 . First, the measured drain current is only given by

very small charging currents of the capacitor formed by the drain electrode, the gate electrode and the gate dielectric (here, the gate electrode overlaps with the source and drain contacts). At a nominal film thickness of $\sim 0.7 - 0.8$ monolayers (ML), the pentacene film percolates and a hole accumulation channel forms (Fig. 3.1 b). These findings are in good agreement with theoretical calculations of 2D film percolation. The percolation threshold of disks with radius r was calculated very accurately in [89] to a surface coverage of $\sim 68\%$. Classical percolation thresholds for Archimedean lattices reach from $\sim 59\%$ for "square" shaped lattices to $\sim 81\%$ for "star" shaped lattices [90, 91]. The situation for pentacene thin films should lay somewhere between the outcomes of these calculations, depending on the growth conditions and thus the shape of the diffusion limited monolayer growth, i.e. either more fractal or more circular, like in the presented example. At this stage, the transfer curve experiences a high threshold voltage and a large hysteresis, due to deep volume traps and thermal surface traps, respectively, within the channel region. The final device characteristics (here ~ 13 ML) are shown in Fig. 3.1 c). Here, the device mobility is fully developed, the hysteresis is minimized and the threshold has shifted to smaller values.

The evolution of device parameters, such as mobility, threshold voltage, and hysteresis, can

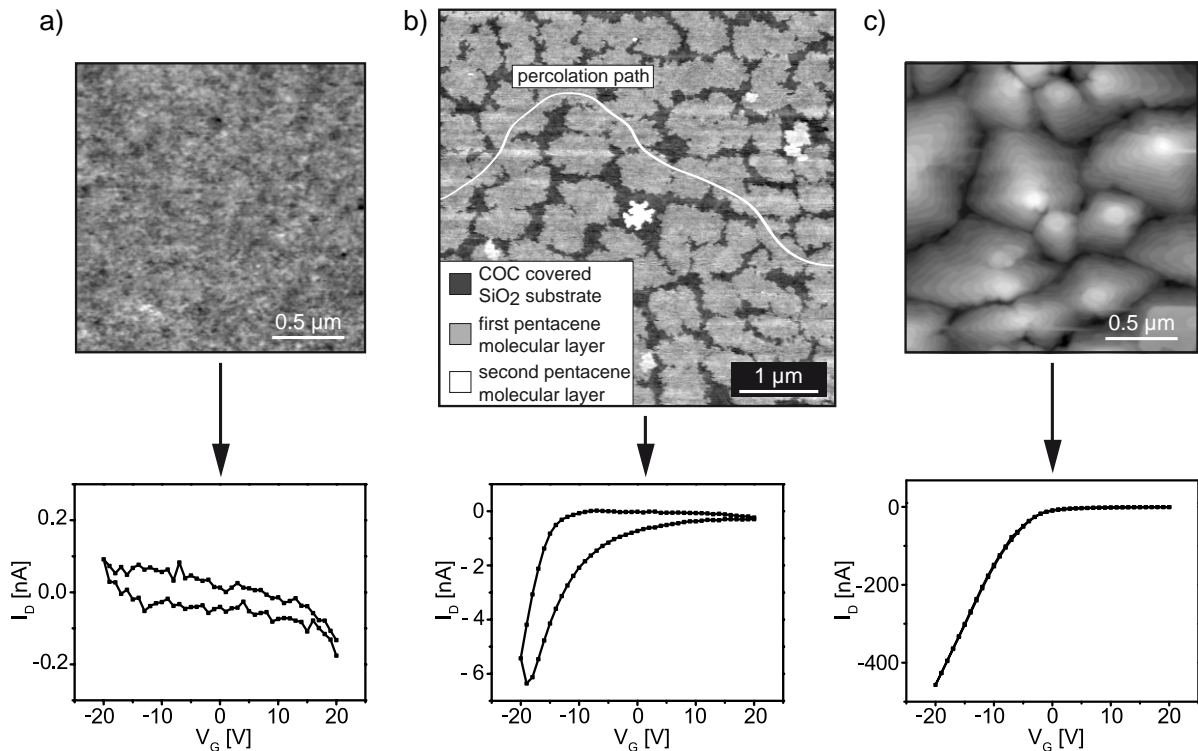


Figure 3.1: Principles of thickness resolved transport measurements (topography via AFM vs. corresponding transport curves). a) AFM micrograph (top) of pristine SiO_2 surface and corresponding transfer curve (bottom). Only small charging currents are measured. b) AFM micrograph (top) of pentacene film percolation, here at 0.8 ML, and corresponding transfer curve (bottom). As the accumulation channel percolates, I_D is small, and the hysteresis is large. c) AFM micrograph (top) of 50 nm pentacene and corresponding transfer curve (bottom). The channel is fully developed, i.e. mobility saturates, hysteresis almost vanishes, and threshold voltage takes on more positive values.

be extracted by evaluating each recorded characteristic curve, and then plotting them against film thickness. There are two types of characteristic curves: output curves, i.e. the change of drain current I_D with applied drain voltage V_D at constant gate voltage V_G , and transfer curves, i.e. the change of I_D with applied V_G at constant V_D (see Fig. 3.2). To be able to measure all three parameters with high thickness resolution, we only measure transfer curves at high sweep rate (up to $5 \frac{V}{s}$) during *in-situ* studies. The output curves were recorded after each deposition process for full device characterization. The device saturation mobility μ_{sat} is pro-

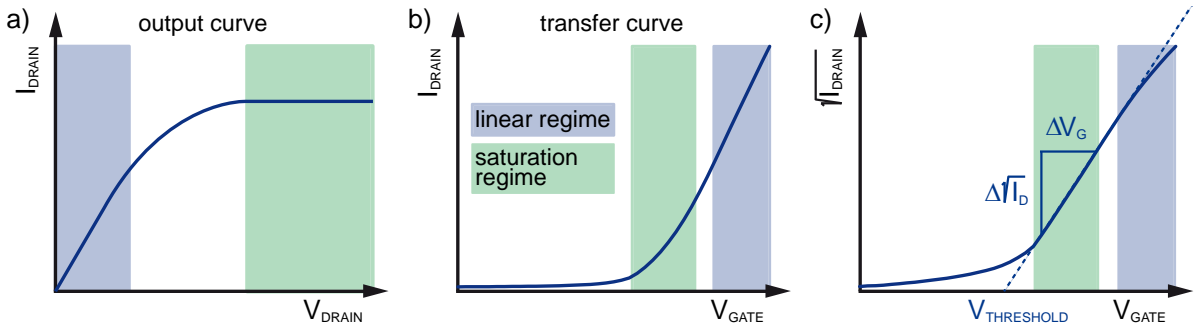


Figure 3.2: Schematic characteristic curves of TFTs. a) Output curve. b) Transfer curve. c) Square root of transfer curve for parameter extraction.

portional to the square of the slope m_{sat} of the square root gate sweep in the saturation regime (Fig. 3.2 c), and the fraction of the channel length L and the channel width W multiplied by the dielectric capacitance C_i :

$$\mu_{sat} = \frac{2L}{WC_i} m_{sat}^2 \quad (3.1)$$

$$\text{with } m_{sat} = \frac{\sqrt{\Delta I_D^{sat}}}{\Delta V_G}$$

A theory for the calculation and extraction of organic thin film transistor parameters was developed by Gilles Horowitz [92–94]. Note, that the device mobility is not to be equated to the internal charge carrier mobility of the organic semiconductor (cf. chapter 1). Crystal imperfections and impurities, interface trap states due to ambient conditions and at the interface to the gate dielectric, as well as contact resistance effects, all affect the measured mobility. Therefore, the extracted mobilities are to be regarded as device properties. The non vanishing threshold voltage V_{th} is mainly caused by deep trap states within the bulk of the film and at the dielectric surface. It is deduced from the intersection of the saturation current tangent with the axis of abscissae, because:

$$I_D^{sat} = \frac{W}{2L} \mu_{sat} C_i (V_G - V_{th})^2 \quad (3.2)$$

The hysteresis is the difference between the two threshold voltages of the respective forth and back sweeps. It is a direct indicator for the presence of thermal traps, which, once filled, can be released at room temperature.

3.2 DEPOSITION SETUP AND IN-SITU SAMPLE HOLDER

The organic semiconductors are grown via molecular beam deposition in an ultra high vacuum (UHV) chamber. The chamber consists of a main volume, including a low energy electron diffraction option and a sublimation cell tower for up to three different materials, and a sample lock, which allows to switch samples without breaking the main chamber vacuum. In the main chamber, the sample is mounted to a manipulator rod and can be positioned to face the LEED setup or the sublimation cells (see Fig. 3.3). A shutter for film deposition is not included in the system, as the sample can be rotated into and out of the molecular beam. Two quartz microbalances are used to control film thickness, one facing in sample surface normal direction and one facing in a 90 degree angle to the sample. The main chamber is pumped by an ion getter pump, the lock by a turbo molecular pump in combination with a scroll pump.

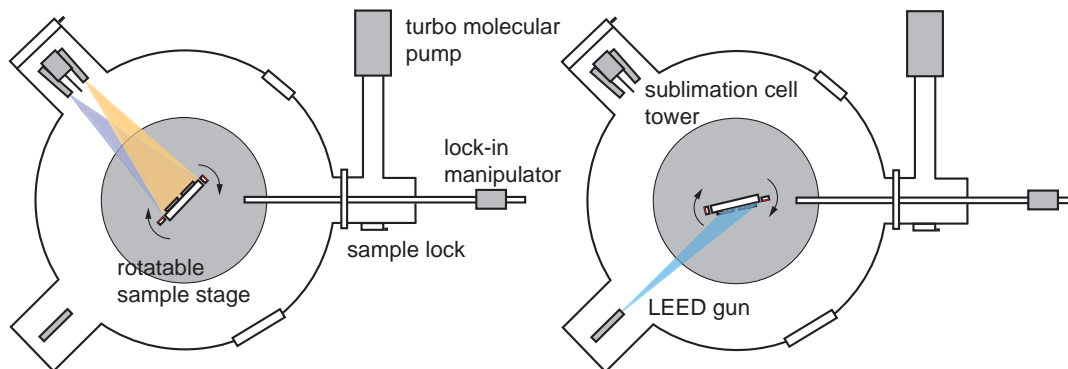


Figure 3.3: Schematic of the UHV chamber. a) Sample in position for organic material sublimation. b) Sample in position for crosslinking via LEED gun.

The sublimation cells implemented in the UHV chamber have been designed to produce a molecular beam which is a good compromise between collimation and homogeneity at the sample position. In general, the collimation can be adjusted to any sublimation cell - sample distance by varying the ratio between crucible outlet and crucible length [95] (here, 1:10 at a distance of ~ 40 cm). The cells are heated by two standard halogen lamps, which are connected by a UHV feedthrough, and can reach temperatures $> 500^\circ\text{C}$. The temperatures are measured via Pt100. A sketch of the cell geometry is shown in Fig. 3.4.

In addition to film deposition, the chamber has been equipped with the possibility to measure transistor characteristics *in-situ* while recording film thickness, i.e. during film growth (see Fig. 3.5). The mounting mechanism of the manipulator rod clamps the sample holder between a guide rail and a ledge with spring contacts. The spring contacts connect the source-, drain-, and gate-electrodes of the bottom contact TFT structures to an electrical feedthrough, which leads to standard coaxial BNC connectors outside the chamber. These can be accessed by a Keithley 2612 source-meter, which applies voltages and reads out current characteristics simultaneously. The TFT structures are contacted by spring contacts built into the shadow masks, which guarantee that only the channel area of the TFTs gets covered by the semicon-

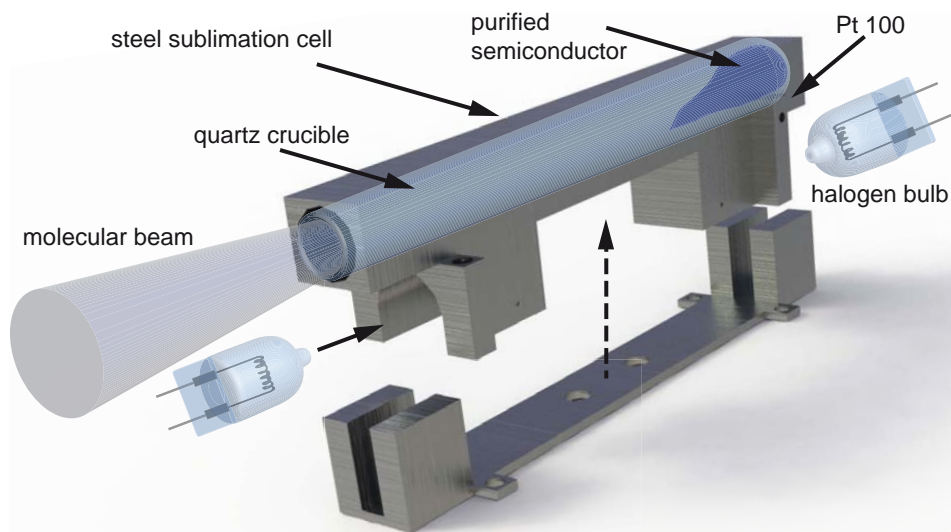


Figure 3.4: Sketch of the sublimation cell in Knudsen geometry.

ducting material. The sample temperature can be elevated using two halogen lamps which are positioned behind the sample holder. It is measured via a Pt100 which is in direct contact with the sample surface. Transfer and output measurements are defined by a self-written Labview program, which allows to perform complete device characterization, i.e. run a set of gate- and drain-voltage sweeps, or to continuously run a loop of gate-sweeps to record device evolution during film formation.

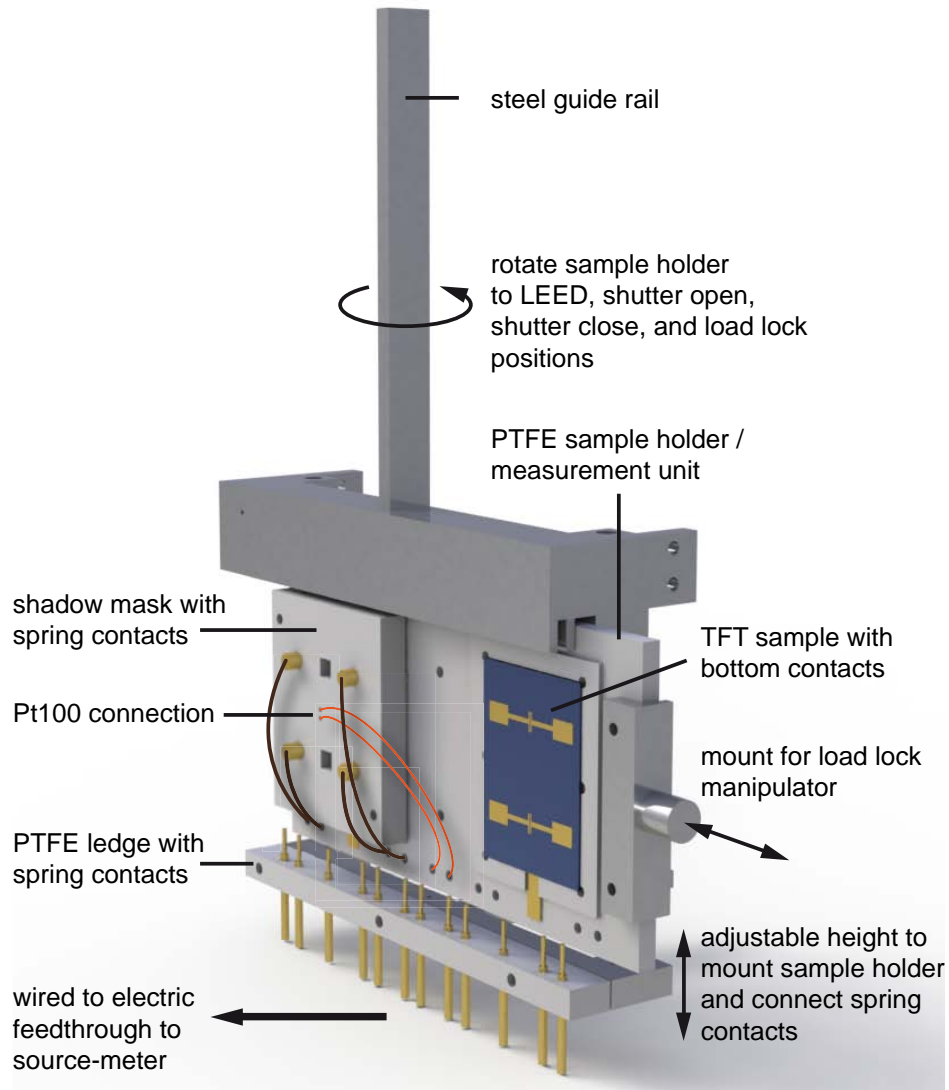


Figure 3.5: Sketch with detailed description of the *in-situ* sample holder.

3.3 FILM PERCOLATION ON ROUGH TECHNICAL SURFACES

Part of the findings presented in this chapter have been published [2]. The full article is attached in appendix A.

The presented system was used to gain insight into phenomena at the dielectric interface and the semiconductor-semiconductor interface. In this section, percolation on rough technical surfaces is discussed.

As seen from Fig. 3.1, the onset of drain current can be anticipated by the topographical conditions when the thin film percolates. This only holds for smooth substrates that allow to resolve sub-monolayers of organic semiconductors with AFM or X-ray scattering techniques. However, the technical surfaces appearing in many flexible plastic electronic devices often show high root mean square (rms) roughness [13]. Using *in-situ* characterization, we overcame these limitations and could determine the early stage growth of pentacene on parylene-C substrates with an rms roughness of ~ 7 nm [2]. The pentacene film percolates within a sub-monolayer as shown in Fig. 3.6, suggesting layer-by-layer conformal coverage of the parylene surface. The ongoing evolution of transistor parameters mirrors the behavior on smooth SiO₂ [87] and the film starts to form a grainy morphology, i.e. overall, the film follows the Stranski-Krastanov growth mode.

These findings raise the question of the boundary conditions, which determine whether a film

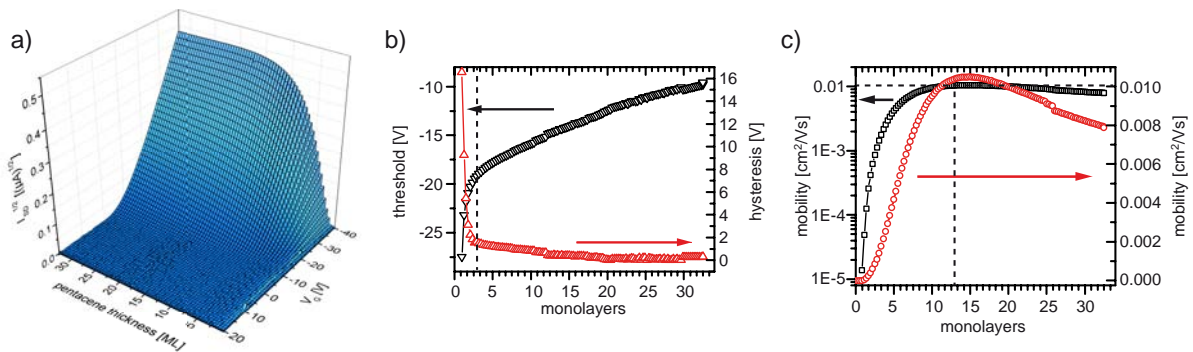


Figure 3.6: Electronic *In-situ* measurements of pentacene channel evolution on rough parylene-C dielectric. a) V_G sweeps, plotted against the nominal pentacene film thickness and the square root of I_D . b) Thickness dependence of threshold voltage and hysteresis. c) Thickness dependence of linear and logarithmic mobilities.

can grow conformally on surfaces with large rms roughness or not. The answer can be found considering the lateral roughness of the surface. Or differently put, one has to ask, how large the lateral correlation length ζ must be so that the molecules do not "see" the rms roughness anymore. It is possible to deduce a condition for the lateral surface roughness, using some simple dimensional considerations. The characteristic length scale for charge transport in organic semiconductors is given by the π -system overlap. Hence, it is necessary to regard height fluctuations at distances matching the unit cell dimensions of organic semiconductors, i.e. distances of the order $R_{uc} = 1$ nm. This information is contained in the height difference cor-

relation function (HDCF) $g(R) = \langle [z(x, y) - z(x', y')]^2 \rangle$, with $R = \sqrt{(x - x')^2 + (y - y')^2}$ [96, 97]. Since the roughness of most surfaces can be described by a self affinity model, this correlation function can be approximated by: $g(R) = 2\sigma^2(1 - e^{-(R/\zeta)^{2h}})$. Here, ζ is the correlation length and the Hurst parameter h quantifies the fractal character of the surface, i.e. $h \rightarrow 0$ for jagged surfaces and $h \rightarrow 1$ for smooth waviness. Note that the HDCF approaches zero for separation much smaller than the correlation length ζ , i.e. it is quite possible that the height difference at unit cell dimensions (lattice distortion) can be very small, even for large σ values. Highly ordered pentacene thin films that have been sublimation grown on smooth SiO₂ surfaces, for example, exhibit lattice distortion of about 1% to 2%, while films with distortions $\geq 10\%$ are already considered amorphous [98]. Therefore, considering a 2% variation as a tolerable value for the HDCF $g(R = R_{uc})$, one can estimate a minimal correlation length ζ for any given rms roughness σ , where thin film growth can still be regarded as highly ordered. Using typical parameters for pentacene and polymeric surfaces (here, $\sigma_{par} = 7 \text{ nm}$, $R_{uc} = 0.5 \text{ nm}$, $h = 1$, and $g(R) = 0.02$) this leads to an estimate for the correlation length of the order 35 nm. In other words, as long as the lateral correlation length is high enough, a high rms σ does not impair crystal structure. A very rough experimental estimation of the correlation length at hand varies between $\sim 50 \text{ nm}$ and $\sim 170 \text{ nm}$. It was deduced from AFM micrographs which are shown in the supporting information of [2] (see appendix B). This clearly lies above the deduced minimum for ζ and thus explains how the early stage percolation is possible. These findings emphasize that, although widely assumed otherwise, materials with high rms roughness can serve as dielectric in organic electronic devices without impairing well defined semiconductor growth.

3.4 IN-SITU INVESTIGATION OF THE FORMATION OF A PENTACENE - C₆₀ AMBIPOLAR TFT

Part of the findings presented in this section have been published [1]. The full article is attached in appendix A.

The importance of understanding the mechanisms at organic-organic heterojunctions was emphasized in chapter 1. The investigation of channel formation within ambipolar devices presents a more elaborate use of the *insitu* technique. In [1], we have gained new insights on the formation of the n-channel and its impact on the preexisting p-channel (Fig. 3.7).

In contrast to the experiment above on unipolar transistors, here we tracked the formation of a pentacene-C₆₀ heterojunction. Therefore, a pre-fabricated top contact pentacene (hole conducting) transistor was transferred into the *in-situ* setup and its characteristics were measured during deposition of C₆₀. It is shown, that the n-channel forming at the pentacene-fullerene interface percolates at much larger film thicknesses than pentacene on SiO₂ or parylene-C. The C₆₀ film starts growing as disjoint drop shaped islands (cf. chapter 2) that slowly form a

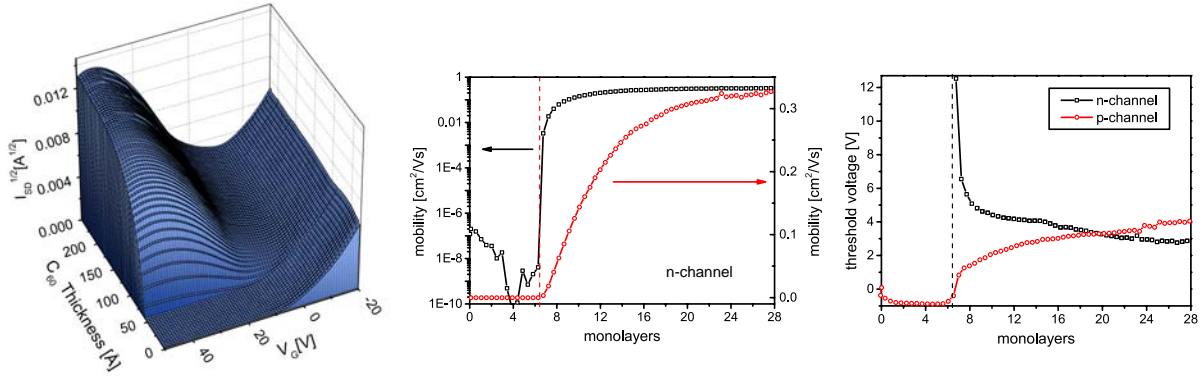


Figure 3.7: Electronic *In-situ* measurements of pentacene and C₆₀ channel evolution during C₆₀ growth. a) V_G sweeps, plotted against the nominal C₆₀ film thickness and the square root of I_D . b) Thickness dependence of linear and logarithmic n-channel mobilities. c) Thickness dependence of n-channel and p-channel threshold voltages.

continuous film at thicknesses of about 5 ML. After percolation, the n-channel behaves very similar to the expected trend for well known hole conductors like pentacene. In the beginning, the electron mobility rises steeply, then saturates as the applied gate voltage is screened more and more by the conduction channel. The same holds for the initial threshold voltage shift to more negative voltages, which is in parts induced by the filling of deep volume traps. The p-channel threshold, on the other hand, also experiences a shift towards more positive voltages as soon as the n-channel develops. This behavior is explained by a charging of the developing heterojunction, driven by Fermi-level alignment, which in turn acts as an additional top gate for the p-channel. We propose that this way a second conduction channel with mobile charge carriers develops at the pentacene-fullerene interface, which has to be depleted for the drain current to vanish. Interestingly, this shift could only be measured for percolated C₆₀ films, as the fullerene islands are disjoint in the beginning and hence, in this configuration, the charging of the interface is confined to the pentacene-C₆₀ contact area.

These findings have lately been confirmed impressively by Kyndiah et al. [99]. The experiment was extended to the investigation of charge transfer (CT) depending on the underlying pentacene film thickness. This way, the additional charge density at the pentacene-fullerene interface could be modeled in dependence of the pentacene surface morphology and with it C₆₀ growth. For pentacene thicknesses in the layer-by-layer growth regime, i.e. until the completion of approximately two monolayers, C₆₀ percolates very early, the threshold voltage shift of the p-channel is large and the additional charge density due to Fermi-level alignment rises. As the pentacene thickness increases, the surface starts to experience grating and the overall coupling of the two conduction channels decreases. This, in turn, leads to a monotonous decrease in CT and, at the same time, a decrease in p-channel threshold voltage shift. In addition, the percolation of C₆₀ delays due to the roughening of the pentacene surface. Moreover, the CT carrier mobility could be estimated, hence confirming our statement in [1] that the additional charges at the organic interface are mobile.

The overall strong threshold voltage shift of several volts can be explained by the large excess

of the capacitance between bottom p-channel and top n-channel and the capacitance of the bottom gate dielectric oxide layer. Kyndiah et al. calculated this excess to one to two orders of magnitude depending on the pentacene thickness.

As these are purely empirical conclusions, we are left with the need for a theoretical model that consolidates these findings by predicting the behavior of similar systems reliably. This thesis has contributed to complete the set of data needed to comprehend the mechanisms of charge transfer, and the technique represents a valuable test platform for further systems.

PREPARATION AND TRANSFER OF ORGANIC SEMICONDUCTOR NANOSHEETS

Part of the findings presented in this chapter have been published [3]. The full article can be found in appendix A.

4.1 CROSSLINKING OF SEMICONDUCTOR THIN FILMS VIA ELECTRON IRRADIATION

The mechanical flexibility is one of the most important properties of organic thin films. We have seen that the growth of well ordered high performance films is not always possible, when being restricted to one specific substrate. This leads on the one hand to limitations in the choice of electrode material, and on the other hand limits the variety of technical substrates. Therefore, the wish for a possibility to separate the growth of thin films from device fabrication, i.e. to transfer prepared films to their intended surfaces, becomes apparent. To this end, supporting layer processing, i.e. using a sacrificial substrate for film formation, which is then dissolved, has proven to be a very useful technique. It has been successfully employed to fabricate free standing conductive polymers like poly(3,4-ethylenedioxythiophene)/poly(styrenesulfonate) (PEDOT/PSS) [100], and to transfer very stable and functional nano-membranes made from crosslinked self assembled monolayers (SAMs) [101]. The challenge of adapting this method to van der Waals - crystals like organic semiconductor thin films is their low mechanical stability. In order to give thin pentacene films a stable, covalently bound backbone, we irradiated the film with a low energy electron (LEE) beam. Andrey Turchanin et al. have shown that the irradiation of SAMs of organic molecules forms covalent bonds, which are much stronger

(one to two orders of magnitude [102]) than the usual van der Waals bonds [45], and they have thoroughly modeled the crosslinking mechanisms for aromatic biphenyl monolayers. The electrons break up C–H bonds of the hydrocarbons, leaving open binding sites (Fig. 4.1). These can then bind to neighboring molecules. The idealized case of pentacene forming a fully crosslinked dimer with biphenyl-like bonds is shown in Fig. 4.1 b for illustration. Of course, also partial crosslinking, destruction, or the formation of smaller molecules by C–C bond breaks can be imagined.

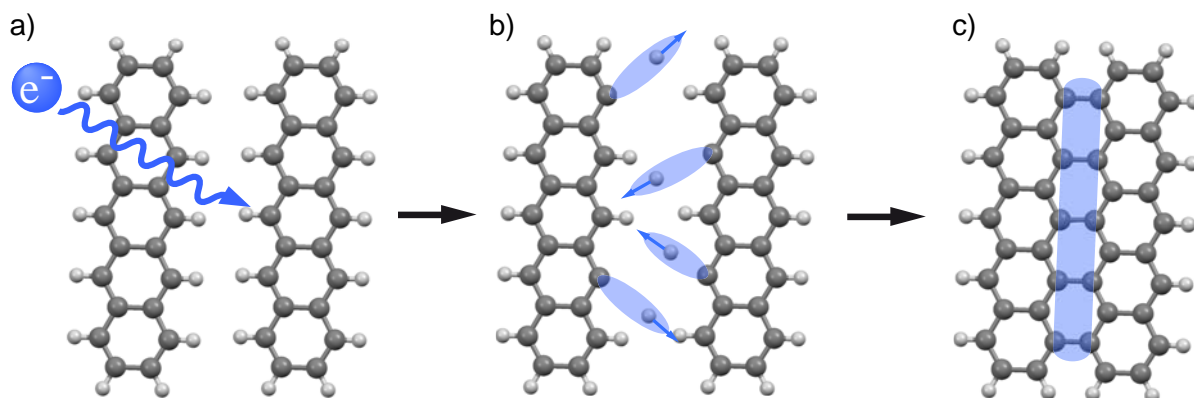


Figure 4.1: Idealized scheme of crosslinking mechanism. a) The pentacene film is irradiated by low energy electrons (LEE). b) Due to irradiation C–H bonds are broken, creating free binding sites. c) Free binding sites of two neighboring molecules form new covalent bonds.

The studies of Turchanin et al. have further revealed, that, instead of being absorbed within the SAM directly, most electrons transmit through the SAM and generate secondary electrons within the substrate [45], which, in return, crosslink the membrane from the bottom. In chapter 2 we have shown that for thicker films (~ 50 nm) the electron beam crosslinks the surface directly (see Fig. 4.2), due to the small electron penetration depth in matter, which has been calculated to be of the order of only a few nanometers in this energy range for various organic materials [103, 104].

We have found that for 50 nm pentacene films, an irradiation time of 20 minutes with 500 eV electrons (i.e. very much larger than typical binding energies of covalent bonds) has proven to decently stabilize the film mechanically, while not impairing film functionality [3]. To check, if the stabilization by the number of electrons at hand is plausible, one can make two considerations: first, if enough electrons are present in the beam with respect to the number of molecules in the surface area of the film, and second, how many bonds per molecule need to be formed to reach a stabilized film. For the first consideration the dose per area has to be estimated. This has been done via the current I_B flowing through a ground electrode: $D = \frac{I_B t}{A}$. Here, $I_B \approx 100$ nA through an irradiated reference surface $A = 4$ mm² at the sample position which leads to a dose of $D = 3.0 \frac{mC}{cm^2}$, i.e. 1.88×10^{16} electrons reach a square centimeter of sample surface. Using these numbers one can check, if complete crosslinking of a few layers is plausible, considering the available number of electrons. From [3] one can assume four *dead* molecular surface layers. With the lateral area of a thin film phase pentacene unit cell

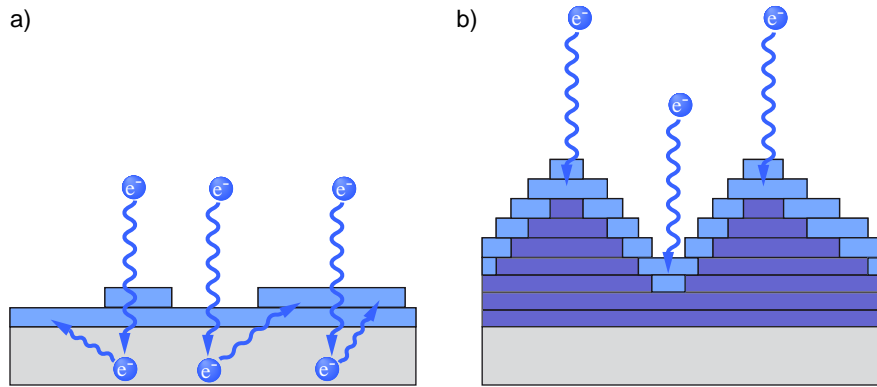


Figure 4.2: Sketch of monolayer vs. multilayer irradiation. a) At very low thickness the electrons transmit through the film into the substrate, where they release secondary electrons. These secondary electrons then initiate the crosslinking process. b) When the film is thicker than the penetration depth of electrons into the material, the surface is crosslinked directly by the primary electron beam.

being $5.9 \text{ \AA} \cdot 7.6 \text{ \AA} \approx 45 \text{ \AA}^2$ [58] and two molecules per unit cell, the first four layers of a square centimeter contain approximately 1.76×10^{15} pentacene molecules. This leaves more than ten electrons per molecule for absorption and, hence, crosslinking.

To address the second consideration, note, that the process of stabilizing a film by forming new covalently bound clusters is a percolation problem. One typical parameter in percolation theory is the percolation threshold f_c , i.e. the critical fraction of formed bonds, at which percolation paths through the lattice exist. Here, let us put the formation of a percolated cluster in analogy to typical multimerization or gelation, at least as a first naive approximation, as the system is very restricted in one dimension and there is no experimental evidence for the exact molecular composition of the crosslinked layer. As a lower limit, assuming the molecule to be intact and stiff, we may state that each molecule can bind in at least four different directions (Fig. 4.3 a), i.e. to a neighbor left and right and in an inter-layer fashion. Naturally, as pentacene has fourteen binding sites available, this is the simplest description, leading to an upper limit for the percolation threshold. In this case, the formation of a percolation path can be modeled by a Bethe lattice (or Cayley tree) with $z = 4$ branches [102, 105, 106] (Fig. 4.3 b). We find that the number of bonds in a cluster N to the n th generation of the lattice can be written as: $N \sim f(z - 1)^n$. The probability that a bond is created is f . Here, the percolation criterion translates to n growing very large. In this case (here $n \rightarrow \infty$) the expression for N converges to two distinct solutions: $N \rightarrow 0 \leftrightarrow f < f_c$ and $N \rightarrow \infty \leftrightarrow f > f_c$. This means that the system percolates above a certain threshold $f_c = \frac{1}{z-1}$. Hence, for $z = 4$, the crosslinked film already percolates, i.e. stabilizes mechanically, when $\frac{1}{3}$ of the bonds are made. Raising z will even lower f_c , and our statement that enough electrons are present in the irradiation beam becomes even more plausible.

Of course, this is only the simplest idea of how a covalent network could form. Unfortunately, from the electronic and structural data given in [3] one can not draw decisive conclusions on the exact molecular nature of the crosslinked film. Nonetheless, two facts are known: first, the

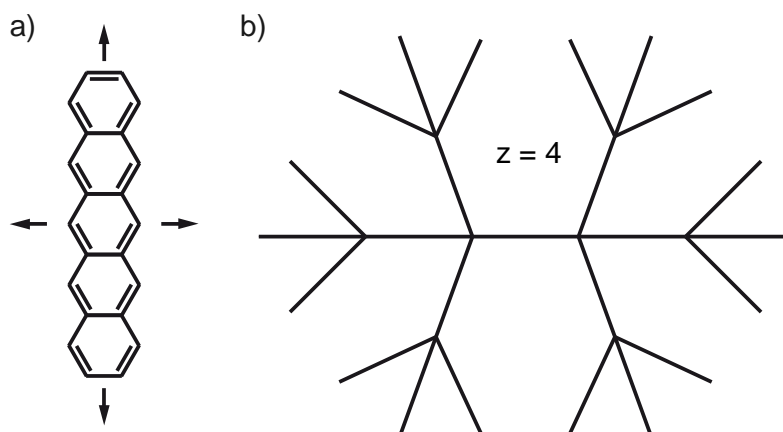


Figure 4.3: Multimerization of pentacene. a) Pentacene molecule with at least 4 possible binding sites. b) Bethe lattice for $z = 4$.

topography of the film stays intact, and second, the irradiated surface is mostly amorphous. While the first fact implies that inter-layer crosslinking is not only present, but paramount, the amorphous nature of the film reveals that there is no order to the lateral "multimerization" of the molecules. To obtain a more complete picture of the configuration and composition, or rather to sensibly choose the right techniques to experimentally apprehend the system, one needs to address possible impacts of irradiating the aromatic thin film:

- The pentacene molecules form large percolation networks as discussed above, either forming biphenyl-like single or multiple bonds to neighboring pentacene molecules, or bind to subjacent or above molecules forming inter-layer bonds.
- Pentacene forms small disjoint clusters or even dimers with increased band gap and stability (cf. [107]).
- The electrons (typically several hundred eV) break up C-C or C=C bonds, either destroying the benzene character of the molecule and thus its aromaticity, or forming new, shorter, acenes with larger band gaps [47].

Using ultraviolet-visible (UV-VIS) spectroscopy in [3], we could already show that crosslinked films lose their characteristic absorption lines, while absorption is enhanced at smaller wavelengths, i.e. the π -system is reduced. In addition, Fourier transform infrared spectroscopy (FTIR) revealed the breaking of C-H bonds in crosslinked films. In the future, the formation of new species of aromatic molecules or complexes of molecules should be investigated via FTIR and Raman spectroscopy in more detail. Quantifying the nature of the crosslinking process within multilayer thin films will help to control and optimize the technique and to evaluate its applicability to other organic semiconductors.

4.2 TRANSFER OF ORGANIC THIN FILMS

The stabilized thin films can now be transferred to any new substrate of choice. The supporting layer processing used to transfer pentacene in deionized (DI) water is shown in Fig. 4.4. After deposition of the semiconductor on a smooth, sacrificial polyvinyl-alcohol (PVA) layer, the film is crosslinked by LEE as described before. To detach the film from the initial substrate, the sample is placed in a beaker with ultra pure (Milli-Q™) DI water. The pentacene film peels off in large sheets that can be handled with tweezers and maneuvered on to a new substrate under water. Parts of the film surface that have not been irradiated disintegrate at the slightest touch. When the sheet is placed over the substrate, both, film and substrate, are pulled out of the water simultaneously and then set to dry under light nitrogen flow. This will laminate the film irreversibly to the new substrate.

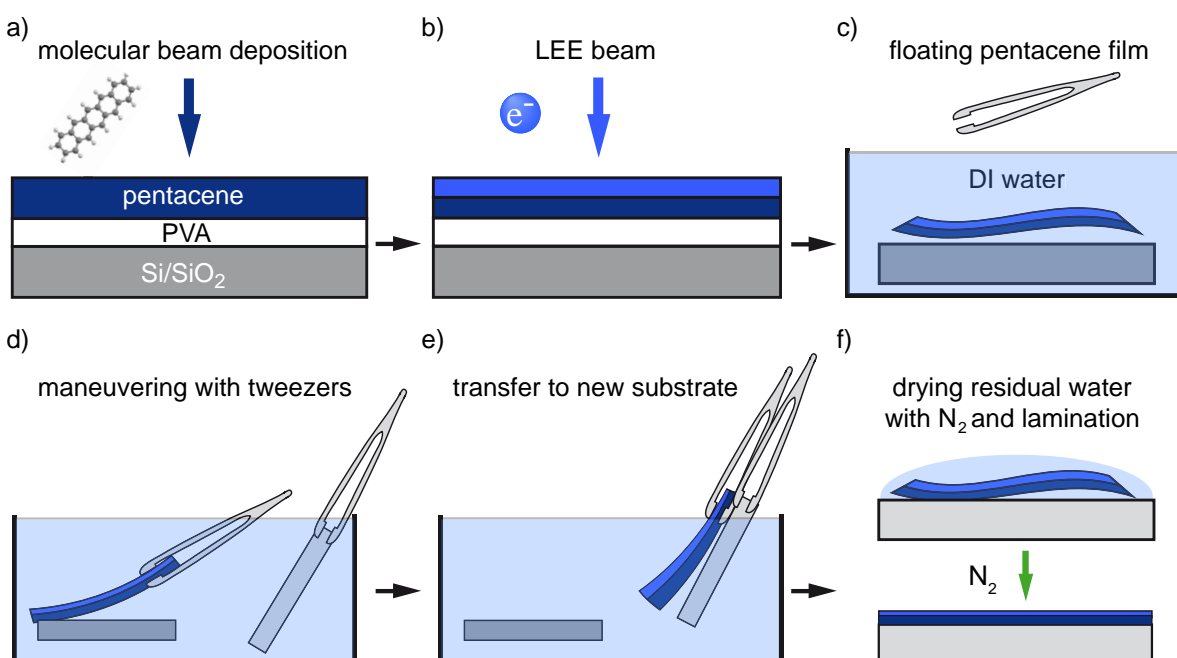


Figure 4.4: Schematic of the transfer of a pentacene thin film to a new substrate. a) Deposition of pentacene to a smooth, PVA coated substrate. b) Irradiation of the pentacene surface via low energy electron beam. c) Dissolution of the sacrificial PVA layer in DI water. d) Navigation of the floating pentacene sheet to new substrate surface. e) Simultaneously pulling the film and the substrate out of the DI water through its meniscus. f) Lamination of the pentacene film to the new substrate by drying the sample with nitrogen.

4.3 POTENTIAL FOR FUTURE APPLICATIONS

By transferring a pentacene thin films to bottom contact TFT test structures, contact resistance could already be lowered by more than two orders of magnitude, with respect to commonly

deposited thin films (cf. [3]), without the typically necessary surface treatment of electrode material [108, 109]. Moreover, besides device optimization, this new techniques opens up a variety of new possible applications. The more obvious possibilities comprise the transfer to all kinds surfaces that are difficult to access, without involving an extra substrate as carrier, be it skin, paper, packaging materials, or as functional layer in van der Waals heterostructures. In a more fundamental scientific sense, the decoupling of film formation and substrate choice makes it possible to study the impact of dielectric interfaces on charge transport independently of film growth. For instance, Someya et al. could relate surface energy manipulation via UV irradiation of SAMs grown on a dielectric surface to charge transport in thin DNTT (dinaphtho[2,3-b:2',3'-f]-thieno[3,2-b]thiophene) films [110]. However, since film formation was also strongly dependent on the surface energy, it was difficult to distinguish the influences of surface energy and film morphology on charge transport. Thin film transfer to the previously modified surfaces could clarify the situation.

The stabilized films are able to span large cavities of the order of mm^2 . This opens the door for free standing semiconductor layers, i.e. for devices using air or vacuum as dielectric. This way, one could characterize the electronic properties of organic thin films in TFT geometry, without the influence of the dielectric interface, as has been done before for organic single crystals [111]. In addition, one could use the maximized access to the semiconductor surface in electrostatic high sensitivity organic sensing applications, e.g. capped in aqueous buffer solution [9] or via ion gel gating (cf. [112]).

In the following, two ideas are proposed to realize such a free standing TFT (Fig. 4.5). The first approach is based on the classic transistor geometry, spanning a pentacene thin film over a predefined TFT structure sans the dielectric within the transistor channel region. The second approach is based on the transfer over a thin silicon nitride (Si_3N_4) pore. Commercial pores are attached to a stable substrate, while the top and bottom sides of the pores are easily accessible (cf. geometry in Fig. 4.5 b). Source and drain contacts would have to be positioned exactly at the pores edges, while a movable gate electrode, e.g. mounted to a translational micrometer screw, approaches from the other side of the pore. This way, one gains the advantage of being able to scan the thickness of the dielectric.

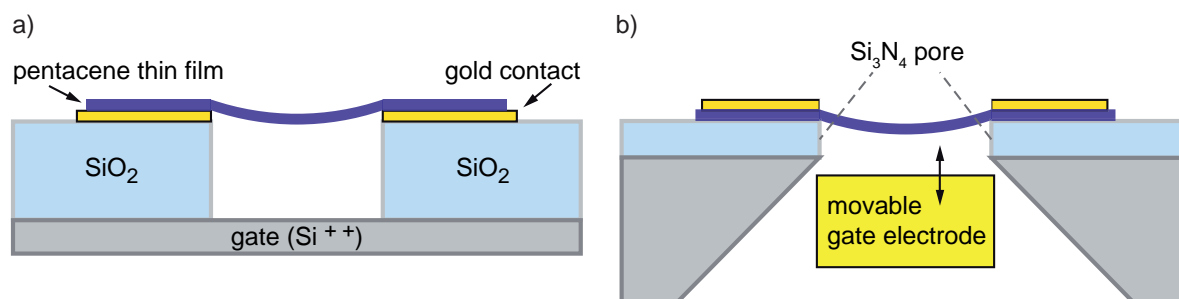


Figure 4.5: Schematic approaches to air dielectric TFTs. a) Transfer to standard bottom contact TFT structure, sans dielectric material in the channel region. b) Transfer to Si_3N_4 pore, gating via movable electrode.

As a first attempt to realize the structure in Fig. 4.5 a, etching of SiO_2 by hydrofluoric acid

was used, as shown in Fig. 4.6. The structures gained by this method were sound and ready to use as the receiving substrate for a transferred pentacene thin film. The transfer however faced the challenge of the film laminating to the bottom of the transistor channel, i.e. the gate electrode. Neither using printing techniques employing polydimethylsiloxane (PDMS) and eicosane ($C_{20}H_{42}$, alkane) stamps presented a solution to this problem.

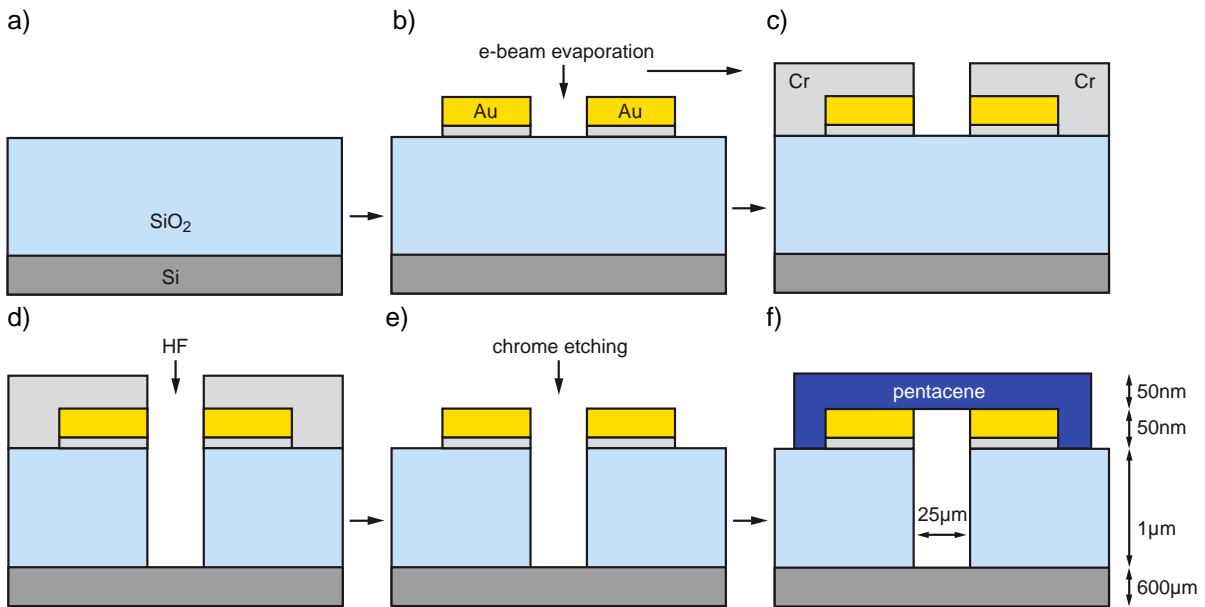


Figure 4.6: Lithographic steps towards air dielectric TFT. a) The base is an Si/SiO₂ substrate with thick (1 μm) oxide layer. b) Definition of 50 nm gold electrodes via shadow mask and electron beam deposition. c) Coverage of the whole sample area, sans the channel region, with 100 nm electron beam deposited chrome. d) Etching of the channel region oxide with hydrofluoric acid (HF) (ca. 20 minutes in 5% HF solution). e) Removal of the chrome layer via commercial chrome etching solution. f) Spanning of pentacene sheet over channel cavity.

Using photo lithography to better define the TFT structures and an elaborate spanning system that holds the ends of the thin film during lamination, could overcome the initial challenges. These adaptations and the idea from Fig. 4.5 b, which is not affected by potential drooping of the film, might be the key to realize a true, free standing, polycrystalline thin film transistor.

FINAL WORDS

The scientific work described in this thesis attended to questions and challenges concerning key interfaces in organic electronic devices. It was shown that semiconductor thin film growth on electrode, dielectric and other semiconducting materials is still subject to ongoing research and optimization.

For this, next to taking advantage of very established methods like X-ray analysis and various microscopy techniques, two more individual and new approaches, namely *in-situ* electronic characterization and transfer of organic semiconductor nanosheets, were developed and optimized.

In-situ characterization of the formation of an ambipolar transistor employing pentacene as the p-type, and fullerene C₆₀ as the n-type conductor, gave access to the thin film thickness dependence of changes in the electronic behavior of the device. In contrast to the mere comparison of devices with and without a second semiconducting layer, important events, like the point of percolation and the saturation of heterojunction formation, could be tracked with a high thickness resolution. Complemented by detailed structural and morphological characterization, the modeling of the attained data and the extension of the method to other systems can serve as a basis for a more refined theoretical understanding of heterojunction formation.

The application of *in-situ* characterization to pentacene growth on rough parylene-C substrates led to mainly one significant conclusion. As long as the lateral correlation length allows for it, a defined layer by layer growth during the first monolayers, which impacts the conduction channel formation, is not impaired by a high root mean square substrate roughness. The quantitative acquisition of these findings is very non trivial using techniques like atomic force microscopy or surface X-ray analysis, but comparably straight forward analyzing the thickness dependence of electronic properties of organic thin films.

Finally, the development of a method to fabricate and transfer semiconducting organic nanosheets grants access to a new set of possibilities to study thin films and to employ them in devices containing interfaces impeding high quality film growth or with unusual layouts. It will be interesting to explore the full potential of this new process, and its appearance in yet

unthought experiments and device applications.

In conclusion, this thesis contributes to the clarification of some important aspects of interface formation in organic electronic devices, while setting up a couple of new approaches for future device fabrication and optimization.

PUBLICATIONS

S. Noever, S. Fischer, B. Nickel, *Dual Channel Operation Upon n-Channel Percolation in a Pentacene-C60 Ambipolar Organic Thin Film Transistor*, *Advanced Materials*, 2013, Vol. 25, Issue 15, 2147-2151.

F. Werkmeister, **S. Noever**, B. Nickel, *Sub-Monolayer Percolation of Pentacene on Rough Parylene-C Dielectrics*, *Organic Electronics*, 2015, Vol. 26, 439-442, (shared first authorship).

C. Liewald, **S. Noever**, S. Fischer, J. Roemer, T. Schüllli, B. Nickel, *Microdiffraction Imaging - a Suitable Tool to Characterize Organic Electronic Devices*, *AIMS Materials Science*, Special Issues (X-ray microscopy in Materials Sciences), 2015, 2(4), 369-378.

A. Guggenmos, M. Jobst, M. Ossiander, S. Radünz, J. Riemensberger, M. Schäffer, A. Akil, C. Jakubeit, P. Böhm, **S. Noever**, B. Nickel, R. Kienberger, F. Krausz, U. Kleineberg, *Chromium / Scandium Multilayer Mirrors for Attosecond Pulses at 145 eV*, *Optical Letters* 2015, Vol. 40, No. 12, 2846-2849.

H. Schamoni, **S. Noever**, B. Nickel, M. Stutzmann, J. A. Garrido *α, ω -Dihexyl-Sexithiophene Thin Films for Solution-Gated Organic Field-Effect Transistors*, *Applied Physics Letters* 2016, Vol. 108, No. 7, 073301.

S. Yazji, C. Westermeier, D. Weinbrenner, M. Sachsenhauser, K.-C. Liao, **S. Noever**, P. Postorino, J. Schwartz, G. Abstreiter, B. Nickel, I. Zardo, A. Cattani-Scholz, *Surface-Directed Molecular Assembly of Pentacene on Aromatic Organophosphonate Self-Assembled Monolayers explored by polarized Raman spectroscopy*, *Journal of Raman Spectroscopy* 2016, Vol. 48, No. 2, 235-242.

S. Noever, M. Eder, F. del Giudice, J. Martin, F. Werkmeister, S. Hallwig, S. Fischer, O. Seeg, N.-E. Weber, C. Liewald, F. Keilmann, A. Turchanin and B. Nickel, *Transferable Organic Semiconductor Nanosheets for Application in Electronic Devices*, *Advanced Materials*, 2017, 1606283.

Following, the attached manuscript appear in order of the amount of contributed content.

A.1 DUAL CHANNEL OPERATION UPON *n*-CHANNEL PERCOLATION IN A PENTACENE - C₆₀ AMBIPOLAR ORGANIC THIN FILM TRANSISTOR

Simon J. Noever, Stefan Fischer, and Bert Nickel
Advanced Materials 2013, Vol. 25, Issue 15, 2147-2151
DOI: [10.1002/adma.201203964](https://doi.org/10.1002/adma.201203964)

This publication has been selected as a highlight contribution in the DESY Photon Science 2013 - Highlights and Annual Report: *Insights in heterojunctions of operational organic electronic devices - In situ characterization of a pentacene - C60 ambipolar thin film transistor.*

Furthermore, it was chosen to feature as the front cover of *Advanced Materials* 2013, Vol. 25, Issue 15. The cover image was designed by Christoph Hohmann (NIM Media Design).

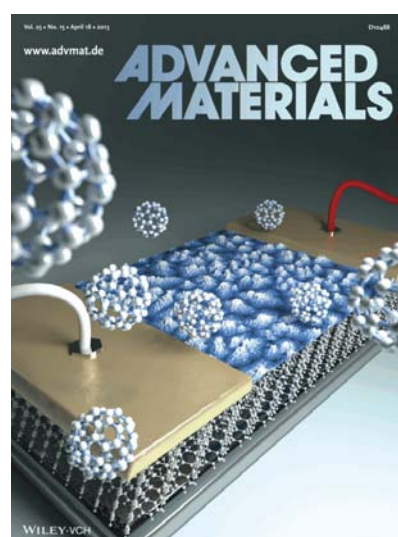
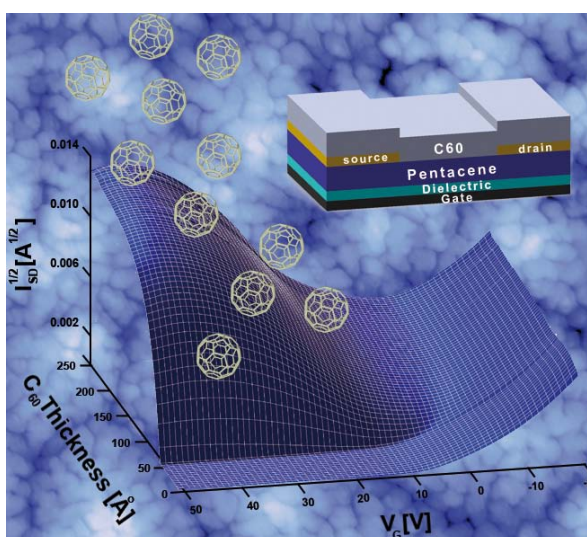
Abstract

Thickness resolved measurements of ambipolar thin-film transistor characteristics track the charging of an organic-organic heterojunction. Combined with structural investigation methods such as AFM and GIXS, this leads to a better understanding of the physics in state of the art devices such as organic solar cells, organic light emitting diodes and light emitting TFTs.

Contribution

The first draft of the manuscript was written entirely by me and I produced the final version. In addition, all figures, except figure 3b, were designed by me. I performed all sample preparations, experiments and data analysis, except the structural X-ray analysis.

Table of Contents Graphic & Journal Cover



Dual Channel Operation Upon n-Channel Percolation in a Pentacene-C₆₀ Ambipolar Organic Thin Film Transistor

Simon J. Noever, Stefan Fischer, and Bert Nickel*

Understanding the physics of organic–organic heterojunctions is essential to optimize state of the art organic electronic devices such as organic solar cells, organic light emitting diodes, and ambipolar thin film transistors (TFTs). Ambipolar, as well as combined unipolar TFTs have been assembled and used by several groups to build elemental circuit elements such as inverters and ring oscillators, while light emitting ambipolar TFTs combine the gate controlling features of a transistor with the light emission of a light emitting diode.^[1–10] Unfortunately, the energetic landscape at organic–organic interfaces is complicated due to a wealth of electrostatic phenomena such as charge transfer, dipole generation, and doping, all related to aspects of the molecular structure, e.g., molecular orientation, crystallinity, interdiffusion, and domain size. In-situ spectroscopy and diffraction experiments allow for probing the evolution of the electronic and molecular structure of ultrathin organic films during deposition and thus have been fundamental to develop physical models. Such models have been extended and quantified by theoretical studies, leading to a variety of structure dependent mechanisms for heterojunction formation.^[11–13] The performance of electronic devices, however, also depends crucially on the balance of several characteristic length scales, i.e., Debye length, depletion width, film thickness, and in particular the spatial location of trap states. Therefore, it is mandatory to track the evolution of device characteristics with film thickness. The inherent lateral geometry of TFTs allows for the in-situ acquisition of characteristic curves before and during semiconductor deposition. So far, such experiments have focused on hole conducting TFTs. The formation of the conducting channel upon percolation was observed, and from the shift of the threshold voltage with thickness, it was possible to identify surface and bulk traps.^[14,15] Here, we expand this technique to ambipolar devices, where the electrostatic situation at the heterojunction is crucial. The basic idea of the experiment is to deposit an electron conducting semiconductor on top of a fully developed p-channel to observe the changes of the device characteristics due to the evolution of an additional n-channel. The in-situ character of this experiment traces electrostatic changes back to the semiconductor layers, rather than external influences like air and humidity, which can significantly alter device characteristics in ex-situ experiments.^[16]

We have chosen to study the heterojunction formation of pentacene and fullerene C₆₀ because these materials exhibit high charge carrier mobilities in vapor deposited TFTs.^[17,18] They have been successfully implemented in various applications, e.g., in organic photovoltaics, and the basic structural and electronic aspects of this heterojunction have already been addressed by atomic force microscopy (AFM), x-ray reflectometry, and photoelectron spectroscopy.^[19–26] We complement our in-situ device measurements by grazing incidence x-ray scattering (GIXS) and AFM measurements.

We have tested several contact geometries for the ambipolar device. The best results were obtained employing the device structure depicted in Figure 1(a). The source and drain contacts are located between the two active materials, making the TFT a hybrid structure with a pentacene top contact and a fullerene bottom contact transistor geometry.^[5] Hereby, both semiconductors are in direct contact with the electrodes. Note that due to disrupted growth of pentacene on bare Au, top contact geometry is favorable compared to bottom contact. On the other hand, for C₆₀, we have not detected a change of growth topology on the

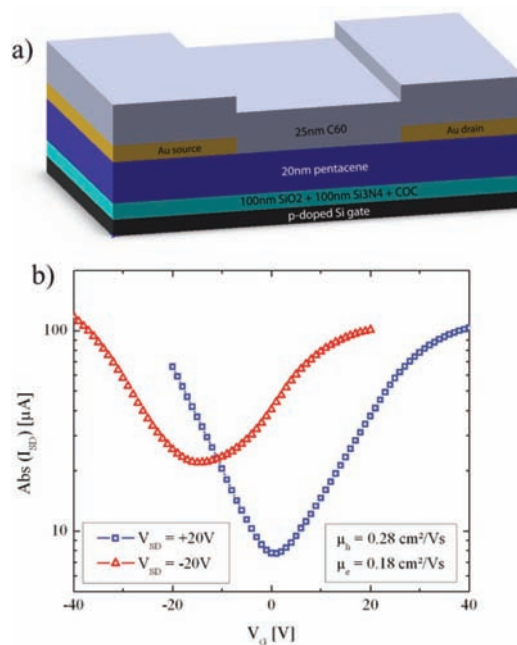


Figure 1. a) Schematic of the ambipolar device structure. b) Transconductance curves of an ambipolar FET for two different source-drain voltages V_{SD} .

S. J. Noever, S. Fischer, Dr. B. Nickel
Fakultät für Physik & CeNS
Ludwig-Maximilians-Universität München
Geschwister-Scholl-Platz 1, 80539 Munich, Germany
E-mail: nickel@lmu.de



DOI:10.1002/adma.201203964

Au contact and adjacent to it. Thus, we observe that the C₆₀ bottom contact allows for efficient electron injection. Here, Au is used as electrode material, as its workfunction matches the HOMO (highest occupied molecular orbital) of pentacene and the LUMO (lowest unoccupied molecular orbital) of C₆₀ reasonably well, offering acceptable injection conditions for holes and electrons into pentacene and C₆₀, respectively.^[3] A further advantage of this transistor geometry is an improved C₆₀ growth on pentacene with respect to the growth on the gate dielectric.^[21,25] We observed the best TFT characteristics with low hysteresis and high mobilities using an SiO₂-Si₃N₄ bilayer as dielectric and a thin cyclic olefin copolymer film of 5–6 nm thickness on top. The transconductance characteristics of the ambipolar transistor in ultra high vacuum and at room temperature are shown in Figure 1(b). The two curves show the characteristic v-shapes for ambipolar transistors and refer to negative (red curve) and positive (blue curve) source-drain voltages. The minimum current indicates the ambipolar regime of simultaneous electron and hole transport. Previous experiments attribute the observation of this ambipolar regime to the existence of two separate conduction channels; the hole conducting channel is located at the pentacene-gate dielectric interface, whereas the electron conducting channel lies at the pentacene-C₆₀ interface.^[27] The saturation mobilities of our device calculate to 0.28 cm² V⁻¹ s⁻¹ and 0.18 cm² V⁻¹ s⁻¹ for holes and electrons, respectively. These values compare to the best performances in ambipolar devices.^[3,5] Additionally, the two channels are well balanced in performance, which is a crucial feature for the application in circuits and light emitting TFTs.

To explore the electrostatic changes during the heterojunction formation, we performed C₆₀ film thickness dependent measurements, i.e., we recorded gate sweeps for positive source-drain voltages (cf. blue curve in Figure 1) during fullerene deposition. The resulting transfer curves and their thickness dependence are shown in Figure 2(a). Initially, the transistor shows the expected unipolar hole conducting characteristics of a pentacene based device. During the first 50 Å of deposition, i.e., about 6 ML (monolayers) C₆₀, the characteristic curves hardly change. Then, at around 55 Å C₆₀ film thickness the device suddenly begins to show electron conducting characteristics as well. The thickness resolved values for the respective threshold voltages for hole and electron conduction channel and the electron mobility are plotted in Figure 2(b) and (c). Beyond 55 Å, the electron mobility starts to rise quickly with increasing film thickness, until it saturates for thicknesses higher than about 150 Å, i.e., well beyond the Debye length. From unipolar devices it is known that the onset of conduction goes along with percolation of the semiconductor layer.^[14] Fast saturation after several pentacene MLs in TFTs has also been described before.^[14,28] The threshold voltages here show similar behavior in a sense that no change is measured for the first 50 Å fullerene film thickness. Beyond that thickness, both, the hole and the electron threshold voltages shift oppositely to more positive and more negative values, respectively, i.e., both channels open earlier with respect to their onset voltage. The n-channel threshold voltage experiences a large shift of roughly $\Delta V_{th} = 7.7$ V within 15 Å, i.e., between a nominal fullerene thickness from 55 Å to 70 Å. Thus, the threshold shift occurs within a much narrower thickness range compared to the evolution of

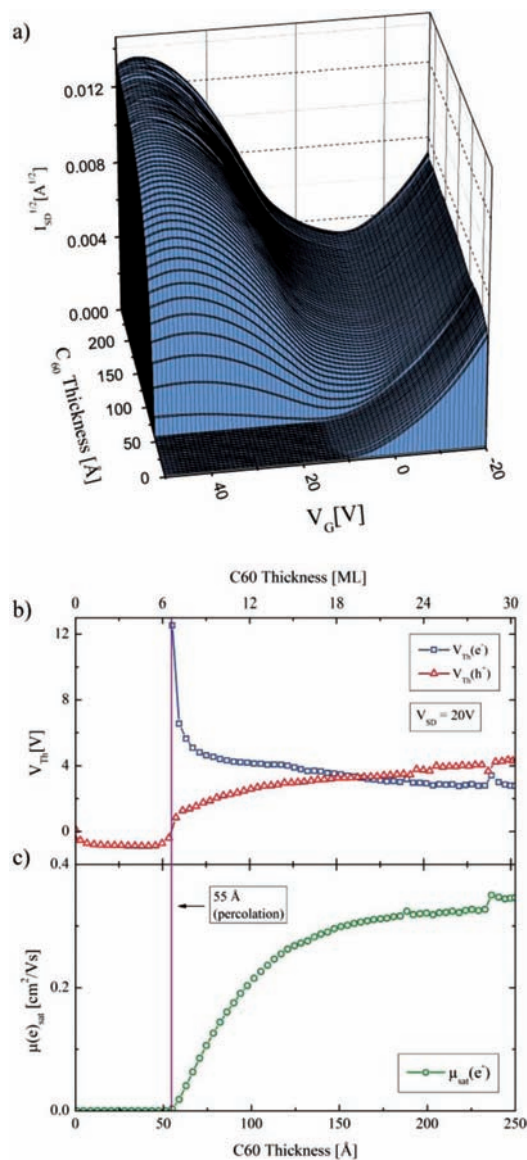


Figure 2. Thickness resolved measurements of the characteristics of an ambipolar FET during C₆₀ growth. a) Transconductance curves of an ambipolar TFT as a function of fullerene thickness. b) Thickness resolved threshold voltages of the hole and electron conducting channels, respectively. Percolation of the electron channel is indicated by the vertical line. c) Thickness resolved electron saturation mobility.

mobility.^[14] Interestingly, the p-channel threshold mirrors this effect, i.e., it also experiences a shift of about $\Delta V_{th} = 2.1$ V to more positive voltages within fullerene deposition of around 10 Å. This behavior is in agreement with previous observations, where a transistor was measured before and after the deposition

of the second semiconductor.^[29] In order to verify, whether structural or morphological changes can account for this behavior, we performed complementary structural analysis of the system using AFM and GIXS. The AFM images show that the fullerene film clearly retraces the pyramid like morphology of the underlying pentacene film (Figure 3(a)). However, it exhibits a drop-like topology with a grain size much smaller than the pentacene grains. This suggests that the delayed conduction onset of the

n-channel after around 55 Å (more than 6 ML) is due to percolation of the C₆₀ droplets. In addition to morphological studies via AFM we also investigated the crystalline structure of the bilayer. The resulting diffraction pattern (Figure 3(b)) shows well known Bragg peaks stemming from ordered thin film growth of pentacene in [00L] direction.^[30–32] This pentacene phase is typical for the employed growth conditions. In addition, this pattern is superimposed by a second set of Bragg features which we have identified to originate from C₆₀ face centered cubic (fcc) growth in [111] direction with a lattice constant of $a = 14.14$ Å. The C₆₀ growth corresponds to the well known fcc structure of single crystals at room temperature.^[33] The resulting structures are depicted in Figure 3(c). Note that reflectometry measurements of C₆₀ on pentacene were interpreted as hexagonally closed packed (hcp) C₆₀, one of the known bulk phases of C₆₀.^[21,25,34] Here, however, the inplane information of the GIXS measurements allows us to discard hcp stacking and identify fcc as the correct phase for our sample (cf. Supporting Information). In reflectometry measurements, the fcc [111] direction and the hcp [00L] direction, with L even, are indistinguishable. We are able to index all observed features by considering the identified pentacene and fullerene phase. The absence of additional, not indexed features allows us to exclude a lying down phase of pentacene at the interface or a crystalline interdiffusion layer. Additional off-specular reflectometry x-ray measurements confirm the pentacene thin film growth in [00L] direction and the C₆₀ fcc growth in [111] direction and point out high crystallinity of the organic thin films (supporting information). Altogether, the structural information suggests that the C₆₀ film follows the underlying pentacene film in a well defined manner without changing its structure.

Consequently, the strong shift of the p-channel threshold voltage has to originate from the electrostatics introduced by the pentacene-C₆₀ heterojunction, rather than from structural changes. Highly ordered organic semiconductors exhibit band-like properties such as band dispersion.^[26] Additional control of doping levels also allows to tailor the depletion width with respect to the Debye length.^[35,36] We assume that pentacene and C₆₀ used here are unintentionally doped semiconductors, as confirmed for pentacene before in double gate experiments.^[37–39] In turn, the Fermi levels of pentacene and C₆₀ are expected to align via interface charging, i.e., by formation of depletion zones or accumulation of charges, depending on the detailed values of the respective Fermi levels. From literature values for the HOMO and LUMO of the two semiconductors we expect the Fermi-level of pentacene to lie above the Fermi-level of C₆₀, i.e., the pentacene side of the interface is to be charged positively, while the C₆₀ side is charged negatively.^[3] For the pentacene film, this situation resembles a double gate TFT, where a second top channel is accumulated by an additional top gate.^[39,40] For simultaneous hole accumulation by the bottom gate, the two hole channels in the pentacene layer do not influence each other due to Debye screening, since the Debye length in pentacene has been found to be a few ML at most.^[14] Sweeping the bottom gate voltage to more positive values will at one point switch the pentacene bottom interface from accumulation to depletion, which would lead to a vanishing hole current flow in single gate unipolar TFTs. Here however, the pentacene layer has to be depleted entirely by the bottom gate in

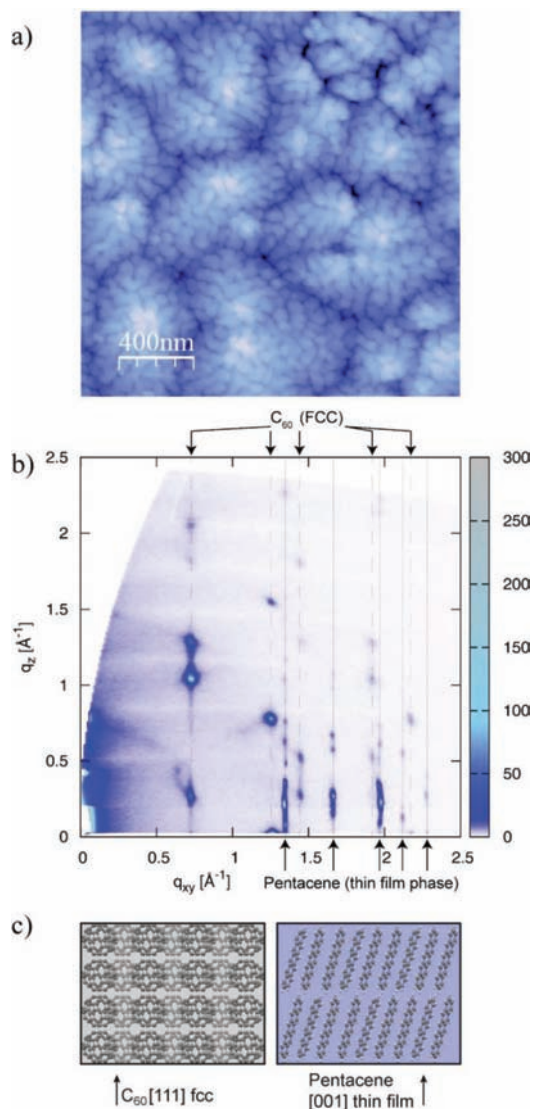


Figure 3. a) AFM height image ($2 \mu\text{m} \times 2 \mu\text{m}$) of a 25 nm thick C₆₀ layer grown on top of a 20 nm thick pentacene thin film layer. b) GIXS measurement of a pentacene-C₆₀ bilayer. All diffraction features can be accounted for by a standing up pentacene thin film phase and [111] fcc growth of fullerene C₆₀ on top of the pentacene. c) Sketch of fcc [111] direction of crystalline C₆₀ and the [00L] thin film phase of pentacene.

order to compensate for the extra top charge at the pentacene- C_{60} interface. Thus, the effective threshold voltage is expected to shift to more positive values, which matches the observed direction of the threshold shift in our device (cf. Figure 2). This confirms the positive precharging of the pentacene top surface and thus the assumption that in pentacene the Fermi-level is closer to the vacuum level than in C_{60} . Furthermore, this experiment is in line with the observation that pentacene double gate transistors are able to form a top channel.^[39] The existence of a second conduction channel has also been demonstrated for other ambipolar transistors employing CuPc and F_{16} CuPc.^[29]

While the expected *n*-channel threshold shift is in agreement with the observation, the increasing film thickness, and thus additional volume trap states, also contributes to the shift, as has been found for pentacene based devices before.^[14,15]

Remarkably, the shifts of both threshold voltages set in with C_{60} percolation. Obviously, not only the C_{60} *n*-channel requires percolation, but also the pentacene top channel. The droplet-like growth behavior of C_{60} on pentacene suggests that the heterojunction is confined to the pentacene- C_{60} contact area. At the beginning of fullerene deposition, the Debye length is much smaller than the lateral distance between C_{60} islands. Thus, before percolation, the inhomogeneous heterojunction landscape resembles a plane of disconnected patches of electrons and holes confined to the interface of the fullerene droplets with the pentacene surface (see Figure 4).^[41] The electrostatics and morphology for bottom hole channel accumulation are summarized in the scheme in Figure 4(a). The AFM

micrograph in Figure 4(b) shows early stage C_{60} growth on pentacene and illustrates the disjunct nature of the heterojunction for low fullerene thickness.

As soon as the C_{60} film develops a percolation path between source and drain contact, the heterojunction extends throughout the whole transistor channel length, and the accumulated holes at the pentacene surface can form a percolated top conduction channel. We observe that the threshold shift occurs within only a few Å after percolation, confirming that the heterojunction charging is confined to the interface within the Debye-length.

In summary, we have presented a well balanced ambipolar organic field effect transistor with high hole and electron saturation mobilities of $0.28 \text{ cm}^2 \text{ V}^{-1} \text{ s}^{-1}$ and $0.18 \text{ cm}^2 \text{ V}^{-1} \text{ s}^{-1}$, respectively. The structure and morphology of the respective films have been analyzed using AFM and GIXS methods. Furthermore, we tracked the formation of a pentacene- C_{60} heterojunction by in-situ measurements during deposition of C_{60} . Upon percolation of the *n*-channel, the heterojunction is charged, acting as an additional top gate for the hole conducting channel. The fact that the *p*-channel threshold does not shift before the *n*-channel develops highlights two interesting findings for bilayer ambipolar TFTs. Apparently, before the C_{60} film percolates, the fullerene islands are electronically floating and the charging of the interface is confined to the pentacene- C_{60} contact area. Secondly, the threshold voltage shift of the *p*-channel upon fullerene percolation implicates the generation of a second hole conducting channel at the pentacene top surface. The introduced method demonstrates a way to evaluate the electrostatic situation in operating organic heterojunction devices. It can be applied to a variety of vapor depositable organic and inorganic materials and give information about the nature of heterojunctions within other devices such as light emitting diodes and solar cells.

Experimental Section

Device fabrication and characterization: Highly doped silicon with a bilayer of 100 nm SiO_2 and 100 nm Si_3N_4 was used as the gate contact and dielectric. The surface of the dielectric was cleaned in three steps. First the samples were sonicated in acetone and isopropanol, respectively. After thorough rinsing in DI (deionized) water, the samples were put in Piranha solvent (concentrated sulfuric acid and 30% hydrogen peroxide solvent at a ratio of 3:1) for 30 minutes. Finally, the samples were plasma cleaned using oxygen plasma (50 W for 30 s, LabAsh). Before depositing the organic materials, a 6 nm thin layer of Topas COC was spin coated onto the silicon nitride surface. We used a 0.25% COC-toluene solvent at 6000 rpm for 30 seconds. Passivating the surface enhances the growth of pentacene and decrease hysteresis effects in organic thin film transistors. 20 nm of pentacene (triple sublimed, Sigma-Aldrich) were deposited onto the dielectric via molecular beam deposition at a rate of 0.1 Å s^{-1} at room temperature and a chamber pressure of $\sim 9 \cdot 10^{-8}$ mbar (as monitored by ion pump current). The 50 nm thick gold source and drain contacts were deposited via electron beam evaporation on top of the pentacene layer. The channel length of 50 μm and the channel width of 2 mm were defined using shadow masks. The hole conducting device was then electrically contacted for the in-situ measurement. 25 nm of the electron conducting C_{60} (sublimed, Sigma-Aldrich) were deposited onto the transistor at a sample temperature of 70 °C and at a rate of 0.1 Å s^{-1} and a chamber pressure of $\sim 1 \cdot 10^{-6}$ mbar. The sample temperature was measured using a type K thermocouple. While growing the C_{60} layer, transconductance curves were measured with a Keithley Instruments

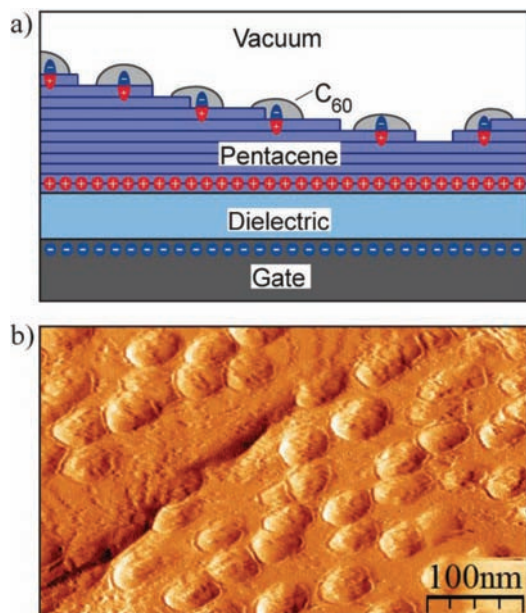


Figure 4. Electronic structure and morphology of the pentacene- C_{60} heterojunction before percolation. a) Scheme of electrostatics in bottom channel hole accumulation (see text). b) Disconnected C_{60} islands (nominal sub-monolayer coverage) on pentacene measured by AFM.



www.MaterialsViews.com

ADVANCED
MATERIALS
www.advmat.de

Source Meter 2612 at a frequency of around 1.25 forth- and back-sweeps per minute. In order to obtain the thickness resolved transistor characteristics the C_{60} layer thickness was measured simultaneously using quartz crystal micro balances.

The GIXS measurements were taken at the W1 beamline at the HASYLAB at DESY in Hamburg. The synchrotron x-ray beam had a wavelength of 1.181 Å. The fabrication of the corresponding samples is equivalent to the samples for the electronic measurements except that the electrodes were omitted.

The AFM micrograph was taken with a Veeco/Digital Instruments NanoScope AFM of the Kothhaus nanophysics group clean room and analyzed with the Nanotec WSxM software.^[42] Sketches were made with Adobe Illustrator, the graphs were plotted with OriginLab Origin.

Supporting Information

Supporting Information is available from the Wiley Online Library or from the author.

Acknowledgements

The authors gratefully acknowledge financial support from the Deutsche Forschungsgemeinschaft (Grant No. DFG Ni 632-4-1) and the Nanosystems Initiative Munich (NIM). Furthermore, financial support by the Bavarian Ministry for Science through the initiative "Solar Technologies Go Hybrid" (SolTech) is gratefully acknowledged.

We want to thank Wolfgang Caliebe and Ulf Brüggmann for support at the W1 beamline at DESY and we appreciate Matthias Fiebig's contribution towards the thickness resolved measurements.

Received: September 21, 2012

Revised: November 5, 2012

Published online: December 20, 2012

- [1] H. Klauk, U. Zschieschang, J. Pflaum, M. Halik, *Nature* **2007**, *445*, 745–748.
- [2] F. S. Kim, X. Guo, M. D. Watson, S. A. Jenekhe, *Adv. Mater.* **2010**, *22*, 478–482.
- [3] S. D. Wang, K. Kanai, Y. Ouchi, K. Seki, *Org. Electron.* **2006**, *7*, 457–464.
- [4] H. Yan, T. Kagata, H. Okuzaki, *Appl. Phys. Lett.* **2009**, *94*, 023305.
- [5] E. Kuwahara, H. Kusai, T. Nagano, T. Takayanagi, Y. Kubozono, *Chem. Phys. Lett.* **2005**, *413*, 379–383.
- [6] P. Cosseddu, A. Bonfiglio, I. Salzmänn, J. P. Rabe, N. Koch, *Org. Electron.* **2008**, *9*, 191–197.
- [7] F. Cicoira, C. Santato, *Adv. Funct. Mater.* **2007**, *17*, 3421–3434.
- [8] J. Zaumseil, R. H. Friend, H. Sirringhaus, *Nat. Mater.* **2006**, *5*, 69–74.
- [9] R. Capelli, S. Toffanin, G. Generali, H. Usta, A. Facchetti, M. Muccini, *Nat. Mater.* **2010**, *9*, 496–503.
- [10] M. A. McCarthy, B. Liu, E. P. Donoghue, I. Kravchenko, D. Y. Kim, F. So, A. G. Rinzler, *Science* **2011**, *332*, 570–573.
- [11] H. Vázquez, W. Gao, F. Flores, A. Kahn, *Phys. Rev. B* **2005**, *71*, 041306(R).
- [12] F. Flores, J. Ortega, H. Vázquez, *Phys. Chem. Chem. Phys.* **2009**, *11*, 8658–8675.
- [13] S. Verlaak, D. Beljonne, D. Cheyns, C. Rolin, M. Linares, F. Castet, J. Cornil, P. Heremans, *Adv. Funct. Mater.* **2009**, *19*, 3809–3814.
- [14] M. Fiebig, D. Beckmeier, B. Nickel, *Appl. Phys. Lett.* **2010**, *96*, 083304.
- [15] C. Ucurum, H. Goebel, F. A. Yildirim, W. Bauhofer, W. Krautschneider, *J. Appl. Phys.* **2008**, *104*, 084501.
- [16] D. Knipp, A. Benor, V. Wagner, T. Muck, *J. Appl. Phys.* **2007**, *10*, 044504.
- [17] D. Braga, G. Horowitz, *Adv. Mater.* **2009**, *21*, 1473–1486.
- [18] A. Virkar, S. Mannsfeld, J. H. Oh, M. F. Toney, Y. H. Tan, G. Liu, J. C. Scott, R. Miller, Z. Bao, *Adv. Funct. Mater.* **2009**, *19*, 1962–1970.
- [19] J. Yang, T. Nguyen, *Organic Electronics* **2007**, *8*, 566–574.
- [20] A. K. Pandey, J.-M. Nunzi, *Appl. Phys. Lett.* **2006**, *89*, 213506.
- [21] I. Salzmänn, S. Duhm, R. Opitz, R. L. Johnson, J. P. Rabe, N. Koch, *J. Appl. Phys.* **2008**, *104*, 114518.
- [22] S. J. Kang, Y. Yi, C. Y. Kim, K. Cho, H. H. Seo, M. Noh, K. Jeong, K.-H. Yoo, C. N. Whang, *Appl. Phys. Lett.* **2005**, *87*, 233502.
- [23] F. Zhu, M. Grobosch, U. Treske, M. Knupfer, L. Huang, S. Ji, S. Yan, *Appl. Phys. Lett.* **2011**, *98*, 203303.
- [24] Y. Tsuruma, A. Al-Mahboob, S. Ikeda, J. T. Sadowski, G. Yoshikawa, Y. Fujikawa, T. Sakurai, K. Saiki, *Adv. Mater.* **2009**, *21*, 4996–5000.
- [25] K. Itaka, M. Yamashiro, J. Yamaguchi, M. Haemori, S. Yaginuma, Y. Matsumoto, M. Kondo, H. Koinuma, *Adv. Mater.* **2006**, *18*, 1713–1716.
- [26] N. Koch, A. Vollmer, I. Salzmänn, B. Nickel, H. Weiss, J. P. Rabe, *Phys. Rev. Lett.* **2006**, *96*, 156803.
- [27] C. Rost, D. J. Gundlach, S. Karg, W. Rieß, *J. Appl. Phys.* **2004**, *95*, 10.
- [28] R. Ruiz, A. Papadimitratos, A. C. Mayer, G. G. Malliaras, *Adv. Mater.* **2005**, *17*, 1795–1798.
- [29] J. Wang, H. Wang, X. Yan, H. Huang, D. Yan, *Appl. Phys. Lett.* **2005**, *87*, 093507.
- [30] C. D. Dimitrakopoulos, A. R. Brown, A. Pomp, *J. Appl. Phys.* **1996**, *80*, 2501.
- [31] S. Schiefer, M. Huth, A. Dobrineski, B. Nickel, *J. Am. Chem. Soc.* **2007**, *129*, 10316–10317.
- [32] S. C. B. Mannsfeld, A. Virkar, C. Reese, M. F. Toney, Z. Bao, *Adv. Mater.* **2009**, *21*, 2294–2298.
- [33] P. A. Heiney, J. E. Fischer, A. R. McGhie, W. J. Romanow, M. Denenstein, J. P. McCauley Jr., Amos B. Smith III, D. E. Cox, *Phys. Rev. Lett.* **1991**, *66*, 22.
- [34] J. L. de Boer, S. van Smaalen, V. Patricek, M. Dusek, M. A. Verheijen, G. Meijer, *Chem. Phys. Lett.* **1994**, *219*, 469–472.
- [35] H. Kleemann, B. Lüssem, K. Leo, *J. Appl. Phys.* **2012**, *111*, 123722.
- [36] H. Kleemann, R. Gutierrez, F. Lindner, S. Avdoshenko, P. D. Manrique, B. Lüssem, G. Cuniberti, K. Leo, *Nano Lett.* **2010**, *10*, 4929–4934.
- [37] S. Verlaak, V. Arkhipov, P. Heremans, *Appl. Phys. Lett.* **2002**, *82*, 745–747.
- [38] T. W. Ng, M. F. Lo, Y. C. Zhou, Z. T. Liu, C. S. Lee, O. Kwon, S. T. Lee, *Appl. Phys. Lett.* **2009**, *94*, 193304.
- [39] M. Göllner, G. Glasbrenner, B. Nickel, *Electroanalysis* **2012**, *24*, 214–218.
- [40] M.-J. Spijkman, K. Myny, E. C. P. Smits, P. Heremans, P. W. M. Blom, D. M. de Leeuw, *Adv. Funct. Mater.* **2011**, *23*, 3231–3242.
- [41] H. Haick, M. Ambrico, T. Ligonzo, R. T. Tung, D. Cahen, *J. Am. Chem. Soc.* **2006**, *128*, 6854–6869.
- [42] I. Horcas, R. Fernandez, J. M. Gomez-Rodriguez, J. Colchero, J. Gomez-Herrero, A. M. Baro, *Rev. Sci. Instrum.* **2007**, *78*, 013705.

A.2 TRANSFERABLE ORGANIC SEMICONDUCTOR NANOSHEETS FOR APPLICATION IN ELECTRONIC DEVICES

Simon. J. Noever, Michael Eder, Fabio del Giudice, Jan Martin, Franz Werkmeister, Stefan Hallwig, Stefan Fischer, Oliver Seeck, Nils-Eike Weber, Clemens Liewald, Fritz Keilmann, Andrey Turchanin, and Bert Nickel

Advanced Materials 2017, *Early View* 1606283

DOI: [10.1002/adma.201606283](https://doi.org/10.1002/adma.201606283)

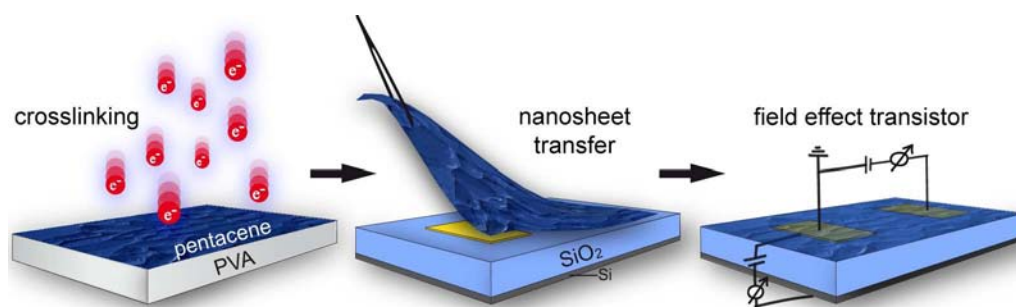
Abstract

A method has been developed to stabilize and transfer nanofilms of functional organic semiconductors. The method is based on crosslinking of their topmost layers by low energy electron irradiation. The films can then be detached from their original substrates and subsequently deposited onto new solid or holey substrates retaining their structural integrity. Grazing incidence X-ray diffraction, X-ray specular reflectivity, and UV-Vis spectroscopy measurements reveal that the electron irradiation of ≈ 50 nm thick pentacene films results in crosslinking of their only topmost ≈ 5 nm (3-4 monolayers), whereas the deeper pentacene layers preserve their pristine crystallinity. The electronic performance of the transferred pentacene nanosheets in bottom contact field-effect devices is studied and it is found that they are fully functional and demonstrate superior charge injection properties in comparison to the pentacene films directly grown on the contact structures by vapor deposition. The new approach paves the way to integration of the organic semiconductor nanofilms on substrates unfavorable for their direct growth as well as to their implementation in hybrid devices with unusual geometries, e.g., in devices incorporating free-standing sheets.

Contribution

The first draft of the manuscript was written entirely by me and I produced the final version. In addition, all figures were designed by me. I performed all experiments, except the ones regarding the UV-VIS and FTIR data, either alone or contributed significantly, and I analyzed all respective measured data.

Table of Contents Graphic



COMMUNICATION

Organic Semiconductors

**ADVANCED
MATERIALS**
www.advmat.de

Transferable Organic Semiconductor Nanosheets for Application in Electronic Devices

Simon J. Noever, Michael Eder, Fabio del Giudice, Jan Martin, Franz X. Werkmeister, Stefan Hallwig, Stefan Fischer, Oliver Seeck, Nils-Eike Weber, Clemens Liewald, Fritz Keilmann, Andrey Turchanin,* and Bert Nickel*

A method has been developed to stabilize and transfer nanofilms of functional organic semiconductors. The method is based on crosslinking of their topmost layers by low energy electron irradiation. The films can then be detached from their original substrates and subsequently deposited onto new solid or holey substrates retaining their structural integrity. Grazing incidence X-ray diffraction, X-ray specular reflectivity, and UV-Vis spectroscopy measurements reveal that the electron irradiation of ≈ 50 nm thick pentacene films results in crosslinking of their only topmost ≈ 5 nm (3–4 monolayers), whereas the deeper pentacene layers preserve their pristine crystallinity. The electronic performance of the transferred pentacene nanosheets in bottom contact field-effect devices is studied and it is found that they are fully functional and demonstrate superior charge injection properties in comparison to the pentacene films directly grown on the contact structures by vapor deposition. The new approach paves the way to integration of the organic semiconductor nanofilms on substrates unfavorable for their direct growth as well as to their implementation in hybrid devices with unusual geometries, e.g., in devices incorporating free-standing sheets.

engineered, even if these material combinations cannot be grown directly by physical vapor deposition techniques.^[6] In this way, vdW heterostructures with tailored electronic and optoelectronic properties can be generated by combining metallic, insulating and semiconducting sheets.^[7] Nanofilms of organic semiconductors are promising candidates to extend this material toolbox for building hybrid devices, which would profit from the physical properties of both inorganic and organic materials.^[8,9] To this end, they have to be prepared in the form of mechanically stable and transferable sheets. However, in contrast to graphene, where atoms are linked via strong covalent bonds, small aromatic molecules in pristine organic semiconductor films are bound via weak vdW forces. Therefore, it is not possible to peel off and deposit organic films to create electronic devices, in contrast to thicker organic crystals, which have been transferred successfully.^[10] Here we demonstrate the preparation and implementation in field effect transistors (FETs) of transferable pentacene nanosheets, stabilized via electron irradiation-induced crosslinking of their surface layers. The irradiated films possess high mechanical stability and therefore they can be removed from the growth substrate and transferred onto

The transfer and microfabrication techniques of graphene and other 2D materials have revolutionized the fabrication of novel layered materials and their implementation in electronic, optoelectronic, and nano-electromechanical devices.^[1–5] By mechanical stacking of various atomically thin sheets (e.g., graphene, MoS₂, or BN), novel van der Waals (vdW) heterostructures are

transferred successfully.^[10] Here we demonstrate the preparation and implementation in field effect transistors (FETs) of transferable pentacene nanosheets, stabilized via electron irradiation-induced crosslinking of their surface layers. The irradiated films possess high mechanical stability and therefore they can be removed from the growth substrate and transferred onto

Dr. S. J. Noever, M. Eder, F. del Giudice, J. Martin, Dr. F. X. Werkmeister, S. Hallwig, S. Fischer, C. Liewald, Dr. F. Keilmann, Dr. B. Nickel
Faculty of Physics and CeNS
Ludwig-Maximilians-Universität München
80539 Munich, Germany
E-mail: nickel@physik.uni-muenchen.de
Dr. S. J. Noever, C. Liewald, Dr. B. Nickel
Nanosystems Initiative Munich (NIM)
80799 Munich, Germany
Dr. O. Seeck
Deutsches Elektronen Synchrotron DESY
22603 Hamburg, Germany
Dr. N.-E. Weber^[†]
Faculty of Physics
University of Bielefeld
33615 Bielefeld, Germany

Prof. A. Turchanin
Institute of Physical Chemistry
Friedrich-Schiller-Universität Jena
07743 Jena, Germany
E-mail: andrey.turchanin@uni-jena.de

Prof. A. Turchanin
Jena Center for Soft Matter (JCSM)
07743 Jena, Germany
Prof. A. Turchanin
Center for Energy and Environmental Chemistry
(CEEC) 07743, Jena, Germany

Prof. A. Turchanin
Abbe Center of Photonics (ACP)
07745 Jena, Germany

^[†]Present address: Scienta Omicron GmbH, 65232 Taunusstein, Germany

DOI: 10.1002/adma.201606283

new solid substrates or suspended across macroscopic cavities and grids as freestanding structures. We characterize in detail the effect of the electron irradiation on structural and optical properties of pentacene nanofilms employing grazing incidence X-ray diffraction (GIXD), X-ray reflectometry (XR), UV-Vis and IR spectroscopy, helium ion microscopy (HIM), and atomic force microscopy (AFM). The functional electronic properties of the formed nanosheets are studied via electric transport measurements of the FET devices. We found that already about 5 nm ($\approx 3\text{--}4$ molecular layers) of crosslinking depth is sufficient to stabilize 50 nm thick pentacene films, whereas the remaining film preserves its pristine structure as well as electronic and optical properties and can be used for functional applications. The transferred pentacene nanosheets show superior charge injection characteristics in the FET devices in comparison to the pentacene films prepared by physical vapor deposition.

Low energy electron irradiation of aromatic self-assembled monolayers results in their lateral crosslinking and conversion into 2D carbon sheets - carbon nanomembranes (CNMs) - with a thickness of only one molecule.^[11] The crosslinking is driven by primary electron irradiation as well as low energy secondary and photoelectrons produced in the substrate resulting in the dissociation of C-H bonds and subsequent formation of the new covalently bonded carbon network in the complete

monolayer, which significantly changes its structural and electronic properties.^[12] Similar to graphene, fully crosslinked CNMs can be removed from their substrates and transferred onto new holey or solid substrates or stacked into vdW heterostructures as free-standing sheets.^[13,14] As the penetration depth of low energy electrons can be precisely tuned in the range of a few nanometers,^[15] we employ this effect to crosslink only the topmost layers of a ≈ 50 nm thick film of pentacene preserving the pristine structure of the deeper layers and therefore the functional electronic properties of the film. Moreover, the smooth bottom interface of the organic film remains accessible for electronic contact resulting in the lower contact resistance of the fabricated devices. In the following, we present the structural and functional characterization of the surface stabilized free-standing pentacene nanosheets prepared in this way.

First, we describe the essential steps to crosslink and transfer pentacene nanosheets, **Figure 1a**. We use a thin sacrificial polyvinyl-alcohol (PVA) layer deposited on a flat and inert substrate such as an oxidized Si wafer or a fused silica glass by spin coating and deposit a 50 nm pentacene film on this substrate by vacuum vapor deposition.^[16] The deposited film is then irradiated in the same vacuum chamber with a defocused electron beam having an electron energy of $E_{\text{irr}} = 500$ eV and an irradiation dose of $D_{\text{irr}} = 3.0$ mC cm^{-2} . To detach the pentacene

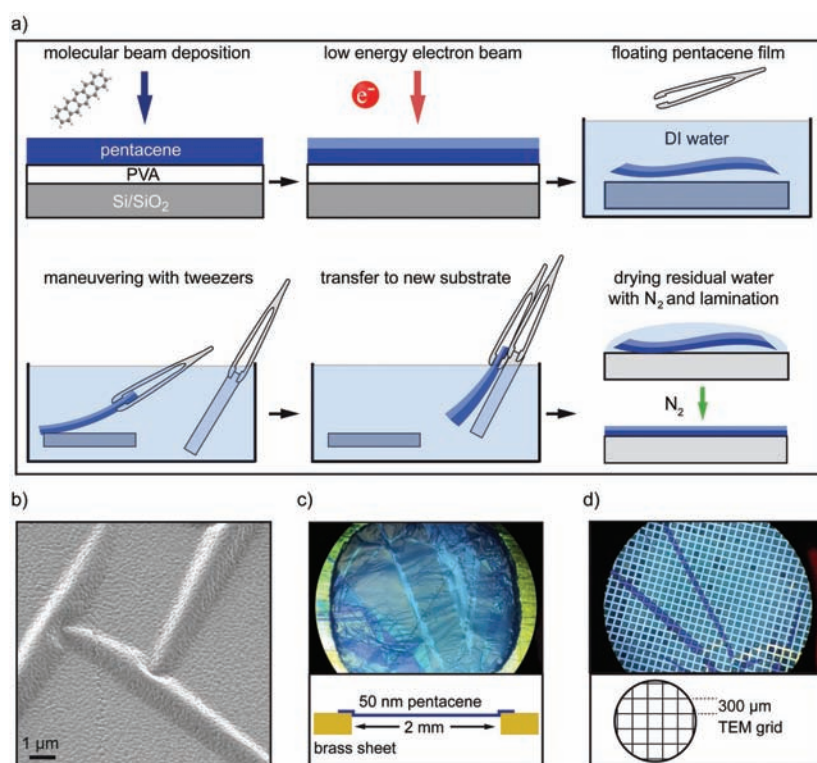


Figure 1. Transfer of thin pentacene films. a) Schematic representation of the transfer method. b) Helium ion microscopy (HIM) image of a crosslinked and transferred 20 nm pentacene film. c) Optical microscopy image of a 50 nm thin pentacene film spanned over a 2 mm hole in a 0.5 mm brass sheet. d) Optical microscopy image of a 50 nm thin pentacene film transferred onto a copper TEM grid (mesh width: 300 μm).

film from the surface, the sample is removed from the vacuum chamber and immersed in deionized water. Since PVA is a water soluble polymer, the sacrificial PVA layer dissolves and the pentacene film remains free-floating in the solvent.^[17,18] These freestanding films with areas up to a size of 1 cm² can then be picked up with tweezers, placed onto new substrates and removed from the water. The crosslinking step is essential for this procedure because pristine (non-irradiated) pentacene films disintegrate at the slightest touch by tweezers or during transfer through the water surface meniscus. After removing the wet nanosheet from water, it is possible to correct its position on the surface and flatten it out by gentle pulling. Upon drying in nitrogen flow, the nanosheets laminate firmly to the new surface, i.e., they adhere irreversibly by van der Waals forces. Note, the pentacene films are sufficiently mechanically stable so that no stabilizing polymeric film, as typically used for atomically thin sheets,^[4,13] is necessary for their transfer. The HIM image in Figure 1b shows a pentacene nanosheet, which was transferred in this way on an oxidized silicon wafer. Folds and wrinkles are recognized indicating the sheet character of the pentacene. The characteristic terrace-like topography of pentacene is conserved after irradiation and transfer (cf. Figure S1, Supporting Information). In Figure 1c,d optical microscopy images of pentacene nanosheets spanning over holes with diameters of several millimeters are presented. The sheets are homogenous with some color variations originating from the wrinkle and folds due to transfer. In Figure 1c, a 50 nm pentacene nanosheet spans a 2 mm diameter hole in a brass sheet, whereas in Figure 1d the nanosheet spans a transmission electron microscope (TEM) grid with a mesh width of 300 μm . As we show in the following, this remarkable mechanical stability results from the lateral crosslinking of only the topmost 3–4 monolayers (ML) of the pentacene films.

To analyze the penetration depth of the crosslinking, we employ specular XR in combination with GIXD measurements.^[19] As seen from the XR data presented in Figure 2, the pristine film shows the characteristic (0 0 L) reflections of the pentacene thin film phase (black curve).^[20] After irradiation, the (0 0 L) peaks broaden and decrease in intensity (red curve). This observation indicates a reduction of the crystallinity due to the electron irradiation induced crosslinking. In comparison to XR, where the total thickness of the film contributes to the signal, in GIXD an evanescent X-ray wave selectively probes only the surface region (cf. Figure 2b). Experimentally, the probing depth is adjusted using the X-ray beam at subcritical incidence angle for total reflection, typically at less than a fraction of a degree from the surface. The smaller the angle, the more surface sensitive is the measurement. GIXD measurements for a pristine pentacene film and films irradiated at two different electron beam energies ($E_{\text{irr}} = 300$ and 800 eV, $D_{\text{irr}} = 3.0 \text{ mC cm}^{-2}$, see Table 1, Supporting Information for details) are shown in Figure 2c. While there is still some GIXD intensity of the first truncation rod (1 1 L) after 300 eV irradiation, the signal vanishes almost completely after 800 eV irradiation. To quantify the number of disordered crosslinked layers, i.e., the number of layers on top of the film which do not contribute to the diffraction signal, we measure the GIXD signal under different incidence angles and model the diffracted intensities within the model of

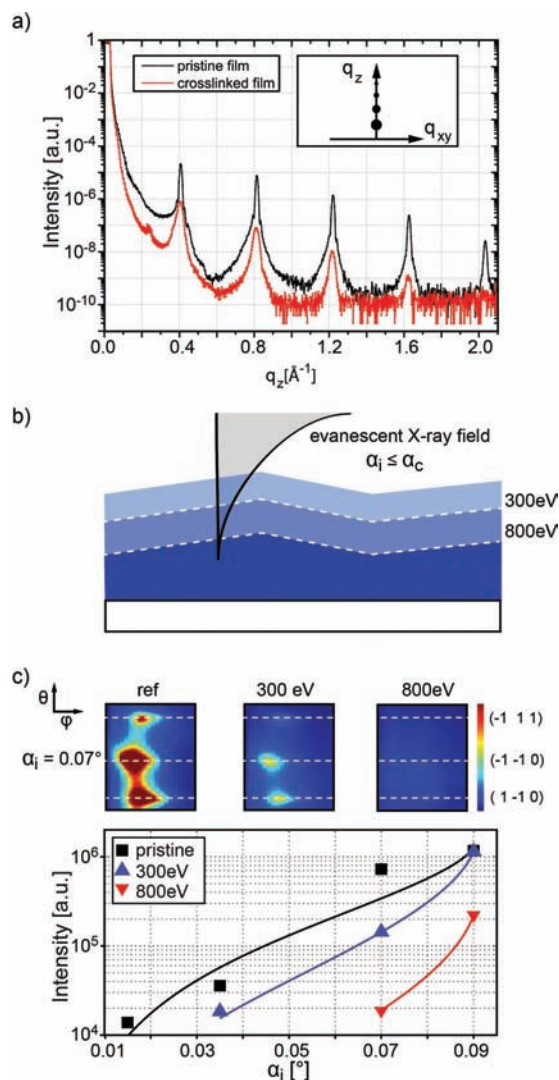


Figure 2. X-ray analysis of the influence of crosslinking on the crystal structure of pentacene thin films. a) Comparison of synchrotron specular X-ray reflectometry measurements of a pristine pentacene thin film (black) on SiO₂ and a strongly crosslinked film (red, 50 min at electron energy >700 eV, $D = 7.5 \text{ mC cm}^{-2}$). The decreasing Bragg signal indicates that the crosslinked film contains less crystalline material. b) Schematic of the evanescent X-ray field penetrating the pentacene surface for different electron irradiation depths. c) GIXD measurements of the first pentacene truncation rod at different angles of incidence and different e-beam energies (here, θ is the out-of-plane angle and ϕ the in-plane angle). Top: exemplary GIXD data for pristine, 300 eV irradiated, and 800 eV irradiated pentacene at $\alpha_i = 0.07^\circ$. Bottom: the highest intensities of the (-1-10) peaks (middle peaks from raw data), plotted against the angles of incidence. The continuous lines represent the fit calculated from the DCGID model for truncation rods, including noncrystalline top layers.

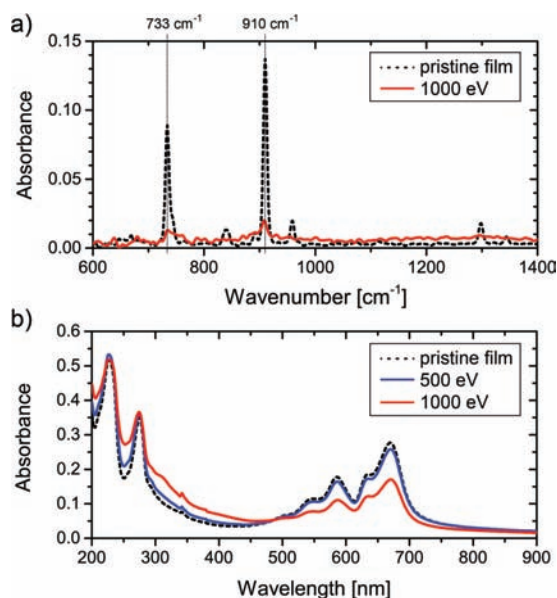


Figure 3. Spectroscopic characterization of the crosslinking process. a) FTIR spectra of a 23 nm pentacene film on Au before and after irradiation with 1 keV electrons (dose 10.3 mC cm^{-2}), shown as dashed black and red curve, respectively. b) UV-Vis measurements of a 50 nm pentacene film on fused silica, before and after irradiation with 500 eV and 1 keV electrons (dose of 3 and 10.3 mC cm^{-2} , respectively), shown as dashed black, blue and red curves, respectively.

depth controlled grazing incidence diffraction (DCGID) (Figure 2c).^[21–24] Details on the fit routine are reported in Figure S2 (Supporting Information). We find that the observed intensities are in agreement with three disordered ML of pentacene (or 4.5 nm crosslinking depth) for 300 eV irradiation and five disordered monolayers pentacene (or 7.5 nm crosslinking depth) for the 800 eV sample. These data unambiguously show that only the topmost layers of the pentacene film lose their crystallinity due to the crosslinking, whereas the pristine crystallinity is preserved in the deeper layers of the film.

To get an insight into the crosslinking mechanisms, we applied Fourier transform infrared (FTIR) spectroscopy. As seen from the FTIR spectra (cf. Figure 3a), after irradiation the characteristic C–H vibrations of pentacene at 910 and 733 cm^{-1} are strongly diminished.^[25,26] Such a behavior is indicative for the hydrogen abstraction via the cleavage of the C–H bonds and formation of new carbon bonds between the unsaturated adjacent aromatic moieties.^[12] Next, we used UV-Vis spectroscopy to characterize the changes in the optical spectra. As seen from Figure 3b, the UV-Vis spectrum of a pristine pentacene film shows the characteristic absorption features in the spectral range of 500–700 nm.^[25] After electron irradiation with two different electron energies (500 eV and 1 keV), the intensity of these characteristic absorbance features is decreased. This effect is stronger for the irradiation with higher energy electrons, which is in agreement with their higher penetration depth and therefore the formation of a thicker crosslinked layer. Using the

Lambert–Beer law and the corresponding inelastic mean free paths of 500 eV and 1 keV electrons, we estimate the thickness of the formed crosslinked layer to about 3 and 17 nm, respectively. The formation of the crosslinked layer is also in agreement with an increase of the intensity in the spectral range at smaller wave lengths (cf. Figure 3b), which is characteristic for the formation of amorphous carbon species.^[27] To summarize the structural and optical study, we conclude that irradiation of pentacene films with electrons in the range of 300–500 eV results in the crosslinking of their topmost 3–4 MLs. These topmost layers have disordered, most probably amorphous, structure, whereas the deeper pentacene layers preserve their pristine crystallinity. Importantly, the formed crosslinked layer provides a sufficient mechanical stability to about 50 nm thick pentacene films in order to transfer them onto new solid and holey substrates as free-standing nanosheets.

In the following, we demonstrate that the formed pentacene nanosheets possess functional semiconducting properties and can be employed in effective field effect devices. To this end, we fabricated bottom-contact, bottom-gate pentacene FETs by vapor deposition of pentacene in vacuum onto the contact structures and studied electric transport properties of these devices before and after the irradiation, Figure 4a. After an irradiation with low energy electrons ($E_{\text{irr}} = 350 \text{ eV}$, $D_{\text{irr}} = 1.5 \text{ mC cm}^{-2}$) no significant alteration in the device performance in comparison to the nonirradiated devices is observed (Figure 4a). This demonstrates that the crosslinked layer does not penetrate into the conduction channel, which is typically confined at the semiconductor-dielectric interface (Figure 4b).^[28] Only after extensive irradiation at higher electron energies and doses ($E_{\text{irr}} = 700 \text{ eV}$, $D_{\text{irr}} = 4.5 \text{ mC cm}^{-2}$) the device performance significantly decreases. In the next step, we transferred the pentacene nanosheets onto prefabricated transistor contact pads of varying bottom-contacts with channel widths of $W_{\text{ch}} = 10 \text{ nm}$ and channel lengths of $L_{\text{ch}} = 5, 10, \text{ and } 20 \text{ }\mu\text{m}$ (see the details in the Experimental Section in the Supporting Information) and compared the device performance with transistor structures prepared via conventional physical vapor deposition. The AFM images of the contact regions in Figure 4b show the morphology on both types of devices. The typical obstructed pentacene growth (i.e., small grained, pillar-like 3D morphology) is observed by direct vapor deposition on gold contacts.^[29] In contrast, the structure of the pentacene films grown on PVA and transferred after the crosslinking onto gold contacts is significantly more homogeneous and shows the characteristic Bragg peaks of the pentacene thin film phase (Figure S3, Supporting Information). The obstructed growth of pentacene on gold has a negative influence on the charge injection properties of pentacene devices and can only be reduced by a proper, often aggressive modification of the gold contacts.^[29–33] The elongated pentacene structures formed on PVA most likely represent the lying phase pentacene.^[34] First, we determine the total resistance R of the devices from the linear region of the output characteristics (Figure S4, Supporting Information) according to $R = V_{\text{D}}/I_{\text{D}}$. The total resistances for devices with different channel lengths are summarized in Figure 4c. The contact resistance is determined from extrapolation to zero channel length.^[35,36] For a gate voltage of $V_{\text{G}} = -15 \text{ V}$, the devices made of the transferred pentacene sheets have a

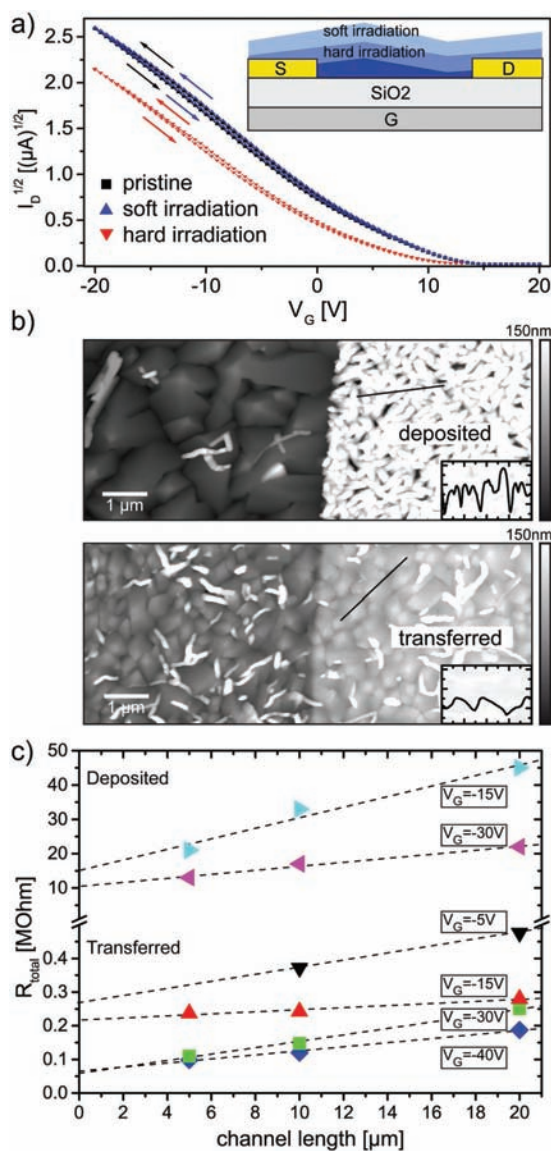


Figure 4. Characterization of the electronic properties in the field effect devices. Characteristic curves of a transistor irradiated at different electron energies and contact resistance analysis of deposited and transferred pentacene on bottom contact transistor geometry. a) Transfer curves of an organic field effect transistor (OFET) with pristine, partially crosslinked, and strongly crosslinked active layer ($V_D = -10$ V). The arrows indicate the sweep direction (inset: schematic of the transistor). When irradiated softly (low electron energy), only the top layers of the pentacene film are crosslinked, i.e., the conduction channel at the dielectric interface is not affected. After hard irradiation (high electron energy), the crosslinked region penetrates the conduction channel and the device performance is reduced. b) AFM height micrographs of the substrate—contact edge in a transistor channel. Pentacene was vapor deposited (top image), and nanosheet transferred (bottom image). The topography

contact resistance of $R_p = 0.22$ M Ω . This is almost two orders of magnitude less than the contact resistance of the transistors produced by the conventional pentacene vapor deposition on the test pads, which was $R_p = 15$ M Ω . This improvement is even more significant for larger gate voltages. Thus for $V_G = -30$ V the contact resistance of the devices made out for the transferred sheets is 0.057 versus 10 M Ω for devices prepared by vapor deposition. All vapor deposited films show nonideal saturation behavior, i.e., a drain current reduction I_D at larger drain voltages. On the other hand, the saturation behavior of the transferred films with 10 and 20 μm channel length is rather good; only the shortest channel (5 μm) shows some nonideal behavior. These findings demonstrate that the crosslinking and transfer technique of pentacene nanosheets enables the fabrication of thin film devices with superior contact characteristics (cf. Figure S4, Supporting Information) and improved saturation behavior for the 10 and 20 μm channel length. The mobilities, typically $\mu \approx 0.1$ cm² V⁻¹ s⁻¹ in our devices, stay largely unaffected, whether by electron irradiation (cf. Figure 4a) or by film transfer.

In summary, we have introduced a novel methodology to fabricate transferrable nanosheets of organic semiconductors with few tens of nanometers thickness via irradiation of their thin films with low energy electrons. The electron irradiation results in crosslinking of the topmost molecular layers, stabilizing the whole film and enabling its transfer as a nanosheet onto new substrates. Because of the low penetration depth of the crosslinking, the studied pentacene nanosheets preserve their functional semiconducting and optical properties. Moreover, employed in bottom contact FETs, they show a reduced contact resistance in comparison to devices fabricated via direct vapor deposition on the gold electrodes. The proposed methodology opens up new possibilities toward the fabrication of organic semiconductor devices with transferrable organic semiconductor nanosheets from a variety of aromatic molecules. It paves the way toward free-standing organic field effect devices, an area which was reserved for single crystals so far, as well as to their integration with other 2D materials in hybrid devices.

Experimental Section

The defocused electron beam was produced using a Perkin Elmer low energy electron diffraction (LEED) gun (PHI Model 11-020 LEED Electronics System). Most experiments have been performed using an electron gun emission current of 5 mA. The doses (mC cm⁻²) were estimated via the measured beam current I_b flowing through a

for the transferred film is unchanged on the gold electrode, while the vapor deposited film shows strong dewetting on the contact. The height scale of both AFM images is 150 nm. The insets show two height profiles above the contacts. The line cut is 2 μm , the y-axis covers 150 nm. c) Total channel resistance using vapor deposited pentacene (top) and nanosheet transferred pentacene (bottom), plotted against transistor channel lengths and evaluated for different applied gate voltages. The intersections of the linear fits with the ordinate indicate the extrapolated contact resistances. The error bars for each data point is less than 10% of their absolute values.

ground electrode: $D = \frac{I_B t}{A}$. For the used setup and an emission current of $I_{em} = 5$ mA, the current through an irradiated reference surface $A = 4$ mm² at the sample position was $\approx I_B = 100$ nA. Some experiments have also been performed with a reduced emission current of 2 mA after filament exchange and refocusing.

Further details for sample preparation and characterization are reported in the Supporting Information.

Supporting Information

Supporting Information is available from the Wiley Online Library or from the author.

Acknowledgements

The authors gratefully acknowledge financial support from the Bavarian Ministry for Science through the initiative "Solar Technologies Go Hybrid" (SolTech) as well as by the Deutsche Forschungsgemeinschaft (DFG) through the SFB 1032. Parts of this research were carried out at the light source PETRA III at DESY, a member of the Helmholtz Association (HGF). A.T. and N.-E.W. acknowledge support by the Deutsche Forschungsgemeinschaft (SPP 1459 "Graphene") and the EMRP project "GraphOhm" (The EMRP is jointly funded by the EMRP participating countries within EURAMET and European Union). The authors thank Dr. Henning Vieker for the help with the acquisition of HIM images and appreciate time for test measurements at neaspec GmbH. Special thanks to Philipp Altpeter for fruitful discussions and his dedicated technical support in the clean room of the former chair of Prof. Kotthaus (LMU), where many experiments were prepared.

Conflict of Interest

The authors declare no conflict of interest.

Keywords

2D materials, electronic devices, nanosheets, organic semiconductors, pentacene

Received: November 20, 2016

Revised: March 12, 2017

Published online:

- [1] A. K. Geim, I. V. Grigorieva, *Nature* **2013**, 499, 419.
- [2] S. Z. Butler, S. M. Hollen, L. Y. Cao, Y. Cui, J. A. Gupta, H. R. Gutierrez, T. F. Heinz, S. S. Hong, J. X. Huang, A. F. Ismach, E. Johnston-Halperin, M. Kuno, V. V. Plashnitsa, R. D. Robinson, R. S. Ruoff, S. Salahuddin, J. Shan, L. Shi, M. G. Spencer, M. Terrones, W. Windl, J. E. Goldberger, *ACS Nano* **2013**, 7, 2898.
- [3] J. W. Suk, A. Kitt, C. W. Magnuson, Y. F. Hao, S. Ahmed, J. H. An, A. K. Swan, B. B. Goldberg, R. S. Ruoff, *ACS Nano* **2011**, 5, 6916.
- [4] A. C. Ferrari, F. Bonaccorso, V. Fal'ko, K. S. Novoselov, S. Roche, P. Boggild, S. Borini, F. H. L. Koppens, V. Palermo, N. Pugno, J. A. Garrido, R. Sordan, A. Bianco, L. Ballerini, M. Prato, E. Lidorikis, J. Kivioja, C. Marinelli, T. Ryhanen, A. Morpurgo, J. N. Coleman, V. Nicolosi, L. Colombo, A. Fert, M. Garcia-Hernandez, A. Bachtold, G. F. Schneider, F. Guinea, C. Dekker, M. Barbone, Z. Sun, C. Galiotis, A. N. Grigorenko, G. Konstantatos, A. Kis, M. Katsnelson, L. Vandersypen, A. Loiseau, V. Morandi, D. Neumaier, E. Treossi, V. Pellegrini, M. Polini, A. Tredicucci, G. M. Williams, B. Hee Hong, J.-H. Ahn, J. Min Kim, H. Zirath, B. J. van Wees, H. van der Zant, L. Occhipinti, A. Di Matteo, I. A. Kinloch, T. Seyller, E. Quesnel, X. Feng, K. Teo, N. Rupesinghe, P. Hakonen, S. R. T. Neil, Q. Tannock, T. Lofwander, J. Kinaret, *Nanoscale* **2015**, 7, 4598.
- [5] F. Withers, O. Del Pozo-Zamudio, A. Mishchenko, A. P. Rooney, A. Gholinia, K. Watanabe, T. Taniguchi, S. J. Haigh, A. K. Geim, A. I. Tartakovskii, K. S. Novoselov, *Nat. Mater.* **2015**, 14, 301.
- [6] B. V. Lotsch, *Annu. Rev. Mater. Res.* **2015**, 45, 85.
- [7] I. S. Osborne, *Science* **2016**, 353, 458.
- [8] D. Jariwala, S. L. Howell, K.-S. Chen, J. Kang, V. K. Sangwan, S. A. Filippone, R. Turrisi, T. J. Marks, L. J. Lauhon, M. C. Hersam, *Nano Lett.* **2016**, 16, 497.
- [9] H. Klauk, *Organic Electronics: Materials, Manufacturing, and Applications*, Wiley-VCH, Weinheim, Germany **2006**.
- [10] E. Menard, V. Podzorov, S. H. Hur, A. Gaur, M. E. Gershenson, J. A. Rogers, *Adv. Mater.* **2004**, 16, 2097.
- [11] A. Turchanin, A. Götzhäuser, *Adv. Mater.* **2016**, 28, 6075.
- [12] A. Turchanin, D. Käfer, M. El-Desawy, C. Wöll, G. Witte, A. Götzhäuser, *Langmuir* **2009**, 25, 7342.
- [13] A. Turchanin, A. Beyer, C. T. Nottbohm, X. H. Zhang, R. Stosch, A. Sologubenko, J. Mayer, P. Hinze, T. Weimann, A. Götzhäuser, *Adv. Mater.* **2009**, 21, 1233.
- [14] C. T. Nottbohm, A. Turchanin, A. Beyer, R. Stosch, A. Götzhäuser, *Small* **2011**, 7, 874.
- [15] S. Tanuma, C. J. Powell, D. R. Penn, *Surf. Interface Anal.* **1994**, 21, 165.
- [16] C.-C. Kuo, T. N. Jackson, *Appl. Phys. Lett.* **2009**, 94, 3304.
- [17] T. B. Singh, T. Meghdadi, S. Gunes, N. Marjanovic, G. Horowitz, P. Lang, S. Bauer, N. S. Sariciftci, *Adv. Mater.* **2005**, 17, 2315.
- [18] G. A. Salvatore, N. Munzenrieder, T. Kinkeldei, L. Petti, C. Zysset, I. Strebel, L. Buthe, G. Troster, *Nat. Commun.* **2014**, 5, 2982.
- [19] S. Schiefer, M. Huth, A. Dobrinevski, B. Nickel, *J. Am. Chem. Soc.* **2007**, 129, 10316.
- [20] B. Nickel, R. Barabash, R. Ruiz, N. Koch, A. Kahn, L. C. Feldman, R. F. Haglund, G. Scoles, *Phys. Rev. B* **2004**, 70, 125401.
- [21] H. Dosch, B. W. Batterman, D. C. Wack, *Phys. Rev. Lett.* **1986**, 56, 1144.
- [22] H. Dosch, *Phys. Rev. B* **1987**, 35, 2137.
- [23] G. H. Vineyard, *Phys. Rev. B* **1982**, 26, 4146.
- [24] I. K. Robinson, D. J. Tweet, *Rep. Prog. Phys.* **1992**, 55, 599.
- [25] C. Westermeier, A. Cernescu, S. Amarie, C. Liewald, F. Keilmann, B. Nickel, *Nat. Commun.* **2014**, 5, 4101.
- [26] D. M. Hudgins, S. A. Sandford, *J. Phys. Chem. A* **1998**, 102, 344.
- [27] N. D. Baydoan, *J. Mater. Sci. Eng. B* **2004**, 107, 70.
- [28] C. Rost, D. J. Gundlach, S. Karg, W. Riess, *J. Appl. Phys.* **2004**, 95, 5782.
- [29] D. Käfer, L. Ruppel, G. Witte, *Phys. Rev. B* **2007**, 75, 085309.
- [30] K. Hong, S. Y. Yang, C. Yang, S. H. Kim, D. Choi, C. E. Park, *Org. Electron.* **2008**, 9, 864.
- [31] Y. Tsuruma, A. Al-Mahboob, S. Ikeda, J. T. Sadowski, G. Yoshikawa, Y. Fujikawa, T. Sakurai, K. Saiki, *Adv. Mater.* **2009**, 21, 4996.
- [32] W. S. Hu, Y. T. Tao, Y. J. Hsu, D. H. Wei, Y. S. Wu, *Langmuir* **2005**, 21, 2260.
- [33] H. Kim, Z. Meihui, N. Battaglini, P. Lang, G. Horowitz, *Org. Electron.* **2013**, 14, 2108.
- [34] H. Yanagisawa, T. Tamaki, M. Nakamura, K. Kudo, *Thin Solid Films* **2004**, 464, 398.
- [35] D. J. Gundlach, L. Zhou, J. A. Nichols, T. N. Jackson, P. V. Necliudov, M. S. Shur, *J. Appl. Phys.* **2006**, 100, 024509.
- [36] G. Horowitz, P. Lang, M. Mottaghi, H. Aubin, *Adv. Funct. Mater.* **2004**, 14, 1069.

A.3 SUB-MONOLAYER PERCOLATION OF PENTACENE ON ROUGH PARYLENE-C DIELECTRICS

Franz X. Werkmeister¹, Simon J. Noever¹, Bert A. Nickel

Organic Electronics 2015, Vol. 26, 439-442

DOI: [10.1016/j.orgel.2015.08.009](https://doi.org/10.1016/j.orgel.2015.08.009)

¹These authors contributed equally.

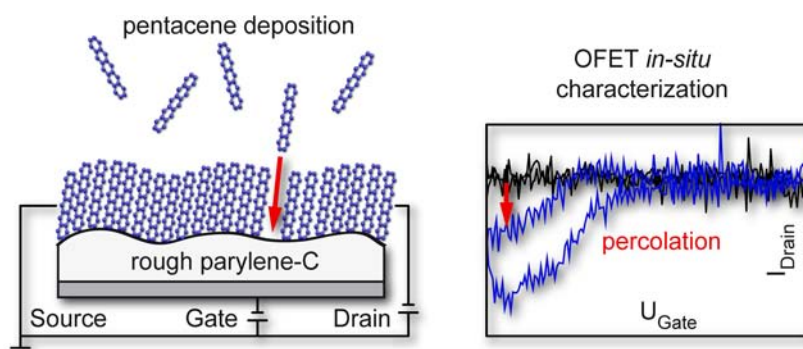
Abstract

We determine the evolution of electrical characteristics of pentacene transistors on rough parylene-C substrates during the physical vapor deposition of pentacene. Here, the changing field effect transistor characteristics are recorded in real time. The root mean square (rms) roughness of the parylene-C dielectric is 7 nm, which is much larger than the size of the pentacene molecule (1.5 nm). In spite of this huge roughness, we observe a source-drain current before nominal film thickness of a monolayer equivalent, i.e. pentacene is able to percolate for sub-monolayers, as in the case for very smooth substrates. This suggests that the pentacene film is able to conformally cover the rough substrate.

Contribution

The *in-situ* setup, which was essential for the findings of this publication, was designed by me during the course of this work. Furthermore, Franz Werkmeister and myself carried out all experiments on the parylene-C samples together. I contributed significantly to the preparation of the final manuscript, i.e. to the main text, all figures and the supporting information.

Table of Contents Graphic





Sub-monolayer percolation of pentacene on rough parylene-C dielectrics

Franz X. Werkmeister^{a,1}, Simon J. Noever^{a,b,1}, Bert A. Nickel^{a,b,*}^aFakultät für Physik & CeNS, Ludwig-Maximilians-Universität München, Munich D-80539, Germany^bNanosystems Initiative Munich (NIM), D-80799 Munich, Germany

ARTICLE INFO

Article history:

Received 26 June 2015

Received in revised form 4 August 2015

Accepted 10 August 2015

Keywords:

Roughness

Percolation

Dielectric

Parylene

ABSTRACT

We determine the evolution of electrical characteristics of pentacene transistors on rough parylene-C substrates during the physical vapor deposition of pentacene. Here, the changing field effect transistor characteristics are recorded in real time. The root mean square (rms) roughness of the parylene-C dielectric is 7 nm, which is much larger than the size of the pentacene molecule (1.5 nm). In spite of this huge roughness, we observe a source-drain current before nominal film thickness of a monolayer equivalent, i. e. pentacene is able to percolate for sub-monolayers, as in the case for very smooth substrates. This suggests that the pentacene film is able to conformally cover the rough substrate.

© 2015 Published by Elsevier B.V.

1. Introduction

In organic electronics, it is well known that the gate dielectric has a huge influence on the growth mode of semiconducting thin films and on device performance [1]. Consequently, organic semiconductor film formation has been studied extensively for a large number of gate dielectric materials [2,3]. In this context, the role of surface roughness of the dielectric is not very clear. Rough dielectric surfaces often impair the performance of organic transistors; this has been observed for inorganic [4] as well as organic dielectrics [5]. However, some studies also report that increasing roughness does not degrade transport properties [6]. Resolving these conflicting reports is of special interest from a technological point of view, since utilizing rough substrates holds various industrial benefits like the lack of need for smoothing- and contact adhesion layers [7]. Most authors report the rms roughness σ , i. e. the variance of the height fluctuations, to quantify the corrugation of surfaces. Strictly speaking, this rms roughness describes the height variations between two surface positions in the limit of large lateral separation R . However, height changes occurring at larger lateral length scale (e.g. waviness) have been found not to impair device performance, in contrast to those at short lateral length scale [8]. The explanation for this very likely originates in the growth mode of the first molecular layers of the semiconducting layer. Typically, transistor performance is investigated for com-

plete devices with rather thick films. However, the charge carrying layer is situated at the dielectric – semiconductor interface within the first few monolayers [9]. Optimization of organic transistors is therefore strongly dependent on insight on early stage thin film formation. Experimental evaluation of such thin layers via AFM is limited by tip quality and tip size and therefore is restricted to feature sizes of several nm up to microns [10,11]. Diffuse X-ray scattering techniques on the other hand allow to study lateral height variations from Angstroms to nm scale [12]. However, most studies focus on surface roughening of films with increasing thickness rather than roughness of ultrathin films on a rough substrate [10]. Especially, sub-monolayer studies of organic semiconductor thin film growth are generally restricted to smooth surfaces such as SiO₂ [13].

A second aspect of the evolution of a conduction channel is, that some organic semiconductors form a non conductive dead layer in presence of highly disturbed electrostatic landscapes [14]. This disturbance can be effected by a rough topography or open binding sites on the dielectric surfaces. In that case the onset of charge transport is delayed. To gain insight into the percolation behavior of semiconducting thin films and thereby the formation of active layers in deposition grown electronic devices, it is advantageous to measure percolation by the onset of device performance.

Here, we explore the influence of the roughness of chemical vapor deposition (CVD) grown parylene-C on OFET performance. The roughness is intrinsic due to the CVD growth of parylene-C [15]. Parylene-C is an FDA approved polymer, which is heavily used as dielectric layer in sensors based on organic semiconductors [16,17]. Parylene, deposited as gate dielectric on organic single crystals, forms a trap free interface enabling record devices [18].

* Corresponding author at: Fakultät für Physik & CeNS, Ludwig-Maximilians-Universität München, Munich D-80539, Germany.

E-mail address: nickel@lmu.de (B.A. Nickel).

¹ These authors contributed equally.

Furthermore, thin films deposited on parylene-C dielectrics, have resulted in high performance organic transistors [19]. Interestingly, intrinsic charge carrier mobility in pentacene thin films has been found to be as high as $20 \text{ cm}^2/\text{Vs}$, on parylene-N [20], which has a similarly rough surface as parylene-C.

Several studies address the morphology and crystallinity of pentacene film on parylene-C by X-ray diffraction [21], micro-Raman spectroscopy [22] and AFM studies [23]. These studies show crystallinity of pentacene films on rough parylene-C surfaces and a characteristic grainy, 3-D like morphology. However, no conclusions were presented about the nature of the first monolayers, which form the accumulation channel in field effect transistors [9].

The *in-situ* deposition experiment here provides experimental access to the growth behavior of the first few monolayers with sub-monolayer precision; we record trans-conductance characteristics of an OFET in real time during deposition of the active material [24,25]. The evolution of the electronic properties of the OFET could thus be studied in dependence of the nominal film thickness.

2. Experiment and discussion

In detail, bottom gate, bottom contact samples were prepared by depositing nominally $1.6 \mu\text{m}$ parylene-C as gate dielectric on a glass slide with an Au gate. Next, 30 nm of Au were patterned by shadow mask onto the parylene-C to yield source and drain contacts with a channel width W of 2 mm and a channel length L of 50 μm .

In the experiment, pentacene was deposited at a rate of ca. 0.01 nm/s onto the sample, which was held at room temperature. Before deposition, a gate sweep was recorded as baseline, then the sample was exposed to the molecular beam and gate sweeps were recorded continuously during the deposition (Fig. 1). The applied source drain voltage (V_{SD}) was held at -20 V for all shown transport measurements. The film thickness was recorded by a quartz crystal microbalance. The resulting dataset included the film thickness, applied gate voltage, and source-drain current for each voltage step in the gate sweeps. Each dataset was completed by the measured source-gate current, to probe for leakage currents through the dielectric, which however were within the noise limit.

The onset of the source-drain current is observed for a nominal pentacene thickness of 1.2 nm, i.e. below the equivalent of a complete monolayer. This onset and the corresponding baseline before deposition are shown in Fig. 1a. The corresponding gate currents after percolation (red curve in Fig. 1b) exhibits no deviation from the sweep prior to drain-current onset (black curve). To demonstrate the early stage evolution of the transistor characteristics, the first five gate voltage sweeps, i.e. *in-situ* measurements to a film thickness of about 5 nm, are depicted in Fig. 1c. The source-drain current increases supralinearly with film thickness. These results were reproducible for different batches of samples and for different deposition rates of 0.01 and 0.02 nm/s.

While the evaluation of the electrical measurements reveal the nature of early stage thin film growth, AFM shows no clear signature from the pentacene layer after percolation (Fig. 2) [26]. The AFM micrograph at nominally 1.37 nm of pentacene (Fig. 2b) looks very similar to the pristine parylene-C surface with an rms roughness of ca. 7 nm rms on-top the Au gate (Fig. 2a), i.e. it is not possible to draw any conclusions about the early growth mode from topography, because the sub-monolayer pentacene film cannot be imaged, a common problem for rough substrates. The combination of both studies suggests that the first layer coated the substrate conformally. Pentacene thin films at higher thicknesses, here a nominal thickness of 12 nm and 57 nm, respectively, exhibit granular topographies with grain sizes $<300 \text{ nm}$ (Fig. 2c and d) [23]. This subsequent island growth for thicker films allows to

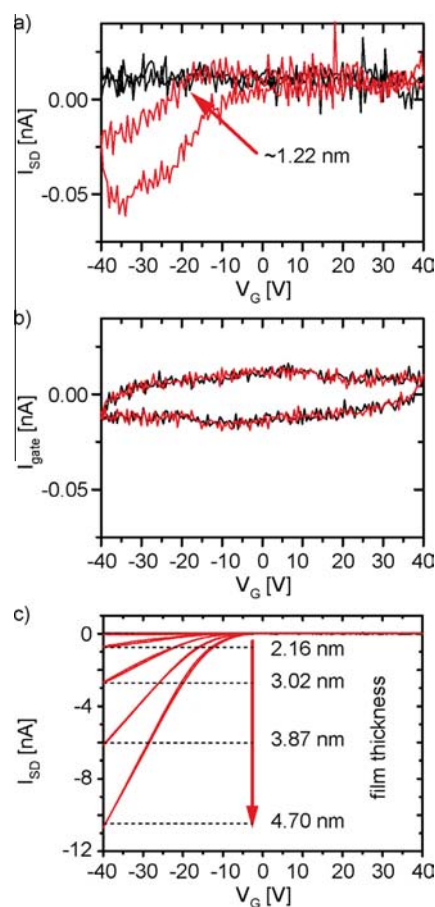


Fig. 1. Early growth stage *in-situ* measurement. (a) Transfer measurements of early-stage pentacene deposition (forward and backward sweeps). First drain currents occur at film thickness of $\sim 1.22 \text{ nm}$ (0.8 ML). (b) Corresponding gate current measurements. Here, the gate sweeps do not indicate any change after percolation. (c) Transfer measurements of the first five gate voltage sweeps during film deposition after drain current onset.

classify the growth mode of pentacene on parylene-C as the Stranski–Krastanov (layer plus island) mode [25].

To understand how charge transport can occur on a sub-monolayer scale on rough surfaces, it is necessary to estimate the influence of height fluctuations at distances matching the unit cell dimensions of organic semiconductors, i.e. distances of the order 1 nm, on the pi-system overlap. As the height difference correlation function approaches zero for separation much smaller than the correlation length ξ [10,12], i.e. it is quite possible that the height difference at unit cell dimensions (lattice distortion) can be very small, even for large rms σ values. This implies that as long as the lateral correlation length is large enough, a rather large rms is tolerable.

Besides the influence of roughness on percolation, it is also important to verify its influence on channel completion, which should, from an electrostatic point of view, occur within the Debye length. However, channel completion could be delayed due to defects and other impurities. To answer this, we evaluate the evolution of mobility, threshold and hysteresis of the OFETs from the current in the saturation regime: $I_{SD} = W/2L * \mu * C_i * (V_G - V_T)^2$.

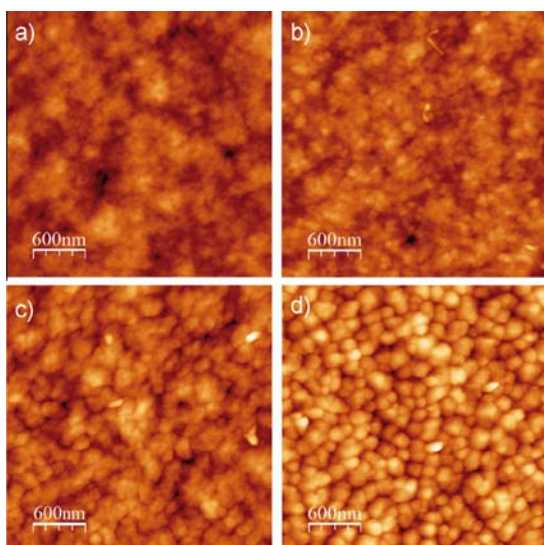


Fig. 2. AFM micrographs of parylene-C covered by different thicknesses of pentacene. (a) Pristine parylene-C surface. (b) 0.9 ML pentacene (1.37 nm) on parylene-C; the film is percolated, i.e. conductive. (c) 12 nm pentacene on parylene-C. (d) 57 nm pentacene on parylene-C. The z-scale is 77.7 nm for all micrographs.

Here, W is the channel width and L is the channel length, μ is the effective charge carrier mobility, C_i the capacitance of the dielectric per area, V_G the applied gate voltage and V_T the threshold voltage. For any given thickness interval, whose range is determined by the sweep speed, the corresponding gate sweeps are shown in Fig. 3a. To clarify the evolution of the device performance, mobility and threshold voltage is extracted from the forward and backward sweeps of the OFETs in the saturation regime from every sweep (Fig. 3b and c, mobility shown for forward sweep direction). The nominal film thickness is chosen as the value at the end of the sweep, and assumed to be constant during the sweep.

During deposition of the first 3 monolayers (ML) the threshold voltage experiences a steep shift of more than 15 V (Fig. 3b). Within the same nominal thickness, the hysteresis, i.e. the difference between forward and backward sweep threshold voltage, decreases rapidly from about 16 V to a value smaller than 1 V. Similar behavior has been observed for pentacene OFETs on SiO_2 [24]. The threshold voltage shift can be explained by an increase of deep electron volume traps with increasing film thickness. Until a film thickness of 3 ML, these traps are within the Debye length of the transistor channel and consequently lay within the accumulation layer. The hysteresis on the other hand arises due to traps at the pentacene surface, which quickly grow out of the OFET channel region. These traps are energetically shallower than the deep traps that cause the threshold shift, since they can be filled and depleted at room temperature. Beyond 3 ML the shifts saturate, because further thickness increase occurs outside of the accumulation channel of the transistor.

On the other hand, saturation mobility reproducibly continues to increase up to a thickness of ca. 20 nm (Fig. 3c), which is far beyond the Debye length. Investigation of the topography of pentacene at the electrode edge reveals small grained pentacene topography with deep valleys (Fig. 4). Such dewetting of pentacene in the vicinity of gold is in fact a well known problem for bottom contact geometry [27]. This suggests that also here, especially for early stage film growth, the impaired film formation near and on the gold contacts disturbs charge injection. Hence, the extracted

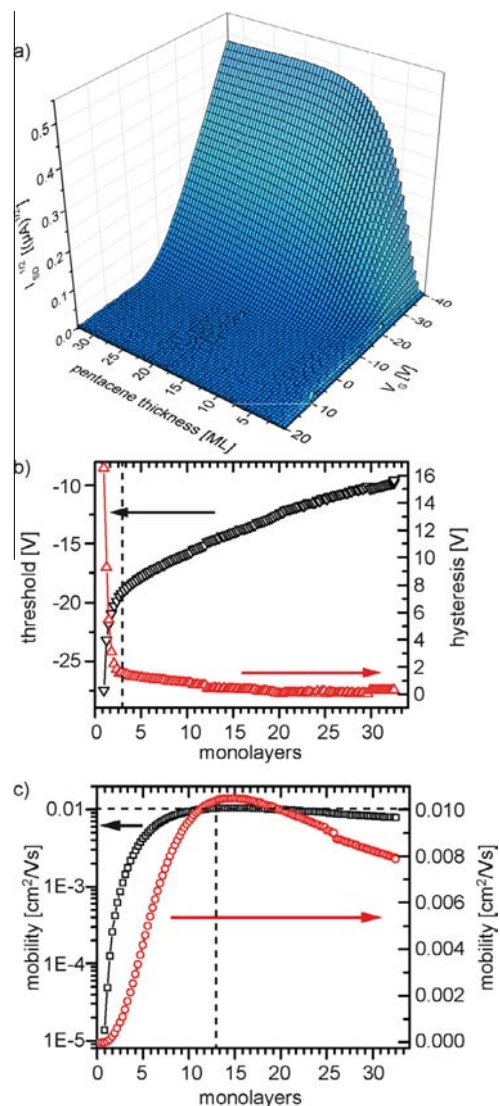


Fig. 3. Electronic data from one *in-situ* growth measurement. (a) Gate voltage (V_G) sweeps, plotted against the nominal pentacene film thickness and the square root of the source drain current I_{SD} . For clarity, only every second sweep and every second gate voltage data point is shown. (b) Threshold voltage (black downward facing triangles) and hysteresis (red upward facing triangles). The vertical dashed line at ~ 3 MLs indicates the region, where the threshold shift turns from rapid to slow. (c) Mobility in linear (red circles) and logarithmic plot (black squares) in dependence of the film thickness (extracted from forward sweeps). The vertical line indicates saturation of the mobility at ~ 13 MLs. (For interpretation of the references to color in this figure legend, the reader is referred to the web version of this article.)

mobilities at early growth might be influenced by poor charge injection and extraction, and therefore may not represent intrinsic charge carrier mobility within the film. The ongoing increase in measured mobility is likely to be caused by the improvement of charge injection with film thickness. The final mobility is probably not limited by the rough dielectric surface, but due to the overall device preparation, which was adapted to the presented *in-situ* study, using bottom contact geometry and pristine surfaces with-

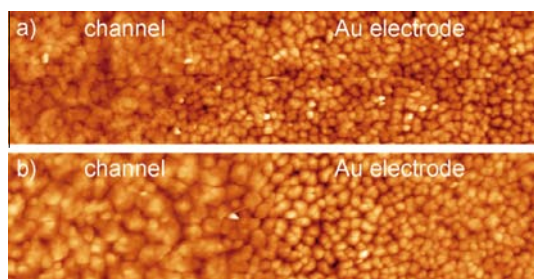


Fig. 4. AFM height micrographs of the OFET channel/Au electrode interface ($10 \mu\text{m} \times 2.5 \mu\text{m}$). The growth differences of pentacene on parylene-C and gold, i. e. smaller grain size and deeper grain gaps on Au are clearly visible. (a) 12 nm thick pentacene film. (b) 57 nm thick pentacene film.

out modifications. In fact, using an optimized device geometry, a mobility of $0.81 \text{ cm}^2/\text{Vs}$ was reported for transistors with top contact geometry on parylene-C dielectrics [28].

3. Conclusion

In conclusion, we performed *in-situ* deposition of pentacene on a rough parylene-C dielectric and observed sub-monolayer percolation of the pentacene film. This initial closed layer of pentacene points to a Stranski–Krastanov growth mode. This demonstrates that conformal monolayer growth is possible on rough substrates. Like in the case of smooth dielectrics, subsequent transistor channel formation is dominated by electrostatic and charge injection phenomena. In fact, saturation of electrical properties is observed for the same film thickness as on smooth substrates. These findings imply that, as long as conformal growth of the organic semiconductor is possible, high surface roughness does not cause impaired device performance. Consequently, one should explore rough substrates as the choice for dielectric material more systematically.

Acknowledgments

We thank Prof. Kersting for providing access to the parylene CVD chamber. The authors gratefully acknowledge financial support from Deutsche Forschungsgemeinschaft through the SFB 1032 (Nanoagents project A07) as well as by the Bavarian State Ministry for Education, Science and the Arts through the initiative “Solar Technologies Go Hybrid” (SolTech).

Appendix A. Supplementary data

Supplementary data associated with this article can be found, in the online version, at <http://dx.doi.org/10.1016/j.orgel.2015.08.009>.

References

- [1] A. Facchetti, M.H. Yoon, T.J. Marks, Gate dielectrics for organic field-effect transistors: new opportunities for organic electronics, *Adv. Mater.* 17 (2005) 1705–1725.
- [2] J. Wunsche, G. Tarabella, S. Bertolazzi, M. Bocoum, N. Coppede, L. Barba, G. Arrighetti, L. Lutterotti, S. Iannotta, F. Cicola, C. Santato, The correlation between gate dielectric, film growth, and charge transport in organic thin film transistors: the case of vacuum-sublimed tetracene thin films, *J. Mater. Chem. C* 1 (2013) 967–976.
- [3] C. Kim, A. Facchetti, T.J. Marks, Gate dielectric microstructural control of pentacene film growth mode and field-effect transistor performance, *Adv. Mater.* 19 (2007) 2561–2566.
- [4] S. Steudel, S. De Vusser, S. De Jonge, D. Janssen, S. Verlaak, J. Genoe, P. Heremans, Influence of the dielectric roughness on the performance of pentacene transistors, *Appl. Phys. Lett.* 85 (2004) 4400.
- [5] H.-G. Min, E. Seo, J. Lee, N. Park, H.S. Lee, Behavior of pentacene molecules deposited onto roughness-controlled polymer dielectrics films and its effect on FET performance, *Synth. Met.* 163 (2013) 7–12.
- [6] K. Shin, C. Yang, S.Y. Yang, H. Jeon, C.E. Park, Effects of polymer gate dielectrics roughness on pentacene field-effect transistors, *Appl. Phys. Lett.* 88 (2006) 072109.
- [7] M. Kaltenbrunner, T. Sekitani, J. Reeder, T. Yokota, K. Kuribara, T. Tokuhara, M. Drack, R. Schwodiauer, I. Graz, S. Bauer-Gogonea, S. Bauer, T. Someya, An ultralightweight design for imperceptible plastic electronics, *Nature* 499 (2013) 458–463.
- [8] G. Lin, Q. Wang, L. Peng, M. Wang, H. Lu, G. Zhang, G. Lv, L. Qiu, Impact of the lateral length scales of dielectric roughness on pentacene organic field-effect transistors, *J. Phys. D Appl. Phys.* 48 (2015) 105103.
- [9] A. Dodabalapur, L. Torsi, H.E. Katz, Organic transistors: two-dimensional transport and improved electrical characteristics, *Science* 268 (1995) 270–271.
- [10] A.C. Dürr, F. Schreiber, K.A. Ritley, V. Kruppa, J. Krug, H. Dosch, B. Struth, Rapid roughening in thin film growth of an organic semiconductor (Diindenoperylene), *Phys. Rev. Lett.* 90 (2003).
- [11] T. Gredig, E.A. Silverstein, M.P. Byrne, Height–height correlation function to determine grain size in iron phthalocyanine thin films, 15th International Conference on Thin Films (Ictf-15), 417 (2013).
- [12] S.K. Sinha, E.B. Sirota, S. Garoff, H.B. Stanley, X-ray and neutron-scattering from rough surfaces, *Phys. Rev. B* 38 (1988) 2297–2311.
- [13] R. Ruiz, B. Nickel, N. Koch, L.C. Feldman, R.F. Haglund, A. Kahn, F. Family, G. Scoles, Dynamic scaling, island size distribution, and morphology in the aggregation regime of submonolayer pentacene films, *Phys. Rev. Lett.* 91 (2003).
- [14] K.P. Weidkamp, C.A. Hacker, M.P. Schwartz, X.P. Cao, R.M. Tromp, R.J. Hamers, Interfacial chemistry of pentacene on clean and chemically modified silicon (001) surfaces, *J. Phys. Chem. B* 107 (2003) 11142–11148.
- [15] J.B. Fortin, T.-M. Lu, Chemical Vapor Deposition Polymerization – The Growth and Properties of Parylene Thin Films, Springer Science & Business Media, 2003.
- [16] A.K. Diallo, J. Tardy, Z.Q. Zhang, F. Bessueille, N. Jaffrezic-Renault, M. Lemiti, Trimethylamine biosensor based on pentacene enzymatic organic field effect transistor, *Appl. Phys. Lett.* 94 (2009) 263302.
- [17] D. Khodagholy, T. Doublet, M. Gurfinkel, P. Quilichini, E. Ismailova, P. Leleux, T. Herve, S. Sanaur, C. Bernard, G.G. Malliaras, Highly conformable conducting polymer electrodes for in vivo recordings, *Adv. Mater.* 23 (2011) H268–H272.
- [18] V. Podzorov, S.E. Sysoev, E. Loginova, V.M. Pudalov, M.E. Gershenson, Single-crystal organic field effect transistors with the hole mobility similar to $8 \text{ cm}^2/\text{Vs}$, *Appl. Phys. Lett.* 83 (2003) 3504–3506.
- [19] C.D. Dimitrakopoulos, B.K. Furman, T. Graham, S. Hegde, S. Purushothaman, Field-effect transistors comprising molecular beam deposited alpha, omega-di-hexyl-hexathienylene and polymeric insulator, *Synth. Met.* 92 (1998) 47–52.
- [20] S.G. Engelbrecht, M. Prinz, T.R. Arend, R. Kersting, Terahertz spectroscopy on hole transport in pentacene thin films, *Appl. Phys. Lett.* 105 (2014) 012101.
- [21] A. Moser, H.G. Flesch, A. Neuhold, M. Marchl, S.J. Ausserlechner, M. Edler, T. Griesser, A. Haase, D.M. Smailgies, J. Jakabovic, R. Resel, Crystallization of pentacene thin films on polymeric dielectrics, *Synth. Met.* 161 (2012) 2598–2602.
- [22] A. Vincze, J. Jakabovic, R. Srnanek, A. Satka, J. Kovac, J. Kovac, Surface and interface properties of thin pentacene and parylene layers, *Cent. Eur. J. Phys.* 7 (2009) 270–278.
- [23] V.A. Skryshevsky, J. Tardy, M. Phaner-Goutorbe, E. Souteyrand, R. Villey, M. Erouel, M. Iazykov, An Afm investigation of surface energy of pentacene films on parylene-C and benzocyclobutene, *Funct. Mater. Lett.* 05 (2012) 1250016.
- [24] M. Fiebig, D. Beckmeier, B. Nickel, Thickness-dependent in situ studies of trap states in pentacene thin film transistors, *Appl. Phys. Lett.* 96 (2010) 083304.
- [25] S.-W. Liu, C.-C. Lee, H.-L. Tai, J.-M. Wen, J.-H. Lee, C.-T. Chen, In situ electrical characterization of the thickness dependence of organic field-effect transistors with 1–20 molecular monolayer of pentacene, *ACS Appl. Mater. Interfaces* 2 (2010) 2282–2288.
- [26] I. Horcas, R. Fernandez, J.M. Gomez-Rodriguez, J. Colchero, J. Gomez-Herrero, A.M. Baro, WsXM: a software for scanning probe microscopy and a tool for nanotechnology, *Rev. Sci. Instrum.* 78 (2007) 013705.
- [27] Y. Tsuruma, A. Al-Mahboob, S. Ikeda, J.T. Sadowski, G. Yoshikawa, Y. Fujikawa, T. Sakurai, K. Saiki, Real-time observation and control of pentacene film growth on an artificially structured substrate, *Adv. Mater.* 21 (2009) 4996.
- [28] T. Yasuda, K. Fujita, H. Nakashima, T. Tsutsui, Organic field-effect transistors with gate dielectric films of poly-p-xylylene derivatives prepared by chemical vapor deposition, *Jpn. J. Appl. Phys.* 1 (42) (2003) 6614–6618.

A.4 MICRODIFFRACTION IMAGING - A SUITABLE TOOL TO CHARACTERIZE ORGANIC ELECTRONIC DEVICES

Clemens Liewald, Simon Noever, Stefan Fischer, Janina Roemer, Tobias U. Schüllli, and Bert Nickel

AIMS Materials Science, Special Issues (X-ray microscopy in Materials Sciences), 2015, 2(4), 369-378

DOI: [10.3934/materci.2015.4.369](https://doi.org/10.3934/materci.2015.4.369)

Abstract

Tailoring device architecture and active film morphology is crucial for improving organic electronic devices. Therefore, knowledge about the local degree of crystallinity is indispensable to gain full control over device behavior and performance. In this article, we report on microdiffraction imaging as a new tool to characterize organic thin films on the sub-micron length scale. With this technique, which was developed at the ID01 beamline at the ESRF in Grenoble, a focused X-ray beam (300 nm diameter, 12.5 keV energy) is scanned over a sample. The beam size guarantees high resolution, while material and structure specificity is gained by the choice of Bragg condition. Here, we explore the possibilities of microdiffraction imaging on two different types of samples. First, we measure the crystallinity of a pentacene thin film, which is partially buried beneath thermally deposited gold electrodes and a second organic film of fullerene C₆₀. The data shows that the pentacene film structure is not impaired by the subsequent deposition and illustrates the potential of the technique to characterize artificial structures within fully functional electronic devices. Second, we investigate the local distribution of intrinsic polymorphism of pentacene thin films, which is very likely to have a substantial influence on electronic properties of organic electronic devices. An area of 40 μm by 40 μm is scanned under the Bragg conditions of the thin-film phase and the bulk phase of pentacene, respectively. To find a good compromise between beam footprint and signal intensity, third order Bragg condition is chosen. The scans show complementary signal distribution and hence demonstrate details of the crystalline structure with a lateral resolution defined by the beam footprint (300 nm by 3 μm). The findings highlight the range of applications of microdiffraction imaging in organic electronics, especially for organic field effect transistors and for organic solar cells.

Contribution

All data were taken by Clemens Liewald, Bert Nickel and myself during test beams at ESRF in Grenoble and DESY in Hamburg. I was significantly involved in all measurements, analyzed the data on buried organic thin films, and wrote the respective parts of the manuscript.



<http://www.aimspress.com/>

AIMS Materials Science, 2(4): 369-378.

DOI: 10.3934/mat.2015.4.369

Received date 12 June 2015,

Accepted date 27 September 2015,

Published date 12 October 2015

Research article

Microdiffraction imaging—a suitable tool to characterize organic electronic devices

Clemens Liewald^{1,2}, Simon Noever^{1,2}, Stefan Fischer¹, Janina Roemer¹, Tobias U. Schüll³, and Bert Nickel^{1,2,*}

¹ Fakultät für Physik & Center for NanoScience (CeNS), Ludwig-Maximilians-Universität München, Geschwister-Scholl-Platz 1, 80539 Munich, Germany

² Nanosystems Initiative Munich, Schellingstrasse 4, 80799 Munich, Germany

³ ID01/ESRF, 71 avenue des Martyrs, CS 40220, F-38043 Grenoble Cedex 9, France

* **Correspondence:** Email: nickel@lmu.de.

Abstract: Tailoring device architecture and active film morphology is crucial for improving organic electronic devices. Therefore, knowledge about the local degree of crystallinity is indispensable to gain full control over device behavior and performance. In this article, we report on microdiffraction imaging as a new tool to characterize organic thin films on the sub-micron length scale. With this technique, which was developed at the ID01 beamline at the ESRF in Grenoble, a focused X-ray beam (300 nm diameter, 12.5 keV energy) is scanned over a sample. The beam size guarantees high resolution, while material and structure specificity is gained by the choice of Bragg condition.

Here, we explore the possibilities of microdiffraction imaging on two different types of samples. First, we measure the crystallinity of a pentacene thin film, which is partially buried beneath thermally deposited gold electrodes and a second organic film of fullerene C₆₀. The data shows that the pentacene film structure is not impaired by the subsequent deposition and illustrates the potential of the technique to characterize artificial structures within fully functional electronic devices. Second, we investigate the local distribution of intrinsic polymorphism of pentacene thin films, which is very likely to have a substantial influence on electronic properties of organic electronic devices. An area of 40 μm by 40 μm is scanned under the Bragg conditions of the thin-film phase and the bulk phase of pentacene, respectively. To find a good compromise between beam footprint and signal intensity, third order Bragg condition is chosen. The scans show complementary signal distribution and hence demonstrate details of the crystalline structure with a lateral resolution defined by the beam footprint (300 nm by 3 μm).

The findings highlight the range of applications of microdiffraction imaging in organic

electronics, especially for organic field effect transistors and for organic solar cells.

Keywords: focused X-ray; polymorphism; multilayer; morphology; scanning X-ray diffraction microscopy; synchrotron

1. Introduction

Organic electronics allow for large scale, low cost, and low energy device fabrication. Today, organic electronics have found mass market application in digital displays consisting of organic light emitting diodes (OLED). In order to improve the performance of organic electronic devices, a detailed understanding of the device physics is essential. The challenge for highly ordered materials is twofold; on the one hand side, intrinsic properties, such as charge carrier mobility, depend on details of the pi-electron overlap [1] and polymorphism. Polymorphism is common among a variety of organic small molecule semiconductors [2–5]. Consequently, the domain size and the mutual distribution of the polymorphs are of great concern [6]. On the other hand, processing steps and interface phenomena often induce additional structural changes at the nm to micron scale, which may influence device performance. Close attention should be paid to contact regions because metal top contacts can influence the underlying organic layer by metal clusters diffusing in the organic film [7], while the growth mode of many organic materials on bottom contact metals is strongly disturbed, which changes the energy alignment of these materials [8]. In practice, top contact configuration in pentacene thin film transistors shows preferable device characteristics when not employing bottom contact electrodes which are functionalized [9]. Furthermore, the manufacturing of multilayer devices, such as organic light emitting diodes, organic photovoltaics and ambipolar organic field effect transistors (OFETs), demands the application of various sequential processing steps, including photolithography, imprint, shadow masks, spin casting, and annealing [10]. These subsequent processing steps can also modify the structure of subjacent films [11].

An experimental approach that allows nm-resolved, non-destructive probing of the crystal structure of organic devices, e.g. on top or below metal contacts of an OFET and in the conduction channel, would be very attractive. Recently, we introduced scattering-type scanning near field infrared optical microscopy (s-SNOM) to probe polymorphism in organic films [6]; however, this gentle technique does not work below Au contacts, which reflect back the IR light so that no information from below is accessible. Transmission electron microscopy (TEM) instead allows to image depth profiles of organic devices with close to molecular resolution, revealing interdiffusion of Au, originating from the top contact deposition [7]. However, the demanding cross section preparation requires cutting the device apart and the electron flux alters [12] or even disintegrates the molecular structure at prolonged exposure.

In principle, X-ray techniques combine all needed properties: X-ray reflectometry, for example, is used to depth profile stratified media on sample surfaces as well as buried layers [13], whereas scattering geometries, such as grazing incidence X-ray scattering allow for surface sensitive probing of thin organic single and multilayers [14,15]. Although X-rays are commonly used to probe rather large areas, typically several hundred microns squared, there is so far only a small amount of reports on scanning X-ray diffraction with a sub-micron focused X-ray beam [16–19]. This microdiffraction imaging was used to study inorganic materials and can for example resolve local strain and lattice

orientation of semiconductors like Si and Ge. Studies using microdiffraction techniques on organic semiconductors are mostly limited to transmission measurements which resolve depth profiles of organic devices [20]. Ideally, the energy should be in the vicinity of ~ 20 keV because irradiating organic carbon compounds with high flux per area X-rays at lower energy leads to severe beam damage by incoherent scattering [21]. Here, we employ microdiffraction imaging in reflection geometry to study organic films, using a beam of 300 nm diameter at an energy of 12.5 keV, and cannot observe any beam damage. In this experiment, we map the lateral distribution of artificial and intrinsic structures in organic single- and multilayer thin-film devices. With microdiffraction imaging, it is possible to resolve the local crystalline structure on the surface and in buried layers, by scanning the beam over the sample and recording the intensity at specific angles, matching designated Bragg conditions. Furthermore, we discuss the current limitations of the lateral resolution and possible applications for this method.

2. Materials and Method

2.1. Sample preparation

The organic semiconductor pentacene served as a model system for our microdiffraction experiments. When grown on silicon oxide, pentacene thin films are known to crystallize in two main structural phases, the so-called thin-film phase (TFP) and bulk phase (BP) [4,5,22–24].

For measuring buried organic structures in working multilayer devices, an ambipolar organic field-effect transistor (OFET) was fabricated. Here, a 40 nm layer of pentacene was used as p-type semiconductor, followed by 40 nm gold top contacts, and finally 30 nm of fullerene C₆₀ as n-type semiconductor. The channel width and length were 2 mm and 50 μm , respectively. Highly n-doped silicon with 300 nm SiO₂ acted as combined gate/dielectric substrate. After consecutively sonicating in acetone, isopropyl alcohol, and de-ionized water for 10 min each, the sample was cleaned with oxygen plasma for 180 s. Prior to pentacene deposition, the dielectric surface was finished with a ~ 5 nm thick layer of cyclic-olefin-copolymere (COC), by spin casting a 0.25% solution of COC in toluene for 30s at 6000 rpm and annealing at 100 $^{\circ}\text{C}$ for 60 s. Pentacene and fullerene C₆₀ layers were produced at room temperature and ~ 90 $^{\circ}\text{C}$, respectively, by molecular vapor deposition, at a rate of 0.1 $\text{\AA}/\text{s}$, respectively, and gold contacts were fabricated by electron beam deposition, at a rate of 1 $\text{\AA}/\text{s}$. All structures were defined by shadow masks under ultra high vacuum conditions. The upper part of the pentacene layer (~ 5 nm) was cross-linked by e-beam irradiation prior to gold evaporation.

To study the polymorphism of TFP and BP pentacene, a 60 nm thick pentacene film was prepared on a silicon wafer with 20 nm thick SiO₂. The substrate was cleaned by sonicating, as described above, and the pentacene film was deposited by molecular vapor deposition, at a rate of 0.1 $\text{\AA}/\text{s}$. With this deposition rate, pentacene crystallizes at room temperature in the TFP with the [001] direction perpendicular to the substrate surface. However for this sample, a substrate temperature between 40 $^{\circ}\text{C}$ and 50 $^{\circ}\text{C}$ was chosen, which is known to induce mixed growth of TFP and BP pentacene [5,22–24] and to exhibit ellipsoidal structures on a sub-micron length scale [6]. The coexistence of the two phases on this sample was verified with an in-house reflectometer prior to the reported experiment.

2.2. X-ray diffraction

2.2.1. Reflectometry

The X-ray reflectometry curve shown here was measured at the P08 beamline at PETRA III at DESY in Hamburg, Germany [25]. Here, the X-ray energy E was set to 18 keV, which corresponds to a wavelength λ of 0.6888 Å.

2.2.2. Microdiffraction imaging

Microdiffraction imaging was performed at the beamline ID01 at the European Synchrotron Radiation Facility (ESRF) in Grenoble, France. Here, the synchrotron X-ray beam with an energy of 12.5 keV, which corresponds to a wavelength λ of 0.9919 Å, was focused by a Fresnel zone plate with a central beam stop, followed by an order sorting aperture (to block unfocused beam parts and higher diffraction orders) to a nominal beam size of 300 nm (for further details, we refer to [17]). A sketch of the measurement geometry is shown in Figure 1a. Here, the angle of the incident beam θ was adjusted to a Bragg condition of the film and the diffracted beam was recorded with a 2D detector (MAXIPIX, 516×516 pixels², 55×55 μm^2 pixel size) [26] with adjusted regions of interest (ROI) at about 40 cm distance from the sample holder. Additionally, lead tape between the incident beam and the detector was used as a beam knife-edge to prevent air scattering from disturbing the recorded signal. To avoid radiation damage from reactive oxygen species, the sample was blown with dry nitrogen. First, the sample was positioned with a light microscope, illuminating from the top. Subsequently, the sample was continuously mapped in real space with a piezoelectric stage for short distances (<100 μm) or a hexapod (>100 μm) with step size resolutions of 5 nm and 100 nm, respectively. This so-called K-Map, a quick mapping procedure developed at ID01 has significantly reduced the measurement time needed for these scans, by optimizing positioning, exposure, and data acquisition [17]. The K-Maps in this report had a size of 40×40 μm^2 and a resolution of 80×40 pixels² (0.5×1 μm^2), leading to a total measuring time of only 16 min and 43 min, corresponding to a pixel time of 0.3 s and 0.8 s, respectively.

However, the lateral resolution of the K-Maps is inherently limited by the footprint f of the beam. In the direction perpendicular to the X-ray beam, the footprint f_{\perp} corresponds to the diameter b of the focused beam, which was set to 300 nm during our experiments. Additionally, in the direction parallel to the incident X-ray beam, the geometrically enlarged footprint f_{\parallel} is given by

$$f_{\parallel} = \frac{b}{\sin(\theta)}, \quad (1)$$

with the beam diameter b and the incident angle θ . Consequently, the footprint f_{\parallel} is smaller for higher incident angles θ , which improves the lateral resolution of the K-Maps. A good lateral resolution in both directions can be achieved with inorganic crystals like VO_2 , Si, or Ge [16–19], owing to their high crystallinity. However, it is difficult to record K-Maps at high incident angles θ for organic crystals, because of their overall lower scattered intensity and their larger lattice constants. Therefore, finding a suitable compromise between footprint size and signal to noise ratio is essential, when measuring crystalline organic thin films. Here, the pentacene samples were measured at the (002) and (003) Bragg conditions.

3. Results and Discussion

We characterized an ambipolar pentacene- C_{60} OFET as a representative sample for multilayer devices, as they are commonly used in organic electronics. A sketch of the experimental geometry is shown in Figure 1 a). Here, the source and drain electrode of the transistor are indicated by the T-structures and the scan profile is indicated by the white arrow. At this position, the gold contacts had a length of 100 μm , each, which adds, together with the channel length of 50 μm , to a total device length of 250 μm . An illustration of the vertical section of the device is shown in Figure 1 b), with the C_{60} layer depicted on top of the gold and the pentacene layer. The pentacene top contact configuration is needed to optimize charge carrier injection in bi-layer ambipolar transistors [15].

To investigate the pentacene layer beneath the gold contacts, we measured two 400 μm scans over the device. First, we performed a reference measurement, to determine the exact sample position [Figure 1 c)]. The incidence angle θ was set to the Au (111) Bragg condition, i.e. 12.15°, which is very pronounced, since vacuum deposited gold on SiO_2 crystallizes in fcc structure in [111] direction [27]. Here, the footprint size parallel to the beam f_1 corresponded to 1.43 μm , according to equation (1). The scan was done using the hexapod because the scan width of 400 μm exceeded the hardware limitation of the high-resolution piezoelectric stage. As seen from Figure 1, the intensity profile of the scan traces the channel geometry quite well. Second, we set the incidence angle to the pentacene TFP (002) Bragg condition, i.e. to 3.69°, which corresponded to a footprint f_1 of 4.65 μm . This led to good signal strength with an acceptable footprint. The intensity profile of the TFP (002) scan indicates a complementary behavior to the Au (111) scan [Figure 1 c)]. The drop in intensity beneath the gold contacts can be explained rather well by absorption of X-rays while passing through the gold layer. The absorption of a planar layer is given by:

$$I_r = I_0 * \exp\left(-\frac{2d}{\mu * \sin(\theta)}\right) \quad (2)$$

where d is the nominal gold layer thickness, θ the incident angle, $\mu = 3.2 \mu\text{m}^{-1}$ the attenuation length of gold and I_0 the scattered intensity without gold. The factor two in the exponent accounts for the way in and out of the gold layer. As a result, the signal intensity should calculate to $I_r \sim 0.68 * I_0$. However, the acquired signal only drops about 20% and is thus higher than expected from this calculation. One explanation for this observation might be the uncertainty of the actual Au film thickness deposited onto the pentacene layer. The quartz microbalances, which were used to read out the nominal Au thickness, do not address any eventual deviations from growth on e.g. smooth SiO_2 surfaces.

For these reasons, the decrease of the pentacene signal beneath the gold contacts could be ascribed to the absorption of the beam propagating through the gold film. Thus, we have no indication that the top contact strongly reduces the crystallinity of the pentacene film.

Furthermore, the pentacene signal increased only slowly with growing distance to the right gold contact, even though no electrode material was present in the beam pathway. Here, the preparation of the contact geometry could have led to a damaged film. For example, removing the shadow mask could have led to a mechanical damage of the subjacent pentacene film after contact fabrication.

Moreover, it is necessary to address the large variations in the pentacene (002) signal, compared to the Au (111) signal. The grain size of pentacene is usually on the micron scale, far larger than for Au, and its topography shows thickness variations of the order of the nominal film thickness when grown on SiO_2 . Therefore, the scattered intensity should depend strongly on the beam position on the

pentacene surface.

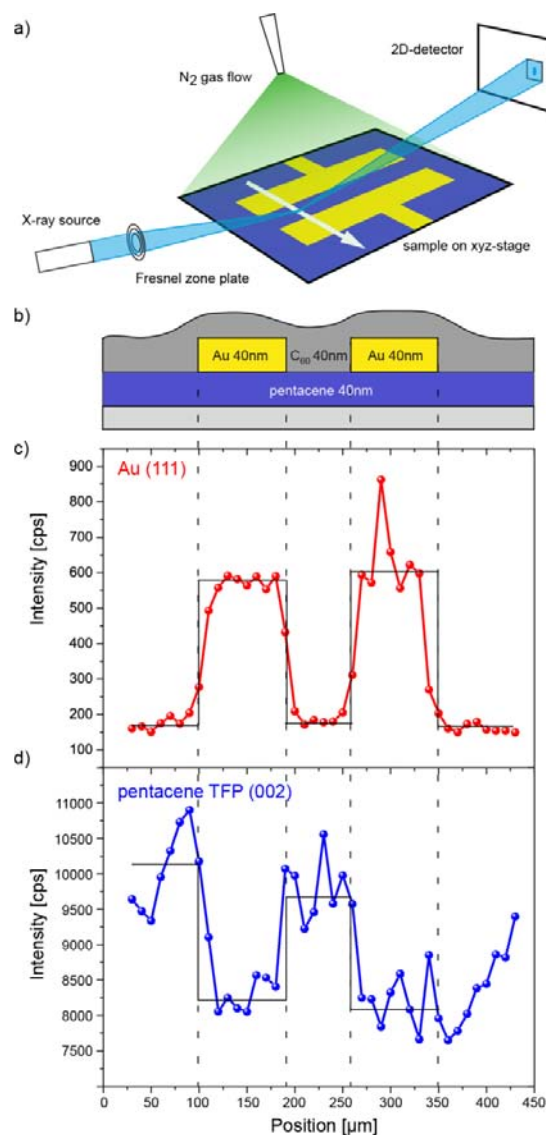


Figure 1. Schematic and X-ray line scans of an ambipolar pentacene-C₆₀ OFET. a) Sketch of the experiment geometry. b) Cross section of the sample geometry. c) Incident angle adjusted to the gold (111) Bragg condition. d) Incident angle adjusted to the pentacene TFP (002) Bragg condition.

As a representative sample for investigating the local polymorphic structure of organic thin films and to determine the potential of the setup to resolve sub-micron features, we investigated a pentacene thin film, which exhibits three different Bragg signatures from the thin-film phase [TFP (00L)], the bulk phase [BP (00L)] and the lying phase, as verified via X-ray reflectometry (Figure 2 a). The crystalline lying phase nucleates after a critical film thickness, which is strongly dependent

on the substrate temperature during the pentacene deposition (>100 nm at room temperature, 30 nm at 87 °C) [24,28]. In contrast, the coexistence of TFP and BP pentacene is induced by temperature dependent stress at the SiO₂ interface [5,6,22–24]. Here, we focus on this coexistence of TFP and BP pentacene. Using s-SNOM with a lateral resolution as small as 20 nm has shown that, in fact, the lateral distribution of TFP and BP pentacene exhibits ellipsoidal structures on a length scale of 100 nm [6]. However, the s-SNOM probes to a depth of typically 30–50 nm [29], whereas X-ray microdiffraction yields information of the whole depth of the film.

To resolve the intrinsic lateral distribution of TFP and BP pentacene, we recorded two 2D K-Maps of the same sector of the sample surface, one for each polymorph. To gain high lateral resolution, we used the piezoelectric motors to move the sample stage. The incident angle θ was set to 5.54° and 5.93°, which corresponded to a footprint of 3.10 μm and 2.90 μm at the TFP (003) and BP (003) Bragg condition, respectively. Choosing the (003) Bragg conditions therefore reduced the footprint by 33% compared to the (002) Bragg conditions. For this system, choosing higher order Bragg conditions led to an undesirable signal to noise ratio. The K-Maps were recorded with the incident beam along the slow scan direction. To image a lateral inhomogeneity with full resolution, the scan size was set to 40 μm and the motor steps were set to 500 nm in the fast scan direction and 1 μm in the slow scan direction.

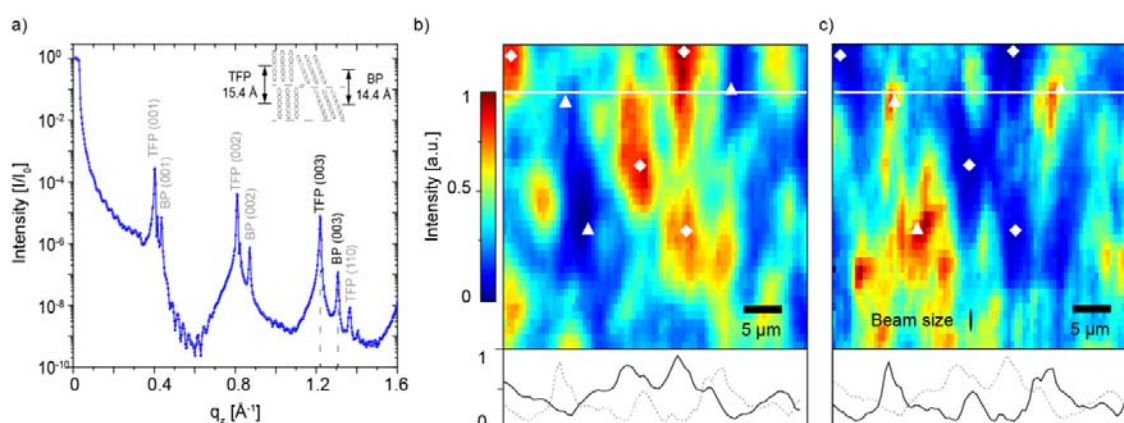


Figure 2. a) Wide (normal) beam X-ray reflectivity of a 60 nm thick pentacene film with the indicated Bragg series of TFP and BP pentacene. Inset shows a sketch of TFP and BP pentacene. b) and c) K-Maps of the microdiffraction X-ray intensity of the same sample area, measured at the TFP(003) and BP(003) Bragg condition, respectively. Diamonds and triangles indicate maxima in TFP and BP intensity, respectively. The continuous line profiles at the bottom correspond to the white section indicated in the map (the dashed lines compare the profile to the respective other phase).

We have blown the samples with dry nitrogen during all measurements to minimize radiation damage from reactive oxygen species, activated by hard X-rays in ambient air. During the short exposure times of the maps and scans shown here (typically several seconds per data point), we could not observe any beam damage for repeated measurements, i.e. loss of Bragg signal, and thus conclude that microdiffraction imaging is suited for investigating organic thin films. Recent test

measurements indicate that beam damage can be further minimized by using higher beam energies, i.e. at 20 keV exposure times of several minutes are possible.

As result, we obtained a map of the TFP and the BP distribution within the thin film [Figure 2 b) and c)]. The two K-Maps show a complementary intensity profile, revealing micron scaled domains exclusively grown in TFP (diamonds) and BP (triangles), respectively. This behavior can also be seen in the line profiles of TFP and BP pentacene. The elongated beam footprint indicated in Figure 2 c) leads to an overall smearing of the signal parallel to the beam direction.

4. Conclusion

We used microdiffraction imaging with a focused X-ray beam to study the structure of organic thin films. Within these films, we were able to resolve intrinsic structures as well as artificial structures, which are used to build organic electronic devices like multilayer ambipolar OFETs. We demonstrated a lateral resolution for organic thin films of 300 nm in the direction perpendicular to the beam and about 3 μm in the direction parallel to the beam. To acquire K-maps with the lateral resolution of the focus size in both directions, two subsequent K-Maps at the same sample position with a sample rotation of 90° would be needed. By further improving the focusing optics, ID01, for example, offers a beam size of 100 nm diameter after its upgrade in 2014 and it will be interesting to see, if this is confirmed in microdiffraction experiments.

Furthermore, changing the measurement geometry from reflection to transmission, could avoid the problem of large footprints parallel to the beam. This transmission geometry would require thinner substrates, e.g. sapphire [30] or ultra-thin Si_3N_4 membranes, which are commonly used for scanning transmission X-ray microscopy (STXM) [31,32].

Nevertheless, the current resolution is already well suited to study organic electronic devices, e.g. organic thin-film transistors, because the commonly used channel lengths of these devices are in the range of 20 μm to 50 μm . Furthermore, the local nanostructure of state of the art organic solar cells, fabricated by self-organization or nanoimprint [33], could also be examined, even with metallic contacts on top. X-ray microdiffraction therefore complements to other scanning techniques, like STXM [32], s-SNOM [6,16], scanning photoresponse microscopy [34], or micro-Raman spectroscopy [19], to gain a deeper understanding of fundamental device physics.

Acknowledgments

The authors gratefully acknowledge financial support from Deutsche Forschungsgemeinschaft through the SFB 1032 as well as by the Bavarian Ministry for Science through the initiative "Solar Technologies Go Hybrid" (SolTech). Parts of this research were carried out at the light source PETRA III at DESY, a member of the Helmholtz Association (HGF). We would like to thank Dr. O. H. Seeck for assistance in using beamline P08.

Conflict of Interest

The authors report no conflict of interests in this research.

References

1. Bredas JL, Beljonne D, Coropceanu V, et al. (2004) Charge-transfer and energy-transfer processes in pi-conjugated oligomers and polymers: A molecular picture. *Chem Rev* 104: 4971–5003.
2. He T, Stolte M, Burschka C, et al. (2015) Single-crystal field-effect transistors of new Cl2-NDI polymorph processed by sublimation in air. *Nat Commun* 6: 5954.
3. Tang Q, Zhang DQ, Wang SL, et al. (2009) A Meaningful Analogue of Pentacene: Charge Transport, Polymorphs, and Electronic Structures of Dihydrodiazapentacene. *Chem Mater* 21: 1400–1405.
4. Schiefer S, Huth M, Dobrinevski A, et al. (2007) Determination of the crystal structure of substrate-induced pentacene polymorphs in fiber structured thin films. *J Am Chem Soc* 129: 10316–10317.
5. Mattheus CC, Dros AB, Baas J, et al. (2003) Identification of polymorphs of pentacene. *Synth Met* 138: 475–481.
6. Westermeier C, Cernescu A, Amarie S, et al. (2014) Sub-micron phase coexistence in small-molecule organic thin films revealed by infrared nano-imaging. *Nat Commun* 5: 5101.
7. Durr AC, Schreiber F, Kelsch M, et al. (2002) Morphology and thermal stability of metal contacts on crystalline organic thin films. *Adv Mater* 14: 961–963.
8. Kahn A, Koch N, Gao WY (2003) Electronic structure and electrical properties of interfaces between metals and pi-conjugated molecular films. *J Polym Sci Part B Polym Phys* 41: 2529–2548.
9. Necliudov PV, Shur MS, Gundlach DJ, et al. (2003) Contact resistance extraction in pentacene thin film transistors. *Solid State Electron* 47: 259–262.
10. Klauk H, (2006) *Organic Electronics: Materials, Manufacturing, and Applications*, 1 Eds., Wiley-VCH.
11. Dam HF, Andersen TR, Pedersen EBL, et al. (2015) Enabling flexible polymer tandem solar cells by 3D ptychographic imaging. *Adv Energy Mater* 5: 1400736.
12. Fuller T, Banhart F (1996) In situ observation of the formation and stability of single fullerene molecules under electron irradiation. *Chem Phys Lett* 254: 372–378.
13. Tolan M, (2013) *X-Ray Scattering from Soft-Matter Thin Films: Materials Science and Basic Research*, Springer.
14. Fritz SE, Martin SM, Frisbie CD, et al. (2004) Structural characterization of a pentacene monolayer on an amorphous SiO₂ substrate with grazing incidence X-ray diffraction. *J Am Chem Soc* 126: 4084–4085.
15. Noever SJ, Fischer S, Nickel B (2013) Dual Channel Operation Upon n-Channel Percolation in a Pentacene-C₆₀ Ambipolar Organic Thin Film Transistor. *Adv Mater* 25: 2147–2151.
16. Qazilbash MM, Tripathi A, Schafgans AA, et al. (2011) Nanoscale imaging of the electronic and structural transitions in vanadium dioxide. *Phys Rev B* 83: 165108.
17. Chahine GA, Richard MI, Homs-Regojo RA, et al. (2014) Imaging of strain and lattice orientation by quick scanning X-ray microscopy combined with three-dimensional reciprocal space mapping. *J Appl Crystallogr* 47: 762–769.
18. Chahine GA, Zoellner MH, Richard M-I, et al. (2015) Strain and lattice orientation distribution in SiN/Ge complementary metal–oxide–semiconductor compatible light emitting microstructures by quick x-ray nano-diffraction microscopy. *Appl Phys Lett* 106: 071902.

19. Zoellner MH, Richard M-I, Chahine GA, et al. (2015) Imaging Structure and Composition Homogeneity of 300 nm SiGe Virtual Substrates for Advanced CMOS Applications by Scanning X-ray Diffraction Microscopy. *ACS Appl Mater Interfaces* 7: 9031–9037.
20. Paci B, Bailo D, Albertini VR, et al. (2013) Spatially-resolved in-situ structural study of organic electronic devices with nanoscale resolution: the plasmonic photovoltaic case study. *Adv Mater* 25: 4760–4765.
21. Reich C, Hochrein MB, Krause B, et al. (2005) A microfluidic setup for studies of solid-liquid interfaces using x-ray reflectivity and fluorescence microscopy. *Rev Sci Instrum* 76.
22. Dimitrakopoulos CD, Brown AR, Pomp A (1996) Molecular beam deposited thin films of pentacene for organic field effect transistor applications. *J Appl Phys* 80: 2501–2508.
23. Knipp D, Street RA, Volkel A, et al. (2003) Pentacene thin film transistors on inorganic dielectrics: Morphology, structural properties, and electronic transport. *J Appl Phys* 93: 347–355.
24. Yanagisawa H, Tamaki T, Nakamura M, et al. (2004) Structural and electrical characterization of pentacene films on SiO₂ grown by molecular beam deposition. *Thin Solid Films* 464: 398–402.
25. Seck OH, Deiter C, Pflaum K, et al. (2012) The high-resolution diffraction beamline P08 at PETRA III. *J Synchrotron Radiat* 19: 30–38.
26. Ponchut C, Rigal JM, Clément J, et al. (2011) MAXIPIX, a fast readout photon-counting X-ray area detector for synchrotron applications. *J Instrum* 6: C01069.
27. Kaefer D, Ruppel L, Witte G (2007) Growth of pentacene on clean and modified gold surfaces. *Phys Rev B* 75.
28. Bouchoms IPM, Schoonveld WA, Vrijmoeth J, et al. (1999) Morphology identification of the thin film phases of vacuum evaporated pentacene on SiO₂ substrates. *Synth Met* 104: 175–178.
29. Govyadinov AA, Mastel S, Golmar F, et al. (2014) Recovery of Permittivity and Depth from Near-Field Data as a Step toward Infrared Nanotomography. *ACS Nano* 8: 6911–6921.
30. Seiki N, Shoji Y, Kajitani T, et al. (2015) Rational synthesis of organic thin films with exceptional long-range structural integrity. *Science* 348: 1122–1126.
31. Collins BA, Cochran JE, Yan H, et al. (2012) Polarized X-ray scattering reveals non-crystalline orientational ordering in organic films. *Nat Mater* 11: 536–543.
32. Hub C, Burkhardt M, Halik M, et al. (2010) In situ STXM investigations of pentacene-based OFETs during operation. *J Mater Chem* 20: 4884–4887.
33. Weickert J, Dunbar RB, Hesse HC, et al. (2011) Nanostructured Organic and Hybrid Solar Cells. *Adv Mater* 23: 1810–1828.
34. Westermeier C, Fiebig M, Nickel B (2013) Mapping of trap densities and hotspots in pentacene thin-film transistors by frequency-resolved scanning photoresponse microscopy. *Adv Mater* 25: 5719–5724.



AIMS Press

© 2015 Bert Nickel, et al. licensee AIMS Press. This is an open access article distributed under the terms of the Creative Commons Attribution License (<http://creativecommons.org/licenses/by/4.0>)

A.5 α, ω -DIHEXYL-SEXITHIOPHENE THIN FILMS FOR SOLUTION-GATED ORGANIC FIELD-EFFECT TRANSISTORS

Hannah Schamoni, Simon Noever, Bert Nickel, Martin Stutzmann, and Jose A. Garrido

Applied Physics Letters 2016, Vol. 108, No. 7, 073301

DOI: [10.1063/1.4942407](https://doi.org/10.1063/1.4942407)

Abstract

While organic semiconductors are being widely investigated for applications requiring an aqueous environment, such as chemical and biochemical sensing, some major drawbacks have not yet been solved to complete satisfaction. These are in particular the rather poor device stability and low charge carrier mobility. In this work, solution-gated organic field-effect transistors (SGOFETs) based on the molecule α, ω -dihexyl-sexithiophene (DH6T), which is reported to exhibit favorable properties in terms of field-effect mobility and structural order, are presented as promising platforms for in electrolyte sensing. To this end, thin films of DH6T were investigated with regard to the influence of the substrate temperature during deposition on the grain size and structural order. We have found that the performance of SGOFETs can be enhanced by choosing suitable growth parameters that lead to a two-dimensional film morphology and a high degree of structural order. Furthermore, the capability of the SGOFETs to detect changes in the pH or ionic strength of the gate electrolyte is demonstrated and successfully simulated with the help of theoretical models. Finally, excellent transistor stability is confirmed by continuously operating the device over a period of several days, which is a consequence of the low threshold voltage of DH6T-based SGOFETs. Altogether, our results demonstrate the feasibility of high performance and highly stable organic semiconductor devices for chemical or biochemical applications.

Contribution

The temperature dependence of DH6T thin film growth was essential to finding optimum parameters for the application in sensing devices. I provided structural X-ray analysis of the films and could thereby discover temperature dependence of the out of plane thin film lattice constant.



α,ω -dihexyl-sexithiophene thin films for solution-gated organic field-effect transistors

Hannah Schamoni,¹ Simon Noever,² Bert Nickel,² Martin Stutzmann,¹
and Jose A. Garrido^{3,4,a)}

¹Walter Schottky Institut and Physik-Department, Technische Universität München, Am Coulombwall 4,
85748 Garching, Germany

²Fakultät für Physik und CeNS, Ludwig-Maximilians-Universität München, Geschwister-Scholl-Platz 1,
80539 München, Germany

³Catalan Institute of Nanoscience and Nanotechnology (ICN2), CSIC and The Barcelona Institute of Science
and Technology, Campus UAB, Bellaterra, 08193 Barcelona, Spain

⁴ICREA, Institució Catalana de Recerca i Estudis Avançats, 08070 Barcelona, Spain

(Received 30 July 2015; accepted 8 February 2016; published online 19 February 2016)

While organic semiconductors are being widely investigated for chemical and biochemical sensing applications, major drawbacks such as the poor device stability and low charge carrier mobility in aqueous electrolytes have not yet been solved to complete satisfaction. In this work, solution-gated organic field-effect transistors (SGOFETs) based on the molecule α,ω -dihexyl-sexithiophene (DH6T) are presented as promising platforms for in-electrolyte sensing. Thin films of DH6T were investigated with regard to the influence of the substrate temperature during deposition on the grain size and structural order. The performance of SGOFETs can be improved by choosing suitable growth parameters that lead to a two-dimensional film morphology and a high degree of structural order. Furthermore, the capability of the SGOFETs to detect changes in the pH or ionic strength of the gate electrolyte is demonstrated and simulated. Finally, excellent transistor stability is confirmed by continuously operating the device over a period of several days, which is a consequence of the low threshold voltage of DH6T-based SGOFETs. Altogether, our results demonstrate the feasibility of high performance and highly stable organic semiconductor devices for chemical or biochemical applications. © 2016 AIP Publishing LLC. [<http://dx.doi.org/10.1063/1.4942407>]

Organic semiconductors offer the possibility to fabricate devices featuring biocompatibility,^{1,2} mechanical flexibility,³⁻⁵ and comparably low production costs.^{1,2} Therefore, a wide range of applications employing organic semiconductors is being currently explored in the fields of biosensing and biomedical technologies.⁶⁻⁸ Among other molecules, oligothiophenes have been studied intensively for their suitability to be applied in field-effect transistors.⁹⁻¹⁷ In the case of solution-gated organic field-effect transistors (SGOFETs), the organic semiconductor is gated through an electrolyte. An electrical double layer, characterized by a rather high interfacial capacitance, builds up at the semiconductor-liquid interface. Consequently, the applied gate bias voltage may be kept well under 1 V,¹⁸⁻²⁰ leading to an improved device stability and the possibility of in-electrolyte applications.^{8,16,17,21,22} Using α -sexithiophene (6T) as active material, biofunctional sensors for the detection of penicillin have been demonstrated previously.¹⁷ However, the stability of the device strongly depends on the characteristics of the employed organic molecules. It is, therefore, of utmost importance to explore the use of molecules which could eventually lead to an improved device stability.

In this work, we report on the implementation of the end-substituted molecule α,ω -dihexyl-sexithiophene (DH6T) in SGOFETs. DH6T has been reported to exhibit favorable properties like an improved structural order in thin films and

an increased field-effect mobility as compared to the unsubstituted 6T.^{23,24} Here, we demonstrate the influence of the substrate temperature during deposition on the morphology and structural order of the thin film by atomic force microscopy (AFM), X-ray reflectivity (XRR), and UV-Vis spectroscopy. Furthermore, we characterize SGOFETs based on DH6T with regard to transistor performance and stability, and we reveal their sensitivity towards changes in the pH and ionic strength of the gate electrolyte.

Organic thin films of DH6T (nominal thickness: 30 nm) were deposited on sapphire substrates by organic molecular beam deposition in an ultrahigh vacuum system as described previously.^{16,17} In order to tune the morphology of the deposited films, the temperature of the sapphire substrate T_{sub} during thin film deposition was varied between room temperature (19 °C) and 55 °C. Typical deposition rates are between 0.5 and 2 Å/min. The fabrication details of the SGOFETs (width-to-length ratio of the transistor channel: $W/L = 4900$) have been described elsewhere^{16,17} and remained unchanged in this work, except for the contact thickness (5 nm Ti/45 nm Au). All measurements were carried out in ambient atmosphere. The transistor and stability characterization and the ion sensing experiments were performed in a 5 mM phosphate buffered saline (PBS) solution at pH 5. To change the ionic strength, KCl solution was added to the buffer. For the pH sensing measurements, a 10 mM PBS solution, whose ionic strength was adjusted to 50 mM with KCl (KPBS), was used. The pH was altered by adding either HCl or KOH solution. The gate voltage was applied via an Ag/AgCl reference electrode in all cases.

^{a)}Author to whom correspondence should be addressed. Electronic mail: joseantonio.garrido@icn.cat

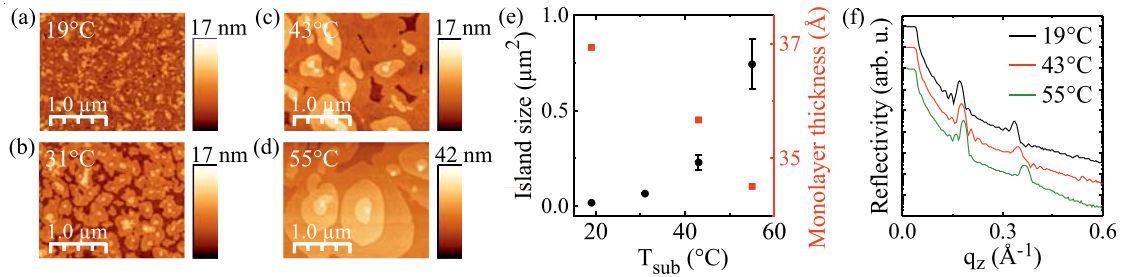
073301-2 Schamoni *et al.*Appl. Phys. Lett. **108**, 073301 (2016)

FIG. 1. Characterization of nominally 30 nm thick DH6T thin films deposited at different substrate temperatures. (a) AFM micrographs for $T_{sub} = 19^\circ\text{C}$ (room temperature), (b) $T_{sub} = 31^\circ\text{C}$, (c) $T_{sub} = 43^\circ\text{C}$, and (d) $T_{sub} = 55^\circ\text{C}$. (e) Average size of the grains versus T_{sub} as extracted from AFM images (black dots) and monolayer thickness in the thin films (red squares) as a function of T_{sub} . The latter was calculated from the position of the first order peak in the X-ray reflectivity spectra of the deposited DH6T films (f).

The temperature of the sapphire substrate T_{sub} was varied and its influence on the morphology of the DH6T layers was investigated. As the AFM micrographs in Figures 1(a)–1(d) illustrate, the grains are larger and exhibit a more three-dimensional topography for higher temperatures. This is understood in terms of an extended diffusion length of molecules with rising temperatures on the substrate surface.²⁵ A quantitative analysis of the average island size for different values of T_{sub} is shown in Figure 1(e) (black dots).

To investigate possible changes in the thin film structure itself, XRR spectra were recorded for films deposited at different T_{sub} (see Figure 1(f)). Garnier *et al.* have reported a monoclinic unit cell in DH6T thin films with an angle $\beta = 111.3^\circ$ and a tilt angle between core and side chains of 16° , leading to an effective molecule length of 38.1 \AA .²³ The theoretical value of the monolayer thickness thereby calculates to 35.5 \AA . From the position of the first order peak, q_1 , the monolayer thickness d of the investigated thin films can be calculated via $d = 2\pi/q_1$. As illustrated in Figure 1(e) (red squares), it lies in the expected range; however, a decrease in the monolayer thickness with increasing T_{sub} is observed, which may be due to a change in the tilt angle of the DH6T molecules towards the substrate surface normal. In addition, the first order peak in the XRR spectra becomes more intense with increasing substrate temperature (see Figures S1(a) and S1(b) (Ref. 26)), indicating a higher degree of structural order in these thin films, as discussed in the following.

Additional information related to the structural order can be obtained from UV-Vis spectroscopy. Absorption spectra of DH6T thin films deposited at various T_{sub} are depicted in Figure 2(a). These are normalized to the intensity of the most prominent peak at about 3.3 eV, which corresponds to the HOMO \rightarrow LUMO transition of molecules for which the interaction with neighboring molecules leads to a Davydov splitting of the LUMO.^{27,28} This absorption peak is most intense and narrow, if the transition dipoles of all molecules are aligned in parallel. The normalized spectra illustrate a change in the shape of this peak with T_{sub} , suggesting a change in the interaction between molecules in the thin film. The quantitative analyses of the average peak intensity and full width at half maximum (FWHM) (Figure 2(b)) reveal an increase in the peak intensity and a decrease in the FWHM with increasing T_{sub} (see Figure S2(a) for non-normalized spectra²⁶). These findings indicate an increase in

the degree of structural order of the thin films for higher substrate temperatures, in agreement with the XRR data presented above. In contrast, no dependence on T_{sub} was found for the intensity of the peak at 4.3 eV (see Figure S2(b) (Ref. 26)). Such a peak has already been observed for thin films of oligothiophenes of various conjugation core lengths and with different substituents and is attributed to the absorption of a single thiophene unit.²⁹ Its independence of T_{sub} originates from the molecular character of the corresponding transition, as opposed to the crystalline HOMO \rightarrow LUMO transition located at 3.3 eV.

DH6T thin films were used as the active material in SGOFETs, the layout of which is sketched in Figure 3(a). The Ti/Au contact pattern was predefined by photolithography, deposited via thermal evaporation and partly covered by a photoresist prior to the organic thin film growth. Exemplary transistor output curves in a 5 mM PBS buffer at pH 5 are shown in Figure 3(b). They show a current level of several $10 \mu\text{A}$ and saturation behavior for high drain-source voltages. Furthermore, the gate-source current is three orders of magnitude smaller than I_{DS} , and cyclic voltammetry measurements show no indication of Faradaic processes in the potential window of the SGOFETs (see Figures S3(a) and 3(b) (Ref. 26)). Therefore, we can conclude that the current modulation is dominated by the field-effect, in agreement with previous reports.^{20,30} From the transfer curve at a drain-source voltage $U_{DS} = -50 \text{ mV}$ (black dots in Figure 3(c)), a

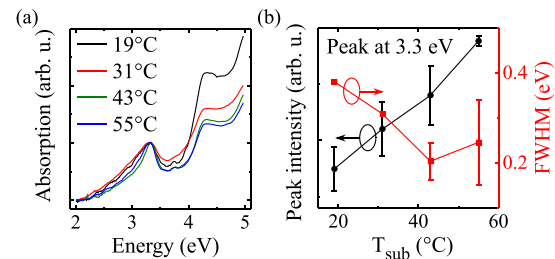


FIG. 2. Optical characterization by UV-Vis spectroscopy of 30 nm thick DH6T films deposited at different substrate temperatures. (a) Absorption spectra, normalized by the intensity of the peak at 3.3 eV. (b) Average peak intensity (black dots) and FWHM (red squares) of the same peak as a function of T_{sub} . The lines were added as a visual guidance. The error bars represent the standard error of the mean values.

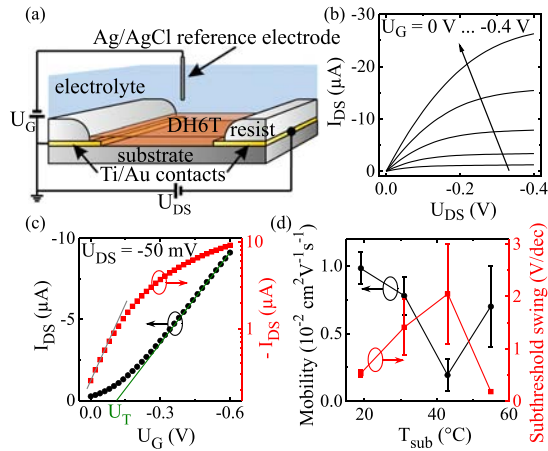
073301-3 Schamoni *et al.*Appl. Phys. Lett. **108**, 073301 (2016)

FIG. 3. Electrical characterization of SGOFETs using 30 nm thick films of DH6T as the active material. The measurements were conducted in 5 mM PBS at pH 5. (a) Device layout. The width-to-length ratio is 4900. (b) Typical output characteristics and (c) corresponding transfer curve at $U_{DS} = -50$ mV on a linear (black dots) and logarithmic scale (red squares). Linear fits to the data are represented by the solid lines and the threshold voltage U_T is indicated. The DH6T thin film of this sample was deposited at $T_{sub} = 19^\circ\text{C}$. (d) Field-effect mobility (black dots) and subthreshold swing (red squares) versus T_{sub} as extracted from the transfer curves. The lines were added as a visual guidance. The error bars represent the standard error of the mean values (see supplementary material²⁶).

transconductance $g_m = 18 \mu\text{S}$ was obtained, which can be used to determine the field-effect mobility μ via $\mu = g_m / (C_{dl} U_{DS}) L/W$. In this equation, C_{dl} is the electrical double layer capacitance of the semiconductor-electrolyte interface, which was estimated to $4 \mu\text{F}/\text{cm}^2$ via electrochemical impedance spectroscopy (see Figure S4 (Ref. 26)). This compares well to the interfacial capacitances of other solution-gated organic field effect transistor systems.^{16,31,32} From the maximum transconductance of the devices, we can estimate a field-effect mobility of up to about $1 \times 10^{-2} \text{ cm}^2/\text{V s}$ for the discussed set of transistors (Figure 3(d)) and of up to $1.9 \times 10^{-2} \text{ cm}^2/\text{V s}$ for devices which organic thin film was deposited at different rates. It is worth noting that the threshold voltage U_T of about -0.1 V is significantly lower than what has been reported for 6T-based SGOFETs of the same layout ($U_T \lesssim -0.3$ V).^{16,17} Such a low U_T might be due to favorable values of, for example, C_{dl} , the surface charge of the semiconductor or the work function of the DH6T molecules.³³ Above all, it enables the operation of the SGOFETs at low voltages, which is of utmost importance for a good device stability.^{8,16,17} To additionally characterize the current onset of the transistors, the subthreshold swing was extracted from a logarithmic plot of the transfer curve (red squares in Figure 3(c)). Its theoretical limit at room temperature is $60 \text{ mV}/\text{dec}$.³⁴ Values as low as $160 \text{ mV}/\text{dec}$ confirm a fast switching behavior of our devices. The deviation from the theoretical limit may result from defect states at the semiconductor-electrolyte interface or from the chosen device geometry.³⁴

Furthermore, the influence of the morphology of the thin films on the transistor characteristics was studied by evaluating field-effect mobility and subthreshold swing as a

function of the substrate temperature during deposition. Figure 3(d) (black dots) illustrates that the best performance was observed at the lowest and highest temperature. This possibly indicates two competing effects: On the one hand, the films are more two-dimensional at low T_{sub} (cf. Figures 1(a)–1(e)), which enhances charge transport and, thus, the field-effect mobility.³⁵ On the other hand, the analysis of the structural properties suggests an improved degree of ordering at high T_{sub} . An increase in structural order has also been reported for α,ω -DH6T thin films in comparison to films of β,β' -DH6T or unsubstituted 6T, and it has been correlated to an increase in field-effect mobility.²³ Thus, the anew increase in mobility at high T_{sub} may presumably be attributed to an improvement of the structural order in the film. As Figure 3(d) (red squares) further illustrates, the subthreshold swing confirms this interpretation: a faster on-switching of the SGOFETs (low subthreshold swing values) is enabled by a two-dimensional film morphology (lowest T_{sub}) and a high degree of structural order (highest T_{sub}). Nevertheless, it has to be noted that the effect of T_{sub} on the thin film is more pronounced for the increase from room temperature to 43°C than for the change from 43°C to 55°C (cf. Figures 1(a)–1(d)). More data statistics will be needed in order to verify the observed trend in μ and in the subthreshold swing (cf. Figure 3(d); see Figure S5 for a visualization of the statistics of μ used in this work²⁶). From the correlation of the subthreshold swing with both the defect density and the field-effect mobility, it may also be concluded that the good transistor performance is the result of a low defect density.

The capability of the DH6T-based SGOFETs to be applied as sensors in aqueous electrolytes, in this particular case as pH sensors, is demonstrated in Figure 4(a). With decreasing pH of the buffer solution, the transfer curves shift to more negative gate voltages, while g_m stays unchanged. Therefore, the pH sensitivity is given by the change in gate voltage U_G per pH with respect to U_G at neutral pH for a fixed value of the drain-source current I_{DS} . U_G experiences a linear dependence over a wide pH range without any hysteresis between decreasing and increasing pH, yielding a sensitivity of $14 \text{ mV}/\text{pH}$. According to the amphifunctional model, which is described in detail in the supplementary material,²⁶ the response of the transistor originates from a pH-dependent surface charge σ_{surf} at the semiconductor-electrolyte interface.³⁶ In order to obtain a good match between experimental data and a simulation using the amphifunctional model (blue line in Figure 4(b)), a monolayer coverage with hydroxide ions and an ionizable surface group of $pK_a 3.3$ have to be assumed. The latter group can be ascribed to oxygen-related moieties.¹⁷ These findings are in agreement with those by Buth *et al.* for devices using 6T as organic semiconductor.¹⁷

Besides the study of the pH sensitivity, the sensitivity of the devices to changes in the ionic strength was investigated by adding KCl to the solution. In Figure 4(c), the corresponding change in U_G for a fixed value of I_{DS} is plotted logarithmically versus the salt activity for two different pH values of the buffer. The ion sensitivity is defined as the slope of the linear fit to the curves at high activity ($a \gtrsim 50 \text{ mmol}/\text{kg}$), yielding values of $-42 \text{ mV}/\text{dec}$ at pH 5 and $-30 \text{ mV}/\text{dec}$ at pH 3 for the presented SGOFET. The ion sensitivity has been

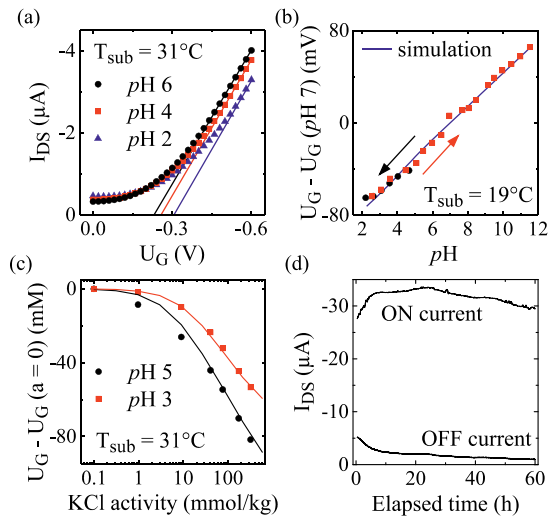
073301-4 Schamoni *et al.*Appl. Phys. Lett. **108**, 073301 (2016)

FIG. 4. Sensing and stability properties of SGOFETs. (a) Transfer curves recorded at three different pH values of the KPBS buffer. The solid lines represent fits to the linear regions. (b) Shift of U_G as a function of the pH of the electrolyte, together with a simulation of the data using the amphifunctional model. (c) Shift of U_G (compared to U_G at a salt activity $a = 0$ mM) as a function of the activity of KCl in the PBS buffer, which pH was adjusted to two different values. The solid lines represent simulations of the experimental data using the amphifunctional model. The substrate temperatures at which the DH6T thin films used in (a)–(c) were deposited are indicated in the graphs. (d) Evolution of the drain-source current I_{DS} during continuous cycling of U_G between 0 V and -0.6 V for $U_{DS} = -0.2$ V, measured in 5 mM PBS at pH 5 and in the dark (deposition temperature of the DH6T thin film: $T_{sub} = 31$ °C). For clarity, only the maxima (ON current) and minima (OFF current) of the measured curve are shown in the graph.

interpreted in terms of the screening of the surface charge due to an increase in the diffuse charge.³⁷ If the surface charge is more negative, i.e., if the buffer is less acidic, the ion screening is more effective, which is confirmed by the higher sensitivity at pH 5 as compared to pH 3. Using a model similar to the amphifunctional model introduced by Härtl *et al.*,³⁷ the experimental data could be reproduced (solid lines in Figure 4(c)) assuming surface charges of $-5.6 \mu\text{C}/\text{cm}^2$ at pH 5 and $-3.5 \mu\text{C}/\text{cm}^2$ at pH 3, respectively, in agreement with the calculations by Buth *et al.* for 6T-SGOFETs.¹⁶

For applications of organic SGOFETs, the device stability during operation is of vital importance. A stability test was performed by switching on and off the SGOFETs continuously. To this end, the gate voltage was cycled between 0 V and -0.6 V for approximately 60 h, while applying a constant drain-source voltage of -0.2 V and recording the drain-source current. Here, the high current level decreased by only 10% with respect to the value after the initial increase in on-current (Figure 4(d)). The latter has been reported before by Roberts *et al.* for organic field-effect transistors immersed into an aqueous environment.^{38,39} However, in contrast to the work by Roberts *et al.*, we observed a slight decrease in the off-current over time (see Figure 4(d)). As the transconductance of the respective device increased from $13 \mu\text{S}$ to $16 \mu\text{S}$ throughout the measurement and the subthreshold swing was reduced from about 550 mV/dec to 230 mV/dec, both changes may possibly be attributed to the passivation of trap states at

the semiconductor-electrolyte interface by water molecules penetrating into the thin film.³⁴

In summary, vacuum-evaporated thin films of the organic semiconductor DH6T were investigated by AFM, XRR, and UV-Vis spectroscopy. We could show that with increasing substrate temperature, the films exhibit an increasingly three-dimensional topography and feature a higher degree of structural order. At the same time, the tilt angle of the molecules towards the substrate surface normal appears to increase. Furthermore, we have fabricated and characterized SGOFETs using these thin films as the active material. The obtained characteristics are comparable to or even exceed those of analogous devices based on 6T.^{16,17} In particular, the low threshold voltage is beneficial for a good transistor stability. Field-effect mobility and subthreshold swing were found to be correlated to the morphology and structural order of the films. This implies that the transistor performance can, to some extent, be tuned by the substrate temperature. Additionally, both pH and ion sensitivity of the SGOFETs were demonstrated, and the data could be simulated using suitable modifications of the amphifunctional model.^{16,17,36,37} Finally, a good device stability was confirmed by switching it on and off continuously over a period of 60 h. The initial increase in the on-off ratio was tentatively attributed to the passivation of trap states at the semiconductor-electrolyte interface by water molecules. During the period of 60 h, the current level decreased by only 10%. In conclusion, SGOFETs based on DH6T are promising platforms for stable in-electrolyte sensing applications. By carefully choosing the growth parameters of the organic thin film, the performance may possibly be further improved.

This work has been partially supported by the Nanosystems Initiative Munich (NIM) and the Deutsche Forschungsgemeinschaft (DFG) through the SFB 1032.

- ¹M. Irimia-Vladu, P. A. Troshin, M. Reisinger, L. Shmygleva, Y. Kanbur, G. Schwabegger, M. Bodea, R. Schwdiauer, A. Mumyatov, J. W. Fergus, V. F. Razumov, H. Sitter, N. S. Sariciftci, and S. Bauer, *Adv. Funct. Mater.* **20**, 4069 (2010).
- ²G. Scarpa, A.-L. Idzko, S. Götz, and S. Thalhammer, *Macromol. Biosci.* **10**, 378 (2010).
- ³T. Someya, T. Sekitani, S. Iba, Y. Kato, H. Kawaguchi, and T. Sakurai, *Proc. Natl. Acad. Sci.* **101**, 9966 (2004).
- ⁴S. Richter, M. Ploetner, W.-J. Fischer, M. Schneider, P.-T. Nguyen, W. Plieth, N. Kiriy, and H.-J. Adler, *Thin Solid Films* **477**, 140 (2005).
- ⁵D. Feili, M. Schuettler, T. Doerge, S. Kammer, K. P. Hoffmann, and T. Stieglitz, *J. Micromech. Microeng.* **16**, 1555 (2006).
- ⁶C. Bartic, B. Palan, A. Campitelli, and G. Borghs, *Sens. Actuators, B* **83**, 115 (2002).
- ⁷T. Someya, A. Dodabalapur, J. Huang, K. C. See, and H. E. Katz, *Adv. Mater.* **22**, 3799 (2010).
- ⁸L. Kergoat, B. Piro, M. Berggren, M.-C. Pham, A. Yassar, and G. Horowitz, *Org. Electron.* **13**, 1 (2012).
- ⁹A. Tsumura, H. Koezuka, and T. Ando, *Appl. Phys. Lett.* **49**, 1210 (1986).
- ¹⁰H. Akimichi, K. Waragai, S. Hotta, H. Kano, and H. Sakaki, *Appl. Phys. Lett.* **58**, 1500 (1991).
- ¹¹Z. Bao, A. Dodabalapur, and A. J. Lovinger, *Appl. Phys. Lett.* **69**, 4108 (1996).
- ¹²R. Hajlaoui, D. Fichou, G. Horowitz, B. Nessakh, M. Constant, and F. Garnier, *Adv. Mater.* **9**, 557 (1997).
- ¹³C. D. Dimitrakopoulos, B. K. Furman, T. Graham, S. Hegde, and S. Purushothaman, *Synth. Met.* **92**, 47 (1998).

073301-5 Schamoni *et al.*Appl. Phys. Lett. **108**, 073301 (2016)

- ¹⁴M. Halik, H. Klauk, U. Zschieschang, G. Schmid, S. Ponomarenko, S. Kirchmeyer, and W. Weber, *Adv. Mater.* **15**, 917 (2003).
- ¹⁵A. Facchetti, M. Mushrush, M.-H. Yoon, G. R. Hutchison, M. A. Ratner, and T. J. Marks, *J. Am. Chem. Soc.* **126**, 13859 (2004).
- ¹⁶F. Buth, D. Kumar, M. Stutzmann, and J. A. Garrido, *Appl. Phys. Lett.* **98**, 153302 (2011).
- ¹⁷F. Buth, A. Donner, M. Sachsenhauser, M. Stutzmann, and J. A. Garrido, *Adv. Mater.* **24**, 4511 (2012).
- ¹⁸M. J. Panzer, C. R. Newman, and C. D. Frisbie, *Appl. Phys. Lett.* **86**, 103503 (2005).
- ¹⁹L. Herlogsson, X. Crispin, N. D. Robinson, M. Sandberg, O.-J. Hagel, G. Gustafsson, and M. Berggren, *Adv. Mater.* **19**, 97 (2007).
- ²⁰M. J. Panzer and C. D. Frisbie, *J. Am. Chem. Soc.* **129**, 6599 (2007).
- ²¹B. Baur, J. Howgate, H.-G. von Ribbeck, Y. Gawlina, V. Bandalo, G. Steinhoff, M. Stutzmann, and M. Eickhoff, *Appl. Phys. Lett.* **89**, 183901 (2006).
- ²²H. U. Khan, J. Jang, J.-J. Kim, and W. Knoll, *J. Am. Chem. Soc.* **133**, 2170 (2011).
- ²³F. Garnier, A. Yassar, R. Hajlaoui, G. Horowitz, F. Deloffre, B. Servet, S. Ries, and P. Alnot, *J. Am. Chem. Soc.* **115**, 8716 (1993).
- ²⁴B. Servet, G. Horowitz, S. Ries, O. Lagorsse, P. Alnot, A. Yassar, F. Deloffre, P. Srivastava, and R. Hajlaoui, *Chem. Mater.* **6**, 1809 (1994).
- ²⁵R. Ruiz, D. Choudhary, B. Nickel, T. Toccoli, K.-C. Chang, A. C. Mayer, P. Clancy, J. M. Blakely, R. L. Headrick, S. Iannotta, and G. G. Malliaras, *Chem. Mater.* **16**, 4497 (2004).
- ²⁶See supplementary material at <http://dx.doi.org/10.1063/1.4942407> for an evaluation of the peak intensity in the XRR spectra, non-normalized UV-Vis spectra, gate-source current and cyclic voltammetry data, electrochemical impedance spectroscopy data, the statistics of the field-effect mobility data, and a detailed description of the amphifunctional model.
- ²⁷A. Yassar, G. Horowitz, P. Valat, V. Wintgens, M. Hmyene, F. Deloffre, P. Srivastava, P. Lang, and F. Garnier, *J. Phys. Chem.* **99**, 9155 (1995).
- ²⁸M. Muccini, E. Lunedei, C. Taliani, D. Beljonne, J. Cornil, and J. L. Brédas, *J. Chem. Phys.* **109**, 10513 (1998).
- ²⁹A. Facchetti, M.-H. Yoon, C. L. Stern, G. R. Hutchison, M. A. Ratner, and T. J. Marks, *J. Am. Chem. Soc.* **126**, 13480 (2004).
- ³⁰G. Tarabella, C. Santato, S. Y. Yang, S. Iannotta, G. G. Malliaras, and F. Cicoira, *Appl. Phys. Lett.* **97**, 123304 (2010).
- ³¹L. Kergoat, L. Herlogsson, D. Braga, B. Piro, M.-C. Pham, X. Crispin, M. Berggren, and G. Horowitz, *Adv. Mater.* **22**, 2565 (2010).
- ³²L. H. Hess, M. V. Hauf, M. Seifert, F. Speck, T. Seyller, M. Stutzmann, I. D. Sharp, and J. A. Garrido, *Appl. Phys. Lett.* **99**, 033503 (2011).
- ³³R. Schroeder, L. A. Majewski, and M. Grell, *Appl. Phys. Lett.* **83**, 3201 (2003).
- ³⁴S. M. Sze and K. K. Ng, *Physics of Semiconductor Devices*, 3rd ed. (Wiley-Interscience, Hoboken and N.J., 2007).
- ³⁵J. Locklin, M. E. Roberts, S. C. B. Mannsfeld, and Z. Bao, *J. Macromol. Sci., Part C: Polym. Rev.* **46**, 79 (2006).
- ³⁶J. Duval, J. Lyklema, J. M. Kleijn, and H. P. van Leeuwen, *Langmuir* **17**, 7573 (2001).
- ³⁷A. Härtl, J. A. Garrido, S. Nowy, R. Zimmermann, C. Wemer, D. Horinek, R. Netz, and M. Stutzmann, *J. Am. Chem. Soc.* **129**, 1287 (2007).
- ³⁸M. E. Roberts, S. C. B. Mannsfeld, N. Queralto, C. Reese, J. Locklin, W. Knoll, and Z. Bao, *Proc. Natl. Acad. Sci.* **105**, 12134 (2008).
- ³⁹M. E. Roberts, S. C. B. Mannsfeld, M. L. Tang, and Z. Bao, *Chem. Mater.* **20**, 7332 (2008).

A.6 CHROMIUM/SCANDIUM MULTILAYER MIRRORS FOR ISOLATED ATTOSECOND PULSES AT 145 eV

Alexander Guggenmos, Michael Jobst, Marcus Ossiander, Stefan Radünz, Johann Riemensberger, Martin Schäffer, Ayman Akil, Clemens Jakubeit, Philip Böhm, Simon Noever, Bert Nickel, Reinhard Kienberger, And Ulf Kleineberg

Optical Letters 2015, Vol. 40, No. 12, 2846-2849

DOI: [10.1364/OL.40.002846](https://doi.org/10.1364/OL.40.002846)

Abstract

Recent advances in the development of attosecond soft x-ray sources toward photon wavelengths below 10 nm are also driving the development of suited broadband multilayer optics for steering and shaping attosecond pulses. We demonstrate that current attosecond experiments in the sub-200-eV range benefit from these improved optics. We present our achievements in utilizing ion-beam-deposited chromium/scandium (Cr/Sc) multilayer mirrors, optimized by tailored material dependent deposition and interface polishing, for the generation of single attosecond pulses from a high-harmonic cut-off spectrum at a central energy of 145 eV. Isolated attosecond pulses have been measured by soft x-ray-pump/NIR-probe electron streaking experiments and characterized using frequency-resolved optical gating for complete reconstruction of attosecond bursts (FROG/CRAB). The results demonstrate that Cr/Sc multilayer mirrors can be used as efficient attosecond optics for reflecting 600 attosecond pulses at a photon energy of 145 eV, which is a prerequisite for present and future attosecond experiments in this energy range.

Contribution

Reflectometry with hard X-ray radiation ($\lambda = 0.71\text{\AA}$) was used to evaluate the quality of the layer system, i.e. spacing and roughness were analyzed. Here, I provided technical support with the X-ray setup alignment and macro writing.



Chromium/scandium multilayer mirrors for isolated attosecond pulses at 145 eV

ALEXANDER GUGGENMOS,^{1,2,*} MICHAEL JOBST,^{2,3} MARCUS OSSIANDER,^{2,3} STEFAN RADÜNZ,^{1,2} JOHANN RIEMENSBERGER,^{2,3} MARTIN SCHÄFFER,^{2,3} AYMAN AKIL,² CLEMENS JAKUBEIT,² PHILIP BÖHM,^{4,5} SIMON NOEVER,^{4,5} BERT NICKEL,^{4,5} REINHARD KIENBERGER,^{2,3} AND ULF KLEINEBERG^{1,2}

¹Fakultät für Physik, Ludwig-Maximilians-Universität München, Am Coulombwall 1, 85748 Garching, Germany

²Max-Planck-Institut für Quantenoptik, Hans-Kopfermann-Str. 1, 85748 Garching, Germany

³Fakultät für Physik, Technische Universität München, James-Frank-Str. 1, 85748 Garching, Germany

⁴Fakultät für Physik and Center for NanoScience (CeNS), Ludwig-Maximilians-Universität München, Geschwister-Scholl-Platz 1, 80539 München, Germany

⁵Nanosystems Initiative Munich, Schellingstrasse 4, 80799 München, Germany

*Corresponding author: alexander.guggenmos@physik.lmu.de

Received 31 March 2015; revised 21 May 2015; accepted 25 May 2015; posted 26 May 2015 (Doc. ID 237220); published 11 June 2015

Recent advances in the development of attosecond soft x-ray sources toward photon wavelengths below 10 nm are also driving the development of suited broadband multilayer optics for steering and shaping attosecond pulses. We demonstrate that current attosecond experiments in the sub-200-eV range benefit from these improved optics. We present our achievements in utilizing ion-beam-deposited chromium/scandium (Cr/Sc) multilayer mirrors, optimized by tailored material dependent deposition and interface polishing, for the generation of single attosecond pulses from a high-harmonic cut-off spectrum at a central energy of 145 eV. Isolated attosecond pulses have been measured by soft x-ray-pump/NIR-probe electron streaking experiments and characterized using frequency-resolved optical gating for complete reconstruction of attosecond bursts (FROG/CRAB). The results demonstrate that Cr/Sc multilayer mirrors can be used as efficient attosecond optics for reflecting 600-attosecond pulses at a photon energy of 145 eV, which is a prerequisite for present and future attosecond experiments in this energy range. © 2015 Optical Society of America

OCIS codes: (320.0320) Ultrafast optics; (230.4170) Multilayers; (340.7480) X-rays, soft x-rays, extreme ultraviolet (EUV); (230.4040) Mirrors.

<http://dx.doi.org/10.1364/OL.40.002846>

The development and optimization of highly reflective near-normal incidence multilayer mirror optics for the water window spectral range [1] defined by the K-shell absorption edges of carbon and oxygen (284 and 543 eV, respectively) has been a topic of intensive research over the recent past [2,3]. The

driving force is the prospect of high-resolution soft x-ray microscopy [4,5], soft x-ray astronomy [6,7], new optics for soft x-ray free-electron lasers [8], or time-resolved attosecond soft x-ray spectroscopy [9,10]. These multilayer mirrors provide a unique approach for beam steering, spatial and spectral shaping, as well as spectral phase control with reasonably low reflective losses. The most appropriate multilayer material combination in the water window spectral range, above the carbon K-edge and below the scandium L₃-edge, is chromium (Cr) and scandium (Sc) [2,11].

In this Letter, we show that optimizing this material system is not only a key to future attosecond experiments in the water window [12], but also facilitates a promising choice for realizing new attosecond experiments at around 130–160 eV, the energy range where attosecond sources with sufficient photon flux are nowadays already available [13], but multilayer optics are very limited.

The dominating generation process for single isolated attosecond pulses is high harmonic generation (HHG) in gases [14] driven by intense phase-stabilized few-cycle laser pulses [15]. Multilayer mirrors allow for spectral filtering of the broadband high harmonic spectrum in the extreme ultraviolet (XUV)/soft x-ray range with a very high precision upon reflection [16,17]. Central energy and bandwidth of the reflected spectrum can be designed in a flexible manner by the proper choice of layer materials and the multilayer stack design [18]. Figure 1 shows a simulation comparison of certain established multilayer material systems reflecting (attosecond) HHG pulses with a central energy of 145 eV and a full width at half-maximum (FWHM) bandwidth of 3 eV at an angle of normal incidence of 5 degrees; parameters were chosen as a trade-off between spectral and temporal resolution in high-resolution attosecond experiments.

Please note that throughout this manuscript, reflectivity simulations and reflectivity fits have been performed using a Matlab multilayer Fresnel code, which uses tabulated values

of the atomic scattering factors from Henke and Gullikson [19]. The simulations show only a weak suppression of unwanted low-energy out-of-band radiation in the range of ≈ 120 eV with lanthanum (La)-based multilayer mirrors (La/Mo, La/B₄C); the inevitable and commonly used metal filter for blocking the near-infrared (NIR) laser radiation [typically a 200-nm-thick palladium (Pd) filter] cannot be used to eliminate the out-of-band radiation due to its transmission properties. As a result, chirped plateau harmonics are not sufficiently suppressed by such multilayer reflectors, which is a prerequisite for filtering isolated single-attosecond pulses from the cut-off area of the high harmonic spectrum. This suppression of low-energy out-of-band radiation is essential for attosecond spectroscopy experiments, e.g., delay measurements [20] or direct observation of electron propagation [21]. Well-established molybdenum/silicon (Mo/Si) mirrors, which are widely used in attosecond experiments at photon energies below the silicon L₃-edge at ≈ 100 eV, suffer from very low reflectivity above 100 eV. Other molybdenum-based multilayer systems like molybdenum/boron carbide (Mo/B₄C), molybdenum/yttrium (Mo/Y), molybdenum/beryllium (Mo/Be), or molybdenum/strontium (Mo/Sr), which on the one hand can provide a higher degree of out-of-band radiation suppression (Mo/B₄C) accompanied with a higher reflectivity (Mo/Y, Mo/Be, Mo/Sr) [22–25] but on the other hand suffer from strong spectral modulations around the main reflectivity Bragg peak by Kiessig fringes and therefore introduce additional group delay dispersion (GDD), which broadens the pulse in the time domain. Furthermore, Mo/Sr is not stable and shows long-term degradation, and beryllium is strongly toxic, thus limiting experimental adoption. A reflection comparison in the time domain of multilayer mirrors composed of Cr/Sc and a high reflective system, here as example Pd/B₄C [26], is shown in the small inset of Fig. 1, which already takes the transmission and the spectral phase of a 200-nm-thick Pd filter into account. Whereas the pulse reflection of the Cr/Sc mirror is close to its Fourier limit and exhibits a Gaussian pulse shape, the Pd/B₄C system shows unwanted temporal pulse broadening due to GDD as well as temporal modulations resulting from the multilayer reflectivity fringes. The Cr/Sc multilayer mirror system, however, combines all the advantages required

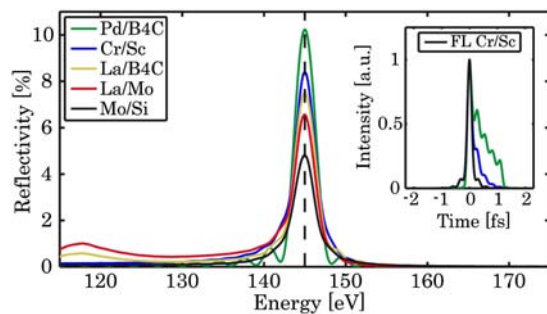


Fig. 1. Simulation comparison of certain multilayer material systems for the reflection of a FWHM bandwidth of 3 eV centered at 145 eV. The small inset shows a comparison of the Cr/Sc and Pd/B₄C system in the time domain including the transmission through a 200-nm-thick palladium (Pd) filter. The black line shows the Fourier limit (FL) of the Cr/Sc mirror reflection.

Table 1. Mirror Parameters

System	d [nm]	γ	σ [nm]	N	Capping
Cr/Sc	4.371	0.4	0.5	65	1.4 nm nat. ox.
La/B ₄ C	4.402	0.5	0.8	50	—
La/Mo	4.423	0.5	0.4	56	3 nm B ₄ C
Pd/B ₄ C	4.402	0.6	0.84	44	—
Mo/Si	4.376	0.5	0.5	60	1.5 nm nat. ox.

for applications with HHG attosecond pulses: sufficient throughput due to the optimized reflectivity [27], suppression of out-of-band radiation components (in case of the lanthanum-based systems a thicker filter can increase the suppression in the 120 eV range but reduces the overall throughput as well), and a nearly (Fourier-limited) Gaussian pulse profile, both in the spectral and temporal domain. The corresponding mirror parameters (period thickness d , ratio γ , interface roughness σ , period number N , and capping) applied in the simulations of Fig. 1, for a bandwidth of 3 eV (FWHM) centered at 145 eV, are depicted in Table 1.

The experimental realization of the Cr/Sc attosecond multilayer mirror was performed by a dual-ion-beam-sputtering technique [12] together with tailored interface polishing [27] for a higher mirror reflectivity.

For a later characterization by attosecond streaking, the mirror was additionally analyzed by two independent measurement techniques, hard x-ray reflectometry and XUV/soft x-ray reflectometry. The hard x-ray reflectometry (XRR) measurement, using a molybdenum K_{α} source with a wavelength of $\lambda \approx 0.071$ nm, was performed on a flat witness sample, grown on a silicon (100) wafer with a native SiO₂ layer. A comparison of the measured and simulated XRR data of the Cr/Sc attosecond mirror is shown in Fig. 2.

The fitting procedure of the XRR measurement, including the native Cr₂O₃ top layer, reveals only a 0.2% shift of the aimed period thickness and a Nevot–Croce [28] interface roughness of $\sigma = 0.198$ nm since even the 9th Bragg order is well resolved. The 5th Bragg order is not completely suppressed and points to a period thickness ratio of $\gamma = 0.405$. Even though every 10th period (chromium layer) was polished with krypton (Kr) ions [27], the multilayer still shows a pronounced periodicity as indicated by very sharp Bragg peaks. The strong periodicity is the prerequisite for a flat spectral phase upon reflection without additionally introduced GDD.

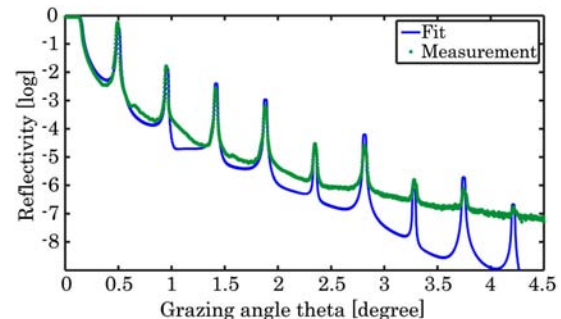


Fig. 2. Hard x-ray reflectometry measurement (green dots) and the fit (solid blue) for the Cr/Sc attosecond mirror.

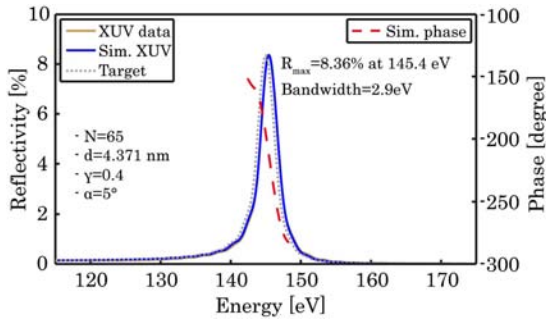


Fig. 3. XUV/soft x-ray reflectometry measurement (solid brown), the corresponding fit (solid blue), and the target design (dotted gray) together with the simulated phase (dashed red).

We have additionally analyzed the Cr/Sc mirror reflectivity at near-normal incidence by XUV/soft x-ray reflectometry, which was performed on a second witness sample. The measured reflectivity profile, together with its simulation and target curve, is shown in Fig. 3.

The Cr/Sc attosecond mirror design exhibits a maximum reflectivity of 8.36% centered at 145.4 eV and reflects over the intended bandwidth of ≈ 3 eV, as depicted by the solid brown line in Fig. 3. We find a perfect match of the simulation (solid blue) and the measurement, with only a 0.27% shift of the measured peak wavelength from the target wavelength (dotted gray). The XUV/soft x-ray measurement was carried out at the Physikalisch-Technische Bundesanstalt (PTB) beamline at BESSY II in Berlin.

As a final application of this Cr/Sc multilayer mirror to attosecond pulses at 145 eV, an attosecond-electron-streaking experiment was performed to characterize the mirrors temporal attosecond pulse response. High harmonics (HH) have been generated in a neon (Ne) gas jet (200 mbar, < 4 fs, 1.5 mJ, $f = 40$ cm), resulting in an HH spectrum with a cut-off energy ranging up to 150 eV, and are then focused by means of a Cr/Sc multilayer-coated double mirror in a second Ne gas jet for photo-ionization.

To characterize the attosecond pulses upon reflection from the Cr/Sc multilayer mirror, we used the well-established XUV/soft x-ray pump/NIR probe-streaking technique [29]. Here, both the attosecond soft x-ray pulse and the NIR laser pulse are focused by a double mirror into neon gas. The soft x-ray pulse photo-ionizes Ne atoms, which frees photoelectrons from the 2p shell, which are then momentum-streaked by the co-propagating temporally synchronized and phase stabilized NIR laser's electric field. The inner part of the double mirror can be moved with respect to the outer part, to introduce a temporal delay between the soft x-ray pulse, which is reflected at the mirror core, and the laser pulse, which is reflected at the outer ring. Changing the delay between the laser and the soft x-ray attosecond pulse yields a typical streaking spectrogram [Fig. 4(a)].

FROG/CRAB [30] analysis allows for a complete reconstruction of both the intensity and the phase of the soft x-ray attosecond pulse, as well as the vector potential of the streaking laser field from a recorded spectrogram [Fig. 4(a)]. Figure 4(b) shows the result of the appropriate FROG/CRAB retrieval as described in [31,32].

Figures 4(c) and 4(d) display the retrieved intensity (solid blue line) and phase (dotted red line) of the soft x-ray pulse, once in the spectral (c) and once in the temporal (d) domain.

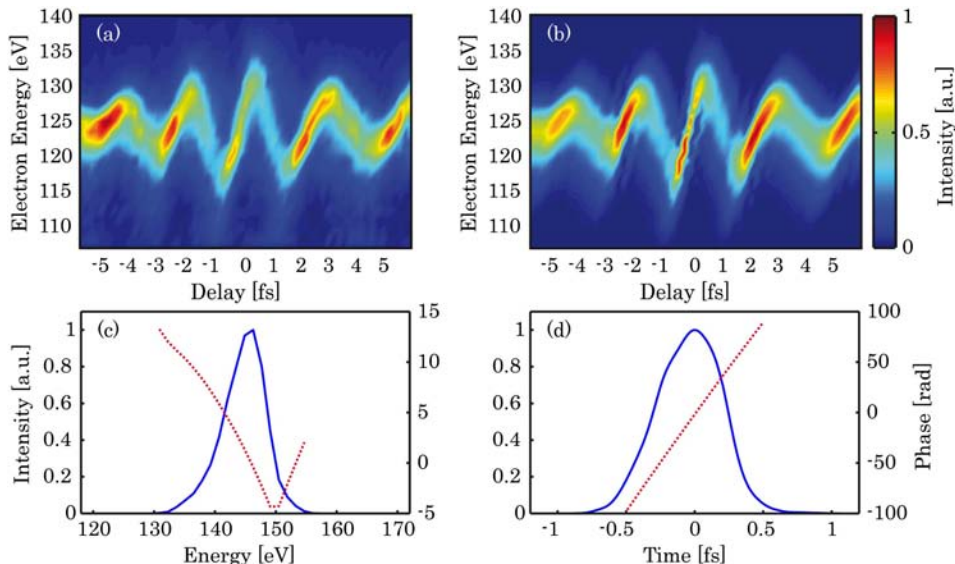


Fig. 4. Cr/Sc multilayer mirror for attosecond pulses. (a)–(d) Results of an attosecond streaking experiment for pulse characterization in neon. (a) Shows the measured electron streaking trace and (b) the retrieved trace performed by FROG/CRAB analyses. (c) The retrieved soft x-ray pulse (solid blue) and the phase (dotted red) in the spectral domain. (d) Soft x-ray pulse and phase in the temporal domain.

Shifted by the binding energy of the Ne-2p electrons (21.6 eV), the soft x-ray pulse shows a central energy of 145.6 eV, which is in good agreement to the target and the previously described results. With the retrieved spectral bandwidth and phase being the most prominent sources of uncertainty, the temporal error can be estimated to be about 20 as. From the retrieved amplitude and phase, we find an attosecond pulse duration of about 580 as in the temporal domain, which is in excellent agreement with the previous estimations (based solely on the mirror reflectivity plus the assumption of a flat mirror phase). A perfect Gaussian Fourier-limited pulse with 2.9 eV bandwidth has a duration of 629 as.

In summary, we have developed and applied an optimized Cr/Sc multilayer mirror for reflecting single isolated attosecond pulses at a photon energy of 145 eV with a pulse duration of 580, which is to the best of our knowledge 27 eV higher than the recent energy limit in tabletop attosecond pump studies [21]. This experimental achievement now paves the way for attosecond experiments above 130 eV, the soft x-ray photon energy range that was not addressed until very recently. The true benefit of this achievement is in its scaling toward the preparation of attosecond pulses at even higher photon energies ranging into the water window spectral range, which will give access to even deeper bound electronic core states and open up new possibilities for attosecond experiments on biomolecules in the foreseen future.

Bundesministerium für Bildung und Forschung (Federal Ministry of Education and Research) (BMBF-05K13WM1); Deutsche Forschungsgemeinschaft (DFG) (EXC158).

We thankfully acknowledge scientific support and valuable discussions by Ferenc Krausz (MPQ, LMU).

REFERENCES

- C. Spielmann, N. H. Burnett, S. Sartania, R. Koppitsch, M. Schnürer, C. Kan, M. Lenzner, P. Wobrauschek, and F. Krausz, *Science* **278**, 661 (1997).
- F. Eriksson, G. A. Johansson, H. M. Hertz, E. M. Gullikson, U. Kreissig, and J. Birch, *Opt. Lett.* **28**, 2494 (2003).
- T. Kuhlmann, S. Yulin, T. Feigl, N. Kaiser, T. Gorelik, U. Kaiser, and W. Richter, *Appl. Opt.* **41**, 2048 (2002).
- T. Gomiak, R. Heine, A. P. Mancuso, F. Staier, C. Christophis, M. E. Pettitt, A. Sakdinawat, R. Treusch, N. Guerassimova, J. Feldhaus, C. Gutt, G. Grübel, S. Eisebitt, A. Beyer, A. Götzhäuser, E. Weckert, M. Grunze, I. A. Vartanyants, and A. Rosenhahn, *Opt. Express* **19**, 11059 (2011).
- W. Chao, J. Kim, S. Rekawa, P. Fischer, and E. H. Anderson, *Opt. Express* **17**, 17669 (2009).
- M. Santos-Lleo, N. Scharfel, H. Tananbaum, W. Tucker, and M. C. Weisskopf, *Nature* **462**, 997 (2009).
- D. Martínez-Galarce, R. Soufli, D. L. Windt, M. Bruner, E. Gullikson, S. Khatri, E. Spiller, J. C. Robinson, S. Baker, and E. Prast, *Opt. Eng.* **52**, 095102 (2013).
- M. Prasciolu, A. F. G. Leontowich, K. R. Beyerlein, and S. Bajt, *Appl. Opt.* **53**, 2126 (2014).
- M. Hentschel, R. Kienberger, C. Spielmann, G. A. Reider, N. Milosevic, T. Brabec, P. Corkum, U. Heinzmann, M. Drescher, and F. Krausz, *Nature* **414**, 509 (2001).
- M. Schultze, K. Ramasesha, C. D. Pemmaraju, S. A. Sato, D. Whitmore, A. Gandman, J. S. Prell, L. J. Borja, D. Prendergast, K. Yabana, D. M. Neumark, and S. R. Leone, *Science* **346**, 1348 (2014).
- F. Schäfers, H.-C. Mertins, F. Schmolla, I. Packe, N. N. Salashchenko, and E. A. Shamov, *Appl. Opt.* **37**, 719 (1998).
- A. Guggenmos, R. Rauhut, M. Hofstetter, S. Hertrich, B. Nickel, J. Schmidt, E. M. Gullikson, M. Seibald, W. Schnick, and U. Kleineberg, *Opt. Express* **21**, 21728 (2013).
- W. Schweinberger, A. Sommer, E. Bothschafter, J. Li, F. Krausz, R. Kienberger, and M. Schultze, *Opt. Lett.* **37**, 3573 (2012).
- T. Popmintchev, M.-C. Chen, D. Popmintchev, P. Arpin, S. Brown, S. Ališauskas, G. Andriukaitis, T. Balciunas, O. D. Mücke, A. Pugzlys, A. Baltuška, B. Shim, S. E. Schrauth, C. Gaeta, L. Plaja, C. Hernández-García, A. Becker, A. Jaron-Becker, M. M. Mumane, and H. C. Kapteyn, *Science* **336**, 1287 (2012).
- A. Baltuška, T. Udem, M. Uiberacker, M. Hentschel, E. Goulielmakis, C. Gohle, R. Holzwarth, V. S. Yakovlev, A. Scrinzi, T. W. Hänsch, and F. Krausz, *Nature* **421**, 611 (2003).
- M. Hofstetter, M. Schultze, M. Fieß, B. Dennhardt, A. Guggenmos, J. Gagnon, V. Yakovlev, E. Goulielmakis, R. Kienberger, E. M. Gullikson, F. Krausz, and U. Kleineberg, *Opt. Express* **19**, 1767 (2011).
- C. Bourassin-Bouchet, S. de Rossi, J. Wang, E. Meltchakov, A. Giglia, N. Mahne, S. Nannarone, and F. Delmotte, *New J. Phys.* **14**, 023040 (2012).
- M. Hofstetter, A. Aquila, M. Schultze, A. Guggenmos, S. Yang, E. Gullikson, M. Huth, B. Nickel, J. Gagnon, V. S. Yakovlev, E. Goulielmakis, F. Krausz, and U. Kleineberg, *New J. Phys.* **13**, 063038 (2011).
- B. L. Henke, E. M. Gullikson, and J. C. Davis, *At. Data Nucl. Data Tables* **54**, 181 (1993).
- M. Schultze, M. Fieß, N. Karpowicz, J. Gagnon, M. Korbman, M. Hofstetter, S. Neppl, A. L. Cavalieri, Y. Komminos, T. Mercouris, C. A. Nicolaides, R. Pazourek, S. Nagele, J. Feist, J. Burgdörfer, A. M. Azzeer, R. Ernstorfer, R. Kienberger, U. Kleineberg, E. Goulielmakis, F. Krausz, and V. S. Yakovlev, *Science* **328**, 1658 (2010).
- S. Neppl, R. Ernstorfer, A. L. Cavalieri, C. Lemell, G. Wachter, E. Magerl, E. M. Bothschafter, M. Jobst, M. Hofstetter, U. Kleineberg, J. V. Barth, D. Menzel, J. Burgdörfer, P. Feulner, F. Krausz, and R. Kienberger, *Nature* **517**, 342 (2015).
- C. Montcalm, B. T. Sullivan, S. Duguay, M. Ranger, W. Steffens, H. Pépin, and M. Chaker, *Opt. Lett.* **20**, 1450 (1995).
- R. Soufli, E. Spiller, D. L. Windt, J. C. Robinson, E. M. Gullikson, L. R. Marcos, M. Fernández-Perea, S. L. Baker, A. L. Aquila, F. J. Dollar, J. A. Méndez, J. I. Larruquert, L. Golub, and P. Boerner, *Proc. SPIE* **8443**, 84433C (2012).
- S. Bajt, *J. Vac. Sci. Technol. A* **18**, 557 (2000).
- B. Sae-Lao and C. Montcalm, *Opt. Lett.* **26**, 468 (2001).
- C. Montcalm, P. A. Kearney, J. M. Slaughter, B. T. Sullivan, M. Chaker, H. Pépin, and C. M. Falco, *Appl. Opt.* **35**, 5134 (1996).
- A. Guggenmos, S. Radünz, R. Rauhut, M. Hofstetter, S. Venkatesan, A. Wochnik, E. M. Gullikson, S. Fischer, B. Nickel, C. Scheu, and U. Kleineberg, *Opt. Express* **22**, 26526 (2014).
- L. Névot and P. Croce, *Rev. Phys. Appl.* **15**, 761 (1980).
- R. Kienberger, E. Goulielmakis, M. Uiberacker, A. Baltuska, V. Yakovlev, F. Bammer, A. Scrinzi, T. Westerwalbesloh, U. Kleineberg, U. Heinzmann, M. Drescher, and F. Krausz, *Nature* **427**, 817 (2004).
- R. Trebino, K. W. DeLong, D. N. Fittinghoff, J. N. Sweetser, M. A. Krumbügel, B. A. Richman, and D. J. Kane, *Rev. Sci. Instrum.* **68**, 3277 (1997).
- J. Gagnon and V. S. Yakovlev, *Opt. Express* **17**, 17678 (2009).
- J. Gagnon, E. Goulielmakis, and V. S. Yakovlev, *Appl. Phys. B* **92**, 25 (2008).

A.7 SURFACE-DIRECTED MOLECULAR ASSEMBLY OF PENTACENE ON AROMATIC ORGANOPHOSPHONATE SELF-ASSEMBLED MONOLAYERS EXPLORED BY POLARIZED RAMAN SPECTROSCOPY

S. Yazji, C. Westermeier, D. Weinbrenner, M. Sachsenhauser, K.-C. Liao, S. Noever, P. Postorino, J. Schwartz, G. Abstreiter, B. Nickel, I. Zardo, and A. Cattani-Scholz

Journal of Raman Spectroscopy 2016, Vol. 48, No. 2, 235-242

DOI: [10.1002/jrs.5007](https://doi.org/10.1002/jrs.5007)

Abstract

Organophosphonate self-assembled monolayers (SAMPs) fabricated on SiO₂ surfaces can influence crystallization of vapor-deposited pentacene and thus can affect device performance of pentacene-based organic thin film transistors. Polarized Raman spectroscopy is demonstrated to be an effective technique to determine the degree of anisotropy in pentacene thin films deposited on three structurally different, aromatic SAMPs grown on silicon oxide dielectrics. Vibrational characterization of pentacene molecules in these films reveals that the molecular orientation of adjacent crystalline grains is strongly correlated on the SAMP-modified dielectric surface, which results in enhanced interconnectivity between the crystallite domains, well beyond the size of a single grain. It is found that vibrational coupling interactions, relaxation energies, and grain size boundaries in pentacene thin films vary with the choice of SAMP. This information clearly shows that molecular assembly of pentacene thin films can be modulated by controlling the SAMP-modified dielectric surface, with potentially beneficial effects on the optimization of electron transfer rates.

Contribution

To correlate structural order of the pentacene films on the different SAMPs to Raman analysis and electronic properties, I performed X-ray reflectometry analysis of all discussed systems and wrote the respective text passage in the manuscript.

Research article

Journal of
RAMAN
SPECTROSCOPY

Received: 12 May 2016

Revised: 24 June 2016

Accepted: 17 July 2016

Published online in Wiley Online Library: 15 August 2016

(wileyonlinelibrary.com) DOI 10.1002/jrs.5007

Surface-directed molecular assembly of pentacene on aromatic organophosphonate self-assembled monolayers explored by polarized Raman spectroscopy

Sara Yazji,^a Christian Westermeier,^b Dominik Weinbrenner,^a Matthias Sachsenhauser,^a Kung-Ching Liao,^c Simon Noever,^b Paolo Postorino,^d Jeffrey Schwartz,^c Gerhard Abstreiter,^a Bert Nickel,^b Ilaria Zardo^{e*} and Anna Cattani-Scholz^{a*}



Organophosphonate self-assembled monolayers (SAMPs) fabricated on SiO₂ surfaces can influence crystallization of vapor-deposited pentacene and thus can affect device performance of pentacene-based organic thin film transistors. Polarized Raman spectroscopy is demonstrated to be an effective technique to determine the degree of anisotropy in pentacene thin films deposited on three structurally different, aromatic SAMPs grown on silicon oxide dielectrics. Vibrational characterization of pentacene molecules in these films reveals that the molecular orientation of adjacent crystalline grains is strongly correlated on the SAMP-modified dielectric surface, which results in enhanced interconnectivity between the crystallite domains, well beyond the size of a single grain. It is found that vibrational coupling interactions, relaxation energies, and grain size boundaries in pentacene thin films vary with the choice of SAMP. This information clearly shows that molecular assembly of pentacene thin films can be modulated by controlling the SAMP-modified dielectric surface, with potentially beneficial effects on the optimization of electron transfer rates. Copyright © 2016 John Wiley & Sons, Ltd.

Additional supporting information may be found in the online version of this article at the publisher's web site.

Keywords: polarized Raman spectroscopy; self-assembled monolayers; pentacene; organophosphonate

Introduction

Chemical and morphological structure at the interface between semiconductor and dielectric in an organic field-effect transistor (OFET) is critical to device performance. Semiconductor–dielectric affinity influences crystal nucleation and growth of organics on the dielectric surface. Growth modes determine both molecular order (overall morphology, domain structure, and grain boundaries) inside crystallites and nanoscale and micro-scale variation in π -conjugated overlap among crystallites in the bulk semiconductor. In particular, surfaces functionalized with self-assembled monolayers (SAMPs) might provide nucleation sites for organic semiconductor crystallization, influencing growth size, dendritic structure, ordering, and homogeneity of crystalline domains.^[1] Moreover, highly ordered and uniform monolayers can electrically passivate the dielectric and neutralize the large number of charge traps ordinarily found on exposed surfaces typically arising from dangling bonds or stoichiometric defects. This effect is particularly important, for example, in low-voltage organic transistors, which operate at supply voltages ≤ 2 V and require consistently thin dielectrics.^[2]

Organic coatings can be grown on semiconductor oxides using various anchoring groups, among which siloxanes are common. In silanization, however, preferential cross-linking of the organic

moieties by Si–O–Si bond formation competes with true monolayer bonding to the surface, which can result in suboptimal surface passivation. In this regard, organophosphonates are preferable to siloxanes for modifying inorganic surfaces (e.g., SiO₂), thanks to their superior monolayer properties.^[3–10] Indeed, aromatic

* Correspondence to: Anna Cattani-Scholz, Walter Schottky Institut, Technische Universität München, Am Coulombwall 4, 85748 Germany. E-mail: cattani@wsi.tum.de; Ilaria Zardo, Department of Physics, University of Basel, Klingelbergstrasse 82, 4056 Basel, Switzerland. E-mail: ilaria.zardo@unibas.ch

a Walter Schottky Institut, Technische Universität München, Am Coulombwall 4, 85748, München, Germany

b Fakultät für Physik and Center for NanoScience, Ludwig-Maximilians-Universität München, Geschwister-Scholl-Platz 1, 80539, München, Germany

c Department of Chemistry, Princeton University, Princeton, New Jersey

d CNR-IOM and Dip. di Fisica, Università di Roma Sapienza, P.le Aldo Moro 5, I-00185, Rome, Italy

e Department of Physics, University of Basel, Klingelbergstrasse 82, 4056, Basel, Switzerland

organophosphonate monolayers (SAMPs) find applications in functionalizing surfaces because of their high stability and excellent passivating properties. High-quality organophosphonate monolayers have shown excellent dielectric and interfacial properties in high-performance OFETs.^[11] In particular, SAMPs grown on the SiO₂ gate dielectric have been shown to enhance critical device parameters such as on/off ratios, carrier mobilities, sub-threshold performance, and threshold voltages in pentacene thin film transistors (TFT).^[12] However, because reports are typically based on OFET device characterization, it is often difficult to understand the dependence of the device performance on fabrication conditions and technologies.

To further elucidate the effect of the SAMPs-based surface functionalization on semiconductor growth and device behavior, we report here a characterization study involving atomic force microscopy (AFM), X-ray analysis, and Raman spectroscopy; this last technique allows us to probe molecular microstructures in thin film polymorphs and to investigate microscopic parameters that are relevant to carrier transport properties. In particular, we use angle-dependent, polarized Raman spectroscopy, which can determine molecular orientation among polycrystalline domains and, through exploiting sensitive Davydov splitting, can evaluate intermolecular interactions. We use pentacene as a model system for organic semiconductor film growth studies given that it is known to be dielectric-dependent,^[13,14] and that film thickness can be easily controlled via vacuum deposition. The symmetry group of pentacene is D_{2h}, with 51 Raman active modes: 18A_g + 7B_{1g} + 11B_{2g} + 15B_{3g}; modes with A_g symmetry are strongly enhanced when excited in the electronic absorption region, as is of interest here. Of particular interest is the C–H in-plane bending modes (1140–1190 cm⁻¹) and the C–C aromatic stretching modes (1330–1390 cm⁻¹). A representative Raman spectrum collected from pentacene deposited on base SiO₂ is presented in Fig. S3 (Supporting Information).

Using pentacene growth on untreated SiO₂ as a reference, we investigate the effects of surface functionalization with several SAMPs: benzylphosphonic acid (1), 9,10-diphenyl-2,6-diphosphonoanthracene (2), and 9,10-dinaphthyl-2,6-diphosphonoanthracene (3). The SAMP of **1** is hydrophobic and hydrocarbon-terminated, and the others (from **2** and **3**) are terminated with somewhat hydrophilic phosphonic acid groups (Fig. 1);

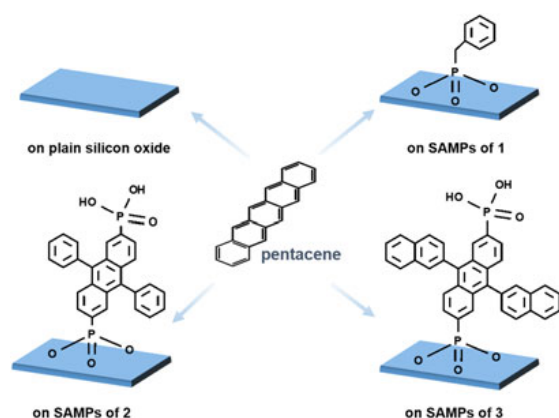


Figure 1. Schematic illustration of the deposition of pentacene on plain (untreated) silicon oxide and on self-assembled monolayers of benzylphosphonic acid (1), 9,10-diphenyl-2,6-diphosphonoanthracene (2), and 9,10-dinaphthyl-2,6-diphosphonoanthracene (3).

the difference in monolayer distal end structure, as well as SAMP footprint dimensions,^[12] may have a major influence on the nucleation process. Anthracene-based phosphonates **2** and **3** were chosen as well on the basis of reports that two-dimensional SAMP surface coverage can strongly affect the crystallization of vapor-deposited pentacene.^[12]

Experimental

9,10-Diphenyl-2,6-diphosphonoanthracene (**1**) and 9,10-dinaphthyl-2,6-diphosphonoanthracene (**2**) were synthesized as previously reported.⁴ Benzylphosphonic acid (**3**) (97%) was purchased from Sigma-Aldrich. Common reagents and organic solvents were purchased from Sigma-Aldrich and were used without further purification. Ultrapure water (Millipore) was used. Highly p-doped (boron; 0.005–0.018 Ohm·cm) silicon wafers with <100> orientation were obtained from Wacker, Burghausen, Germany and were cut into 9 × 9 mm² pieces. Contact angle measurements were performed using a home-built setup on one to two samples of untreated or SAMP-bonded SiO₂ substrates; data were collected at three different locations on each sample. A 1 μL drop of deionized water was deposited on the surface, and an image of the droplet was immediately recorded. The contact angles were determined via image processing. Standard deviations were between 1° and 5° for all samples; the latter value was taken as the estimated maximum error (±5°) for all measurements mean values. AFM was carried out using a Digital Instruments MultiMode instrument equipped with a Nanoscope V controller. Standard silicon cantilevers (force constant of 10–130 N/m in air) were used for all measurements.

Self-assembled monolayers of phosphonates: Silicon oxide-coated Si electrode surfaces were cleaned with acetone under sonication for 10 min followed by rinsing successively with isopropyl alcohol and water. The samples were further washed with a solution of water/H₂O₂ 30%/NH₄OH 5:1:1 at 80 °C for 10 min followed by washing with sonication in water for 10 min, cleaned under an oxygen plasma (200 W, 5 min), and then used immediately for preparing the SAMPs shown in Fig. 1. Following previously reported procedures,^[7] the SAMPs were formed on the clean, native oxide of single crystal Si by holding the substrate vertically in a 2.5 μM solution of the acid dissolved in anhydrous tetrahydrofuran; the solvent was allowed to evaporate slowly so that the meniscus traversed the surface of the substrate, thereby transferring the phosphonic acid onto the Si/SiO₂ surface; this procedure is known as the 'T-BAG'.^[7] The solution reservoir was large enough such that there was no appreciable change in the concentration of the phosphonic acid during this process. Coated samples were then gently removed from their holders and put into an oven at 120 °C for 18–20 h to convert the hydrogen bonded phosphonic acid monolayer to the covalently bonded SAMP. Hydrogen bonding among phosphonate head groups can give rise to surface multilayers. For this reason, all samples were carefully sonicated twice in methanol for 10 min, then with sonication in a solution of water/tetrahydrofuran/triethylamine 10:3:1 for 5 min and finally in water for 10 min. Samples were dried under a nitrogen flux. Up to five cycles of the T-BAG process were repeated to obtain a completely covered, SAMP-terminated Si/SiO₂ substrate. Any residual multilayers were removed by washing in methanol with sonication and then gently wiping. AFM analysis probed the homogeneity of the monolayers formed: spots of greater thickness could be observed locally and may be assigned to residual multilayers. Surface

Raman spectroscopy on surface-directed molecular assembly of pentacene

roughness of samples was measured for a scan area $5\ \mu\text{m} \times 5\ \mu\text{m}$ and compared with that of the bare substrate. The root mean square values of roughness were found to be between 0.21 nm and 0.34 nm, which are close to 0.21 nm for the bare substrate. Significant changes of the surface wetting behavior were recorded following SAMP formation. For the SAMP of **1**, the SAMP of **2**, and the SAMP of **3** water contact angles of $\Theta = 73^\circ$, $\Theta = 68^\circ$, $\Theta = 52^\circ$ were measured, respectively, in good agreement with reported water wetting behavior for the SAMP of **2** on silicon carbide.^[15] Complementary analysis by X-ray photoelectron spectroscopy at the C1s and P2s ionization edges clearly confirmed the presence of organophosphonates on the surfaces.

Pentacene deposition: Prior to pentacene deposition, the Si/SiO₂ substrates (with different dielectric modifications) were transferred into the deposition chamber and annealed in vacuum at 100 °C for 1 hour. Molecular beam deposition was subsequently applied to grow 100 nm thick films of pentacene (Sigma-Aldrich, triple-sublimed) at a deposition rate of $0.3\ \text{\AA s}^{-1}$, a substrate temperature of 25 °C, and a pressure of about 1×10^{-7} mbar. All the samples were prepared under identical deposition conditions in the same chamber.

Raman spectroscopy: Polarization-dependent Raman spectroscopy was performed in backscattering configuration. The 676.4 nm line of a Kr⁺ laser was used for excitation and was focused on the sample surface using a 100x objective (0.95 NA), resulting in a beam spot size of about 840 nm in diameter. The power of the incident light was 300 μW (equivalent to $\sim 49\ \text{kW/cm}^2$), with fluctuation below 1%. This power has no detrimental effect on the molecule monolayers and is well below the threshold where thermal effects are observed. The scattered light was collected by an XY Raman Dilor triple spectrometer with a multichannel charge-coupled device detector. The sample was positioned on a XY piezo-stage, which allowed the scanning of the surface with 10 nm precision over an area of $100 \times 100\ \mu\text{m}^2$; excitation polarization was rotated through a $\lambda/2$ plate. A linear polarizer was used to analyze the polarization of the scattered light ϵ_s . Because the efficiency of the spectrometer depends on the polarization of the incoming light, a $\lambda/2$ plate at the entrance to the spectrometer was added in order to change the polarization of the light into the most efficient direction.

Thin film transistors: For fabrication of TFT highly p-doped silicon substrate with 300 nm thermally grown SiO₂ was used as gate contact and dielectric. The surface was cleaned by sonication in acetone and isopropyl alcohol at 50 °C for 15 min each and subsequently rinsed with deionized water. Two of the cleaned substrates were functionalized with SAMPs of **2** following the procedure mentioned previously, whereas two other substrates were not functionalized but served as reference with bare SiO₂ surface. Ninety nanometers of pentacene were grown via molecular beam deposition onto the SAMP treated and untreated substrates simultaneously. As source and drain contact, 2 nm titanium and 50 nm gold were evaporated on top of the pentacene film via electron beam evaporation. The dimensions of the transistor channel with a length of 50 μm and a width of 4 mm were defined using shadow masks. The transistor devices were then electrically contacted with a point probe station, and device characteristics were measured under ambient conditions using a Keithley Instruments Source Meter 2612.

Results and discussion

A convenient route for the modification of several silicon-based devices has been established in our group.^[8,9] Here, SAMPs are

used to modulate the surface properties of the silicon oxide dielectric in an effort to improve crystallite ordering of pentacene overgrowth. For the four differently functionalized surfaces, we keep the growth conditions for pentacene deposition identical that allowed us to obtain crystalline films as shown by X-ray reflectivity measurements reported in Fig. S1 (Supporting Information). Data analysis shows that pentacene is nucleated predominantly in the thin film phase; the weak signal on the shoulder of the thin film phase (001) peak can be ascribed to the presence of small amounts of another structural phase. AFM images and the integrated Raman intensities of the C–C ring stretching mode at $\sim 1374\ \text{cm}^{-1}$ for pentacene were compared (Fig. 2) with the four surface treatments investigated. We notice that the Raman signal observed was coming just from the pentacene, because Raman measurements carried out on SAMPs before pentacene deposition did not show any significant signal. Both techniques clearly show the influence of surface functionalization on pentacene morphology. It is worth to notice the different intrinsic spatial resolution being the Raman spectra collected every 250 nm along a 10 μm path.

The bare SiO₂ substrate yields large crystallites of pentacene with grain sizes larger than $1 \times 1\ \mu\text{m}^2$; initial pentacene aggregation is almost entirely two-dimensional. According to diffusion-limited aggregation theory, SiO₂ apparently provides few nucleation centers: Pentacene molecules can diffuse over a large area before encountering a seed; three-dimensional growth then takes place and terrace-shaped grains are formed. In contrast, substrates functionalized with SAMPs of **2** or **3** show smaller, submicron grains about $0.2 \times 0.2\ \mu\text{m}^2$, that are more tightly packed than on bare SiO₂. Thus, SAMP-functionalization apparently provides many nucleation sites; three-dimensional growth starts immediately, yielding a more packed structure. This behavior can be related to the larger spacing between molecules of the SAMP because of the lateral phenyl and naphthyl groups of **2** and **3**, respectively. This idea has been recently proposed^[12] where the comparison between theoretical and measured footprints and theoretical calculation suggests an increased intermolecular interaction within the SAMP because of superposition of the lateral groups. Moreover, the presence of the hydrophilic phosphonic acid groups at the distal ends of SAMPs of **2** and **3** may further favor pentacene nucleation, because increased hydrophilicity reduces the diffusion length of pentacene. In confirmation, pentacene grown on the SAMP of **1**, a rather small molecule compared with **2** and **3** with no lateral groups and no hydrophilic phosphonic acid groups at the distal end, has small and large grains; this can be explained by diffusion-limited aggregation theory in which both two-dimensional and three-dimensional aggregation mechanisms coexist.

Pentacene grown on monolayers prepared from either **2** or **3** shows a less dendritic, more tightly packed structure with smaller grain domains than found on the SAMP of **1**. Small grain domains are usually undesirable: Grain boundaries with low-order regions contain many morphological defects, which in turn are linked to the creation of charge carrier traps. However, carrier mobilities and threshold voltages in organic thin-film transistor devices are determined by charge traps in the channel region, most of which are located not at the grain boundaries of the organic semiconductor, but instead at the organic/insulating-layer interface.^[16,17] This argument may explain why in some cases organic thin-film transistors with smaller grain sizes show higher mobilities than counterparts with larger grain sizes: It is the structural order and molecular orientation within the active channel at the semiconductor-dielectric interface that is a key.^[18] In order to

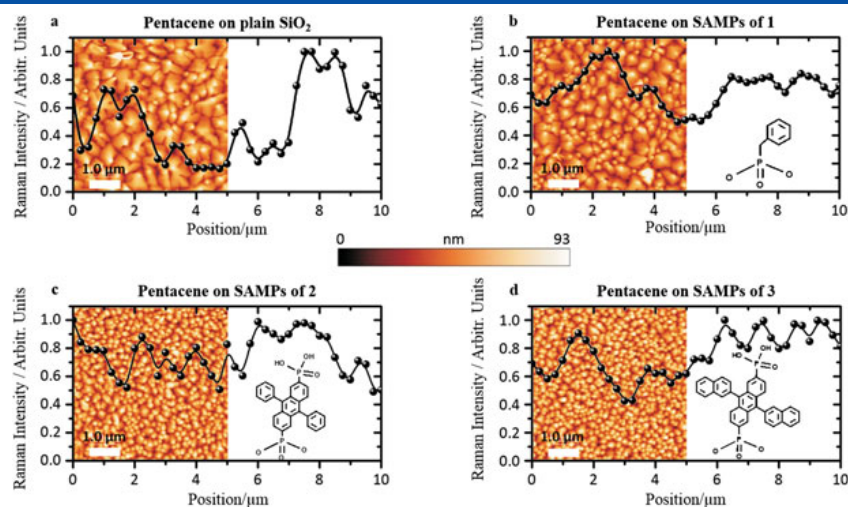


Figure 2. Integrated intensities of the short axis mode (black spheres) extracted from a spatially resolved Raman spectroscopy scan along $10\ \mu\text{m}$ together with a $5 \times 5\ \mu\text{m}^2$ atomic force microscopy scan performed on pentacene on (a) reference (plain) SiO_2 , (b) SAMP of **1**, (c) SAMP of **2**, and (d) SAMP of **3**. Raman spectra were collected every 250 nm. Intensities were extracted from multi-Lorentzian fits and were normalized to the maximum intensity obtained along each line scan, separately. The solid lines serve as a guide to the eye. The scale bar for the height of the atomic force microscopy scans is the same for all the scans. The schematic drawing of the different molecules used is given as an inset in (b), (c), and (d).

confirm this hypothesis, we carried out detailed studies on the effects of dielectric modification with SAMs of **2** on the trap states of pentacene and its electrical properties. Interestingly, the transport characteristics of pentacene TFT based on inferior, commercial Si/SiO_2 substrate can be drastically improved via functionalization of the substrate, as shown in Fig. 3 and Fig S2 (Supporting Information). All the devices built on the untreated SiO_2 substrate do not show a well-behaved transistor characteristic because the transistor current I_{SD} between source and drain cannot be properly suppressed by the applied gate voltage V_{GS} . This situation drastically changes because of functionalization of the SiO_2 dielectric with SAM of **2**. Through this, the so-called threshold voltage of the transistor is shifted towards zero gate voltage and the transfer characteristics exhibit a well-defined on-off-behavior. These results

clearly demonstrates the drastic effect of the SAM interface on charge transport, as it has been already observed for devices based on pentacene grown on somewhat highly ordered SAMs.^[12,19] We have further investigated by Raman spectroscopy whether crystallization of pentacene on all SAM functionalized substrates can influence growth size, dendritic structure, ordering, and homogeneity of crystalline domains. In particular, it has been observed that the orientation of the molecules in adjacent grains is of great importance for the performance of transistor devices.^[20] The charge transport between low-angle grain boundaries, where the relative orientation of molecules in adjacent grains is less than 15° , is expected to be more efficient than between high-angle boundaries. We hypothesize that a closely packed film of the aromatic organophosphonate SAMs simply converts the two-dimensional surface of the oxide into a three-dimensional lattice. This three-dimensional lattice acts as a template and induces pentacene nucleation with predominant direction and growth of crystalline domains of pentacene with lower grain boundary angles and thus higher interconnectivity. In order to access this hypothesis, we carried out a detailed study of the preferential grain orientation for pentacene grown on bare silicon oxide and for pentacene deposited on the different SAMs. This information can be gathered via polarized Raman spectroscopy.^[21–25] Different scattering intensities can be observed for pentacene depending on the geometry of the Raman tensor, and the scattering geometry because the Raman intensity can be described as a function of the crystal orientation, the scattering geometry, that is, excitation and scattered polarizations, respectively. Indeed, the Raman tensor varies for different point group symmetries and their irreducible representations that define the crystalline structure. The short axis C–C aromatic stretching mode at $1374\ \text{cm}^{-1}$ can be used to probe the orientation of pentacene molecules and to determine the degree of their local molecular order.^[21] The mode at $1374\ \text{cm}^{-1}$ is a C–C ring stretch modes with the carbon atoms predominantly vibrating along the short axis. This mode can be used to probe the in-plane orientations of the short-axis of the pentacene backbones in the

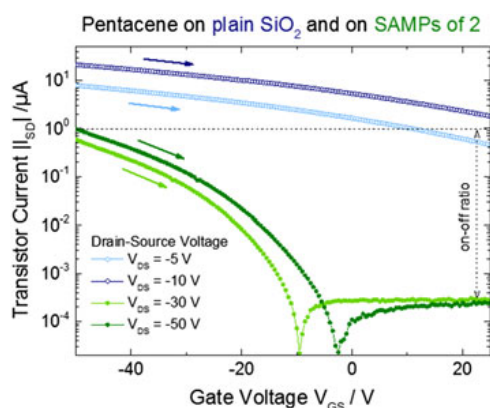


Figure 3. Comparison of transfer characteristics for devices based on a pentacene film deposited on plain SiO_2 and deposited on SAMs of **2**. The sweep direction is indicated by arrows as well as the on-off ratio, which is only well defined for the devices on SAMs of **2**.

Raman spectroscopy on surface-directed molecular assembly of pentacene

films, because a maximum Raman scattering intensity will be observed when the laser polarization aligns parallel to the short axis. Because this mode has A_g symmetry, an intensity maximum should be observed when excitation and detection polarization are parallel to each other (parallel configuration, PC), while the crossed configuration (CC) should show zero intensity. Significant measurements on pentacene deposited on untreated SiO_2 and on the different SAMPs are displayed in Fig. 4. Two components of the scattered light were collected with polarizations perpendicular to each other, H and V, as the polarization of the excitation was varied in steps of 20° . The polar plots obtained from pentacene deposited on SiO_2 and on SAMPs of **3** (Fig. 4 (a) and (d)) are well described by the Raman tensor of the A mode with triclinic symmetry C_1 , as discussed in the Supporting Information. In contrast, the polar plots obtained from pentacene deposited on SAMPs of **1** and **2** (Fig. 4 (b) and (c)) showed that the two components H and V of the scattered light always have similar intensity and are 90° out of phase. This is expected for structures with higher symmetry, such as tetragonal, as discussed in the Supporting Information. Furthermore, in order to investigate the effect of SAMP structures on the degree of local molecular order in deposited pentacene

films, polarization-dependent Raman measurements were conducted at different positions on the pentacene deposited on the untreated SiO_2 control (Fig. S4, Supporting Information) and on pentacene deposited on SAMPs from **2** (Fig. S5, Supporting Information). It is worth noting that the absolute values of maximum intensities from pentacene deposited on SAMPs of **2** measured at various positions were similar, suggesting good homogeneity in the pentacene layer over the probed area; this is not the case for pentacene deposited on untreated SiO_2 . These results clearly indicate that the dielectric surface functionalization induces a different crystallite organization for pentacene grown on SAMPs of **2** compared with pentacene grown on the plain SiO_2 . In particular, analysis of the anisotropy of the Raman signal of the untreated and SAMP-treated systems can better clarify the influence of dielectric functionalization on the growth of pentacene. The anisotropy gives an indication of the degree of molecular order of the system, with $\alpha = (I_{\text{max}} - I_{\text{min}}) / I_{\text{max}}$ and $\alpha = 1$ for purely ordered phases and $\alpha = 0$ for purely disordered phases. For pentacene grown on all different SAMPs, anisotropy values ranging between 0.5 and 0.8 were measured at different positions. High anisotropy indicates that a large proportion of the pentacene molecular backbones are

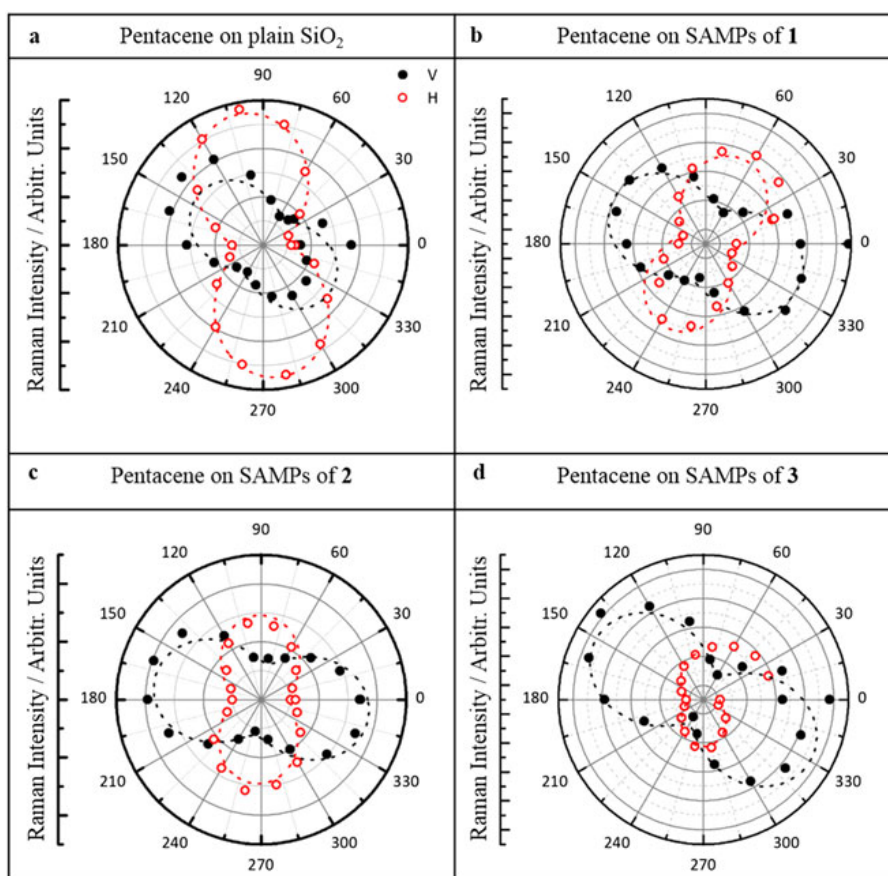


Figure 4. Raman intensities of the short axis mode of pentacene deposited on a reference of plain SiO_2 (a), (b) on SAMPs of **1**, (c) on SAMPs of **2**, and (d) of SAMPs of **3**. The parallel (H) and perpendicular (V) components of the Raman signal with respect to the optical table plane are plotted as open, red and full, black circles, respectively. The dashed red and black lines are sine fits to the data.

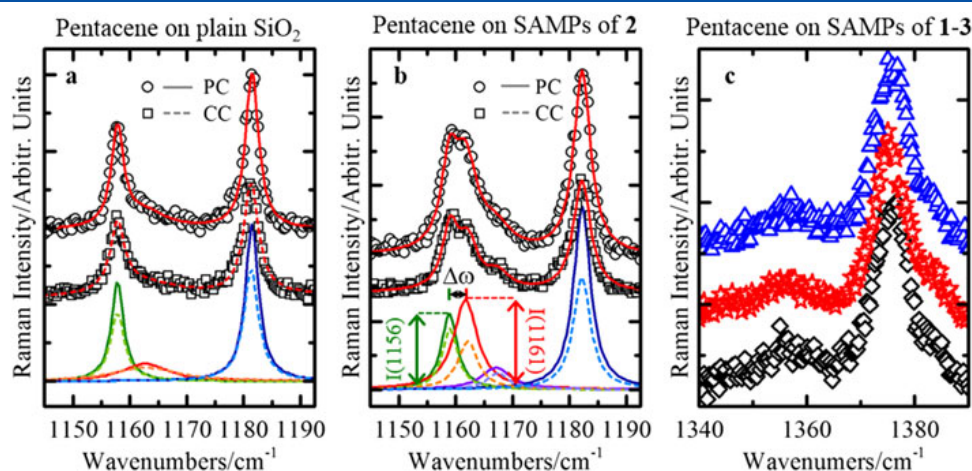


Figure 5. Raman spectra collected on pentacene (a) reference plain SiO_2 and on (b) SAMPs from **2**, in parallel (open circles) and crossed (open squares) configurations. The individual Lorentzian contributions are deconvolved and are depicted as solid and dashed lines for the parallel and crossed configurations, respectively. (c) Spectra collected in parallel configuration on SAMPs of **1** (black open diamonds), SAMPs of **2** (red open stars), and SAMPs of **3** (blue open triangles) in the spectra range of the C–C stretching modes between 1310 and 1380 cm^{-1} .

aligned in the same direction, that is, there is high molecular order on the micrometer scale. Randomly oriented crystallites with sizes much smaller than the laser spot would lead to very low Raman anisotropy, while crystallites with sizes comparable with or larger than the laser spot would exhibit high Raman anisotropy. Here, as shown in Fig. 2, pentacene deposited on untreated SiO_2 exhibits large crystalline grains of size comparable with or bigger than the laser spot. In contrast, pentacene deposited on SAMPs prepared of **2** and **3** exhibits a high density of much smaller crystallites. In consequence for pentacene grown on SiO_2 only about 1–4 grains were probed simultaneously by the laser spot, while more of them (~16) were probed simultaneously for pentacene deposited on SAMPs of **2** or **3**. Therefore, the high values of the anisotropy measured for pentacene deposited on SAMPs is even more surprising and can be explained only if a large number of crystalline grains were oriented in the same direction. This results in low-angle grain boundaries and in a better interconnectivity of pentacene domains on SAMPs, as suggested previously.

A thorough Raman study of pentacene modes can provide information not only on molecular microstructure in the deposited organic semiconductor films but also on intermolecular interactions. In particular, two major parameters that determine the electron-transfer rate and ultimately the charge mobility can be assessed: the intermolecular interactions and the relaxation

energies.^[25] The first parameter can be evaluated by studying the in-plane C–H bending modes for the hydrogen atoms at the end and on the side of the pentacene molecule, which occur at 1158 cm^{-1} and 1178 cm^{-1} , respectively, both with A_g symmetry. The two differently oriented pentacene molecules per unit cell lead to splitting of these intramolecular modes into a doublet, called Davydov splitting ω .^[25] The Davydov splitting can be resolved using polarizations of incident and scattered light either parallel (PC) or perpendicular (CC) to each other. Indeed, ω becomes more significant when the coupling between vibrations is increased and is expected to vary inversely proportional to the separation distance between molecules to the power of three. Increased splitting can be viewed as an indicator of stronger interactions, which result in a higher intermolecular transfer integral and, therefore, in higher electron transfer rates and charge mobility. Davydov splitting of the C–H in-plane bending modes, particularly the one at 1158 cm^{-1} , is enhanced by excitation with a red line. For this reason, investigation focused on this mode to gain information on possible differences in Davydov splitting and on relative intensities for differently functionalized substrates. Typical spectra collected from pentacene deposited on SiO_2 and on SAMPs from **2** are shown in Fig. 5. Davydov splitting for pentacene deposited on the SiO_2 control could not be clearly observed. Increases of the peak at

Table 1. Parameters related to Davydov splitting and to λ_{reorg} .

	$\Delta\omega$ (cm^{-1})	I_{R}^{PC} (arb. u.)	ω_1 (meV)	FWHM 1351 (cm^{-1})	FWHM 1371 (cm^{-1})
SiO_2				18.7 ± 2.6	7.2 ± 1.3
SAMPs of 1	4.5 ± 0.9	5.9 ± 1.7	12.6 ± 1.3	11.3 ± 0.6	7.5 ± 0.2
SAMPs of 2	2.9 ± 0.1	1.3 ± 0.4	10.1 ± 0.2	13.2 ± 1.1	7.2 ± 0.2
SAMPs of 3	5.3 ± 0.9	6.4 ± 2.0	13.7 ± 1.2	11.8 ± 0.7	7.6 ± 0.2

The values are given by the average over the result of the analysis of several spectra collected at different positions. The errors are given by the standard deviation.

SAMPs, self-assembled monolayers; FWHM, full width at half maximum.

Raman spectroscopy on surface-directed molecular assembly of pentacene

about 1161 cm^{-1} measured in CC mode, that is, a Davydov doublet, could be resolved on all other samples with SAMP treated substrates; the lower Raman shift peak remains dominant because of excitation in resonance. The influence of different SAMP structures is reported in Table 1, which shows an effect on Davydov splitting in terms of ω as well as on the relative intensity, $I_R = I(1156)/I(1161)$, of the two modes. The vibrational coupling energy $\omega_1 = \sqrt{2\omega_0\Delta\omega}$, with ω_0 the wavenumber of the mode at the higher wavenumber,^[25] could be estimated. These results clearly indicate that Davydov splitting and, hence, intermolecular interactions are maximized for pentacene deposited on SAMPs from **3** and **1**, suggesting a positive effect of the dielectric functionalization on pentacene intermolecular organization. This conclusion is confirmed by the analysis of the full width at half maximum (FWHM) of the vibrational modes, which is related to the relaxation energy λ_{reorg} , the second parameter that we can evaluate by Raman spectroscopy.^[25] The λ_{reorg} includes the molecular geometry modifications that occur when an electron is added to or removed from a molecule as well as the modifications in the surrounding medium because of polarization effects. It has been shown that efficient transport takes place in OFET devices when λ_{reorg} is small.^[25] The relaxation energy decreases with increasing degree of intermolecular order and is, therefore, related to the FWHM of the vibrational modes. Namely, a small FWHM implies that the pentacene layer is homogeneous and ordered and, consequently, has a low λ_{reorg} .

In particular, the in-plane C–C stretching modes between 1300 and 1600 cm^{-1} provide the larger contribution to the relaxation energies associated with hole-vibrational and electron-vibrational couplings in pentacene.^[25] Among them, the C–C stretching modes between 1310 and 1380 cm^{-1} account for 70% of the total λ_{reorg} for pentacene molecules^[25]; spectra in this range are reported in Fig. 5(c) and the FWHM values for the modes at 1351 cm^{-1} and 1371 cm^{-1} are reported in Table 1. The FWHM of the mode at 1371 cm^{-1} is constant within experimental error, while the FWHM of the mode at 1351 cm^{-1} is reduced when pentacene is deposited on a SAMP; SAMP structures that yield the best results in this regard are those from **3** and **1**, consistent with our results from the study of Davydov splitting. Our results clearly show that the vibrational coupling interactions and the relaxation energies in pentacene thin films vary with the choice of the SAMP, and that more tightly pentacene packed structures may have potential beneficial effects on the optimization of electron transfer rates.

Conclusions

Through AFM, X-ray analysis, Raman spectroscopy, and electrical characterization, we have shown that aromatic organophosphonate monolayers can act as effective nucleation sites for the crystallization of pentacene and can influence molecular microstructure and intermolecular interactions in the deposited pentacene thin films. Grain sizes of pentacene crystallites grown on bare SiO_2 dielectric are larger than those grown on SAMPs. However, the transport characteristics of pentacene TFT based on inferior, commercial Si/SiO_2 substrates are drastically improved by SAMP dielectric functionalization. Moreover, the high values of optical anisotropy for pentacene deposited on SAMPs indicate that a large number of neighboring crystallites are oriented in the same direction. This may confirm our hypothesis that a closely packed film of the aromatic

organophosphonate SAM converts the two-dimensional surface of the SiO_2 into a three-dimensional lattice that acts as a template and induces pentacene nucleation with predominant direction.^[12] Analysis of morphologies and estimations of relaxation energies support this conclusion, showing the formation of low-angle grain boundaries with tight contact and high homogeneity for pentacene films grown on the SAMPs. Intermolecular interactions estimated by analyzing Davydov splitting in the Raman spectra are maximized for pentacene deposited on SAMPs of **3** and **1**, supporting our hypothesis that dielectric modification can strongly affect pentacene nucleation and can induce growth of crystalline domains with favorable interconnectivity. Our results show the significance of both interface modification and morphology control for the optimization of pentacene thin films.

Acknowledgements

The authors acknowledge funding by the DFG (grants AB 35/8-1, TO 266/2-1), the NSF (CHE-0924104), and the Nanosystems Initiative Munich. BN acknowledges financial support from the Bavarian Ministry for Science through the initiative 'Solar technologies go hybrid (SolTech)'. Support by M. Schmidt and L. Scarpa is gratefully acknowledged.

References

- [1] S. A. Di Benedetto, A. Facchetti, M. A. Ratner, T. J. Marks, *Adv. Mater.* **2009**, *21*, 1407.
- [2] M. Halik, H. Klauk, U. Zschieschang, G. Schmid, C. Dehm, M. Schütz, S. Maisch, F. Effenberger, M. Brunnbauer, F. Stellacci, *Nature* **2004**, *4*, 963.
- [3] A. Cattani-Scholz, K.-C. Liao, A. Bora, A. Pathak, C. Hundschell, B. Nickel, J. Schwartz, G. Abstreiter, M. Tornow, *Langmuir* **2012**, *28*, 7889.
- [4] A. Cattani-Scholz, K.-C. Liao, A. Bora, A. Pathak, M. Krautloher, B. Nickel, J. Schwartz, M. Tornow, G. Abstreiter, *Angew. Ch. Int. Ed.* **2011**, *50*(37), A11.
- [5] K. S. Midwood, M. D. Carolus, M. P. Danahy, J. E. Schwarzbauer, J. Schwartz, *Langmuir* **2004**, *20*, 5501.
- [6] J. Shang, F. Cheng, M. Dubey, J. M. Kaplan, M. Rawal, X. Jiang, D. S. Newburg, P. A. Sullivan, R. B. Andrade, D. M. Ratner, *Langmuir* **2012**, *28*(6), 3338.
- [7] E. L. Hanson, J. Schwartz, B. Nickel, N. Koch, M. F. Danisman, *J. Am. Chem. Soc.* **2003**, *125*, 16074.
- [8] B. M. Silverman, K. A. Wiegand, J. Schwartz, *Langmuir* **2005**, *21*, 225.
- [9] A. Cattani-Scholz, D. Pedone, M. Dubey, S. Neppel, B. Nickel, P. Feulner, J. Schwartz, G. Abstreiter, M. Tornow, *ACS Nano* **2008**, *2*, 1653.
- [10] M. Hofmann, A. Cattani-Scholz, A. D. Mallorqui, I. D. Sharp, A. Fontcuberta, I. Morral, L. Moreno i Codinachs, *Physica Status Solidi A* **2010**, *208*(6), 1333.
- [11] H. Ma, O. Acton, D. O. Hutchins, N. Cernetica, A. K.-Y. Jen, *Phys. Chem. Chem. Phys.* **2012**, *14*, 14110.
- [12] K.-C. Liao, A. G. Ismail, L. Kreplak, J. Schwartz, I. G. Hill, *Adv. Mater.* **2010**, *22*, 3081.
- [13] S. H. Kim, M. Jang, H. Yang, C. E. Park, *J. Mater. Chem.* **2010**, *20*, 5612.
- [14] R. Ruiz, D. Choudhary, B. Nickel, T. Toccolli, K.-C. Chang, A. C. Mayer, P. Clancy, J. M. Blakely, R. L. Headrick, S. Iannotta, G. G. Malliaras, *Chem. Mat.* **2004**, *16*, 4497.
- [15] M. Auernhammer, S. J. Schoell, M. Sachsenhauser, K.-C. Liao, J. Schwartz, I. D. Sharp, A. Cattani-Scholz, *Appl. Phys. Lett.* **2012**, *100*, 101601.
- [16] S. D. Wang, T. Miyadera, T. Minari, Y. Aoyagi, K. Tsukagoshi, *Appl. Phys. Lett.* **2008**, *93*, 043311.
- [17] C. Westermeier, M. Fiebig, B. Nickel, *Adv. Mater.* **2013**, *25*, 5719.
- [18] M. C. J. M. Vissenberg, M. Matters, *Phys. Rev. B* **1998**, *57*, 12964.
- [19] H. S. Lee, D. H. Kim, J. H. Cho, M. Hwang, Y. Jang, K. Cho, *J. Am. Chem. Soc.* **2008**, *130*, 10556.

- [20] B. Bräuer, A. Virkar, S. C. B. Mannsfeld, D. P. Bernstein, R. Kukreja, K. W. Chou, T. Tyliszczak, Z. Bao, Y. Acremann, *Chem. Mater.* **2010**, *22*, 3693.
- [21] D. T. James, B. K. C. Kjellander, W. T. T. Smaal, G. H. Gelinck, C. Combe, I. McCulloch, R. Wilson, J. H. Burroughes, D. D. C. Bradley, J.-S. Kim, *ACS Nano* **2011**, *5*(12), 9824.
- [22] V. Presser, B.-E. Schuster, M. B. Casu, U. Heinemeyer, F. Schreiber, K. G. Nickel, T. Chassé, *J. Raman Spectrosc.* **2009**, *40*, 2015.
- [23] D. T. James, J. M. Frost, J. Wade, J. Nelson, J.-S. Kim, *ACS Nano* **2013**, *7*, 7983.
- [24] X. Wang, K. Broch, R. Scholz, F. Schreiber, A. J. Meixner, D. Zhang, *J. Phys. Chem. Lett.* **2014**, *5*, 1048.
- [25] H.-L. Cheng, Y.-S. Mai, W.-Y. Chou, L.-R. Chang, X.-W. Liang, *Adv. Funct. Mat.* **2007**, *17*, 3639.

Supporting information

Additional supporting information may be found in the online version of this article at the publisher's web site.

SUPPORTING INFORMATION

B.1 SUPPORTING INFORMATION FOR "DUAL CHANNEL OPERATION UPON N-CHANNEL PERCOLATION IN A PENTACENE-C60 AMBIPOLAR ORGANIC THIN FILM TRANSISTOR"

Copyright WILEY-VCH Verlag GmbH & Co. KGaA, 69469 Weinheim, Germany, 2012.

ADVANCED MATERIALS

Supporting Information

for *Adv. Mater.*, DOI: 10.1002/adma.201203964

**Dual Channel Operation Upon n-Channel Percolation in a
Pentacene-C₆₀ Ambipolar Organic Thin Film Transistor**

*Simon J. Noever, Stefan Fischer, and Bert Nickel**

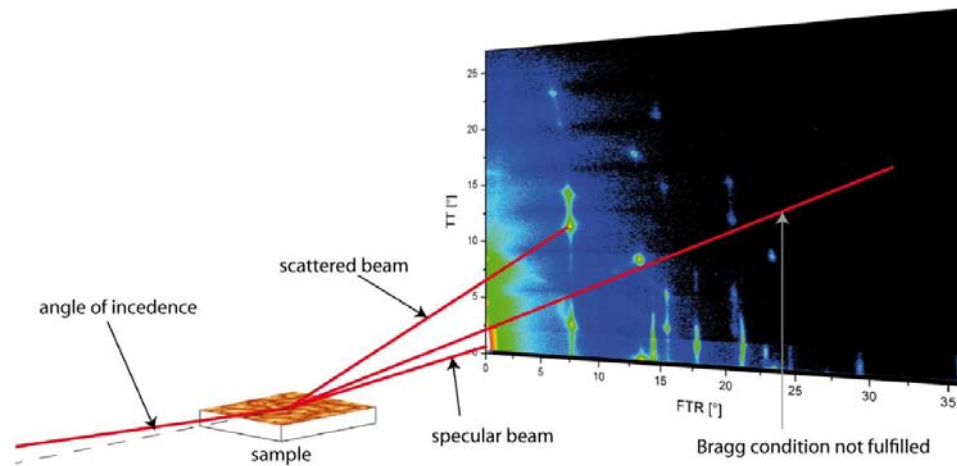
Submitted to **ADVANCED
MATERIALS**

Supporting information for:

Dual channel operation upon n-channel percolation in a pentacene-C₆₀ ambipolar organic thin film transistor

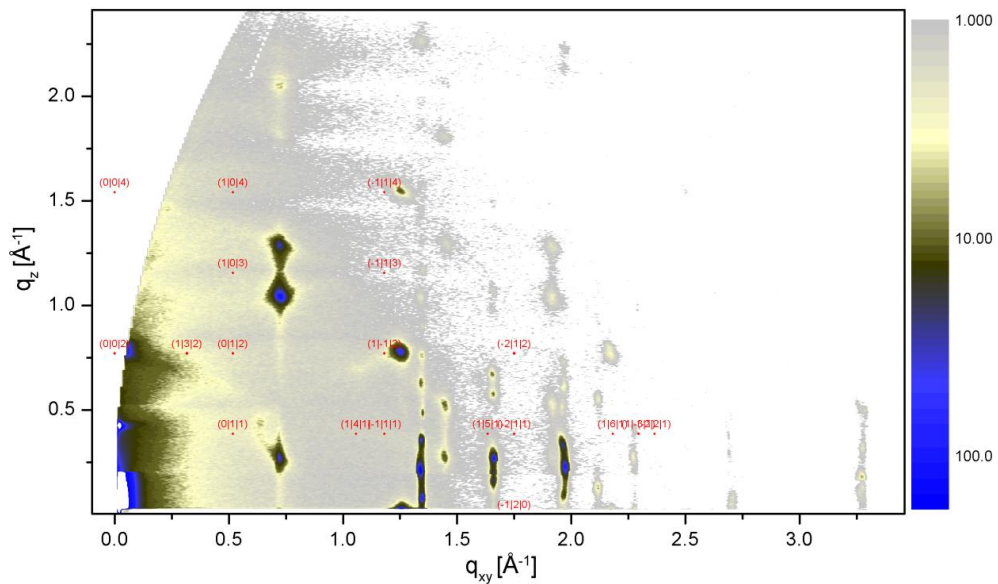
By *Simon J. Noever, Stefan Fischer and Bert Nickel**

[*] S. Noever, Priv.-Doz. Dr. Bert Nickel
Fakultät für Physik & CeNS
Ludwig-Maximilians-Universität München
Geschwister-Scholl-Platz 1, 80539 Munich (Germany)
E-mail: nickel@lmu.de



Calculated hcp features of C_{60} :

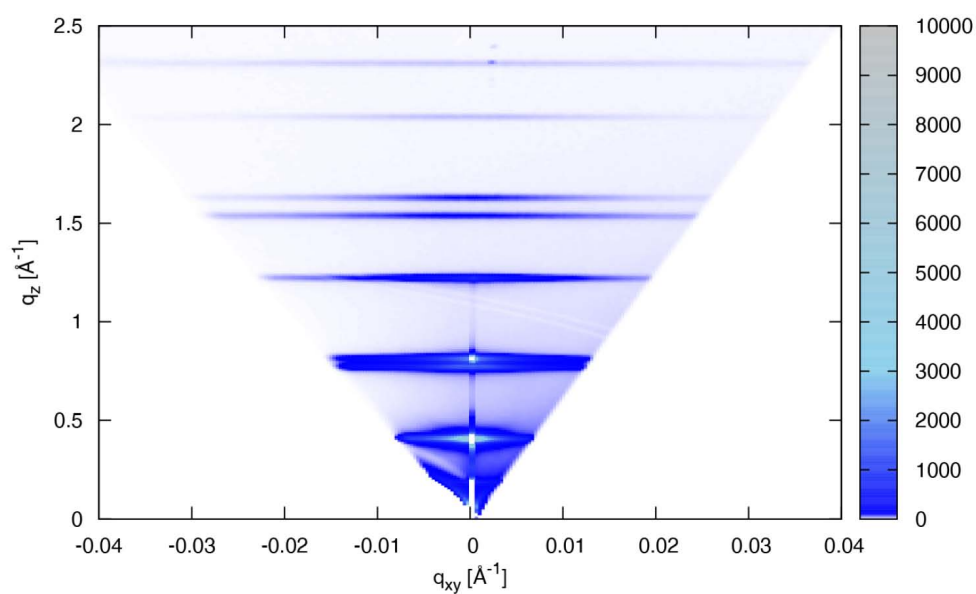
GIXS measurement of the pentacene- C_{60} bilayer. The indices show the calculated positions for hcp stacking of fullerene C_{60} . Clearly the measured features cannot account for such a crystal structure.



Submitted to **ADVANCED MATERIALS**

Off-specular x-ray measurement:

The off-specular diffraction pattern of a pentacene-C₆₀ bilayer emphasizes the good crystallinity of both semiconductors (notice the scales of the in-plane and the out-of-plane components of the momentum vector q).



B.2 SUPPORTING INFORMATION FOR "TRANSFERABLE ORGANIC SEMICONDUCTOR NANOSHEETS FOR APPLICATION IN ELECTRONIC DEVICES"

Copyright WILEY-VCH Verlag GmbH & Co. KGaA, 69469 Weinheim, Germany, 2017.

ADVANCED MATERIALS

Supporting Information

for *Adv. Mater.*, DOI: 10.1002/adma.201606283

Transferable Organic Semiconductor Nanosheets for
Application in Electronic Devices

*Simon J. Noever, Michael Eder, Fabio del Giudice, Jan
Martin, Franz X. Werkmeister, Stefan Hallwig, Stefan Fischer,
Oliver Seeck, Nils-Eike Weber, Clemens Liewald, Fritz
Keilmann, Andrey Turchanin,* and Bert Nickel**

SUPPORTING INFORMATION

**Transferable organic semiconductor nanosheets
for application in electronic devices**

*Simon J. Noever, Michael Eder, Fabio del Giudice, Jan Martin, Franz Werkmeister, Stefan Hallwig,
Stefan Fischer, Oliver Seeck, Nils-Eike Weber†, Clemens Liewald, Fritz Keilmann,
Andrey Turchanin* and Bert Nickel**

Dr. Simon J. Noever, Michael Eder, Stefan Fischer, Fabio del Giudice, Jan Martin,
Stefan Hallwig, Clemens Liewald, Franz Werkmeister, Dr. Fritz Keilmann, PD. Dr. Bert Nickel
Faculty of Physics and CeNS, Ludwig-Maximilians-Universität München, 80539 Munich,
Germany

Simon J. Noever, Clemens Liewald, PD. Dr. Bert Nickel
Nanosystems Initiative Munich (NIM), 80799 Munich, Germany
E-mail: nickel@physik.uni-muenchen.de

Dr. Oliver Seeck
Deutsches Elektronen Synchrotron DESY, 22603 Hamburg, Germany

Dr. Nils-Eike Weber
Faculty of Physics, University of Bielefeld, 33615 Bielefeld, Germany
Present Addresses: † Scienta Omicron GmbH, 65232 Taunusstein, Germany

Prof. Dr. Andrey Turchanin
Institute of Physical Chemistry, Friedrich-Schiller-Universität Jena, 07743 Jena, Germany
Jena Center for Soft Matter (JCSM), 07743 Jena, Germany
Center for Energy and Environmental Chemistry Jena (CEEC), 07743 Jena, Germany
Abbe Center of Photonics (ACP), 07745 Jena
E-mail: andrey.turchanin@uni-jena.de

Experimental

Sample preparation: For all experiments, the pentacene (Sigma Aldrich triple sublimed, additionally purified by Creaphys) thin films were deposited at a rate of $\sim 0.1 \text{ \AA s}^{-1}$ under equal conditions. Sample temperatures were held at room temperature, while the chamber pressure was kept below $1 \cdot 10^{-7}$ mbar. The Si/SiO₂ substrates were cleaned *via* sonicating in acetone and isopropanol for 10 minutes, respectively. After thorough rinsing with DI water, the substrates were plasma cleaned using oxygen plasma (50 W for 30 s, LabAsh).

The PVA layers were produced using the following protocol: first a 5 % PVA (Fluka Polyvinyl alcohol 6-98) solution in DI water was prepared *via* stirring at 800 rpm at 75 °C for 3 hours. Afterwards, the solution was filtered using a standard folded paper filter, and spincast onto the substrates (here, oxidized, highly doped Si wafers) for 60 seconds at 4000 rpm, leading to layer thicknesses of ~ 200 nm. The brass sheet in Fig. 2 was cleaned with acetone and isopropanol prior to lamination with the pentacene film.

The gold structures for the SNOM samples (cf. SI) were defined *via* positive photolithography. First the sample surfaces were coated by LOR 3B (MicroChem) at 4000 rpm and soft baked for 3 minutes at 150 °C. A layer of S1813 G2 (Microposit) was spincast at 5000 rpm followed by a 3 minute soft bake at 115 °C. This photoresist was illuminated by a Karl Suss Maskaligner MJB3 and developed with Microposit 351 Developer, diluted with DI water 1:3. The structures (3 nm Cr, followed by 50 nm Au) were deposited *via* electron beam deposition at $\sim 1 \text{ \AA s}^{-1}$. For the lift off, Microposit 1165 remover was used, followed by rinsing in acetone and IPA.

Characterization: GIXD measurements were taken at the P08 beamline at PETRA III / DESY in Hamburg using an X-ray energy of 18 keV. The diffraction signal was recorded using a Perkin Elmer XRD 1621 detector. An oxidized Si wafer with a 300 nm SiO₂ layer served as substrate.

For the UV-VIS measurements, 50 nm pentacene films were deposited on fused silica, *i.e.* transparent glass substrates. The absorbance spectra were recorded using a PerkinElmer Lambda EZ201 spectrometer in wavelength scan mode. Each measurement was corrected by a baseline recorded with cleaned and bare silica substrates.

Vibrational spectroscopy data were recorded using a Nicolet Nexus FTIR equipped with a ThermoFisher SAGA grazing incidence accessory. A 23 nm pentacene layer was deposited onto a 100 nm Au film. Before each FTIR measurement, the atmosphere was allowed to stabilize for 10 minutes, and no nitrogen or dry air purge was used. Background spectra were recorded from a clean Au film and used for the automatic baseline correction of the Omnic v6.2 software.

The AFM micrographs were measured in tapping mode with a Veeco Dimension 3100 AFM and analyzed using Gwyddion 2.40. The SEM images were taken at a Zeiss-LEO 982.

Helium ion microscopy was conducted with a Carl Zeiss Orion Plus instrument employing secondary electrons collected by an Everhart-Thornley detector. For this image, the film was grown on a 300 nm Au/mica substrate, crosslinked *via* a high dose flood gun (electron energy: 300 eV, dose: 250 mC/cm²) and transferred onto an oxidized Si wafer.

Transistor characteristics were recorded *via* a Keithley Instruments Source Meter 2612. The transfer curves in Fig. 4 were measured under high vacuum. The transistor had a channel width of 2 mm and a channel length of 50 μm. The contact resistance measurements were taken under

ambient conditions. The transistor layouts for the contact resistance measurements were Generation 4 test wafers, purchased from the Fraunhofer IPMS, which were cleaned using the same protocol as all Si/SiO₂ substrates. The gate-dielectric substrate consisted of n-doped Si ($n \sim 3E17 \text{ cm}^{-3}$) topped by a 230 nm thick SiO₂ thermal oxide layer. 30 nm Au on a high work function ITO (indium tin oxide) adhesion layer served as source and drain contacts. The pentacene nanosheets were transferred to the test pads as described in Fig. 1 and stored in a desiccator to remove residual water.

Table T1: Specifications of crosslinked samples from main manuscript

Sample	electron energy	Emission current	irradiation time	approx. dose
GIXS sample 1	300 eV	5 mA	1200 seconds	3.0 mC/cm ²
GIXS sample 2	800 eV	5 mA	1200 seconds	3.0 mC/cm ²
TFT sample 1	350 eV	5 mA	600 seconds	1.5 mC/cm ²
TFT sample 2	700 eV	5 mA	1800 seconds	4.5 mC/cm ²
Spectroscopy sample 1	500 eV	2 mA	1200 seconds	3.0 mC/cm ²
Spectroscopy sample 2	1000 eV	2 mA	1200 seconds	10.3 mC/cm ²
All other samples	500 eV	5 mA	1200 seconds	3.0 mC/cm ²

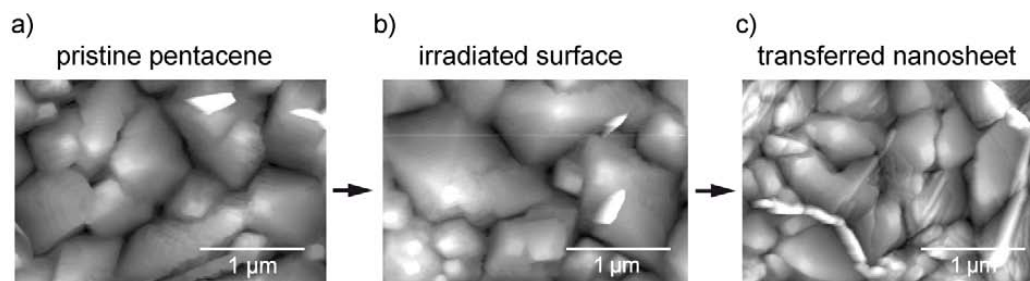


Figure S1: AFM micrographs of pristine, irradiated and transferred pentacene surface. a) The AFM height micrograph shows typical pyramidal growth mode of pentacene. b) After irradiation by a low energy electron (LEE) beam, AFM image indicates unchanged pentacene topography. c) After transfer to a new substrate, AFM image shows slightly disturbed topography from the transfer and drying, but otherwise unchanged characteristics. The z-scale for all AFM micrographs is 50 nm, the film thickness is 50 nm in all cases.

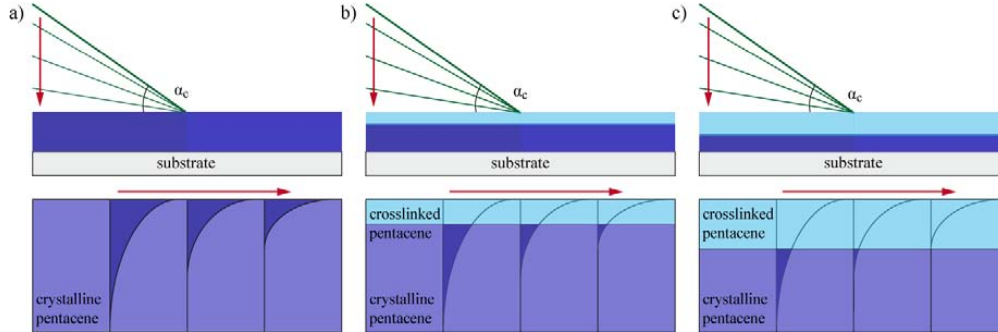


Figure S2: GIXD measurements Scheme of the grazing angle dependent penetration depth of the evanescent wave into pristine and crosslinked surfaces. The angle of incidence α_i controls the probe depth of the X-ray beam. Here, different angles below the critical angle for total reflection α_c are shown. With decreasing angle, the probe depth is more and more confined to the surface region.

The fitted total intensities of the scattered beam are calculated by the product of transmission functions and the structure factor as follows:

$$I = |T_i^2 |S_{-p}| T_f^2 |$$

The transmission functions calculate to:

$$T_{i,f} = \frac{2 \sin \alpha_{i,f}}{\sin \alpha_{i,f} + \sqrt{\sin^2 \alpha_{i,f} - \sin^2 \alpha_c}}$$

while the structure factor is given by the following term:

$$S_{-p} = \frac{\left| e^{\frac{-pa}{\Delta}} - e^{-iNQ_z a} \right|^2}{|1 - e^{-iQ_z a}|^2}$$

with p dead layers on top of the sample surface. N is the number of molecular layers within the film thickness (here, $N = 33$), Δ is the scattering depth of the evanescent wave, and $a = 15.4 \text{ \AA}$ is the lattice spacing in z -direction. $Q_z = q_z - 0.1909 \text{ \AA}^{-1}$ is the momentum transfer parallel to the sample surface normal of the examined peak, corrected by the tilt of the unit cell with respect to said surface. This tilt was extracted from the detector image position of the first truncation rod peak, which is positioned at the sample horizon for upright crystal structures. The momentum

transfer can be calculated to:

$$q_z = k_i^z - k_f^z = \frac{2\pi}{\lambda} \left[\sqrt{\sin^2 \alpha_i - 2\delta - 2i\beta} + \sqrt{\sin^2 \alpha_f - 2\delta - 2i\beta} \right], \text{ with } 2\delta = \sin^2 \alpha_c, \text{ and } 2i\beta =$$

$i \frac{\mu\lambda}{2\pi}$, where $\mu = 5.8 \cdot 10^{-9} \text{\AA}^{-1}$ is the absorption factor (data taken from henke.lbl.gov). The

scattering depth of the evanescent wave calculates to:

$$\Delta = \frac{\lambda}{2\pi(l_i + l_f)}, \text{ with } l_{i,f} = \frac{\sqrt{2}}{2} \sqrt{(2\delta - \sin^2 \alpha_{i,f}) + \sqrt{(\sin^2 \alpha_f - 2\delta)^2 + (2\beta)^2}}.$$

$\alpha_c = 0.0915^\circ$ is the critical angle for pentacene (measured via X-ray reflection. α_i is the angle of incidence. The diffraction angle $\alpha_f = 1.149^\circ$ was extracted from the detector data. The wavelength was set to $\lambda = 0.6888 \text{\AA}$, i.e. a photon energy $E_{ph} = 18 \text{keV}$, for all experiments. For the whole fit, surface roughness and grain topography as well as exponential decay of electron beam inside the film are neglected. The fit parameters were the number of dead layers p and a scaling factor to normalize the intensities.

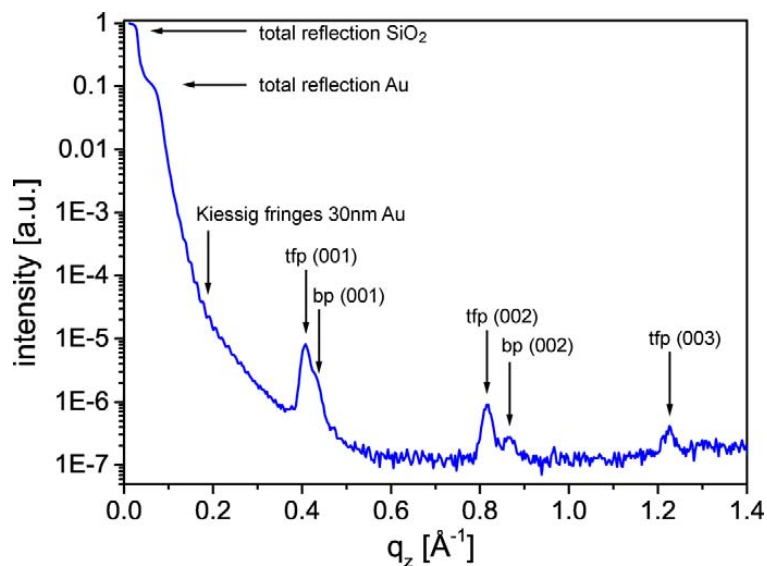


Figure S3: Crystallinity of transferred pentacene. In-house specular X-ray reflectometry measurement of crystalline pentacene after film transfer to an SiO₂ substrate with Au transistor structures. The dominant pentacene polymorph is thin film phase (tfp). The small bulk phase (bp) features are probably due to long storage. The overall small intensity of the Bragg features is due to the low signal to noise ratio (in-house compared to synchrotron) and the small flake size of ~ 2 μm .

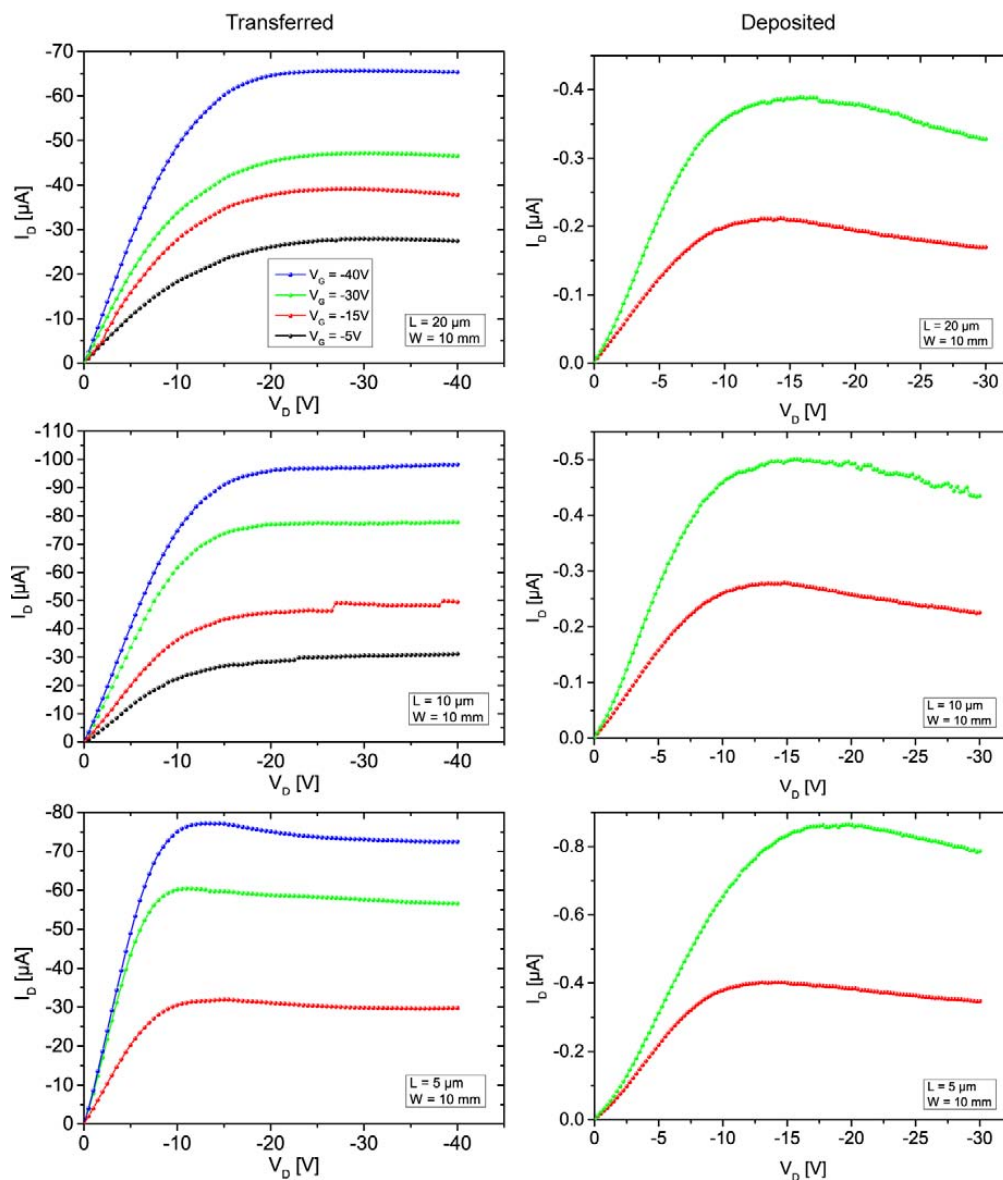


Figure S4: Output characteristics of transferred and deposited FETs for contact resistance evaluation. The source-drain sweeps were measured at room temperature under ambient conditions. From them, the necessary data is extracted to calculate the channel resistances, discussed in the main text.

B.3 SUPPORTING INFORMATION FOR "SUB-MONOLAYER PERCOLATION OF PENTACENE ON ROUGH PARYLENE-C DIELECTRICS"

SUPPORTING INFORMATION

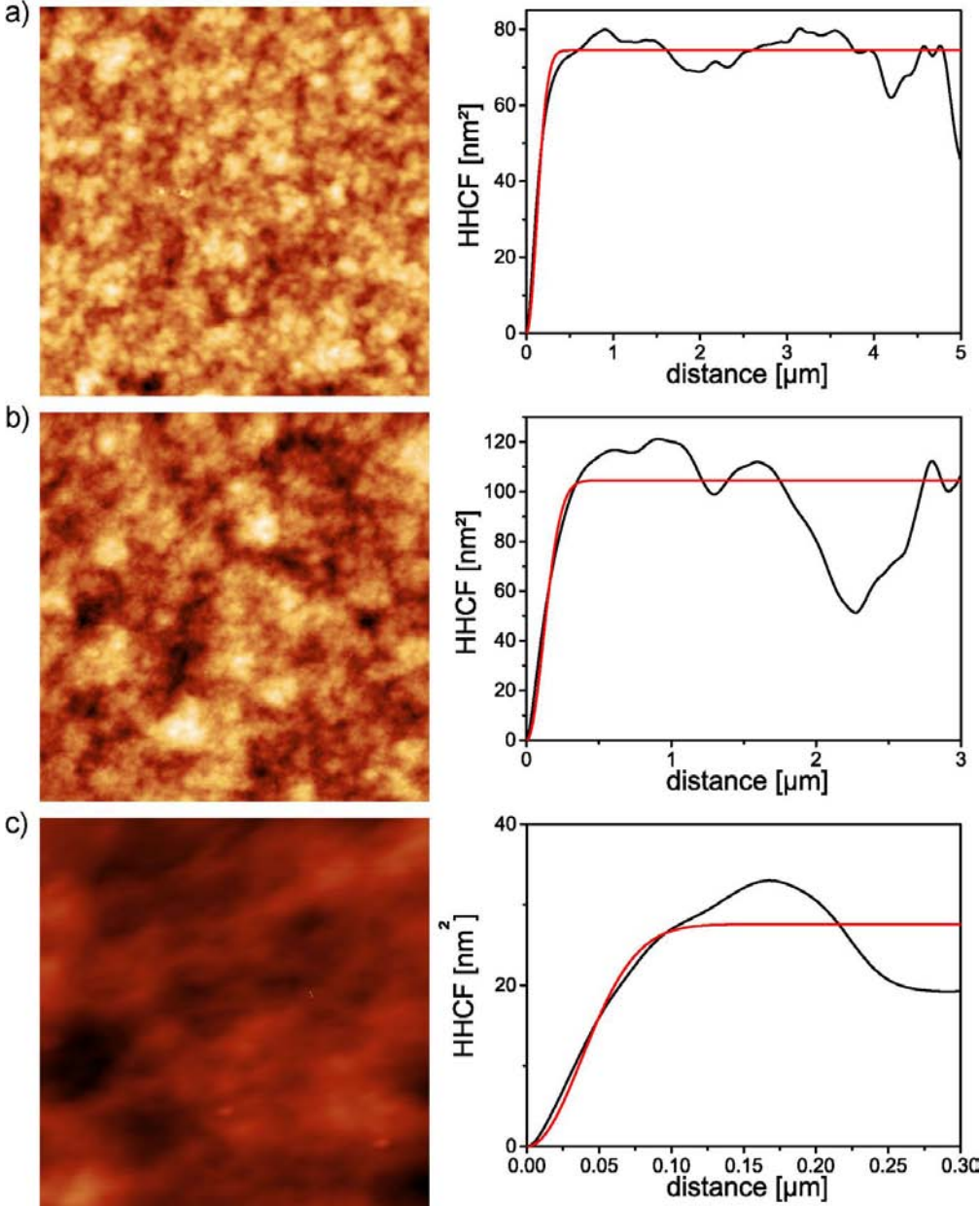


Figure S1. Height-height-correlation-function (HHCF) analysis of AFM micrographs of different sizes. a) 5x5 μm micrograph and the respective HHCF (black) with Gaussian fit (red). From the fit, the correlation length is 169 nm and the rms 6.0 nm. b) 3x3 μm micrograph and the respective HHCF (black) with Gaussian fit (red). From the fit, the correlation length is 167 nm and the rms 7.2 nm. c) 0.3x0.3 μm micrograph and the respective HHCF (black) with Gaussian fit (red). From the fit, the correlation length is 53 nm and the rms 3.7 nm. The significant drop in rms roughness and correlation length with decreased scan size implies that one would need to measure at even smaller length scales, i.e. beyond the resolution limit of our AFM, to evaluate the surface with respect to molecular ordering. The height scale for all micrographs is 50 nm.

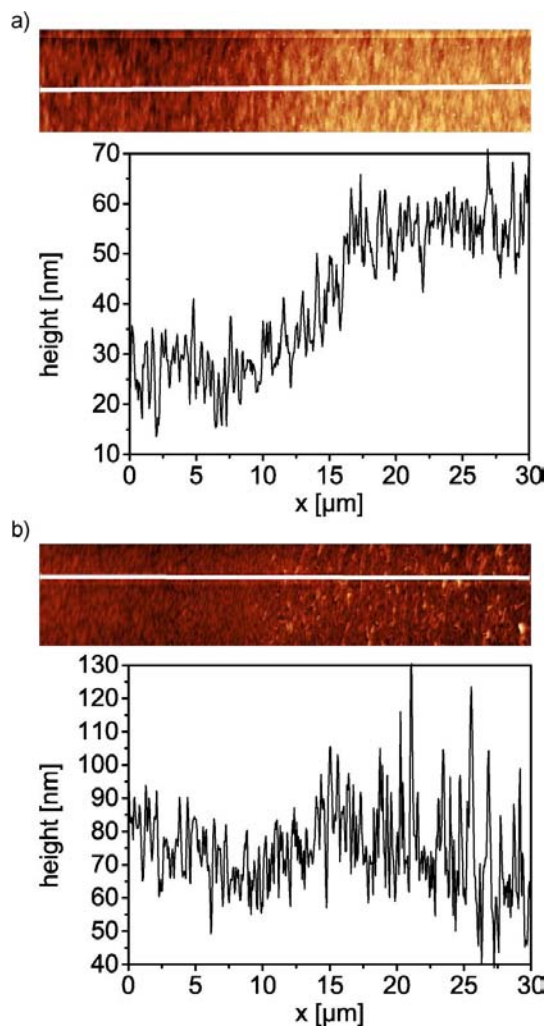


Figure S2. Height profiles of Au electrode edges on parylene-C surface. a) AFM micrograph (length: 30 μm , scale: 80 nm) of the pure gold electrode grown on parylene-C and a profile cut from left to right. The 30 nm Au electrode edge is clearly visible in the profile. b) AFM micrograph (length: 30 μm , scale: 170 nm) of the Au electrode edge topped with a 50 nm layer of pentacene and a profile cut from left to right. The 30 nm Au electrode can be discerned in the profile, while it is difficult to see it beneath the

pentacene layer in the topography image due to plane correction. Only the change in pentacene growth indicates the subjacent electrode. The white lines in the AFM micrographs indicate the profile positions.

B.4 SUPPORTING INFORMATION FOR " α,ω -DIHEXYL-SEXTHIOPHENE THIN FILMS FOR SOLUTION-GATED ORGANIC FIELD-EFFECT TRANSISTORS"

SUPPLEMENTARY INFORMATION

 α,ω -Dihexyl-sexithiophene thin films for solution-gated organic field-effect transistorsHannah Schamoni,¹ Simon Noever,² Bert Nickel,² Martin Stutzmann,¹ and Jose A. Garrido^{1,*}¹*Walter Schottky Institut and Physik-Department,**Technische Universität München, Am Coulombwall 4, 85748 Garching, Germany*²*Fakultät für Physik, Ludwig-Maximilians-Universität München,**Geschwister-Scholl-Platz 1, 80539 München, Germany*

(Dated: April 30, 2015)

The amphifunctional model

Charges and potentials at the organic semiconductor-electrolyte interface are responsible for the pH and ion sensitivity of solution-gated organic field-effect transistors (SGOFETs). The site-binding model is employed to describe the surface charge due to ionizable surface groups.¹ In this model, surface atoms, represented by A, and water molecules in the solution form amphoteric surface groups AH, which can either release or take up a proton, depending on the pH of the solution. The dissociation constant K_a is given by

$$K_a = \frac{[A^-] \cdot [H^+]_{surf}}{[AH]},$$

where $[A^-]$ and $[AH]$ are the concentrations of the deprotonated and protonated surface sites, respectively. The number of deprotonated surface groups depends on the pK_a of the corresponding moieties and on the local pH at the interface via

$$N_{A^-} = N_S / (1 + 10^{pK_a + \log([H^+]_{surf})}),$$

yielding a charge due to protonated species of $\sigma_{A^-} = -eN_{A^-}$ where e is the elementary charge. N_S is the total number of ionizable surface sites. $[H^+]_{surf}$ is the proton activity at the surface, which is related to proton activity in the bulk of the solution $[H^+]_{bulk}$ via a Boltzmann factor,

$$[H^+]_{surf} = [H^+]_{bulk} \cdot \exp\left(-\frac{e\varphi_0}{k_B T}\right),$$

with φ_0 being the surface potential, k_B being the Boltzmann constant and T the temperature.

A second charging mechanism of the organic surface is the specific adsorption of hydroxide ions.² The resulting charge σ_{ads} is described by the Freundlich isotherm on a heterogeneous hydrophobic surface:³

$$\sigma_{ads} = -eN_0 \left(\frac{[OH^-]_{surf}}{[OH^-]_0} \right)^{k_B T / Q^*}$$

Q^* is a decay constant, and the maximum hydrogen concentration $[OH^-]_0$ in an aqueous solution is about 1 mol/L. Furthermore, the electric charge in the organic semiconductor σ_{elec} is taken into account,⁴ which is controlled by the gate voltage U_G and related to the double layer capacitance C_{dl} and the surface potential via

$$\sigma_{elec} = C_{dl}(U_G - \varphi_0).$$

Altogether, charge neutrality between σ_{elec} , the surface charge $\sigma_{surf} = \sigma_{ads} + \sigma_{A^-}$ and the charge in the diffuse layer σ_{diff} has to be ensured:

$$\sigma_{elec} + \sigma_{surf} + \sigma_{diff} = 0$$

By solving the equations given above for the surface potential φ_0 , the response of the transistor to changes in the pH or ion concentration in the electrolyte can be simulated.

Optical characterization by UV-Vis spectroscopy of DH6T thin films

The absorption spectra of DH6T thin films deposited at different substrate temperatures T_{sub} are shown in Figure S1a. From all spectra, a baseline was subtracted to normalize them to the absorption at the absorption edge. The peak intensity of the peaks at 3.3 eV and 4.3 eV is defined as the difference in intensity between the dip at 3.6 eV and the respective peak. In Figure S1b, both average peak intensities are plotted as a function of the substrate temperature. The interpretation of the influence of T_{sub} can be found in the main text.

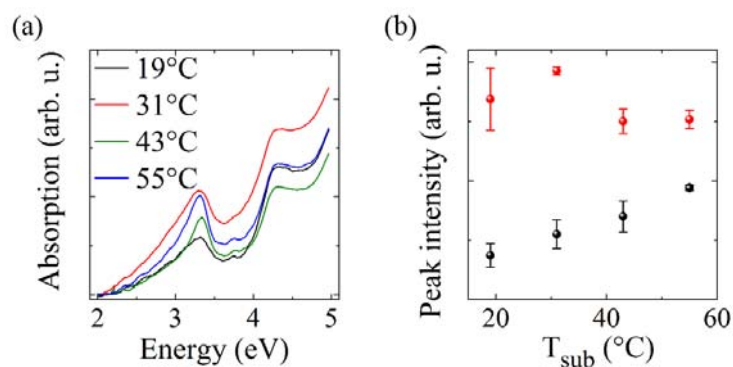


Figure S1: Optical characterization by UV-Vis spectroscopy of 30 nm thick DH6T films deposited at different substrate temperatures. (a) Absorption spectra. (b) Average intensity of the peaks at 3.3 eV (black symbols) and 4.3 eV (red symbols) as a function of T_{sub} .

Electrochemical impedance spectroscopy

Figure S2 displays electrochemical impedance spectroscopy data of a SGOFET, showing the magnitude of the impedance and its phase as a function of the frequency of the applied AC voltage in a Bode plot. During the measurement, a DC voltage of -0.4 V vs. the Ag/AgCl reference electrode was applied; this potential is larger than the threshold voltage, and thus sufficient to induce the hole conductive channel at the semiconductor's surface. Between 0.1 Hz and 100 Hz, the phase is close to -90° , which indicates a mostly capacitive behavior of the semiconductor-electrolyte interface in this frequency range.

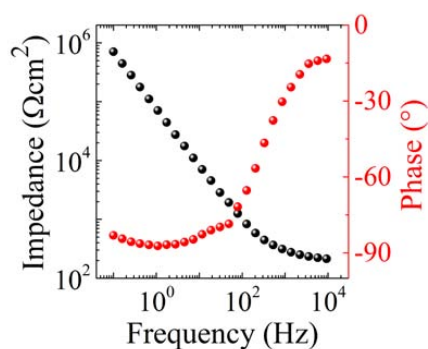


Figure S2: Electrochemical impedance spectroscopy data of a SGOFET visualized in a Bode plot, showing the magnitude of the impedance (black symbols) and its phase (red symbols).

References

- ¹ D. E. Yates, S. Levine, and T. W. Healy, *J. Chem. Soc., Faraday Trans. 1* **70**, 1807 (1974).
- ² K. G. Marinova, R. G. Alargova, N. D. Denkov, O. D. Velev, D. N. Petsev, I. B. Ivanov, and R. P. Borwankar, *Langmuir* **12**, 2045-2051 (1996).
- ³ H.-J. Butt, K. Graf, and M. Kappel, *Physics and chemistry of interfaces*, Physics textbook (Wiley-VCH, Weinheim, 2006).
- ⁴ J. Duval, J. Lyklema, J. M. Kleijn, and H. P. van Leeuwen, *Langmuir* **17**, 7573-7581 (2001).

B.5 SUPPORTING INFORMATION FOR "SURFACE-DIRECTED MOLECULAR ASSEMBLY OF PENTACENE ON AROMATIC ORGANOPHOSPHONATE SELF - ASSEMBLED MONOLAYERS EXPLORED BY POLARIZED RAMAN SPECTROSCOPY"

SUPPORTING INFORMATION

Surface-Directed Molecular Assembly of Pentacene on Aromatic Organophosphonate Self-Assembled Monolayers Explored by Polarized Raman Spectroscopy

Sara Yazji, Christian Westermeier, Dominik Weinbrenner, Matthias Sachsenhauser, Kung-Ching Liao, Simon Noever, Paolo Postorino, Jeffrey Schwartz, Gerhard Abstreiter, Bert Nickel, Ilaria Zardo, and Anna Cattani-Scholz

Reflectometry measurements. A curved multilayer mirror was used to filter the $K\alpha$ line of a sealed Mo X-ray tube ($\lambda=0.71 \text{ \AA}$). The incident beam size was collimated to 0.2 mm times 7.5 mm by a slit system. The reflected intensity was recorded by a LaBr3 scintillation detector (FMB Oxford) in $\theta/2\theta$ geometry and was corrected for footprint effects. The Bragg equation $q_z = (4\pi/\lambda)\sin(\theta)$ was used to convert the scattering angle (2θ) into momentum transfer q_z . Reflectometry measurements are shown in Fig. S1.

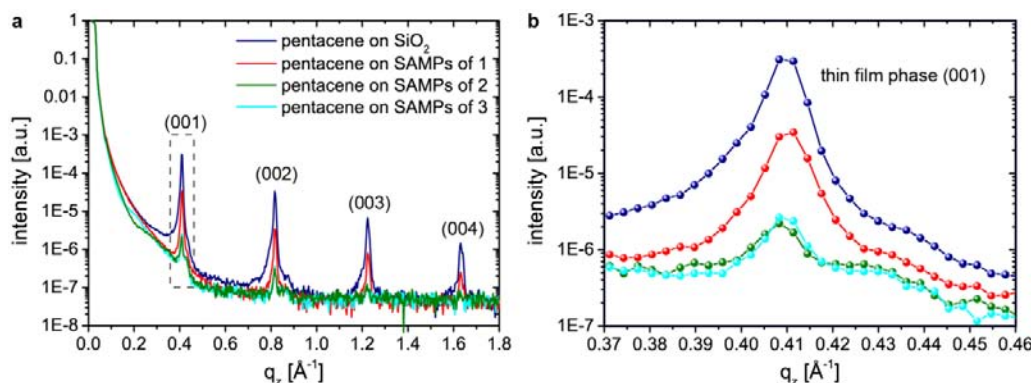


Fig. S1 (a) Reflectometry measurement of pentacene layers on bare SiO_2 , and on SAMPs of 1-3, as indicated. The Bragg peak series originates from the so-called thin-film phase of pentacene in (00L) direction. (b) Close-up of the (001) peak. The intensity is highest for pentacene grown on plain SiO_2 .

Electrical measurements. A comparison of devices based on pentacene films deposited on SAMP of 2 treated substrate with those devices deposited on the untreated, plain SiO_2 substrate clearly demonstrates the drastic effect of the SAMP interface on charge transport within the pentacene layer on top. In this study, six transistors each were fabricated in parallel on SAMP of 2 and on plain SiO_2 substrates. Since the transfer curves of the six transistors within each batch were very similar, representative characteristics of one transistor on SAMP of 2 and of one transistor on plain SiO_2 are shown in Fig. S2. All the devices built on the untreated SiO_2 substrate do not show a well-behaved transistor characteristic since the transistor current ISD between source and drain cannot be properly suppressed by the applied gate voltage VGS, as shown in Figure S2a. Here, a persistent accumulation of positive charge carriers, i.e. holes, within the pentacene film is presumably induced by localized negative charges inside deep trap states at the dielectric-semiconductor interface, whereby the electric field associated with the applied gate voltage is screened and the transistor current cannot be controlled appropriately. This situation drastically changes due to functionalization of the SiO_2 dielectric with SAMP of 2 (see Fig. S2b). Through this, the so-called threshold voltage of the transistor is shifted towards zero gate voltage and the transfer characteristics exhibit a well-defined on-off-behavior (see Fig. S2c). At the same time, the hysteresis of the characteristic curves is increased, which indicates an increased density of shallow traps at the dielectric-semiconductor interface

associated with the SAMP coverage. Corresponding to the trap-and-release model, the density of shallow trap states, that can be thermally released, also determines the mobility of charge carriers in organic semiconductors.¹ Thus, the increased hysteresis due to shallow traps is in line with a reduced charge carrier mobility of $1.7 \times 10^{-3} \text{ cm}^2\text{V}^{-1}\text{s}^{-1}$ for samples based on SAMP treated dielectric compared to $3 \times 10^{-2} \text{ cm}^2\text{V}^{-1}\text{s}^{-1}$ on plain SiO_2 . These values of the carrier mobility are obtained in the linear regime as well as in the saturation regime of the devices as described by Nickel et al.² Obviously, the presence of the SAMP on top of the SiO_2 dielectric prevents the disadvantageous influence of deep trap states at the SiO_2 surface in our system. However, the phosphonic acid groups at the distal ends of the SAMP seem to act as shallow charge traps within the active channel of the transistor.

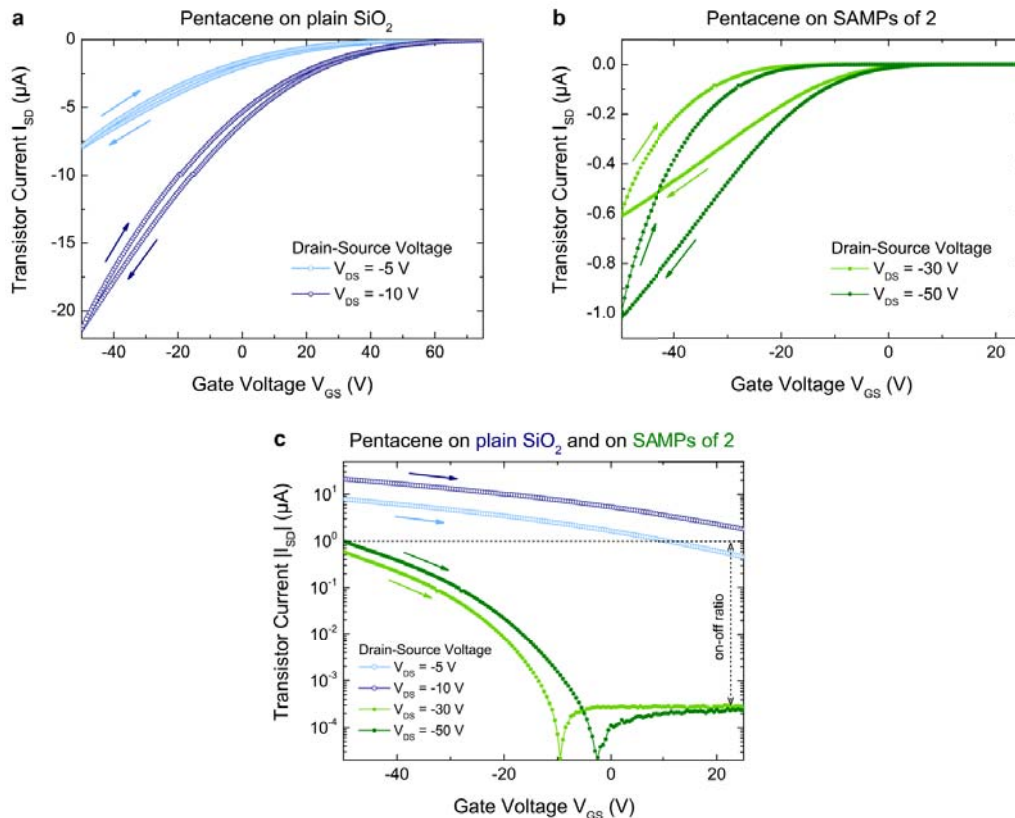


Fig. S2 Transfer characteristics for devices based on a pentacene film deposited on plain SiO_2 (a) and deposited on SAMPs of 2 (b). Comparison of transfer characteristics for both types of devices, i.e. on plain SiO_2 and on SAMPs of 2 (c). The sweep direction is indicated by arrows as well as the on-off ratio, which is only well-defined for the devices on SAMPs of 2.

Raman spectroscopy.

In the frame of this work we have used Raman spectroscopy to first elucidate, by spatially resolved Raman measurements, morphological variations in pentacene growth on different modified dielectrics. Furthermore we have applied it to measure, by analyzing the splitting of the intramolecular modes (Davydov splitting) two fundamental parameters that influence charge transport in organic semiconductor thin-films: intermolecular interactions and relaxation energies. Finally we have carried out a detailed study, by angle-dependent, polarized Raman spectroscopy, of the optical anisotropy observed for pentacene grown on bare silicon oxide and for pentacene deposited on SAMPs of 2.

Spatially resolved Raman spectroscopy.

Spatially resolved Raman measurements were made on pentacene grown on the control SiO_2 substrate and SAMP-modified surfaces to determine crystallite grain size and density structure, and were compared with AFM scanning data (Fig. 2 and Table S1). Spectra were measured every 250 nm over a $10 \mu\text{m}$ line to evaluate grain size from intensity variation with position change; spectra were collected with the same integration time of 60 s and at a fixed excitation power. As an

example, a representative Raman spectrum³ collected from pentacene deposited on SiO₂ is shown on Fig. S3. A multi-Lorentzian fitting analysis was done to extract the integrated intensity of the short axis mode centered at ca. 1376 cm⁻¹. This mode describes molecular vibration along the short axis of the pentacene molecule, and is an aromatic C-C stretching mode with Ag symmetry. Integrated intensities of this short axis mode for all samples are depicted in Figure 2 as a function of the laser position. It is clear that the control sample exhibits the largest variation in this intensity, 83% (Fig. 2a). In contrast, pentacene on SAMPs from 1 and 2 showed intensity variations of 50%, while pentacene on the SAMP from 3 showed intensity variations of 60%. These results are in line with the reduced size of the crystallites as probed by the laser beam, but they also indicate an increased homogeneity in the orientation of the pentacene crystallites on the SAMP-modified surface. Furthermore, since resolution is controlled by the laser spot size (diameter ca. 840 nm), quantitative information on the grain size of the control sample can be obtained. Integrated intensities were analyzed as a function of laser position with a multi-Gaussian fit. The resulting full-width-half-maxima (FWHM) of the peaks correlate with the pentacene grain size; the peaks replicate the landscape of the sample surface. In this way it was found that the FWHM of these peaks range between 0.45 and 1.98 μm for all the samples, in good agreement with the large grains observed via AFM, which also validates Raman spectroscopy as a method to probe pentacene film morphologies.

	Average height (nm)	Max. height (nm)	RMS roughness (nm)
Plain SiO ₂	43.6	89.9	13.3
SAMPs of 1	41.2	92.8	13.6
SAMPs of 2	40.7	86.6	13.8
SAMPs of 3	40.4	80	12.8

Table S1. Results of AFM roughness analysis, showing lower average and maximum heights for the more tightly packed SAMPs.

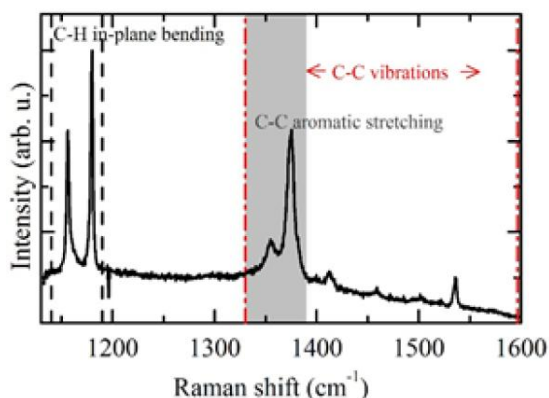


Fig. S3 Representative Raman spectrum collected from pentacene deposited on bare SiO₂, where peaks arising from different molecular vibrations are indicated.

Polarization dependence. To investigate the effect of SAMP structures on the degree of local molecular order in deposited pentacene films, polarization-dependent Raman measurements were made at different positions on the pentacene deposited on the untreated SiO₂ control (Fig. S4) and on pentacene deposited on SAMPs from 2 (Fig. S5). In both cases two components of the scattered light were collected with polarizations perpendicular to each other, H and V, as the polarization of the excitation was varied in steps of 20°.

The azimuthal dependence of the short axis was probed at the positions marked along the line scans where the short axis has different intensities. This was done to verify that different orientations of the pentacene crystallites were one possible origin of these different intensities. Indeed, this anisotropy α gives an indication of the degree of molecular order of the system, with $\alpha = (I_{max} - I_{min})/I_{max}$, and $\alpha = 1$ for purely ordered phases and $\alpha = 0$ for purely disordered phases. Raman intensities I_s can be described as a function of the crystal orientation via the Raman scattering tensor \mathfrak{R} and of the scattering geometry, i.e. excitation and scattered polarizations ϵ_i and ϵ_s , respectively (Equation 1).

$$I_s \propto |\varepsilon_i \cdot \mathfrak{R} \cdot \varepsilon_s|^2 \quad (1)$$

The polar plots obtained from pentacene deposited on SiO₂ (Figure S4) are well described by the Raman tensor of the A mode with triclinic symmetry, C1. In this case, \mathfrak{R} has the form as shown in Equation 2.

$$\mathfrak{R} = \begin{pmatrix} a & d & e \\ d & b & f \\ e & f & c \end{pmatrix} \quad (2)$$

The two components H and V of the scattered light exhibit different amplitudes, reflecting the components a , b , and d of the Raman tensor. The anisotropy values α ranged between 0.5 and 0.8. The ratio of the maximum intensity of the two components changed with position, which means that crystallites probed at these different positions were differently oriented with respect to the polarization direction of the incident light. This was also confirmed by the angular position of the maximum intensity, which gives an indication of the mean in-plane orientation of the pentacene backbones. Namely, the polar plots obtained at positions 1 and 2 in Figure S4 showed maxima rotated by about 30°. Additionally, the two components of the scattered intensity at positions 1 and 3 were 45° out of phase, indicating that the Raman tensor has off-diagonal elements. This is a further indication that pentacene with controlled thickness on SiO₂ crystallizes in a triclinic structure. In contrast, the polar plots that are obtained at different positions from pentacene that is deposited on SAMPs from 2 (Fig. S5) showed that the two components H and V of the scattered light always had a similar intensity and were 90° out of phase; this is expected for structures with higher symmetry, such as tetragonal. Indeed, they can be described by the Raman tensor of the A_{1g} mode of the form shown in Equation 3.

$$\mathfrak{R} = \begin{pmatrix} a & 0 & 0 \\ 0 & a & 0 \\ 0 & 0 & b \end{pmatrix} \quad (3)$$

The angular position of the maximum intensity of each component was the same within error at the different probed positions, indicating a similar orientation for the probed crystallites.

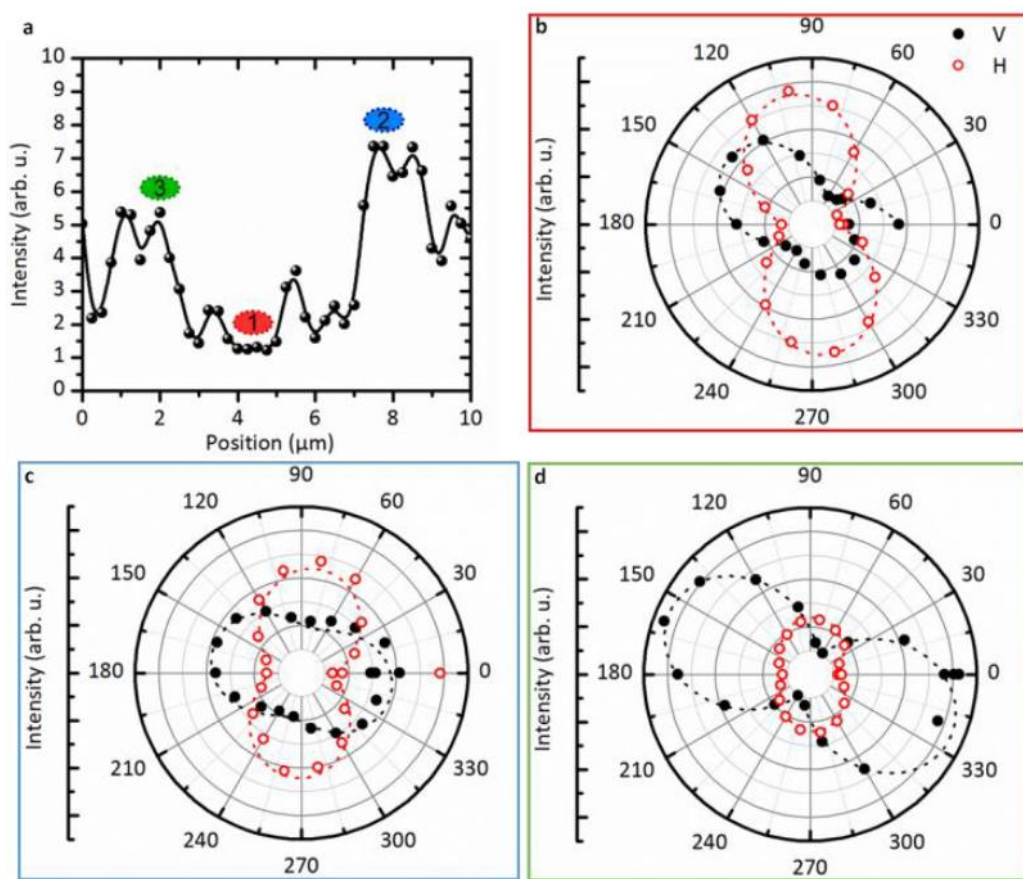


Fig. S4 (a) Integrated intensities of the short axis mode (black spheres) extracted from spatially resolved Raman spectroscopy scans along 10 mm of pentacene deposited on a reference of plain SiO₂. The solid line serves as a guide to the eye. Azimuthal dependence of the short axis mode at the positions 1 (b), 2 (c), and 3 (d) are marked in (a). The parallel (H) and perpendicular (V) components of the Raman signal with respect to the optical table plane are plotted as open and full circles, respectively. The dashed red and black lines are sine fits to the data.

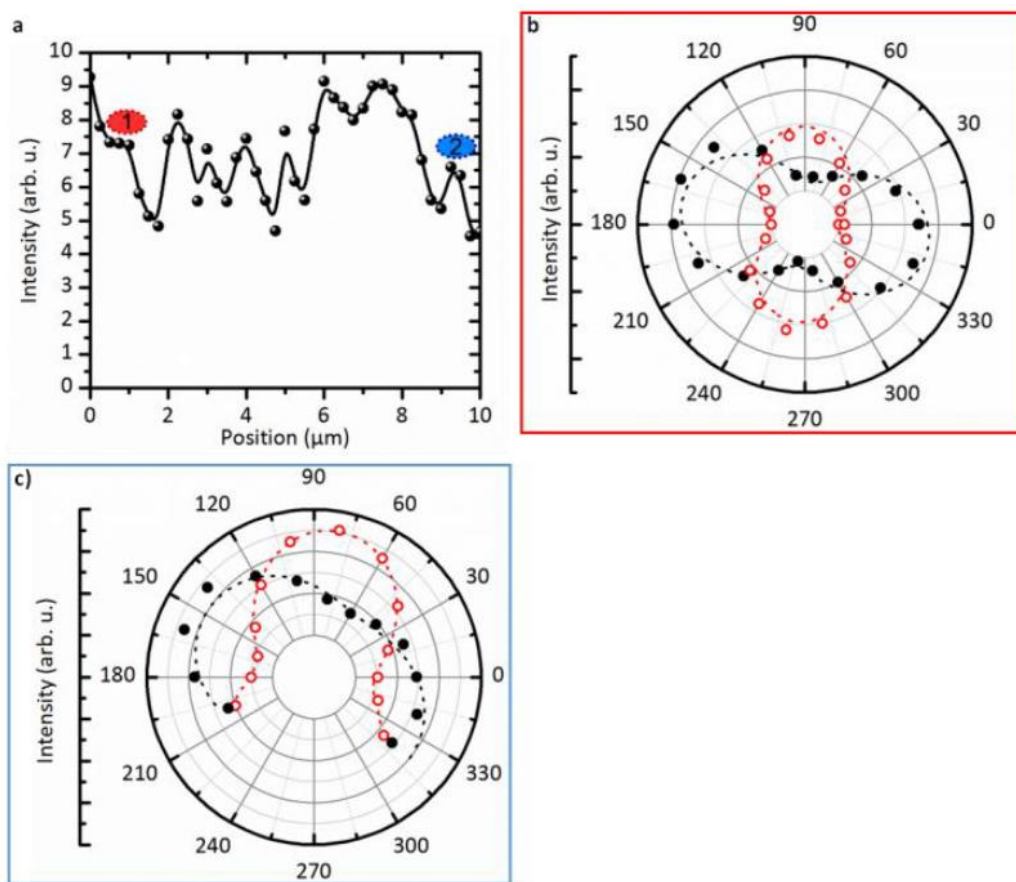


Fig. S5 (a) Integrated intensities of the short axis mode (black spheres) extracted from spatially resolved Raman spectroscopic scans over 10 μm on pentacene deposited on SAMPs of 2. The solid line serves as a guide to the eye. Azimuthal dependence of the short axis mode at the positions 1 (b), and 2 (c) are marked in (a). The parallel (H) and perpendicular (V) components of the Raman signal with respect to the optical table plane are plotted as open and full circles, respectively. The dashed red and black lines are sine fits to the data.

BIBLIOGRAPHY

- [1] S. J. Noever, S. Fischer, and B. Nickel. Dual channel operation upon n-channel percolation in a pentacene-c60 ambipolar organic thin film transistor. *Adv Mater*, 25(15):2147–51, 2013.
- [2] Franz X. Werkmeister, Simon J. Noever, and Bert A. Nickel. Sub-monolayer percolation of pentacene on rough parylene-c dielectrics. *Organic Electronics*, 26:439–442, 2015.
- [3] S. J. Noever, M. Eder, F. del Giudice, J. Martin, F. X. Werkmeister, S. Hallwig, S. Fischer, O. Seeck, N.-E. Weber, C. Liewald, F. Keilmann, A. Turchanin, and B. Nickel. Transferable organic semiconductor nanosheets for application in electronic devices. *Adv Mater*, 2017.
- [4] C. Liewald, S. Noever, S. Fischer, J. Roemer, T. Schuelli, and B. Nickel. Microdiffraction imaging - a suitable tool to characterize organic electronic devices. *AIMS Materials Science*, 2:369 – 378, 2015.
- [5] A. Guggenmos, M. Jobst, M. Ossiander, S. Radunz, J. Riemensberger, M. Schaffer, A. Akil, C. Jakubeit, P. Bohm, S. Noever, B. Nickel, R. Kienberger, and U. Kleineberg. Chromium/scandium multilayer mirrors for isolated attosecond pulses at 145 ev. *Opt Lett*, 40(12):2846–9, 2015.
- [6] H. Schamoni, S. Noever, B. Nickel, M. Stutzmann, and J.A. Garrido. Alpha,omega-dihexyl-sexithiophene thin films for solution-gated organic field-effect transistors. *Appl. Phys. Lett.*, 108(7):073301, 2015.
- [7] S. Yazji, C. Westermeier, D. Weinbrenner, M. Sachsenhauser, K.-C. Liao, S. Noever, P. Postorino, J. Schwartz, G. Abstreiter, B. Nickel, I. Zardo, and A. Cattani-Scholz. Surface-directed molecular assembly of pentacene on aromatic organophosphonate self - assembled monolayers explored by polarized raman spectroscopy. *J. Raman Spectrosc.*, 48(2):235–242, 2016.
- [8] Yifan Yao, Huanli Dong, and Wenping Hu. Charge transport in organic and polymeric semiconductors for flexible and stretchable devices. *Adv. Mater.*, pages n/a–n/a, 2015.
- [9] Martin Göllner, Georg Glasbrenner, and Bert Nickel. An electrochemical transducer based on a pentacene double-gate thin-film transistor. *Electroanalysis*, 24(2):214–218,

- 2012.
- [10] F. X. Werkmeister, T. Koide, and B. A. Nickel. Ammonia sensing for enzymatic urea detection using organic field effect transistors and a semipermeable membrane. *J. Mater. Chem. B*, 2016.
- [11] S. C. B. Mannsfeld, B. C. K. Tee, R. M. Stoltenberg, C. V. Chen, S. Barman, B. V. O. Muir, A. N. Sokolov, C. Reese, and Z. N. Bao. Highly sensitive flexible pressure sensors with microstructured rubber dielectric layers. *Nature Materials*, 9(10):859–864, 2010.
- [12] Tsuyoshi Sekitani and Takao Someya. Stretchable organic integrated circuits for large-area electronic skin surfaces. *MRS Bulletin*, 37(03):236–245, 2012.
- [13] M. Kaltenbrunner, T. Sekitani, J. Reeder, T. Yokota, K. Kuribara, T. Tokuhara, M. Drack, R. Schwodiauer, I. Graz, S. Bauer-Gogonea, S. Bauer, and T. Someya. An ultra-lightweight design for imperceptible plastic electronics. *Nature*, 499(7459):458–63, 2013.
- [14] Xiaohan Wu, Yan Ma, Guoqian Zhang, Yingli Chu, Juan Du, Yin Zhang, Zhuo Li, Yourong Duan, Zhongyong Fan, and Jia Huang. Thermally stable, biocompatible, and flexible organic field-effect transistors and their application in temperature sensing arrays for artificial skin. *Advanced Functional Materials*, 25(14):2138–2146, 2015.
- [15] J. Reeder, M. Kaltenbrunner, T. Ware, D. Arreaga-Salas, A. Avendano-Bolivar, T. Yokota, Y. Inoue, M. Sekino, W. Voit, T. Sekitani, and T. Someya. Mechanically adaptive organic transistors for implantable electronics. *Advanced Materials*, 26(29):4967–4973, August 2014.
- [16] M. Irimia-Vladu. "green" electronics: biodegradable and biocompatible materials and devices for sustainable future. *Chem Soc Rev*, 43(2):588–610, 2014.
- [17] B. C. Thompson and J. M. J. Frechet. Organic photovoltaics - polymer-fullerene composite solar cells. *Angewandte Chemie-international Edition*, 47(1):58–77, 2008.
- [18] S. Reineke, F. Lindner, G. Schwartz, N. Seidler, K. Walzer, B. Lussem, and K. Leo. White organic light-emitting diodes with fluorescent tube efficiency. *Nature*, 459(7244):234–U116, 2009.
- [19] Yanqin Miao, Zhixiang Gao, Hua Wang, Husheng Jia, Xuguang Liu, Bingshe Xu, and Bin Wei. Extremely high chromatic-stability white organic light-emitting device with symmetrical cascade emissive layer. *Organic Electronics*, 23:199–207, 2015.
- [20] Henning Sirringhaus. 25th anniversary article: Organic field-effect transistors: The path beyond amorphous silicon. *Advanced Materials*, 26(9):1319–1335, 2014.
- [21] F. Withers, O. Del Pozo-Zamudio, A. Mishchenko, A. P. Rooney, A. Gholinia, K. Watanabe, T. Taniguchi, S. J. Haigh, A. K. Geim, A. I. Tartakovskii, and K. S. Novoselov. Light-emitting diodes by band-structure engineering in van der waals heterostructures. *Nat Mater*, 14(3):301–306, 2015.
- [22] Xiaomu Wang and Fengnian Xia. Van der waals heterostructures: Stacked 2d materials shed light. *Nat Mater*, 14(3):264–265, 2015.
- [23] Eiji Kuwahara, Haruka Kusai, Takayuki Nagano, Toshio Takayanagi, and Yoshihiro

- Kubozono. Fabrication of a logic gate circuit based on ambipolar field-effect transistors with thin films of c60 and pentacene. *Chemical Physics Letters*, 413(4-6):379–383, 2005.
- [24] S. D. Wang, K. Kanai, Y. Ouchi, and K. Seki. Bottom contact ambipolar organic thin film transistor and organic inverter based on c60/pentacene heterostructure. *Organic Electronics*, 7(6):457–464, 2006.
- [25] Constance Rost, Siegfried Karg, Walter Riess, Maria Antonietta Loi, Mauro Murgia, and Michele Muccini. Ambipolar light-emitting organic field-effect transistor. *Applied Physics Letters*, 85(9):1613, 2004.
- [26] Jana Zaumseil, Richard H. Friend, and Henning Sirringhaus. Spatial control of the recombination zone in an ambipolar light-emitting organic transistor. *Nature Materials*, 5(1):69–74, 2005.
- [27] R. Capelli, F. Dinelli, M. A. Loi, M. Murgia, R. Zamboni, and M. Muccini. Ambipolar organic light-emitting transistors employing heterojunctions of n-type and p-type materials as the active layer. *Journal of Physics: Condensed Matter*, 18(33):S2127–S2138, 2006.
- [28] Ebinazar B. Namdas, Peter Ledochowitsch, Jonathan D. Yuen, Daniel Moses, and Alan J. Heeger. High performance light emitting transistors. *Applied Physics Letters*, 92(18):183304, 2008.
- [29] Hirotake Kajii, Hitoshi Tanaka, Yusuke Kusumoto, Takahiro Ohtomo, and Yutaka Ohmori. In-plane light emission of organic light-emitting transistors with bilayer structure using ambipolar semiconducting polymers. *Organic Electronics*, 16:26–33, 2015.
- [30] Fatemeh Maasoumi, Mujeeb Ullah, Paul E. Shaw, Jun Li, Paul L. Burn, Paul Meredith, and Ebinazar B. Namdas. Charge transport and recombination in heterostructure organic light emitting transistors. *Organic Electronics*, 25:37–43, 2015.
- [31] C. Deibel, T. Strobel, and V. Dyakonov. Role of the charge transfer state in organic donor-acceptor solar cells. *Adv Mater*, 22(37):4097–111, 2010.
- [32] M. Linares, D. Beljonne, J. Cornil, K. Lancaster, J. L. Bredas, S. Verlaak, A. Mityashin, P. Heremans, A. Fuchs, C. Lennartz, J. Ide, R. Mereau, P. Aurel, L. Ducasse, and F. Castet. On the interface dipole at the pentacene-fullerene heterojunction: A theoretical study. *Journal of Physical Chemistry C*, 114(7):3215–3224, 2010.
- [33] N. Koch. Electronic structure of interfaces with conjugated organic materials. *Physica Status Solidi-Rapid Research Letters*, 6(7):277–293, 2012.
- [34] K. Akaike, N. Koch, and M. Oehzelt. Fermi level pinning induced electrostatic fields and band bending at organic heterojunctions. *Applied Physics Letters*, 105(22):223303, 2014.
- [35] A. V. Akimov and O. V. Prezhdo. Nonadiabatic dynamics of charge transfer and singlet fission at the pentacene/c60 interface. *J Am Chem Soc*, 136(4):1599–608, 2014.
- [36] J. Beltran, F. Flores, and J. Ortega. The role of charge transfer in the energy level alignment at the pentacene/c60 interface. *Phys Chem Chem Phys*, 16(9):4268–74, 2014.

- [37] Fabio Bussolotti, Jinpeng Yang, Alexander Hinderhofer, Yuli Huang, Wei Chen, Satoshi Kera, Andrew T. S. Wee, and Nobuo Ueno. Origin of the energy level alignment at organic/organic interfaces: The role of structural defects. *Physical Review B*, 89(11):115319, 2014. PRB.
- [38] Yulia Krupskaya, Ignacio Gutiérrez Lezama, and Alberto F. Morpurgo. Tuning the charge transfer in fx-tenq/rubrene single-crystal interfaces. *Advanced Functional Materials*, pages n/a–n/a, 2015.
- [39] Seung Goo Lee, Hwa Sung Lee, Shichoon Lee, Chang Wan Kim, and Wi Hyoung Lee. Thickness-dependent electrical properties of soluble acene-polymer blend semiconductors. *Organic Electronics*, 24:113–119, 2015.
- [40] Jui-Fen Chang, Wei-Ren Chen, Sheng-Miao Huang, Yi-Chien Lai, Xuan-You Lai, Yaw-Wen Yang, and Chia-Hsin Wang. High mobility ambipolar organic field-effect transistors with a nonplanar heterojunction structure. *Organic Electronics*, 27:84–91, 2015.
- [41] C. R. Zhang, J. S. Sears, B. Yang, S. G. Aziz, V. Coropceanu, and J. L. Bredas. Theoretical study of the local and charge-transfer excitations in model complexes of pentacene-c60 using tuned range-separated hybrid functionals. *J Chem Theory Comput*, 10(6):2379–88, 2014.
- [42] S. Gelinas, A. Rao, A. Kumar, S. L. Smith, A. W. Chin, J. Clark, T. S. van der Poll, G. C. Bazan, and R. H. Friend. Ultrafast long-range charge separation in organic semiconductor photovoltaic diodes. *Science*, 343(6170):512–6, 2014.
- [43] S. M. Falke, C. A. Rozzi, D. Brida, M. Maiuri, M. Amato, E. Sommer, A. De Sio, A. Rubio, G. Cerullo, E. Molinari, and C. Lienau. Coherent ultrafast charge transfer in an organic photovoltaic blend. *Science*, 344(6187):1001–1005, 2014.
- [44] Chengmei Zhong, Hyosung Choi, Jin Young Kim, Han Young Woo, Thanh Luan Nguyen, Fei Huang, Yong Cao, and Alan J. Heeger. Ultrafast charge transfer in operating bulk heterojunction solar cells. *Advanced Materials*, 27(12):2036–2041, 2015.
- [45] A. Turchanin, D. Kafer, M. El-Desawy, C. Woll, G. Witte, and A. Golzhauser. Molecular mechanisms of electron-induced cross-linking in aromatic sams. *Langmuir*, 25(13):7342–52, 2009.
- [46] A. K. Geim and I. V. Grigorieva. Van der waals heterostructures. *Nature*, 499(7459):419–425, July 2013.
- [47] N. Schworer and H.C. Wolf. *Organic Molecular Solids*. Wiley-VCH, 2006.
- [48] M. Pope and C.E. Swenberg. *Electronic Processes in Organic Crystals and Polymers*. Oxford University Press, 1999.
- [49] A. Miller and E. Abrahams. Impurity conduction at low concentrations. *Phys. Rev.*, 120(3):745–755, 1960.
- [50] W. WARTA, R. STEHLE, and N. KARL. Ultrapure, high mobility organic photoconductors. *Applied Physics A-materials Science & Processing*, 36(3):163–170, 1985.
- [51] A. Virkar, S. Mannsfeld, J. H. Oh, M. F. Toney, Y. H. Tan, G. Y. Liu, J. C. Scott, R. Miller, and Z. Bao. The role of osts density on pentacene and c-60 nucleation, thin

- film growth, and transistor performance. *Advanced Functional Materials*, 19(12):1962–1970, 2009.
- [52] O. D. Jurchescu, J. Baas, and T. T. M. Palstra. Effect of impurities on the mobility of single crystal pentacene. *Applied Physics Letters*, 84(16):3061–3063, April 2004.
- [53] C. C. Mattheus, A. B. Dros, J. Baas, A. Meetsma, J. L. de Boer, and T. T. M. Palstra. Polymorphism in pentacene. *Acta Crystallographica Section C-crystal Structure Communications*, 57:939–941, August 2001.
- [54] Alex C. Mayer, Alexander Kazimirov, and George G. Malliaras. Dynamics of bimodal growth in pentacene thin films. *Phys. Rev. Lett.*, 97(10):105503–, 2006.
- [55] C. Westermeier, A. Cernescu, S. Amarie, C. Liewald, F. Keilmann, and B. Nickel. Sub-micron phase coexistence in small-molecule organic thin films revealed by infrared nano-imaging. *Nature Communications*, 5:4101, June 2014.
- [56] C. Westermeier, M. Fiebig, and B. Nickel. Mapping of trap densities and hotspots in pentacene thin-film transistors by frequency-resolved scanning photoresponse microscopy. *Advanced Materials*, 25(40):5719–+, October 2013.
- [57] Benedikt Rösner, Nina Zeilmann, Ute Schmidt, and Rainer H. Fink. Employing microspectroscopy to track charge trapping in operating pentacene ofets. *Organic Electronics*, 15(2):435–440, 2014.
- [58] S. Schiefer, M. Huth, A. Dobrinevski, and B. Nickel. Determination of the crystal structure of substrate-induced pentacene polymorphs in fiber structured thin films. *Journal of the American Chemical Society*, 129(34):10316–+, 2007.
- [59] H. Yanagisawa, T. Tamaki, M. Nakamura, and K. Kudo. Structural and electrical characterization of pentacene films on sio2 grown by molecular beam deposition. *Thin Solid Films*, 464:398–402, 2004.
- [60] W. S. Hu, Y. T. Tao, Y. J. Hsu, D. H. Wei, and Y. S. Wu. Molecular orientation of evaporated pentacene films on gold: Alignment effect of self-assembled monolayer. *Langmuir*, 21(6):2260–2266, 2005.
- [61] Y. Tsuruma, A. Al-Mahboob, S. Ikeda, J. T. Sadowski, G. Yoshikawa, Y. Fujikawa, T. Sakurai, and K. Saiki. Real-time observation and control of pentacene film growth on an artificially structured substrate. *Adv Mater*, 21(48):4996–5000, 2009.
- [62] Daniel Käfer, Lars Ruppel, and Gregor Witte. Growth of pentacene on clean and modified gold surfaces. *Physical Review B*, 75(8), 2007.
- [63] T. Yasuda, T. Goto, K. Fujita, and T. Tsutsui. Ambipolar pentacene field-effect transistors with calcium source-drain electrodes. *Applied Physics Letters*, 85(11):2098–2100, September 2004.
- [64] W. KRATSCHEMER, L. D. LAMB, K. FOSTIROPOULOS, and D. R. HUFFMAN. Solid c-60 - a new form of carbon. *Nature*, 347(6291):354–358, September 1990.
- [65] H. W. KROTO, J. R. HEATH, S. C. OBRIEN, R. F. CURL, and R. E. SMALLEY. C-60 - buckminsterfullerene. *Nature*, 318(6042):162–163, 1985.
- [66] M. T. Dang, L. Hirsch, and G. Wantz. P3ht:pcbm, best seller in polymer photovoltaic

- research. *Advanced Materials*, 23(31):3597–3602, August 2011.
- [67] P. A. HEINEY. Structure, dynamics and ordering transition of solid c-60. *Journal of Physics and Chemistry of Solids*, 53(11):1333–1352, November 1992.
- [68] W. I. F. DAVID, R. M. IBBERSON, J. C. MATTHEWMAN, K. PRASSIDES, T. J. S. DENNIS, J. P. HARE, H. W. KROTO, R. TAYLOR, and D. R. M. WALTON. Crystal-structure and bonding of ordered c60. *Nature*, 353(6340):147–149, September 1991.
- [69] X. M. Zhang, S. Mizukami, T. Kubota, Q. L. Ma, M. Oogane, H. Naganuma, Y. Ando, and T. Miyazaki. Observation of a large spin-dependent transport length in organic spin valves at room temperature. *Nature Communications*, 4:1392, January 2013.
- [70] G. Priebe, B. Pietzak, and R. Konenkamp. Determination of transport parameters in fullerene films. *Applied Physics Letters*, 71(15):2160–2162, October 1997.
- [71] A. Tapponnier, I. Biaggio, and P. Guľnter. Ultrapure c[sub 60] field-effect transistors and the effects of oxygen exposure. *Applied Physics Letters*, 86(11):112114, 2005.
- [72] T. A. Witten and L. M. Sander. Diffusion-limited aggregation, a kinetic critical phenomenon. *Phys. Rev. Lett.*, 47(19):1400–1403, November 1981.
- [73] J. A. VENABLES, G. D. T. SPILLER, and M. HANBUCKEN. Nucleation and growth of thin-films. *Reports On Progress In Physics*, 47(4):399–459, 1984.
- [74] Z. Y. Zhang and M. G. Lagally. Atomistic processes in the early stages of thin-film growth. *Science*, 276(5311):377–383, 1997.
- [75] S.M. Sze. *Physics of Semiconductor Devices*, 2nd ed. Wiley, New York, 1981.
- [76] K.F. Brennan. *The Physics of Semiconductors - With Applications to Optoelectronic Devices*. Cambridge University Press, 1999.
- [77] T. Breuer and G. Witte. Diffusion-controlled growth of molecular heterostructures: Fabrication of two-, one-, and zero-dimensional c-60 nanostructures on pentacene substrates. *Acs Applied Materials & Interfaces*, 5(19):9740–9745, October 2013.
- [78] J. Als-Nielsen and D. McMorrow. *Elements of Modern X-ray Physics*. John Wiley & Sons, 2000.
- [79] H. Dosch, B. W. Batterman, and D. C. Wack. Depth-controlled grazing-incidence diffraction of synchrotron x radiation. *Phys Rev Lett*, 56(11):1144–1147, 1986.
- [80] H. Dosch. Evanescent absorption in kinematic surface bragg diffraction. *Physical Review B*, 35(5):2137–2143, 1987.
- [81] I. K. Robinson and D. J. Tweet. Surface x-ray-diffraction. *Reports on Progress in Physics*, 55(5):599–651, 1992.
- [82] George H. Vineyard. Grazing-incidence diffraction and the distorted-wave approximation for the study of surfaces. *Physical Review B*, 26(8):4146–4159, 1982.
- [83] R. Ruiz, B. Nickel, N. Koch, L. C. Feldman, Jr. Haglund, R. F., A. Kahn, F. Family, and G. Scoles. Dynamic scaling, island size distribution, and morphology in the aggregation regime of submonolayer pentacene films. *Phys Rev Lett*, 91(13):136102, 2003.
- [84] Aldo Brillante, Ivano Bilotti, Raffaele Guido Della Valle, Elisabetta Venuti, Alberto

- Girlando, Matteo Masino, Fabiola Liscio, Silvia Milita, Cristiano Albonetti, Pasquale D'Angelo, Arian Shehu, and Fabio Biscarini. Structure and dynamics of pentacene on sio₂: From monolayer to bulk structure. *Physical Review B*, 85(19), 2012.
- [85] S. Bommel, N. Kleppmann, C. Weber, H. Spranger, P. Schafer, J. Novak, S. V. Roth, F. Schreiber, S. H. Klapp, and S. Kowarik. Unravelling the multilayer growth of the fullerene c60 in real time. *Nat Commun*, 5:5388, 2014.
- [86] F. Dinelli, M. Murgia, P. Levy, M. Cavallini, F. Biscarini, and D. M. de Leeuw. Spatially correlated charge transport in organic thin film transistors. *Phys Rev Lett*, 92(11):116802, 2004.
- [87] Matthias Fiebig, Daniel Beckmeier, and Bert Nickel. Thickness-dependent in situ studies of trap states in pentacene thin film transistors. *Applied Physics Letters*, 96(8):083304, 2010.
- [88] T. Cramer, A. Kyndiah, A. Kloes, M. Murgia, B. Fraboni, and F. Biscarini. Charge density increase in submonolayer organic field-effect transistors. *Physical Review B*, 91(20), 2015.
- [89] J. Quintanilla. Measurement of the percolation threshold for fully penetrable disks of different radii. *Phys Rev E Stat Nonlin Soft Matter Phys*, 63(6 Pt 1):061108, 2001.
- [90] R. M. Ziff. Spanning probability in 2d percolation. *Phys Rev Lett*, 69(18):2670–2673, 1992.
- [91] P. N. Suding and R. M. Ziff. Site percolation thresholds for archimedean lattices. *Physical Review E*, 60(1):275–283, 1999.
- [92] G. Horowitz and P. Delannoy. An analytical model for organic-based thin-film transistors. *Journal of Applied Physics*, 70(1):469–475, 1991.
- [93] G. Horowitz, R. Hajlaoui, H. Bouchriha, R. Bourguiga, and M. Hajlaoui. The concept of "threshold voltage" in organic field-effect transistors. *Adv. Mater.*, 10(12):923f, 1998.
- [94] G. Horowitz, P. Lang, M. Mottaghi, and H. Aubin. Extracting parameters from the current-voltage characteristics of field-effect transistors. *Advanced Functional Materials*, 14(11):1069–1074, 2004.
- [95] M.A. Herman. Physical problems concerning effusion processes of semiconductors in molecular-beam epitaxy. *Vacuum*, 1982.
- [96] S. K. Sinha, E. B. Sirota, S. Garoff, and H. B. Stanley. X-ray and neutron-scattering from rough surfaces. *Physical Review B*, 38(4):2297–2311, 1988.
- [97] A. C. Dürr, F. Schreiber, K. A. Ritley, V. Kruppa, J. Krug, H. Dosch, and B. Struth. Rapid roughening in thin film growth of an organic semiconductor (diindenoperylene). *Physical Review Letters*, 90(1), 2003.
- [98] A. M. Hindleleh and R. Hosemann. Microparacrystals - the intermediate stage between crystalline and amorphous. *Journal of Materials Science*, 26(19):5127–5133, 1991.
- [99] Adrica Kyndiah, Tobias Cramer, Cristiano Albonetti, Fabiola Liscio, Stefano Chiodini, Mauro Murgia, and Fabio Biscarini. Charge transfer and percolation in c60/pentacene field-effect transistors. *Advanced Electronic Materials*, 1(11):n/a–n/a, 2015.

- [100] Francesco Greco, Alessandra Zucca, Silvia Taccola, Arianna Menciassi, Toshinori Fujie, Hiroki Haniuda, Shinji Takeoka, Paolo Dario, and Virgilio Mattoli. Ultra-thin conductive free-standing p-dot/pss nanofilms. *Soft Matter*, 7(22):10642, 2011.
- [101] M. Schnietz, A. Turchanin, C. T. Nottbohm, A. Beyer, H. H. Solak, P. Hinze, T. Weimann, and A. Golzhauser. Chemically functionalized carbon nanosieves with 1-nm thickness. *Small*, 5(23):2651–5, 2009.
- [102] R.A.L. Jones. *Soft Condensed Matter*. Oxford University Press, 2002.
- [103] J. C. Ashley and V. E. Anderson. Interaction of low-energy electrons with silicon dioxide. *Journal of Electron Spectroscopy and Related Phenomena*, 24(2):127–148, 1981. ISI Document Delivery No.: MP262 Times Cited: 58 Cited Reference Count: 40 Ashley, jc anderson, ve Elsevier science bv Amsterdam.
- [104] S. Tanuma, C. J. Powell, and D. R. Penn. Calculations of electron inelastic mean free paths .5. data for 14 organic-compounds over the 50-2000 ev range. *Surface and Interface Analysis*, 21(3):165–176, 1994.
- [105] H. A. Bethe. Statistical theory of superlattices. *Proceedings of the Royal Society of London A: Mathematical, Physical and Engineering Sciences*, 150(871):552–575, 1935.
- [106] J. Stejny. Radiation cross-linked paraffins and percolation model. *Macromolecules*, 17(10):2055–2062, 1984.
- [107] Christina Enengl, Sandra Enengl, Marek Havlicek, Philipp Stadler, Eric D. Glowacki, Markus C. Scharber, Matthew White, Kurt Hingerl, Eitan Ehrenfreund, Helmut Neugebauer, and Niyazi Serdar Sariciftci. The role of heteroatoms leading to hydrogen bonds in view of extended chemical stability of organic semiconductors. *Advanced Functional Materials*, 25(42):6679–6688, 2015.
- [108] Hyeok Kim, Zheng Meihui, Nicolas Battaglini, Philippe Lang, and Gilles Horowitz. Large enhancement of hole injection in pentacene by modification of gold with conjugated self-assembled monolayers. *Organic Electronics*, 14(9):2108–2113, 2013.
- [109] C. Bock, D. V. Pham, U. Kunze, D. Kačlifer, G. Witte, and Ch Wołll. Improved morphology and charge carrier injection in pentacene field-effect transistors with thiol-treated electrodes. *Journal of Applied Physics*, 100(11):114517, 2006.
- [110] Pollawat Prisawong, Peter Zalar, Amir Reuveny, Naoji Matsuhisa, Wonryung Lee, Tomoyuki Yokota, and Takao Someya. Vacuum ultraviolet treatment of self-assembled monolayers: A tool for understanding growth and tuning charge transport in organic field-effect transistors. *Adv. Mater.*, 28(10):2049–2054, 2016.
- [111] E. Menard, V. Podzorov, S. H. Hur, A. Gaur, M. E. Gershenson, and J. A. Rogers. High-performance n- and p-type single-crystal organic transistors with free-space gate dielectrics. *Advanced Materials*, 16(23-24):2097–+, 2004.
- [112] J. Lee, L. G. Kaake, J. H. Cho, X. Y. Zhu, T. P. Lodge, and C. D. Frisbie. Ion gelled polymer thin-film transistors: Operating mechanism and characterization of gate dielectric capacitance, switching speed, and stability. *Journal of Physical Chemistry C*, 113(20):8972–8981, 2009.

MERCI UND SERVUS!

Bert Nickel, ich danke Dir für Deine Förderung und Dein Vertrauen. Deine guten Ideen, Dein Interesse und Deine Gelassenheit machen es möglich in Deiner Gruppe motiviert und mit viel Freude zu forschen.

Joachim Rädler, Dein Lehrstuhl hat mir während meines Diploms und der Promotion eine vielseitige Forschungsumgebung und eine tolle Atmosphäre geboten.

Tausend Dank an meine Studenten Stefan Fischer, Michael Eder, Janina Roemer und Fabio del Giudice. Wir haben zusammen doch so einiges erkundet und dafür gesorgt, dass das was wir machen auch ein bisschen Anerkennung fand.

Stefan Fischer, als Röntgenmaster bist Du ehrlich und gelassen, sagst was Du denkst, und weißt ein Feierabendbier zu schätzen. Mit anderen Worten, mit Dir arbeitet man gerne in einer Gruppe!

Felix Segerer, Dein Charme und Dein Witz haben auch mich für Dich gewonnen. Und wenn man eine kleine Ablenkung braucht, lässt Du einen niemals hängen. Beziehungsweise im Kreis drehen ...

Lieber Philip Böhm, bleibe immer so offen und leicht. Die Welt braucht mehr von Deiner Sorte. Tout amour!

Franz "X." Werkmeister, danke Dir für viele gute Ideen. Und auch für Dein Vertrauen! Wer auch immer eine Frage zur wissenschaftlichen Literatur hat, der möge Dich fragen.

Christian Westermeier, danke für die Motivation, das Organisieren und gute Gespräche. Nur noch schnell eine Mail!

Danke Martin Göllner. Ich freue mich auf zukünftige Projekte unter Freunden, unternehmerisch, am Herd und am Tresen!

Martin Huth, Dein Enthusiasmus und Deine gute Laune sind ansteckend!

Matthias Fiebig, Mentor aller Klassen: Du hast eine Generation Nickel's geprägt.

Lieben Dank an die gesamte Nickel Gruppe, für eine tolle Zeit (und das beste Mittagessen).

Gerlinde Schwake, danke fürs Zuhören, fürs Erzählen und dafür, dass Du die Pflanzen so liebevoll gepflegt und mehr als einmal gerettet hast. Du bist klasse!

Susi Kempfer, danke Dir für eine tolle Atmosphäre im Büro. Und für das Gehirntraining, ich konnte es gut gebrauchen.

Stefan Manus, kein Gerät, dass nicht von Dir gerettet oder getuned wurde. Ein Hoch auf Fahrräder und Kaffeemaschinen!

Wilhelm Fenzl, an Deine Anekdoten werden sich viele Kollegen noch lange erinnern.

Dem Lehrstuhl Kotthaus, danke ich für den Reinraum. Philipp Altpeter, danke für Deine Unterstützung und einige gute Ideen.

Merci an die Werkstatt, besonders Christian Neubert, wir konnten mit Eurer Hilfe viele experimentelle Aufbauten genau nach unserem Geschmack entwerfen.

Ich möchte mich auch bei all denjenigen bedanken, die die Kollaborationen an denen ich mitwirken durfte möglich gemacht haben.

Habe die Ehre, liebe Braun's und Euren wunderbaren Kaffee!

Danke an den ganzen Lehrstuhl, von gestern bis heute. Es war schön!

Zu guter Letzt bin glücklich und dankbar für meine Eltern Ursel und Hans (und irgendwie auch Nellis), die mich immer unterstützen und mir Selbstvertrauen schenken, für meinen Bruder Till, und für meine Nordlichter, besonders Edith und Erwin. Ich freue mich auf alles was nun kommt, zusammen mit meiner Freundin Mareike, mit der ich bedingungslos ich selbst sein kann. Und ich bin froh über so tolle Freunde (Adrian, Robert, Martin, Alfons, Tom, Symeon und die vielen anderen, die mich begleitet haben). Mit ihnen kann ich all die anderen Charaktere leben, die in mir wohnen.